UNIVERSITY OF CALGARY

Membrane Dynamics of Inferior Colliculus Neurons in the Young Rat

by

Adrien F. Tennent

A THESIS
SUBMITTED TO THE FACULTY OF GRADUATE STUDIES
IN PARTIAL FULFILMENT OF THE REQUIREMENTS FOR THE
DEGREE OF MASTER OF SCIENCE

DEPARTMENT OF NEUROSCIENCE
CALGARY, ALBERTA
JANUARY, 2008

© Adrien François Tennent 2008

UNIVERSITY OF
CALGARY

The author of this thesis has granted the University of Calgary a non-exclusive license to reproduce and distribute copies of this thesis to users of the University of Calgary Archives.

Copyright remains with the author.

Theses and dissertations available in the University of Calgary Institutional Repository are solely for the purpose of private study and research. They may not be copied or reproduced, except as permitted by copyright laws, without written authority of the copyright owner. Any commercial use or re-publication is strictly prohibited.

The original Partial Copyright License attesting to these terms and signed by the author of this thesis may be found in the original print version of the thesis, held by the University of Calgary Archives.

Please contact the University of Calgary Archives for further information:
http://www.ucalgary.ca/archives/
Tel: (403) 220-7271

Abstract

The brain slice preparation was used to obtain whole cell recordings from neurons of the central nucleus of the inferior colliculus. Four types of spiking profiles were observed in response to depolarizing current clamp pulses, and various subthreshold and superthreshold responses indicate an Andronov-Hopf fixed point bifurcation for all four spiking response types. Frequency selectivity was observed as resonance, and is provided by both the bifurcation and the slow resonant current I_h. Additionally, subthreshold oscillations were observed at depolarized potentials, and appear to share the same frequency selective mechanism as that responsible for the resonance response. Distinct from oscillations, transient hyperpolarization (TH), and spikelet events were also observed. The mechanism underlying TH generation is likely activation of calcium activated potassium conductances following calcium induced calcium release from intracellular stores, whereas voltage gated sodium current is necessary for spikelet generation.

Acknowledgements

I would like to thank various principal investigators and fellow students of the University of Calgary department of neuroscience for the valuable education they have provided. Specifically, I would like to thank my supervisor, Dr. Bin Hu, for the opportunity to learn about the brain for the last three years, in addition to teaching me scientific self-sufficiency, and resourcefulness. As well, I thank my supervisory committee members for their patience, encouragement, and insightful suggestions.

For the sake of brevity I cannot thank all of the fellow students who have contributed to my education, however I thank Steven Peters for answers to my many questions on the topics of the brain and physiology, as well as insightful scholarly discussions and excellent camaraderie in the lab. Thanks also to Dr. Fernando Fernandez for literary and scientific guidance on the topic of nonlinear dynamics, as well as Hamish Mehaffey for the same reasons in addition to extensive comments on a rough draft of this thesis. For general advice in techniques and scientific presentation, I thank Dr. Mike Molineux and Dr. Bruce McKay.

I am also indebted to instructors outside of this department. I would also like to thank the organizers of the 2006 McGill Nonlinear Dynamics in Biological Sciences Course, which provided me an opportunity to learn and observe the usefulness of mathematical tools in understanding the function of biological systems. A large portion of my graduate education was provided by proxy from: Dr. Bard Ermentrout by means of his excellent software *XPPAUT*, Dr. Eugene Izhikevich for his readable yet comprehensive book *Dynamical Systems in Neuroscience*, and Dr. Bertil Hille for his

book *Ion Channels of Excitable Membranes*, which captured my attention during my undergraduate studies and guided me towards graduate studies in neuroscience.

The generosity of Dr. Ray Turner by way of equipment and other resources was greatly appreciated, as was the careful histological preparations by Mirna Kruskic, and the confocal microscope provided by Dr. Minh Dang Nguyen. For the curse of curiosity and careful investigations, I thank my parents and other role models including Dr. Dorothy Paul, Dr. Jim Plant, and Dr. Gerry Poulton. Last but not least, I am also grateful to the provincial government of Alberta and the Canadian federal government for all financial support, without which these pursuits of curiosity would not be possible.

Table of Contents

Approval Page ii
Abstract iii
Acknowledgements iv
Table of Contents vi
List of Figures and Illustrations ix
List of Symbols, Abbreviations and Nomenclature xiv
Epigraph xviii

CHAPTER ONE: GENERAL INTRODUCTION 1
- 1.1 Neural-computation 1
- 1.2 The Central Auditory System: An Overview 1
  - 1.2.1 The Cochlea and Auditory Nerve 2
  - 1.2.2 The Cochlear Nucleus 3
  - 1.2.3 The Olivary Complex 3
  - 1.2.4 The Lateral Lemniscal Nuclei 4
  - 1.2.5 The Inferior Colliculus 5
  - 1.2.6 The Medial Geniculate Body 7
  - 1.2.7 The Auditory Cortex 8
- 1.3 Physiology of ICC Neurons: Coding of Sound Features 10
- 1.4 ICC Neuron Firing Properties and Voltage Gated Conductances 10
- 1.5 Biophysics Governing Subthreshold Dynamics and Action Potential Generation 12
  - 1.5.1 Ion Channels: Description of Dynamics 12
  - 1.5.2 Neuronal Conductance Models 18
  - 1.5.3 Dynamical Systems Theory and Neuronal Spiking 23
    - 1.5.3.1 Rationale for Identification of Fixed Point Bifurcations in Neurons 29
  - 1.5.4 Resonance 32
- 1.6 Hypotheses and Objectives 39

CHAPTER TWO: EXPERIMENTAL PROCEDURES 43
- 2.1 Brain Slice and Intracellular Recordings 43
  - 2.1.1 Offline Adjustments of Recordings 45
- 2.2 Stimulus Protocols 46
- 2.3 Analysis of Intracellular Recordings 47
  - 2.3.1 Calculation of Impedance Profiles: Spectral Techniques, their Validation, and Confidence Intervals. 47
    - 2.3.1.1 Test for Stationarity. 48
    - 2.3.1.2 Estimation of Confidence Intervals 49
  - 2.3.2 Analysis of Spiking Responses to Pulse and Ramp Current Clamp Stimuli 50
  - 2.3.3 Analysis of subthreshold oscillations (STOs) 51
- 2.4 Modeling 51
- 2.5 Histology and Fluorescence Imaging 52
- 2.6 Figures and Statistics 53

CHAPTER THREE: FIRING RESPONSES AND THE GOVERNING ION CHANNEL DYNAMICS 54

3.1 Overview 54
3.2 Results: Firing Response Profiles, and the Separation of Firing Response Types 54
  3.2.1 Separation of the Onset Response from Tonic Responses 55
  3.2.2 The Onset Response and Insight into its Mechanism 72
  3.2.3 The Adaptive Response and Insight into its Mechanism 77
  3.2.4 The Accelerating Response and Insight into its Mechanism 86
3.3 Results: Subthreshold and Firing Properties for Identification of the Fixed Point Bifurcation 89
  3.3.1 The Steady-State Membrane Voltage Input Current Relationship 89
  3.3.2 Bistability 92
  3.3.3 Minimum Spiking Frequency, and Gain 105
  3.3.4 Subthreshold Oscillations 108
  3.3.5 First Spike Latency 140
3.4 Summary of Results 148
3.5 Discussion 149
  3.5.1 Firing Response Types in the ICC 149
  3.5.2 Identity of the Fixed Point Bifurcation 154
  3.5.3 Why is the Identity of the Fixed Point Bifurcation Important? 159

CHAPTER FOUR: TEMPORAL FILTERING AND RESONANCE 164
4.1 Overview 164
4.2 Results 165
  4.2.1 Calculation of the Impedance Profile 165
  4.2.2 Parameters of the Impedance Profiles 172
  4.2.3 Effect of Mean Membrane Voltage on Resonance 180
  4.2.4 Mechanism of Resonance: Voltage Gated Ion Channels. 202
    4.2.4.1 The Role of I_h Current in the Resonance Response 202
    4.2.4.2 The Role of Voltage Gated Calcium Current in the Resonance Response 210
    4.2.4.3 The Role of Voltage Gated Sodium Current in the Resonance Response 215
4.3 Summary of Results 218
4.4 Discussion 218
  4.4.1 Functional Role of Subthreshold Frequency Selectivity 223

CHAPTER FIVE: SPONTANEOUS STOCHASTIC EVENTS IN ICC NEURONS (TRANSIENT HYPERPOLARIZATIONS, AND SPIKELETS) 225
5.1 Overview 225
5.2 Results 225
  5.2.1 Characteristics of Transient Hyperpolarizations 225
    5.2.1.1 The Transient Hyperpolarization Waveform 225
    5.2.1.2 Voltage Dependence 233
    5.2.1.3 Transient Hyperpolarizations Observed in Firing Response Types 240
  5.2.2 Characteristics of Spikelets 240
  5.2.3 Mechanism of Transient Hyperpolarizations 247
    5.2.3.1 Synaptic Receptors: A Mechanism for Transient Hyperpolarizations? 247

5.2.3.2 Voltage Gated Ion Channels: A Mechanism for Transient Hyperpolarizations? 250
5.2.4 Mechanism of Spikelets 258
5.2.4.1 Voltage Gated Ion Channels: A Mechanism for Spikelets? 258
5.3 Summary of Results 261
5.4 Discussion 262
5.4.1 Mechanism of Transient Hyperpolarization Generation 263
5.4.1.1 Proposed Experiments to Determine the Mechanism of TH Generation 266
5.4.2 The Functional Role of Transient Hyperpolarizations 269
5.4.3 Spikelets: Mechanism....270
5.4.4 Spikelets: Functional Role....271

CHAPTER SIX: GENERAL DISCUSSION....272
6.1 Overview....272
6.2 Firing Responses and the Governing Ion Channel Dynamics 273
6.3 Temporal Filtering and Resonance 275
6.4 Spontaneous Stochastic Events in ICC Neurons (Transient Hyperpolarizations, and Spikelets)....278
6.5 Association of Neurochemistry to Firing Response Types 279
6.6 Conclusion 281

APPENDIX A: INTRACELLULAR BIOTIN LABELLING....283

REFERENCES 284

List of Figures and Illustrations

Figure 1.1 Circuit model of a neuron describing a generic conductance......................... 13

Figure 1.2 Voltage dependent parameters that define the dynamics of a low threshold potassium channel. 19

Figure 1.3 Circuit describing the conductance based model. 21

Figure 1.4 Phase plane diagrams of reduced sodium potassium model, with subcritical Andronov-Hopf fixed point bifurcation. 25

Figure 1.5 The Bifurcation diagram for the reduced sodium potassium model. 30

Figure 1.6 Steady state I_{DR} current relationship with membrane voltage. 34

Figure 1.7 Steady state I_{Nap} current relationship with membrane voltage. 37

Figure 3.1 Instantaneous spike frequency adaptation and acceleration is observed in tonic firing responses to current clamp pulse stimuli. 56

Figure 3.2 Phasic onset response proceeds to tonic firing with increased current pulse amplitude. 58

Figure 3.3 Proportion of firing response types, according to the instantaneous firing frequency profile. 60

Figure 3.4 Phasic and tonic responses were separated by the range of current pulse amplitudes that evoke a single spike, the onset-range. 62

Figure 3.5 Onset-range and τ_{APH} are non-normally distributed. 65

Figure 3.6 Exponential fits of subthreshold membrane voltage responses to a current clamp pulse, quantification of the overshoot (OS) and after pulse hyperpolarization (APH). 67

Figure 3.7 An improvement of neuron response type separation is achieved by plotting the two measured parameters, τ_{APH} and onset-range, against each other. .. 70

Figure 3.8 A comparison of τ_{APH} between strong onset and sustained firing responses. 73

Figure 3.9 The membrane time constant τ_m of the onset response neurons is significantly smaller than that of sustained firing neurons. 75

Figure 3.10 The time constants of exponential fits to the overshoot and the after pulse hyperpolarization are similar. 78

Figure 3.11 The resting membrane voltage of the onset response neuron is significantly more hyperpolarized than that of the sustained firing response neurons. 80

Figure 3.12 Effect of I_h blockade by ZD7288 on the overshoot and after pulse hyperpolarization. 82

Figure 3.13 The instantaneous spike frequency profile of the adaptive response was fit with a bi-exponential function. 84

Figure 3.14 Adaptation was quantified by parameters of a bi-exponential fit to the instantaneous firing frequency profile. 87

Figure 3.15 The plot of steady-state membrane potential in response to steady-state input current is monotonically increasing. 90

Figure 3.16 Voltage gated sodium current is not activated in the steady state response near spike threshold. 93

Figure 3.17 Stutter firing of spikes observed in a tonic firing cell. 96

Figure 3.18 Stutter firing of observed in a cell that also exhibits an onset-range........ 98

Figure 3.19 Test for spike hysteresis, an indication of bistability. 100

Figure 3.20 Representative response to current-clamp ramp stimuli. 103

Figure 3.21 There is no difference in minimum spike frequency between response types. 106

Figure 3.22 The steady-state firing frequency to current relationship is used to measure spike frequency gain. 109

Figure 3.23 Largest spike frequency gain is observed in the accelerating response type. 111

Figure 3.24 The F-I relationship is similar when obtained by current clamp pulse or a slow ramp input. 113

Figure 3.25 Subthreshold oscillations observed in a weak onset response neuron are only present at depolarized potentials. 115

Figure 3.26 Subthreshold oscillations observed in a strong-onset response neuron are present at resting membrane potential, and the oscillation frequency is largely invariant of the mean membrane potential. 117

Figure 3.27 STO observed between spikes in the sustained firing response neuron. 119

Figure 3.28 STOs are observed before and after spiking in response to a current-clamp ramp stimulus for a narrow range of current. 121

Figure 3.29 STO frequencies are distributed between 2 and 16 Hz. 123

Figure 3.30 No difference in STO frequency was observed across cell response types. 126

Figure 3.31 The STO frequency correlates with the minimum firing frequency. 128

Figure 3.32 No correlation was observed between STO frequency and the mean membrane voltage. 130

Figure 3.33 STOs are observed despite blockade of I_h current by CsCl. 132

Figure 3.34 STOs were observed despite blockade of I_h by CsCl. 134

Figure 3.35 Blockade of voltage gated sodium channels by tetrodotoxin abolished STOs. 136

Figure 3.36 Application of TTX abolishes STOs. 138

Figure 3.37 The maximum FSL is longest in the accelerating response type, shortest in the onset type, and jumps in the FSL were observed in the accelerating response type. 141

Figure 3.38 Jumps in latency are observed in the accelerating response type. 143

Figure 3.39 The maximum latency of the onset response type is significantly smaller than the adaptive type. 145

Figure 4.1 Impedance profile calculated from a ZAP input protocol. 166

Figure 4.2 Impedance profile calculated from a LPFGWN input protocol. 168

Figure 4.3 Spectral estimates calculated for the LPFGWN stimulus are superior to those calculated for the ZAP stimulus, as indicated by their confidence intervals. 170

Figure 4.4 Impedance spectra are similar when obtained from either ZAP, or LPFGWN stimuli. 173

Figure 4.5 An optimal window size was obtained by calculating the Fano factor for increasing window sizes. 175

Figure 4.6 A representative impedance profile with the measured parameters indicated. 177

Figure 4.7 A peak in the impedance profile is observed for neurons that exhibit resonance. 181

Figure 4.8 Resonance was observed across different firing response types, and was most common to the onset response type. 183

Figure 4.9 Resonance is most often observed amongst neurons of the strong-onset response category. 185

Figure 4.10 Strong-onset response neurons exhibit stronger resonance behaviour. 187

Figure 4.11 The impedance profile is independent of the low pass filter cut-off frequency. 190

Figure 4.12 Resonance was observed in impedance profiles of strong-onset response type neurons despite manipulation of the mean membrane potential. 192

Figure 4.13 Strong onset response neurons did not exhibited any trend with respect to the mean membrane potential for the four impedance profile measurements (F_r, Q, W, and Zmax). 194

Figure 4.14 Resonance was observed in impedance profiles of adaptive response type neurons despite manipulation of the mean membrane potential. 196

Figure 4.15 No trends were observed with respect to the mean membrane potential for the four impedance profile measurements (F_r, Q, W, and Zmax) in the adaptive firing response neurons. 198

Figure 4.16 I_h blockade reduces the resonance response, as observed in the impedance profile. 200

Figure 4.17 Effect of I_h blockade on the impedance profile measurements. 204

Figure 4.18 Blockade of I_h reduces hyperpolarization induced sag, yet a rebound depolarization remains. 206

Figure 4.19 Resonance observed in a conductance model with leak and I_h current. 208

Figure 4.20 I_{CaLVA} blockade reduces the resonance response, as observed in the impedance profile of a strong-onset response neuron. 211

Figure 4.21 Effect of I_{CaLVA} blockade on the impedance profile measurements of a strong-onset response neuron. 213

Figure 4.22 Blockade of voltage gated sodium channels attenuates resonance at depolarized, but not hyperpolarized voltages. 216

Figure 5.1 The uniform waveform of transient hyperpolarizations. 227

Figure 5.2 Quanta were not observed in either the distribution of transient hyperpolarization amplitude or minimum slope. 229

Figure 5.3 The time course of the waveform is similar between the after hyperpolarization and the transient hyperpolarization. 231

Figure 5.4 Transient hyperpolarizations exhibit strong voltage dependence. 234

Figure 5.5 Transient hyperpolarization event frequency correlates positively with the mean membrane potential. 236

Figure 5.6 Transient hyperpolarizations were also observed in voltage clamp. 238

Figure 5.7 The estimated TH reversal potential is lower than the chloride equilibrium potential. 241

Figure 5.8 TH were most often observed in the accelerating response type, and less so in adaptive and onset response types. 243

Figure 5.9 Spikelet event frequency correlates positively with the mean membrane potential. 245

Figure 5.10 The time course of the waveform is similar between the spikelet and the TH. 248

Figure 5.11 THs remained despite either increasing the concentration of synaptic blockers, or switching picrotoxin for bicuculline. 251

Figure 5.12 The transient hyperpolarizations are insensitive to voltage gated sodium channel blockade by TTX. 253

Figure 5.13 Transient Hyperpolarizations are insensitive to both KIR blockade with barium, and calcium channel blockade with cadmium. 256

Figure 5.14 Spikelets are abolished following blockade of voltage gated sodium channels by TTX 259

List of Symbols, Abbreviations and Nomenclature

Symbol	***Definition***
2-APB	2-aminoethoxydiphenyl
AC	auditory cortex
ACh	acetylcholine
ACSF	artificial cerebral spinal fluid
AH	Andronov-Hopf
AM	amplitude modulation
AN	auditory nerve
ANOVA	analysis of variance
AP5	DL-2-amino-5-phosphopentanoic acid
APH	after pulse hyperpolarization
ATP	adenosine-5'-triphosphate
A_x	generic amplitude term for exponential fitting
BK	big conductance calcium and voltage-activated potassium channels
cAMP	adenosine monophosphate
CAS	central auditory system
CGP55845	((2*S*)-3-[[(1*S*)-1-(3,4-dichlorophenyl)ethyl]amino-2-hydroxypropyl](phenylmethyl)phosphinic acid
CICR	calcium induced calcium release
CN	cochlear nucleus
CPA	cyclopiazonic acid
DCIC	dorsal cortex of the inferior colliculus
DMSO	dimethyl sulfoxide
DNQX	6,7-dinitroquinoxalinedione
EBIO	1-ethyl-2-benzimidazolinone
E_{Cl}	chloride reversal potential
E_{IPSP}	inhibitory postsynaptic potential reversal
E_K	potassium reversal potential
E_K	potassium reversal potential
E_{Na}	sodium reversal potential
E_r	generic reversal potential
E_x	generic reversal potential
F	Faraday constant 96,485•coulomb/mole
f(t)	time dependent frequency modulation
f_{max}	maximum modulation frequency
fo	minimum modulation frequency
F_r	resonant frequency
FS	fast spiking neuron
FSL	first spike latency
F_w	window Fano factor
$f(w)$	power spectral density
$\hat{f}(w)$	power spectral density estimate

GABA	gamma-aminobutyric acid
GABA_A	type A gamma-aminobutyric acid receptor
λ_k	window weights for windowed averaging spectral analysis
GDP	guanosine diphosphate
GDP-β-S	guanosine-5’-*O*-(2-thiodiphosphate)
g_K	potassium conductance
g_l	leak conductance
g_{Na}	sodium conductance
GTP	guanosine-5'-triphosphate
$\bar{g}_x$	maximal conductance
$g_x(V)$	generic voltage dependent conductance
h	probability of the inactivation gate, specific to I_h current, being in a state conducive to closing the ion channel
HEPES	*4-(2-hydroxyethyl)-1-piperazineethanesulfonic acid*
HH	the Hodgkin-Huxley model
IC	inferior colliculus
I_{CaLVA}	low voltage activated calcium current
ICC	central nucleus of the inferior colliculus
I_{DR}	delayed rectifier potassium current
$iFreq(t)$	instantaneous firing (spiking) frequency
I_h	Hyperpolarization activated cyclic nucleotide dependent mixed cation current
I_K	voltage gated potassium current
I_{Na}	voltage gated sodium current
I_{Nap}	persistent sodium current
IP3	inositol triphosphate
IPSP	inhibitory postsynaptic potential
ISI	interspike interval
Iss	steady state input current
I_x	current of the generic ionic specie x, conducted by the generic conductance g_x
k	sample index
Kv1.x	potassium channel principle subunits responsible for delayed rectifier current
LLN	lateral lemniscal nuclei
LNIC	lateral nucleus of the inferior colliculus
LPFGWN	low pass filtered Gaussian white noise
LSO	lateral superior olive
m	probability of the inactivation gate being in a state conducive to closing the ion channel
M	number of samples for windowed averaging spectral analysis

mACh	muscarinic acetylcholine receptor (metabotropic)
mesV	Mesencephalic trigeminal sensory neurons
MG	medial geniculate
MGB	medial geniculate body
MGd	dorsa division of the medial geniculate
MGm	medial division of the medial geniculate
MGv	ventral division of the medial geniculate
minis	action potential independent miniature postsynaptic
MSO	medial superior olive
μ_w	window mean
n	probability of the activation gate being in a state conducive to opening the ion channel
N	total number of samples recorded
$n_\infty(V)$	voltage dependent steady state activation for the activation gate n
OC	olivary complex
OS	overshoot, at the onset of a current-clamp pulse
p	number of activation gates contained in the ion channel
P	probability
PB	phosphate buffer
PIN	posterior intralaminar nucleus of the thalamus
PSD	power spectral density
q	number of inactivation gates contained in the ion channel
Q	sharpness of the frequency selectivity, the ration of the maximum impedance over the input resistance
R	gas constant, ($8.314 J \bullet K^{-1} mol^{-1}$)
R^2	coefficient of determination
RC	resistance-capacitance product
R_{in}	input resistance
RMS	root mean square
RS	regular spiking neuron
σ_w	window standard deviation
SK	small conductance calcium and voltage-activated potassium channels
SMOC	spontaneous miniature outward currents
SN	saddle-node
STO	subthreshold oscillation
STOC	spontaneous transient outward currents
T	temperature (degrees Kelvin)
T	duration of the ZAP stimulus

τ_{APH}	time constant of the after pulse hyperpolarization
τ_m	membrane time constant
$\tau_n(V)$	voltage dependent time constant of the activation gate n
τ_{OS}	time constant of the overshoot
τ_x	generic time constant for exponential fitting
TEA	tetraethylammonium
TH	TH
Tris	trishydroxymethylaminomethane (2-amino-2-hydroxymethyl-1,3-propanediol)
TTX	tetrodotoxin
V	membrane potential, voltage
v	number of degrees of freedom
$V_{1/2}$	voltage of half maximal activation
V_A	arbitrary voltage
VGCC	voltage gated calcium channel
Vss	steady state membrane potential
W	width of the resonance peak, the measured distance between points on the impedance profile equal to the input resistance
X	generic ion
$X(w)$	amplitude spectrum
χ^2	Chi square
Z	valence
ZAP	impedance amplitude profile
Z_{max}	the maximum impedance
α	confident interval
π	3.1412 (Pi)

Epigraph

"...[neural properties] are invariant under continuous, one-to-one transformations of the coordinates of phase space and fall within the domain of topology, a branch of mathematics which may be intrinsically better fitted for the preliminary description and classification of biological systems than analysis, which includes differential equations. This suggestion is of little practical value at present, since too little is known of the topology of vector fields in many-dimensional spaces, at least to those interested in theoretical biology. Nevertheless, the most logical procedure in the description of a complex biological system might be to characterize the topology of its phase space, then to establish a set of physically identifiable coordinates in the space, and finally to fit differential equations to the trajectories, instead of trying to reach this final goal at one leap."

Richard FitzHugh

Mathematical Models of Threshold Phenomena in the Nerve Membrane,

Bulletin of Mathematical Biophysics (1955)

Chapter One: General Introduction

1.1 Neural-computation

Understanding the biophysical basis and computational implications of spike generation is a central issue in the study of the nervous system. The underlying decision of when and how to fire a spike is brought about by linear and nonlinear computations translating synaptic input. Not all neurons are the same, either in terms of their responses to synaptic input, or their computational role in a functioning network. These realizations engender a desire to understand the roles of intrinsic voltage gated ion channels and their interactions in the generation of a spike.

In this study, we investigate the diversity of spike firing responses in the central nucleus of the inferior colliculus, and wish to gain a description of the temporal filtering of synaptic currents associated with each of these firing responses. In addition, we seek a dynamical description of the firing response of these cells, which offers insight into the interactions of the non-linear elements (e.g. voltage gated conductances) that govern spiking and provide a basis for constructing conductance models of these neurons.

This introduction has two major components: an overview of the auditory system with specific detail paid to the inferior colliculus, and a description of voltage gated currents and their role in the dynamics governing spike firing.

1.2 The Central Auditory System: An Overview

The central auditory system (CAS) is composed of a complicated network of projections between the cochlea, multiple brainstem nuclei, the midbrain, the thalamus, and the cortex. In addition to bilateral projections from most nuclei, all of these projections are bidirectional, in that they have both ascending and descending projections. This synaptic complexity is unrivalled by other sensory systems, including the visual system, and in spite of this daunting complexity the auditory pathway can be treated as seven interrelated parts with distinguishing features in terms of response properties, neurochemical identity, separation of information streams, and integration with other modalities. These parts are: the cochlea and auditory nerve (AN), the cochlear nucleus (CN), the olivary complex (OC), the lateral lemniscal nuclei (LLN), the inferior colliculus (IC), the medial geniculate body (MG), and the auditory cortex (AC). A simplified description of the subthalamic ascending auditory pathway proceeds as a divergence of the auditory information from the auditory nerve at the cochlear nucleus, subsequent projection to all auditory brainstem nuclei, and convergence of auditory information from all auditory brainstem nuclei at the level of the IC (Winer and Schreiner 2005). Two parallel streams of auditory information emerge amongst these nuclei. The neurons of the lemniscal stream respond to tonotopic, temporal, and amplitopic features of sound, whereas those of the nonlemniscal stream represent biologically relevant features of sound, and form centers in which interaction with other sensory modalities occur (Hu 2003; Shore and Zhou 2006; Zhou and Shore 2006).

1.2.1 The Cochlea and Auditory Nerve

In the peripheral auditory system, an incoming acoustic signal is transmitted mechanically to the cochlea where it is encoded by spikes at the auditory nerve by highly complex transformations. It is well established that the primary role of the cochlea is separation of spectral information prior to transmission via the auditory nerve, and the transmission capacity of the auditory nerve serves as a bottle neck for auditory information. It seems likely, from the combination of theoretical and experimental work on auditory nerve responses to different classes of sound, that a complex transformation between the cochlear hair cells and the auditory nerve serves to compress the auditory space by means of extraction of relevant sound features before it is encoded by spikes (Smith and Lewicki 2005; Smith and Lewicki 2006). This compression of information is likely a theme at each of the many projections along the CAS.

1.2.2 The Cochlear Nucleus

Followed by an apparent compression of sound information at the level of the auditory nerve, the cochlear nucleus acts as a point of divergence of auditory information into new and non-equivalent maps (Osen 1972), most often while maintaining the cochlear map of tonotopy. The CN is the first stage of the CAS with intrinsic inhibition (Adams and Mugnaini 1987), which in part facilitates network feedback (Berrebi and Mugnaini 1991), and in combination with specialized postsynaptic neurons leads to different, yet distinct, response patterns to stereotypical sound stimuli, as indicated by the temporal profile of the neuronal responses (Møller et al. 1973). Such responses include complex temporal profiles like that of the pauser/buildup response of the dorsal cochlear nucleus, or the phase locked response of the anterior ventral cochlear nucleus bushy cell. These differences arise from a difference in function, which in the case of the bushy cell is to reliably reproduce the auditory nerve response, so that its output can be used to determine interaural time differences in the olivary complex on the order of microseconds.

1.2.3 The Olivary Complex

The olivary complex is the first site of binaural processing among many in the ascending auditory pathway. Interaural level and time difference are sound features extracted by the lateral superior olive (LSO) and the medial superior olive (MSO) respectively, and coincide with respective high and low frequency regions of the tonotopic (cochlear) map. These computed parameters are essential for accurate spatial localization of sound sources (Yin and Chan 1990). The structure of the bilateral input into the olivary nuclei provides the best known task-specific structures in the auditory system, where bilateral inputs from the ventral division of the cochlear nucleus arrive at different times depending on differences in propagation time along axonal delay lines. Computation is brought about by the degree of coincidence between the ipsilateral and contralateral synaptic input, which may be largely excitatory in the case of the MSO, or ipsilateral excitatory and contralateral inhibitory in the case of the LSO.

1.2.4 The Lateral Lemniscal Nuclei

The predominance of glycinergic neurons in the lateral lemniscal nuclei provides neurochemical uniqueness in comparison to other auditory brainstem nuclei. The dorsal lateral lemniscus is composed almost entirely of GABAergic neurons, whereas the ventral lateral lemniscus is composed primarily of glycinergic neurons (Saint Marie et al. 1997). The inhibitory identity of these nuclei, combined with the precision of spike timing responses in relation to sound onset, suggest an important role in processing of temporal information in its primary target, the inferior colliculus, and suggests a role for coding sound duration in the IC (Nayagam et al. 2005). The auditory system is a unique modality in the sense that it employs two chemically distinct inhibitory transmitters, although glycine as a neurotransmitter is restricted to subcollicular nuclei.

1.2.5 The Inferior Colliculus

The IC is the largest of the auditory nuclei of the vertebrate brain, and serves as a center of convergence of both ascending and descending input. It is apparent that the IC is a center of an immense amount of integration as it is an obligatory synaptic terminus for all but a very few ascending inputs to the medial geniculate body (MGB) of the thalamus (Aitkin and Phillips 1984; Malmierca et al. 2002), and receives many additional descending inputs from all auditory cortical areas (Winer et al. 1998), and MGB (Kuwabara and Zook 2000). The complexity of this integration is also apparent from the five fold larger number of neurons in comparison to auditory brainstem and thalamic nuclei (Kulesza et al. 2002), and the large number of intracollicular connections of the intrinsic and commissural variety (Aitkin and Phillips 1984; Oliver et al. 1991). This complexity suggests extensive processing of auditory information prior to ascending bilateral projection to the MGB (Andersen et al. 1980) in addition to the descending projections from the IC, which diverge to almost all brainstem nuclei, from which it receives input (Huffman and Henson 1990).

The IC is a bilateral structure that is subdivided into three principle divisions: the central nucleus (ICC), the lateral nucleus (LNIC), and the dorsal cortex (DCIC). The central nucleus is a highly myelinated region situated centrally in each of the bilateral inferior colliculi in the coronal slice, and is covered on the external borders by the lateral nucleus and dorsal cortex. The functional differences between these nuclei are a product of the different modalities that they receive. The ICC is exclusively auditory, and makes up the lemniscal auditory pathway, whereas the nonlemniscal auditory pathway is composed of the LNIC and DCIC which are both polymodal. The LNIC is polysensory, as it receives both auditory and somatosensory input (Aitkin et al. 1978), and is thought to represent an auditory space map, as is well established in the case of avian predators like the owl (Takahashi et al. 2003) (although this subdivision is referred to as the external nucleus in this species). The DCIC receives auditory input from the ICC, as well as extensive input from the cerebral auditory cortex (Winer et al. 1998). The role of the DCIC in hearing is unknown (Popper and Fay 1992; Webster et al. 1992), however it most likely acts as a center of integration of ascending and descending input, and the output may serve to influence the response of the lemniscal subdivision (ICC), as is likely the case during the experimental observation of corticofugal modulation (Yan and Suga 1998; Zhang et al. 2000; Zhou and Jen 2000; Ma and Suga 2001; Jen et al. 2002; Yan and Ehret 2002; Jen and Zhou 2003; Suga and Ma 2003; Yan 2003; Yan et al. 2005; Zhou and Jen 2005; Ma and Suga 2007).

As in the case of most subcortical auditory nuclei, the ICC contains a tonotopic map in its topography, and coincides with the layered structure of its neuropil and axonal plexi. In the case of the medial superior olive, the dendrites are arranged in sheets, whereas the dorsal cochlear nucleus and MGB exhibit greater topographic contrast with laminated structure that is defined by axonal plexi (Imig and Morel 1985; Malmierca et al. 2005). The ICC assumes the topology of the latter with fibrodendritic laminae oriented from ventrolateral to dorsomedial, and caudolateral to rostromedial. These laminae are composed of interspersed disk shaped cells and axonal plexi of ascending and intrinsic axonal fibers. The disk shaped cell dendrites are oriented in parallel with these dendrites, in contrast with the less abundant stellate cells, which are less constrained to inputs within a single lamina with dendrites that extend beyond the borders of the laminae

(Peruzzi et al. 2000). Both ascending and descending projections from the IC are topographically organized to correlate with the tonotopic arrangement of the characteristic frequency in the central nucleus of the IC (Saldana et al. 1996). To date, no correlations are known between neuronal morphology and neurochemistry or firing response type (Winer and Schreiner 2005).

1.2.6 The Medial Geniculate Body

Although segregation of lemniscal and nonlemniscal pathways arises early in the ascending auditory pathway at the level of the dorsal cochlear nucleus (Shore and Zhou 2006), the segregation is definite at the level of the MGB. The lemniscal auditory thalamus is exclusively the ventral medial geniculate (MGv), which does not have any internal connections linking it with the other nonlemniscal divisions of the MGB (Sherman and Guillery 2006): the medial (MGm), the dorsal (MGd), and the posterior intralaminar nucleus (PIN) (Hu 2003). In lieu of intrinsic connections, the MG engages in a large amount of communication with hippocampal, cortical and limbic centers. These limbic affiliations are somewhat unique to this sensory modality (Namura et al. 1997), and some anatomical evidence exits for their existence in the visual system as well (Linke et al. 1999).

The auditory thalamus has improved auditory feature selection over subthalamic auditory nuclei, as demonstrated by suppression of neuronal locking to the envelope of fluctuating noise in a phenomenon known as locking suppression (Las et al. 2005). The ability to respond preferentially to structured signals in comparison to simpler stimuli occurs more prominently in the nonlemniscal divisions, as demonstrated by presence of combination sensitive neurons in the dorsal division of the MG (Olsen and Suga 1991;

Olsen and Suga 1991; Komura et al. 2005), and may explain why these nonlemniscal regions project most diffusely to many cortical auditory areas where one might argue that the salient features extracted in the nonlemniscal region may be incorporated into multiple behavioural outcomes. The medial division projects to all cortical auditory areas, and is thus the most diffusely projected division in comparison to all divisions of the MG.

1.2.7 The Primary Auditory Cortex

The manner which the auditory cortex organizes lemniscal and nonlemniscal input is very different from that of the subcortical nuclei. Instead of segregating lemniscal and nonlemniscal inputs to specific subdivisions, afferent inputs are organized not only to specific cortical regions, but further to specific layers within these regions. The nonlemniscal medial and dorsal divisions terminate diffusely in cortical layers 1 and layer 6, and selectively in layers 3 and 4 (Kimura et al. 2003), whereas the lemniscal ventral division terminates predominantly in layers 3 and 4 (Huang and Winer 2000; Donishi et al. 2006). Horizontal connections exist between these cortical auditory regions, via horizontal cells in layers 1, 3, and 6.

The cortex has obvious control over subcortical responses by way of robust corticothalamic projections from cortical layer 6 onto the thalamus (Alitto and Usrey 2003; Sherman and Guillery 2006). This projection onto thalamic neurons is both monosynaptically excitatory and inhibitory via intermediate GABAergic neurons present in the thalamic reticular nucleus or within the thalamus itself. These descending corticothalamic connections are robust in number, and greatly outnumber those of the ascending thalamocortical projections. Additional direct control over subcortical nuclei is provided by corticofugal projections that originate from layers 5 and 6 and terminate in the IC, olivary complex, and the cochlear nucleus (Winer and Lee 2007).

Heterogeneity of neuronal spiking responses is well known at the level of the cortex, and neurochemical and morphological correlates of the spiking responses have been identified. Of the six best identified spiking responses, the regular spiking (RS) and fast spiking (FS) responses serve as good examples (Izhikevich 2007). The spiking responses are distinct in terms of the excitability class outlined by Hodgkin (Hodgkin 1948), as class I and class II respectively (Izhikevich 2007). Class I and II refer to respective continuous and discontinuous firing frequency relationships with respect to input current. Observation of spiking and additional subthreshold response characteristics has permitted the identification of the fixed point bifurcation in each of these cell types, such that appropriate models may be constructed that replicate the response characteristics. The goal of such modeling is the identification of roles of voltage gated ion channels in spiking responses, and more specifically the necessary relationships between voltage gated currents in terms of their maximal conductances, activation curves, and time constant curves (Fernandez et al. 2005; Fernandez et al. 2005; Molineux et al. 2005; Wu et al. 2005; Fernandez et al. 2007). Additionally, such models allow the creation of neuronal network models to investigate conditions sufficient to produce in vivo responses, for which a network mechanism is thought to be responsible (Izhikevich et al. 2004). A similar classification of neurons in the ICC has not been attempted, and forms one of the major objectives of this study. We believe that such a classification is of merit, given the obligate role of the IC as an obligate integrative center of ascending auditory information.

1.3 Physiology of ICC Neurons: Coding of Sound Features

The IC's position in the neuraxis of the central auditory system, as an integrative center of brainstem nuclei, suggests that it may serve a physiological role in sound feature extraction. This assumption is supported, at least partially, by the IC's improved coding of naturalistic signals in comparison to non-naturalistic ones (Escabi et al. 2003). More specifically, it is clear that the IC is capable of extracting frequency modulation (Casseday et al. 1997), amplitude modulation (AM) (Nelson and Carney 2007), and sound duration (Casseday et al. 2000). The IC is the first stage in the ascending auditory pathway with responses to sound duration.

Amplitude modulation responses are observed in the brainstem nuclei, as synchronous responses to temporal envelopes. A new coding strategy for AM is observed at the level of the IC, with the emergence of average firing rate responses in addition to synchronous responses (Joris et al. 2004). This represents a shift from temporal coding strategies to rate level coding, and is a common theme in subsequent auditory nuclei in addition to an increasing tolerance for other stimulus parameters, such as sound pressure level, modulation depth, and carrier. What role this shift plays in improvement of signal detection is yet unknown, but may play a role in improving signal detection in the presence of spectrally coherent noise at subsequent auditory nuclei, as in the phenomenon of comodulation masking release (Las et al. 2005).

1.4 ICC Neuron Firing Properties and Voltage Gated Conductances

Studies employing intracellular recording in the ICC with the goal of identifying intrinsic membrane properties have been sparse (Peruzzi et al. 2000; Sivaramakrishnan and Oliver 2001; Bal et al. 2002; Ono et al. 2005; Tan et al. 2007). Despite the relative importance of the ICC in the auditory pathway as an almost obligatory processing center of inputs from all brainstem auditory nuclei (Aitkin and Phillips 1984) and descending control from the cortex and thalamus, little is known about mechanisms underlying different firing properties in ICC neurons. In addition, there has been to date no reliable correlation between firing responses and neurochemical identities. This correlation has proven difficult given the lack of distinct morphological features (Bal et al. 2002), in spite of the use of fluorescently labelled GABAergic neurons (Ono et al. 2005).

It is known that ICC neurons are heterogeneous in their firing responses to pulse stimuli in current-clamp recordings (Peruzzi et al. 2000; Sivaramakrishnan and Oliver 2001). Such studies have grouped responses to depolarizing current pulses into categories of: onset (phasic firing), sustained (tonic firing), and pause-build (phasic firing, with a pause prior to tonic firing). In addition, a rebound response to hyperpolarizing current pulses provides another criterion for sub classification of these responses. This firing type heterogeneity is thought to be the result of expression of specific voltage gated potassium channels, where expression of an A-type current in pause-build neurons is most certain (Sivaramakrishnan and Oliver 2001). Aside from potassium channels, the hyperpolarization activated cyclic nucleotide dependent mixed cation current (I_h) is also expressed in great quantity in the ICC, and likely has a role in temporal processing of synaptic input (Koch and Grothe 2003; Koch et al. 2004). However, the role of I_h in the firing profile has been ignored (Sivaramakrishnan and Oliver 2001), as well as the role of voltage gated calcium channels (N'Gouemo and Morad 2003).

Despite the recognition of various firing responses, there has been no study to date to investigate the firing dynamics of these cells with specific concern to such parameters as the minimum firing frequency, bistability, first spike latency, nor subthreshold features such as membrane potential oscillations or resonance. These factors are crucial in determining the underlying transition from rest to firing, which in turn define the computational properties of the neuron, their behaviour to transient inputs, and their ability to synchronize to common inputs. This underlying transition, a bifurcation, is introduced in section 1.5.3.

1.5 Biophysics Governing Subthreshold Dynamics and Action Potential Generation

The purpose of this portion of the introduction is to form a basis needed to understand the observed phenomenon of resonance, spiking, and oscillations in ICC neurons. This includes a mathematical description of ion channel dynamics, and their implementation in conductance models used to evaluate explanations for neuronal firing and subthreshold behaviour.

1.5.1 Ion Channels: Description of Dynamics

A neuron is essentially a dielectric membrane with holes that can be transiently opened or closed, and allow the selective passage of certain ions. This realization allows the representation of a patch of neuronal membrane as a capacitance in parallel with conductances (Figure 1.1) (Hille 2001). The conductance term may or may not be variable. However in many cases the conductance is dependent on voltage, intracellular or extracellular modulator, or a combination of these. The battery in series with each conductance in Figure 1.1 represents the electromotive force available for the ion species to flow through the conductance. This electromotive force is referred to as the reversal potential of the conductance in question. The reversal potential is equal to the equilibrium potential in the case that the conductance is perfectly selective for the ion in question.

The equilibrium potential is calculated by the Nernst equation (Equation 1.1) given the difference in concentrations of the ion between the inside $[X]_{inside}$ and the outside $[X]_{outside}$ of the cell, the gas constant R, the temperature T, Faraday's constant F, and the valence Z of the ion (positive sign for positively charged ion). The equilibrium potential is equal to the reversal potential of the species, when the conductance is perfectly selective for the particular ion species.

$$\textbf{Equation 1.1} \quad E_x = \frac{RT}{ZF} \ln \frac{[X]_{outside}}{[X]_{inside}}$$

In the case that the conductance is not perfectly selective for a particular ion species, and the current of this conductance is of a mixed ionic species, the conductance of the other species must be taken into account, and an accurate estimate of the reversal potential is achieved with the Goldman-Hodgkin-Katz voltage-equation (Hodgkin and Katz 1949). The current through this conductance can be treated as ohmic (Equation 1.2), and produces a linear relationship between the current through the conductance and the membrane potential V in the case where the conductance term is voltage independent. This description is a close approximation within the physiological membrane potential ranges of -100 mV to +40 mV to the slightly more accurate description afforded by the nonlinear Goldman-Hodgkin-Katz current-equation (Johnston and Wu 1995).

Equation 1.2 $I_x = g_x(V - E_x)$

This linearity is illustrated by the example of doubling the membrane potential, which in turn drives twice the amount of current through the conductance. However, most ion

Figure 1.1 Circuit model of a neuron describing a generic conductance.

The dielectric property of the membrane is a thin insulator and is represented by a capacitance (C_M). The permeability of an ion species X is represented by a variable conductance g_x. The ionic species X is at different concentrations across the membrane and the conductance g_x is selective for X. There is an electromotive force (emf) imposed on this ion. Were the ion X to be positive, this electromotive force would have to be overcome in order for X to flow from the outside to the inside of the cell through the conductance g_x, given the polarity of the emf.

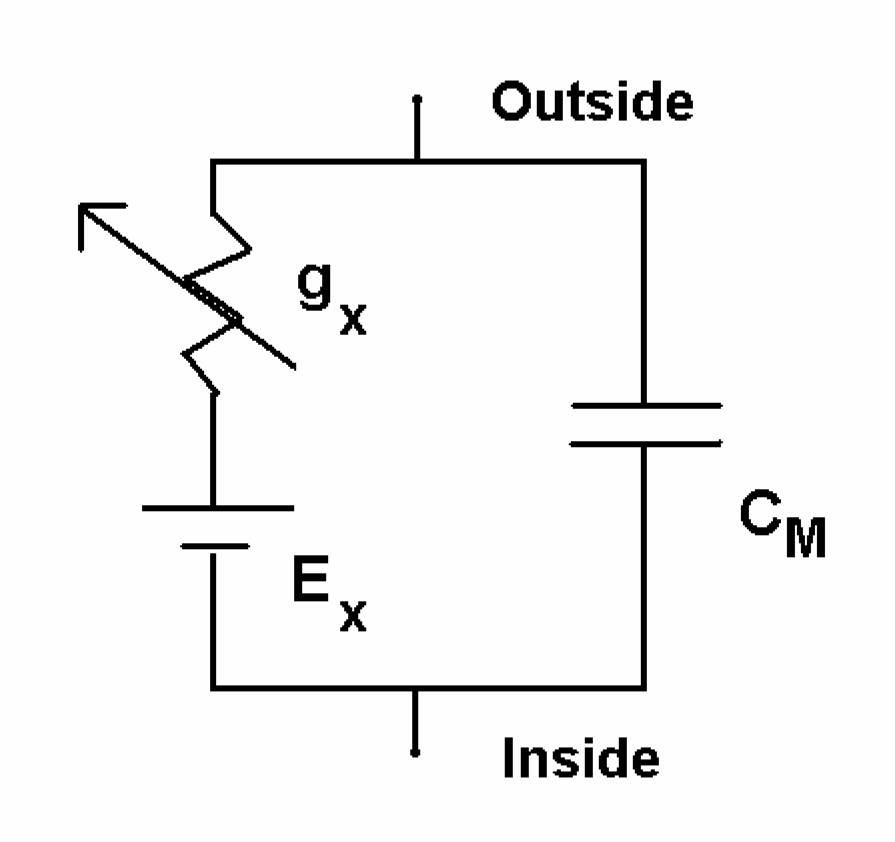
Outside
g_x
C_M
E_x
Inside

channel conductances have voltage dependence $g_x(V)$, and make the relationship described by Equation 1.2 nonlinear. The voltage dependence of these channels is afforded by voltage sensitive domains present in the ion channel (Grabe et al. 2007) that alter ion channel's transitions between open and closed conformations (Hille 2001). This voltage dependence is represented by the following equation (Hodgkin and Huxley 1952):

Equation 1.3 $I_x = n^p m^q \bar{g}_x (V - E_x)$

In this description, the channel pore is controlled by an activation gate n and an inactivation gate m, where each channel has p and q respective copies of these gates. These gates are used in likeness to the voltage sensing domains, which in reality control the state of the voltage gated channel (Hille 2001). The value of n is the probability of one activation gate being in a state conducive to opening the pore. Each of the gate probabilities are thought to be independent of each other, and the probability of all p activation gates being conducive to an open pore is n^p. Likewise, the inactivation gates control the closing of the channel. When the channel is in the maximally open state, that is $n^p m^q \to 1$, the conductance of the channel approaches the maximal conductance $\bar{g}_x$. These probabilities are voltage and time dependent, and are properly described as functions of both: $n(V,t)$, and $m(V,t)$. This dependency is governed by a first order reaction, which represents transitions between the permissive and non-permissive states, with respective $\alpha_n(V)$ and $\beta_n(V)$ rate constants, as illustrated for the n gate:

Equation 1.4 $$1 - n \underset{\beta_n(V)}{\overset{\alpha_n(V)}{\rightleftharpoons}} n$$

The mathematical description of this reaction is a first order differential equation:

Equation 1.5 $$\frac{dn}{dt} = \alpha_n(V)(1-n) - \beta_n(V)n$$

A change of variables (Equation 1.6; Equation 1.7) converts Equation 1.5 into the more tangible Equation 1.8:

Equation 1.6 $$\tau_n(V) = \frac{1}{\alpha_n(V) + \beta_n(V)}$$

Equation 1.7 $$n_\infty(V) = \frac{\alpha_n(V)}{\alpha_n(V) + \beta_n(V)}$$

Equation 1.8 $$\frac{dn}{dt} = \frac{n_\infty(V) - n(V)}{\tau_n(V)}$$

The $n_\infty(V)$ variable represents the steady state value of the n gate, that is the value of n that is reached after holding the membrane potential at a constant potential for a sufficient amount of time, and this amount of time depends on the value the time constant of the gate $\tau_n(V)$. In other words, the activation/inactivation gates do not change their values instantaneously, and their time course is constrained by their time constants $\tau_n(V)$, as depicted in the differential equation of Equation 1.8. Given sufficient time, that is several multiples of their time constant, the activation/inactivation gates will reach certain steady state probabilities $n_\infty(V)$. Variables that are constrained temporally in this manner are referred to as dynamical variables, and examples of $\tau_n(V)$, and $n_\infty(V)$ are shown in Figure 1.2 to demonstrate their voltage dependence.

1.5.2 Neuronal Conductance Models

The concept of modeling receives some animosity within the biological sciences, and is likely founded in a poor understanding of the appropriateness and limitations of a model. Succinctly, a model cannot prove a hypothesis, can only reject a hypothesis, and provides an examination of possibilities under formal constraints. The latter statement suggests it is important to implement a model with variables that represent internal parameters of the system. Specifically, it is important to use the component current and their dynamical descriptions in order to gain a respect for the roles of each of the currents, and their interactions that are responsible for the behaviour of the neuron.

A conductance based model of a neuron is essentially an expansion of Figure 1.1, where additional conductance terms are added. These additional conductances can enhance or oppose each other, with different time constants, giving rise to the wealth of neuronal dynamics observed experimentally. The equation describing the membrane potential of this conductance model is derived from Kirchhoff's current law. For the purpose of illustration, we consider a system with two conductance terms, sodium and potassium (Figure 1.3). To reduce this model to two dynamical variables, we make the assumption that the sodium conductance ($\bar{g}_{Na}m$) evolves very quickly with time, and reaches its steady state levels ($\bar{g}_{Na}m_\infty$) instantaneously and thus tracts the evolution of membrane voltage. This reduces the system to two dynamical variables, voltage V and potassium activation n as follows:

Figure 1.2 Voltage dependent parameters that define the dynamics of a low threshold potassium channel.

A) Example voltage dependent steady-state activation profile for the gating particle n is a Boltzmann equation (parameters: low threshold potassium current (Izhikevich 2007)). The voltage of half activation ($V_{1/2}$) and reversal potential for potassium is (E_k) shown. B) Example voltage dependent time constant profile (parameters: low threshold potassium current (Rothman and Manis 2003)).

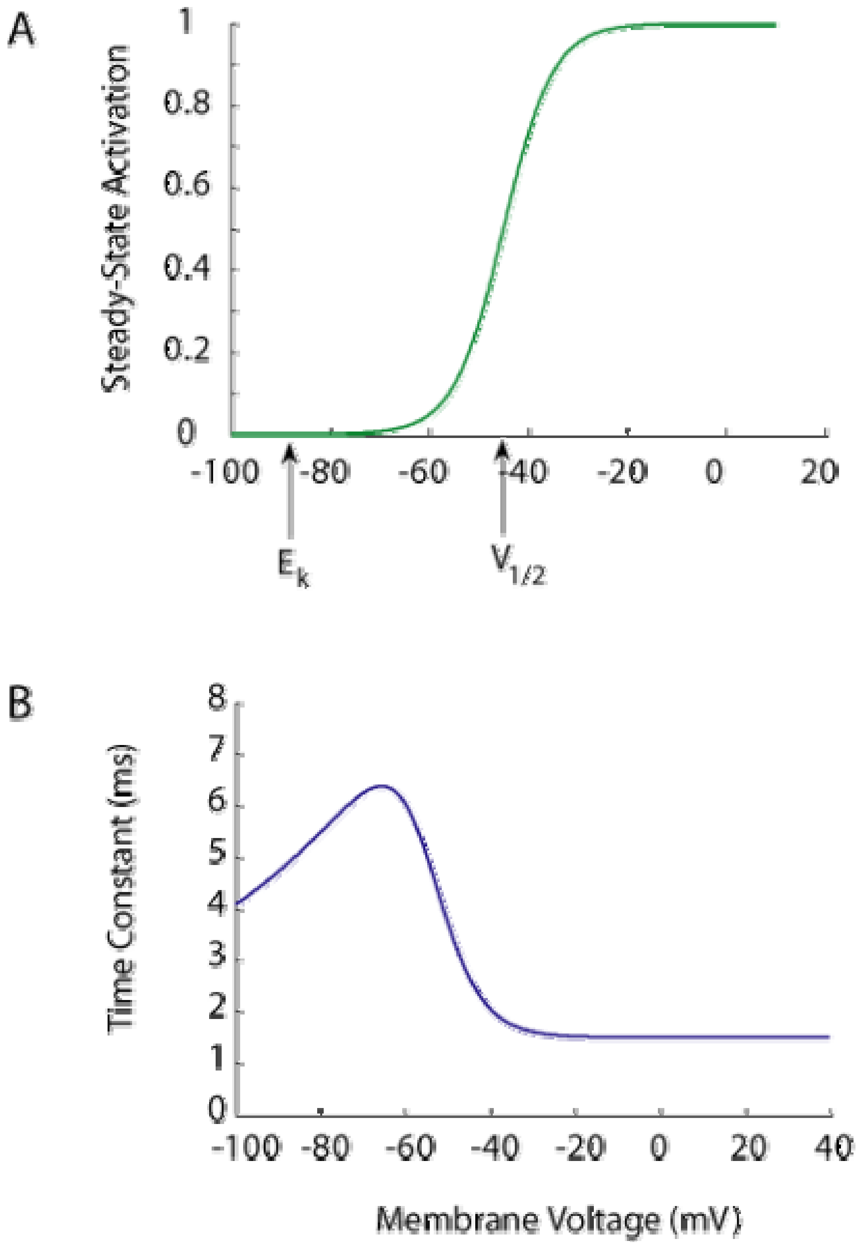
A
Steady-State Activation
1
0.8
0.6
0.4
0.2
0
-100
-80
-60
-40
-20
0
20
E_k
$V_{1/2}$
B
Time Constant (ms)
8
7
6
5
4
3
2
1
0
-100
-80
-60
-40
-20
0
20
40
Membrane Voltage (mV)

Figure 1.3 Circuit describing the conductance based model.

The generic conductance g_x has been replaced by conductances for sodium g_{Na}, potassium g_K, and leak g_l.

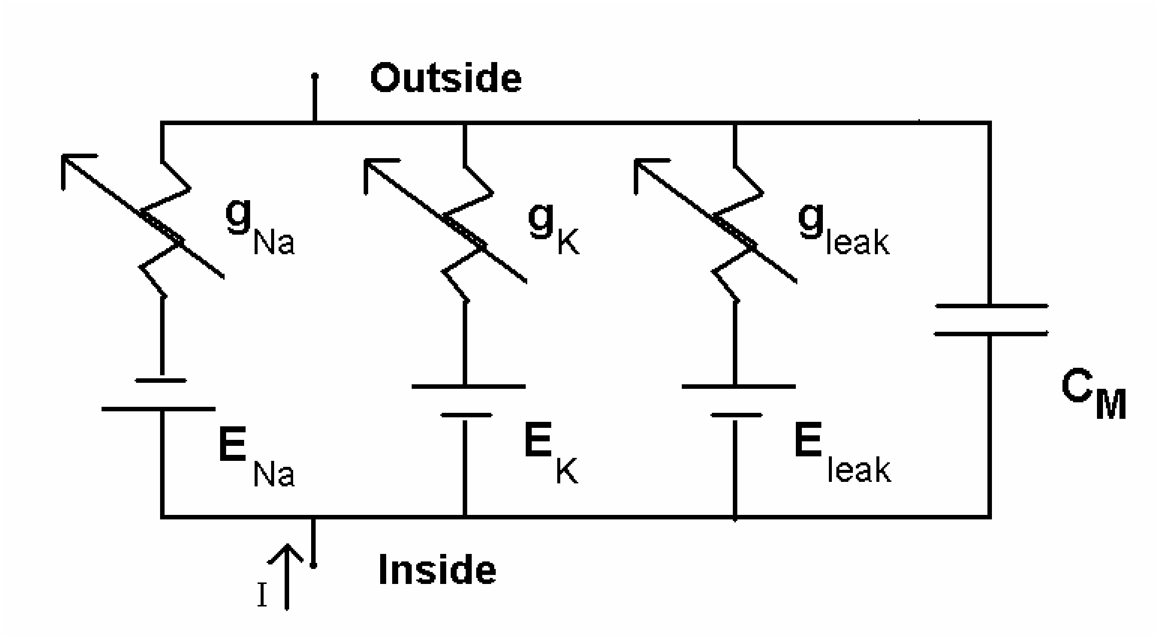
Outside
g_{Na}
g_K
g_{leak}
C_M
E_{Na}
E_K
E_{leak}
Inside
I

Equation 1.9 $$\frac{dV}{dt} = (I - \bar{g}_{Na} m_{\infty} (V - E_{Na}) - \bar{g}_{K} n \ (V - E_{k}) - \bar{g}_{leak} (V - E_{leak}))/C,$$

Equation 1.10 $$\frac{dn}{dt} = \frac{(n_{\infty} - n)}{\tau_{n}},$$

where I is the current applied by an external electrode, $\bar{g}_{Na}$ and $\bar{g}_{K}$ are the respective maximal sodium and potassium conductances, and $\bar{g}_{leak}$ is a voltage independent leak conductance.

1.5.3 Dynamical Systems Theory and Neuronal Spiking

Dynamical systems theory (also known as nonlinear dynamics) is a method for analyzing systems of differential equations (Strogatz 2000; Izhikevich 2007). A dynamical system is one whose behaviour is described by variables that are dynamic, that is, constrained by some sort of evolution with time. As described previously (see section 1.5.2), the neuronal membrane potential is adequately represented by a set of these dynamic variables (voltage, activation/inactivation gates), and their evolution in time is constrained by differential equations; in addition, the evolution of these variables is influenced by the state of the other variables such that the variables are coupled and hence form a system of differential equations. In the case of a neuronal conductance model (Equation 1.9 and Equation 1.10), the differential equations are nonlinear. Analytical solutions to nonlinear differential equations can be difficult if not impossible to obtain. Instead, a description of the voltage trajectory is often obtained using graphical techniques.

The two dimensional model of Equation 1.9 and Equation 1.10 will be used to illustrate a useful graphical technique called phase plane analysis. This technique provides a graphical description of the system, and permits predictions of how dynamical variables, such as voltage (V), will evolve with time. Before the technique is described in detail, an analogy is presented to provide the reader a sense of what is being accomplished with this technique. Considering a section of river, with water flowing in fairly complex patterns around obstacles like rocks, for some unknown reason, an experimenter would like to have a description of this flow. To accomplish this, it might be possible to drop a particle, such as a ping-pong ball, at many locations within the stream and observe the course of the particle. Subsequently the experimenter may create a flow field to describe how the particle moves in each region of the river. The phase plane technique is akin to this method in describing the behaviour of the membrane potential of the conductance model, starting from any initial condition. Furthermore, the course or flow of the ping-pong ball may change when the flow rate of the river is changed, which is also a fair analogy for the change in the behaviour of the membrane potential when the input current is changed. The parameter that affects the dynamics of the system is referred to as the bifurcation parameter, which is the flow rate in the case of the river, and the input current in the case of the neuronal conductance model.

The axes of the phase plane are the dynamic variables, and coordinates within this plane are possible values (states) of the dynamical variables (Figure 1.4). These value sets, the points in the phase plane, are subject to change with time as defined by the differential equations that describe them. To illustrate how these variables will change with time, a flow field is constructed and plotted for an array of equally spaced points in the phase plane, where the orientation of the flow at a set of variables is described by vectors that depict how a variable will evolve with time (Figure 1.4A). The slope of the

Figure 1.4 Phase plane diagrams of reduced sodium potassium model, with subcritical Andronov-Hopf fixed point bifurcation.

To demonstrate the Andronov-Hopf bifurcation, phase planes were generated with different electrode currents densities: A) 40, B) 44, and C) 60 μA/cm^2. In A), no stable limit cycle exists, and membrane potential trajectory (purple) approaches the fixed point, via a spiral, after a single spike. The flow field is indicated by vectors (black, with points on the vector heads). The V-nullcline (orange) and the N-nullcline (green) intersect at the stable fixed point. In B), an unstable limit cycle exists (blue circle), and separates the subthreshold responses from the spiking response that approaches the stable limit cycle. The subthreshold response (thin purple trajectory), and the superthreshold spiking responses (thick purple trajectory) are observed following respective initial conditions inside and outside of the unstable limit cycle. In C), the unstable limit cycle has collapsed onto the fixed point, such that only the stable limit cycle exists and initial conditions anywhere in the phase plane form trajectories that approach this stable limit cycle. See chapter 2 for details and parameters of the model.

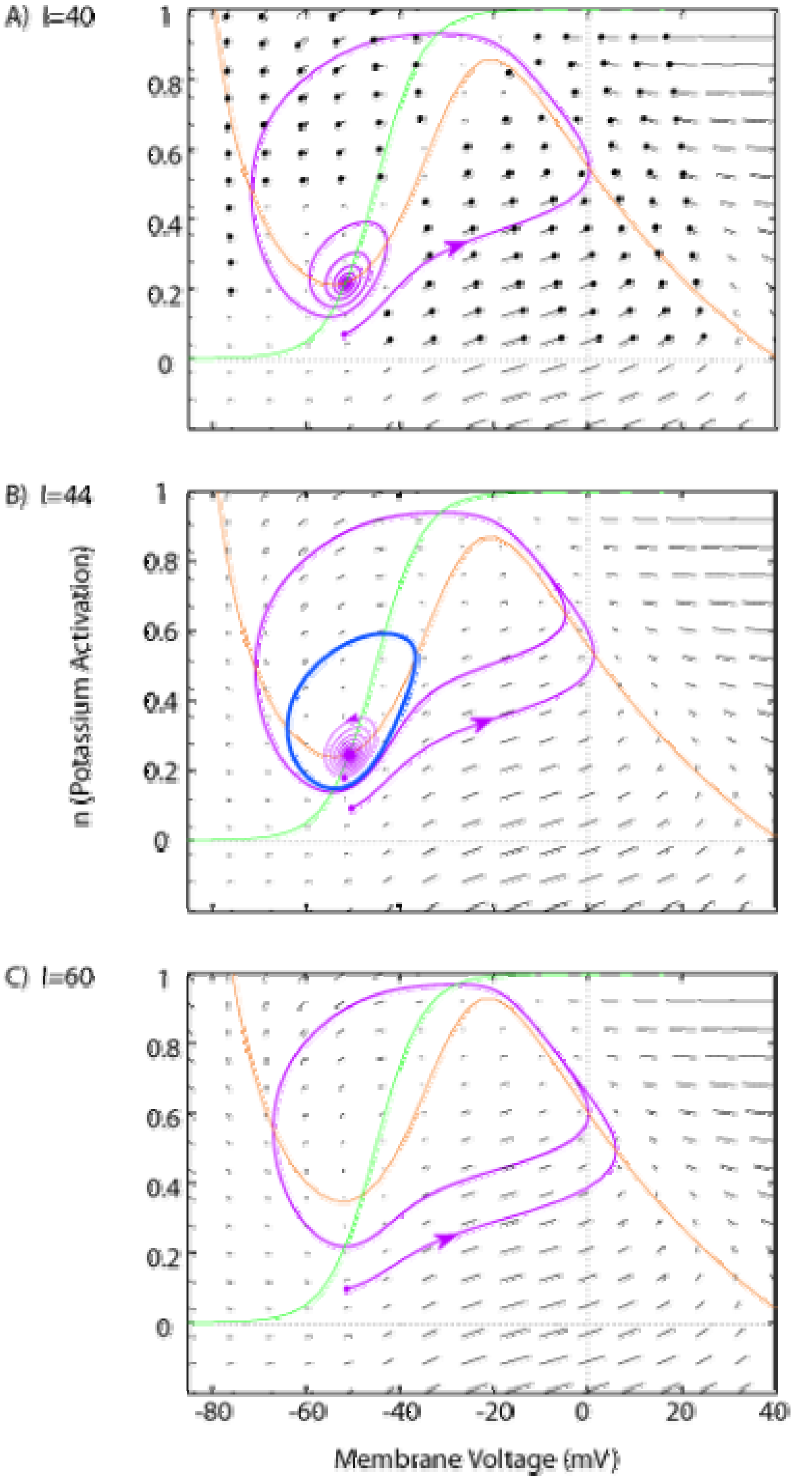
A) I=40
B) I=44
C) I=60
n (Potassium Activation)
1
0.8
0.6
0.4
0.2
0
-80
-60
-40
-20
0
20
40
Membrane Voltage (mV)

vector indicates the direction of change in the dynamical variable, and the size of the arrow indicates how quickly this evolution will occur. With the flow field description, it is possible to predict the trajectory of a system, which is how the variables will evolve and where they will end up as time approaches infinity.

The resting potential of a neuron is synonymous with a stable fixed point. Using the two dimensional conductance model (Equation 1.9; Equation 1.10) as an example, it is possible to predict the resting membrane potential by determining the region in the phase plane where all of the dynamical variables have zero rate of change, or in other words, where the differential equations are equal to zero. Nullclines are regions of the parameter space for which the differential equation is equal to zero (Figure 1.4), and the fixed point occurs where these nullclines intersect. In the situation where initial conditions close to the fixed point converge onto the fixed point, this fixed point is a stable fixed point. In other words, this fixed point is the attractor of this region of the phase plane. The nature of the fixed point determines the shape of the trajectory that approaches the fixed point, as either a node or a focus. In our example the parameters of the differential equations have been adjusted such that the fixed point is a focus, where the fixed point is approached by a spiralling trajectory (Figure 1.4A, B). The presence of a focus provides a basis by which membrane potential oscillations and resonance phenomena exist, and we will discuss these items after the introduction of some experimental results. We forgo a detailed description of the fixed point identification, and briefly mention that it is accomplished by calculation of eigenvalues of the Jacobian (Izhikevich 2007).

Of primary interest to neurobiologists is loss of fixed point stability at the point where the input current reaches the bifurcation value, where the neuron is forced into a limit cycle trajectory, or tonic spiking state (Figure 1.4C). We forgo a description of analysis of stability of the fixed point and simply mention that it requires the calculation of Lyapunov coefficients (Izhikevich 2007). The loss of fixed point stability is the result of a changing flow field brought about by increasing the bifurcation parameter, the input current. Additionally, as the flow field changes, additional attractors that take the form of continuous cycles can take form. These cycles are referred to as limit cycles, and are either stable or unstable. The stable limit cycle, is synonymous with the spiking state of the neuron, and in the condition where the input current is greater than the bifurcation value, the spiking state is the only attractive region of the phase plane (Figure 1.4C). The limit cycle in this case represents tonic firing. In our example, in which the dynamics are known as a subcritical Andronov-Hopf bifurcation (AH bifurcation), two attractors, a stable fixed point and a stable limit cycle, coexist for the same input current value for a specific range of current values (Figure 1.4B), a range referred to as the bistable range (Figure 1.5). Therefore, while the trajectory is locked into the limit cycle (the tonic firing state), it is possible to perturb the membrane voltage with a fast transient input and push it into a region of the phase plane where the stable fixed point is the attractor. The system will reside at the constant voltage of the fixed point until another perturbation pushes the membrane voltage into a region of phase space where the limit cycle is the only stable attractor. This condition of overlapping stable limit cycle and stable fixed point forms the basis of bistability, which forms the basis of the stutter spiking phenomenon that we will discuss later after the introduction of some experimental results. Separation of these two regions of the phase plane, and their associated attractors, is provided by another limit cycle, albeit an unstable one, that repels all trajectories (Figure 1.4B).

1.5.3.1 Rationale for Identification of Fixed Point Bifurcations in Neurons

The bifurcation detailed in the previous example is a subcritical Andronov-Hopf bifurcation (AH bifurcation), and is only one of four possible bifurcations by which the stability of the resting membrane potential is lost when the applied bias current is increased in a conductance model. Here we restrict our discussion to co-dimensional-1 bifurcations, and mention briefly the other possible bifurcations: saddle-node on invariant circle, saddle-node homoclinic, and supercritical Andronov-Hopf. Regardless of the number of dynamical variables present in the conductance model, only these four bifurcations are possible (Izhikevich 2007). There is a range of input current values (the bistable range) where both the limit cycle and the fixed point are stable, and the neuron can remain in either the spiking (limit cycle), or the stable voltage (fixed point) (corresponding to Figure 1.4B). The unstable limit cycle is indicated by open circles, and provides separation between two regions of the phase plane with either a fixed point bifurcation bestows a specific behavioural repertoire that defines how it converts synaptic input into spikes. In the case of the AH bifurcation this repertoire includes responses such as a minimum firing frequency, anode break excitation, short first spike latency, bistability, and resonance. Under the condition of intrinsic membrane noise (White et al. 2000), the response repertoire is extended to include subthreshold oscillations (Dorval and White 2005).

Figure 1.5 The Bifurcation diagram for the reduced sodium potassium model.

The solid line represents the fixed points of the dynamical system, which is the steady state membrane voltage as a function of current applied via the whole cell electrode. A steady state membrane voltage does not exist for input current greater than that of the bifurcation point, where the fixed point becomes unstable (dashed line) and the neuron can only exhibit spiking (corresponding to Figure 1.4C). Spiking is indicated by the solid circles, which correspond to stable limit cycles. The circles represent the maximum and minimum voltage values for the limit cycle, which are the maximum and attractor or limit cycle attractor. Transitions between either of the two phase plane regions can be achieved by small perturbations, such as those brought about by intrinsic noise.

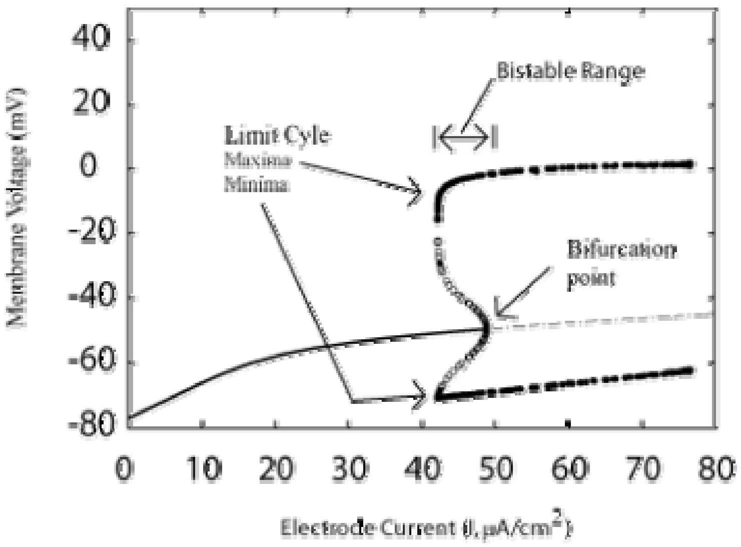
Membrane Voltage (mV)
40
20
0
-20
-40
-60
-80
0
10
20
30
40
50
60
70
80
Electrode Current (I, μA/cm²)
Bistable Range
Limit Cyle
Maxima
Minima
Bifurcation point

The bifurcation is a reflection of the synergistic behaviour of fast intrinsic currents that act on a time scale similar to that of the time constant of the membrane; however, slower currents are present and accommodate during the firing response to produce spike frequency acceleration and adaptation. This distinction allows the separation of dynamic variables into fast and slow subsystems, and the subsequent contribution of each to the spiking and subthreshold response (Rotstein et al. 2006; Izhikevich 2007). Also worth mentioning, is the ability of the fast subsystem to produce slow membrane potential responses, devoid of influences from slowly gated currents, as in the case of long first spike latency (Fernandez et al. 2007).

1.5.4 Resonance

Resonance is a response to a preferred frequency, and arises in systems that attenuate both high frequency and low frequency inputs. The capacitance associated with the neuronal membrane acts to attenuate high frequency input, and a certain class of voltage gated ion channels act to attenuate low frequency input. These currents belong to a class of currents referred to as resonant currents (Hutcheon and Yarom 2000), and attenuate low frequency input by opposing deflections of the membrane potential caused by synaptic currents. As mentioned previously in our description of the conductance model as a dynamical system, a fast subsystem that defines spiking will provide a resonant response given that the fixed point defined by the fast subsystem is a focus. In this section, we explore the ability of the slower subsystem to provide resonance, especially at membrane voltages more hyperpolarized than the activation ranges of the currents belonging to the fast subsystem.

A current is classified as resonant depending on whether its voltage sensitivity is controlled by either an activation or inactivation gate, in addition to the relation between its reversal potential E_r and half maximal activation voltage $V_{1/2}$. A slow delayed rectifier potassium current (I_{DR}), an outward current composed of Kv1.x subunits, is an example of a resonant current. An activation gate n provides voltage sensitivity with a half maximal activation voltage ($V_{1/2}$) larger than the reversal potential E_k. Given the steady-state activation profile (similar in shape to the low threshold potassium channel of Figure 1.2A), the steady-state current response is calculated by multiplication with the linear driving force ($V-E_k$), and provides an explanation into how this current opposes deflections of the membrane potential (Figure 1.6). Provided that the cell is resting at some arbitrary potential V_A within the activation range of the current, a deflection in membrane potential will alter the I_{DR} current according to the slope of the steady state I-V. A depolarizing deflection will activate, and increase, I_{DR} which will serve to hyperpolarize the membrane, in the same fashion a hyperpolarizing deflection will deactivate, and decrease, I_{DR} and act to restore the membrane potential to its original value. These compensations for deflections in the membrane potential do not occur instantaneously, because the activation gates require some finite amount of time to change as determined by their time constant at that voltage ($\tau_n(V)$, similar in shape to the low threshold potassium channel of Figure 1.2B). This time constant determines the maximum speed that this current can track the membrane potential, and hence the maximum input frequency that this current can attenuate. I_h current is also a resonant current, despite being an inward current, by virtue of an inactivation gate with a half

Figure 1.6 Steady state I_{DR} current relationship with membrane voltage.

A possible resting membrane potential is shown (V_A), with the instantaneous slope demonstrating the increase and decrease in I_{DR} current following respective depolarization and hyperpolarization.

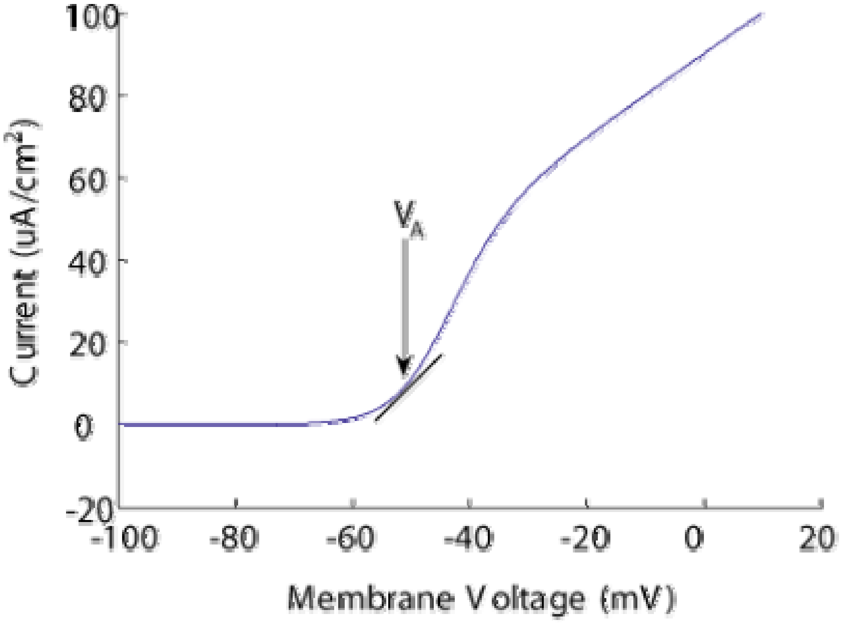

Current (uA/cm^2)
100
80
60
40
20
0
-20
V_A
-100
-80
-60
-40
-20
0
20
Membrane Voltage (mV)

maximal activation voltage smaller than the reversal potential of the mixed cation conductance.

Amplifying currents are those that exacerbate deflections of the membrane potential, and can be identified by a negative conductance region in the steady-state current-voltage relationship (Figure 1.7). In the case of persistent sodium current (I_{Nap}), the activation gate with $V_{1/2}$ lower than E_{Na} creates a condition where depolarizing deflections cause the activation, and increased recruitment of inward current, which further depolarizes the membrane. In the same fashion, a deflection in the hyperpolarization deactivates this inward current and further hyperpolarizes the membrane.

A current that contains both activating and inactivating gates exhibits both amplifying and resonant properties. Inactivating sodium and T-type currents are examples of currents that contain activating and inactivating gates, which control their conductances. Given the positions of the $V_{1/2}$ of both gates in relation to the reversal potentials for each current, both currents have similar amplifying/resonant behaviour (Lacinova 2005; Magistretti et al. 2006). The steady state activation and inactivation profiles, along with the driving force create regions of both a negative and positive conductance within the physiological voltage range. Currents of this type provide an amplifying response in the negative conductance region, and a resonant response in the positive conductance region. With these examples in mind, it becomes apparent that the currents themselves are not necessarily classified as resonant or amplifying; rather it is the gates that should be classified as such. In other words, resonant gates provide negative feedback to regulate the membrane potential, whereas amplifying gates are

Figure 1.7 Steady state I_{Nap} current relationship with membrane voltage.

Negative conductance region is observed for voltages between -60 and -20 mV.

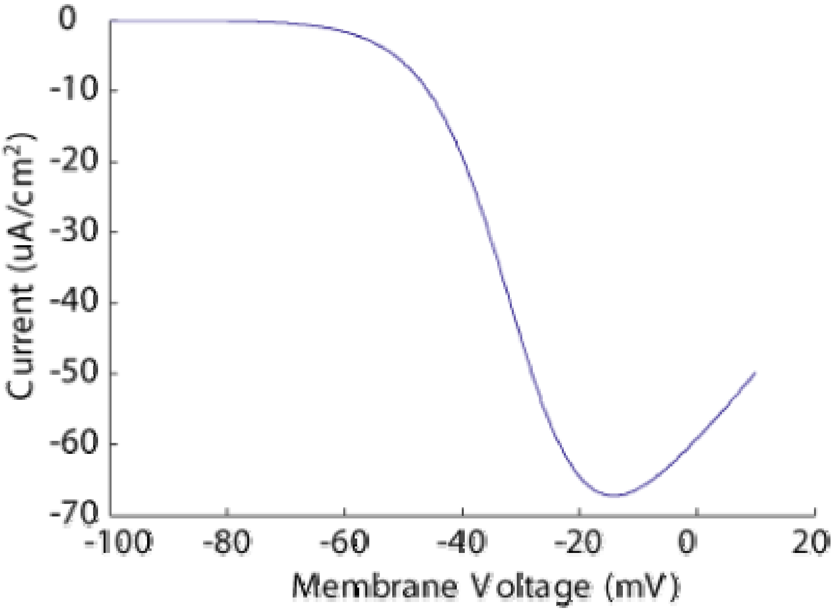
0
-10
-20
-30
-40
-50
-60
-70
Current (uA/cm^2)
-100
-80
-60
-40
-20
0
20
Membrane Voltage (mV)

elements of positive feedback that will drive the membrane potential towards the reversal for the current that they control on the condition that a resonant gate is not present (either in the same current, or a different current).

1.6 Hypotheses and Objectives

The goal of this research was two fold, with investigations of subthreshold and superthreshold responses of ICC neurons. Primarily we wished to gain a better understanding of the manner in which ICC neurons process synaptic currents. Specifically, we sought a description of temporal filtering of synaptic current. Additionally we wished to determine the fixed point bifurcation, so that a proper description of the firing responses may be compared across firing response types and accurate models could be built in the future.

To obtain these descriptions, current-clamp recordings were obtained from ICC neurons in brain slice. The whole cell recording technique also permitted intracellular labelling of ICC neurons for post hoc morphological descriptions, in the hope of determining the morphological identity of the firing phenotypes. Two main hypotheses were proposed in this study.

Hypothesis #1:

ICC neurons exhibit heterogeneity in their temporal filtering characteristics

Question 1:

What are the subthreshold resonant frequencies?

Approach:

To generate an impedance profile, broad band stimuli will be used to probe the subthreshold response of ICC neurons.

Question 2:

What types of firing response coincide with resonance?

Approach:

In addition to the presentation of the broadband stimuli to address question 1, current pulses will also be presented in order to identify the firing response type.

Question 3:

What voltage gated conductances are responsible for the resonance response?

Approach:

Ion channel blockers will be applied to determine the influence of certain voltage gated conductances on the resonance response.

Question 4:

What cellular morphology correlates with resonating cells?

Approach:

Biotin will be used as an intracellular label, by including it in the internal solution used in the whole cell recordings. Cellular morphology will be viewed using confocal microscopy to determine morphological features including: cell shape, number of dendrites, types of branching, soma diameter, and course of the axon.

Hypothesis #2:

Firing Responses of ICC neurons can be described and identified by a dynamical systems approach, where different neuronal spiking responses are the result of different fixed point bifurcation types.

Question 1:

Do ICC neurons have a minimum firing frequency?

Approach:

Firing frequency in response to pulse and ramp current-clamp stimuli will be measured.

Question 2:

Do ICC neurons exhibit bistability? Given a bias current, can ICC neurons exhibit both a spiking solution and a rest state simultaneously?

Approach:

Firing responses to ramp current-clamp stimuli will determine whether the neurons continue to fire on the down slope past the firing threshold on the up slope. Additionally, the observation of a response referred to as stutter firing will indicate bistability. Special attention will be paid to stutter firing.

Question 3:

Do ICC neurons exhibit subthreshold membrane potential oscillations?

Approach:

In response to current-clamp pulse stimuli, the subthreshold membrane potential will be observed. Spectral analysis techniques will determine the frequency and amplitude of the oscillations, as well as their dependence on the holding level.

Question 4:

Are there major differences in the first spike latency between firing response types?

Approach:

Investigate the relationship between first spike latency and the current-clamp pulse amplitude across firing response types

Chapter Two: Experimental Procedures

2.1 Brain Slice and Intracellular Recordings

Recordings from 211 neurons were obtained from 64 Sprague-Dawley rats with postnatal ages between 10 days and 16 days supplied by Charles River (Saint-Constant, Quebec, Canada). The method used to prepare coronal brain slices was similar to that used elsewhere (Peruzzi et al. 2000; Sivaramakrishnan and Oliver 2001). Rats were anaesthetized with halothane prior to cervical transection; the brain was removed and cooled with 5 °C artificial cerebral spinal fluid (ACSF) for 10 seconds, and placed on an ice cold plastic surface for further dissection. In preparation for slicing, the brain was blocked out with two transections as follows. Coronal transections of the brain were made caudal to the rostral border of the cerebellum, and cerebellum and structures caudal to the cerebellum were discarded. A second para-coronal transection was made rostral to the rostral border of the superior colliculus, and the cortex and forebrain was discarded. The para-coronal transection was made in a plane anterior to and rotated in the anterior direction from the coronal plane such that the transection was perpendicular to the axis of the IC. The surface created by the second transection was glued to the vibratome with cyanoacrylamide cement. This slicing orientation was chosen in order to obtain a greater number of slices, where the mounting surface was oriented perpendicular to the axis of the IC. The central nucleus was identified as a central region in each of the lobes of the IC with high opacity, and slices containing both the SC and the IC were used, to ensure that the slices were from a rostral location in the brain, where the external nucleus was excluded. Similarly, exclusion of rostral nuclei such as the rostral pole was possible by excluding slices rostral to the fibers of the lateral lemniscus. Slices were incubated in artificial cerebral spinal fluid (ACSF) at 32 ºC for a minimum of period of 1 hour prior to recording. All recordings were made at 32-34 °C unless otherwise mentioned, with an ACSF flow rate of 2 mL/min. Synaptic blockers were bath applied in all experiments in the following concentrations: 25 µM AP5 (DL-2-amino-5-phosphopentanoic acid; Tocris Cookson, Ballwin, MO), 10 µM DNQX (6,7-dinitroquinoxalinedione; Tocris Cookson), 10 µM Picrotoxin (Sigma, St. Louis, MO), 5 µM strychnine (Sigma), 1 µM CGP55845 ((2*S*)-3-[[(1*S*)-1-(3,4-dichlorophenyl)ethyl]amino-2-hydroxypropyl](phenylmethyl)phosphinic acid; Tocris Cookson). ACSF was preoxygenated with carbogen (95% O_2, 5% CO_2) gas and composed of the following (mM): 126 NaCl, 3 KCl, 2.8 MgCl, 25.9 $NaHCO_3$, 11.1 glucose, and 1.2 $CaCl_2$. The composition of the internal solution was as follows (mM): 130 K-gluconate, 0.1 EGTA, 10 HEPES, 7 NaCl, 0.3 $MgCl_2$, 5 di-Tris-creatine phosphate, 2 Tris-ATP, and 0.5 Na-GTP, pH 7.3, with KOH. Biotin was also added to the internal solution to a concentration of 0.1%. The chloride and potassium equilibrium potentials were calculated using the Nernst equation (Equation 1.1), as -74.2 mV and -96.8 mV respectively.

Whole cell patch recordings were made in current clamp with an Axopatch 200B amplifier, and Clampex 9.2 software (Axon Instruments, Foster City, CA). Recordings were acquired using a Digidata 1322A 16 bit analog to digital converter with a 10^6 sample buffer (Axon Instruments), and stored to the hard drive. Recordings were sampled at either 10 or 20 kHz. To avoid aliasing, the membrane potential was low pass filtered using the built-in Axopatch 200B analog low pass Bessel filter prior to sampling, and corner frequencies of 2 and 5 kHz were used for sampling rates of 10 and 20 kHz respectively.

Pipettes were fabricated with a Sutter Instruments P97 puller using borosilicate glass with 1.5 mm outer diameter and 0.86 mm internal diameter. Pipettes were backfilled with internal solution, and the resistances were typically 7-9 MΩ using a chlorided silver wire in contact with the internal solution and an AgCl pellet as the bath ground.

To facilitate post hoc histological identification, an attempt to maintain cellular integrity of the cell was made. On the condition that the recordings were completed and the cell was still alive, as indicated by stable resting membrane potential and adequate spike height (>40 mV from threshold), the patch pipette was removed by abruptly pulling the pipette away from the cell, with care taken to avoid stretching and breaking the cell. The slices were then stored in paraformaldehyde at 4 °C up to four weeks prior to further histological processing.

2.1.1 Offline Adjustments of Recordings

Three types of corrections of the membrane potentials were performed, for recordings made in current clamp. Pipette offset was carefully zeroed prior to obtaining tight seal to ensure an accurate measurement of membrane potential. The liquid junction potential of 15 mV was subtracted from all membrane potential recordings, where the junction potential was calculated from the valence, concentration, and mobility of all ion species using the generalized Henderson equation (Barry 1994). Membrane potential deflections as a result of voltage drop across the pipette access resistance was compensated online, and further offline adjustment was performed when necessary. Likewise, voltage clamp command voltage was corrected by subtracting the 15 mV liquid junction potential.

2.2 Stimulus Protocols

Step and ramp current-clamp stimulus protocols were provided by Clampex software. In order to analyze subthreshold impedance, we generated two types of stimulus files with custom software written in Matlab 7.0 (Mathworks, Natick, Massachusetts). The first stimulus, the ZAP protocol (impedance amplitude profile) was generated as a frequency modulated sinusoid with linearly increasing frequency over the duration of the protocol, as follows:

Equation 2.1 $I = I_o \sin(2pif(t)t)$

Equation 2.2 $f(t) = f_o + (f_{\max} - f_o)(t/2T)$

Where I_o is an amplitude scaling term, T is the total duration of the stimulus, and the frequency modulation f(t) is a function of the minimum frequency f_o and the maximum frequency f_{max}. The frequency of the stimulus was either between 0 to 15 Hz, or 0 to 30 Hz.

The second stimulus, low pass filtered Gaussian white noise (LPFGWN), was generated by sampling a Gaussian random variable at the sampling rate (10 or 20 kHz), and subsequent low pass filtering with a four-pole Butterworth filter with a corner frequency of 40 Hz, unless otherwise indicated. To permit easy scaling of this signal to a desired root-mean-square (RMS) value, the RMS of the filtered noise was normalized to 1 pA, and was subsequently scaled during recording as necessary to produce membrane potential deflections that did not exceed 10 mV. An effort was made for the LPFGWN signal to use all of the available 10^6 samples available in the Digidata 1322A buffer, such that the LPFGWN stimuli were of 100 and 50 second durations for 10 or 20 kHz sampling rates. Test pulses were included in select LPFGWN protocols with 4 second durations and amplitudes equal to the RMS value of the LPFGWN. These test pulses served to assess the input resistance (R_{in}) of the neuron.

2.3 Analysis of Intracellular Recordings

Analysis was restricted to neurons with resting membrane potentials of -70 +/-5 mV, and action potentials amplitudes greater than 40 mV. Spike times were measured at the peak of the spike.

Only records without action potentials were used in the calculation of impedance profiles when the ZAP protocol was used. The selection of records for the LPFGWN protocol was less stringent, as records with spike numbers <10 were used with the rationale that any effects of sparse spiking was offset by window averaging techniques applied to this the long stimulus.

The activation and inactivation of voltage gated currents were taken into account during measurement of the membrane time constant, and the input resistance (R_{in}). In order to exclude the activation or inactivation of voltage gated currents in the measurement of the membrane time constant, an exponential fit was made to the first 20 ms of the subthreshold membrane voltage response to a 50pA depolarizing current-clamp pulse. The input resistance was measured four seconds after the onset of the current pulse, and well after the membrane potential had reached a steady state.

2.3.1 Calculation of Impedance Profiles: Spectral Techniques, their Validation, and Confidence Intervals.

The calculation of the impedance profiles was performed by first calculating the spectral content of both the input stimulus current and the membrane potential output, and then taking the ratio of the latter over the former. The exact method by which the spectral content was calculated depended on the type of stimulus, where two different spectral techniques were used. In the case of the ZAP stimulus, the amplitude spectrum was calculated by implementing the fast Fourier transform available in Matlab (Mathworks, Natick, Massachusetts) to generate a single sided spectrum normalized by the length of the signal. No windowed averaging was performed when the ZAP stimulus was used, and the spectral resolution was 0.0191 Hz for a 30 second ZAP protocol. In the case of the LPFGWN stimulus, the power spectral density was calculated by implementing Welch's periodogram available in Matlab with windows of length 2.5×10^5 samples, and a Hamming window with 0% overlap. The resulting spectral resolution was 0.1526 Hz. The choice to use a windowed averaging method for the LPFGWN was made to improve the spectral estimates for the low frequencies of interest between 1-40 Hz, which was of merit given the stationarity of the input signal, and the ample length of the recording.

2.3.1.1 Test for Stationarity.

Windowed averaging employed by Welch's method requires bivariate stationarity (Chatfield 2004). To ensure that the signals were at least univariate stationary for the window sizes used, tests for the first and second statistical moments were used to compare between the window and the entire signal. To test for difference in the first moment (the signal mean), the means of each of the windows were calculated and compared to the mean of the entire signal by a Z-test with a $P<0.01$ confidence interval. To test the second moment (the autocovariance), the Fano factor was calculated for increasing window sizes, and a window size was chosen that exceeded that for which the Fano factor had reached saturation. The Fano factor for a window is described by:

Equation 2.3 $$F_w = \frac{{\sigma_w}^2}{\mu_w},$$

were σ_w and μ_w are the respective standard deviation and mean of the window.

2.3.1.2 Estimation of Confidence Intervals

The confidence interval for the spectra was calculated with knowledge that the estimates of power spectral density are Chi-square distributed (Marmarelis and Marmarelis 1978; Chatfield 2004), as:

Equation 2.4 $$\frac{v\hat{f}(w)}{f(w)}$$

Where $\hat{f}(w)$ is an estimate of the power spectral density $f(w)$, and v is the number of degrees of freedom of the window. The degrees of freedom is a function of the window weights λ_k, the number of samples of the window M, and the number of samples in the entire record N:

Equation 2.5 $$v = 2N / \sum_{k=-M}^{M} \lambda_k^2$$

The weights of the Hamming window are defined as:

Equation 2.6 $$\lambda_k = 0.53836 - 0.46164\cos\left(\frac{2 \cdot pi \cdot k}{M-1}\right)$$

Therefore the 100(1-α)% confidence interval was estimated as:

$$\frac{v\hat{f}(w)}{\chi^2_{v,\alpha/2}} \text{ to } \frac{v\hat{f}(w)}{\chi^2_{v,1-\alpha/2}}$$

where $\chi^2_{v,\alpha/2}$ and $\chi^2_{v,1-\alpha/2}$ are values in the Chi-square distribution that coincide with probabilities $\alpha/2$ and $1-\alpha/2$ for a number of degrees of freedom v (Zar 1974).

In the case of a ZAP input protocol, the amplitude spectrum $\mathrm{X}(w)$ was calculated using the FFT method. The power spectral density was calculated as the magnitude square of the amplitude spectrum (Marmarelis and Marmarelis 1978; Chatfield 2004), as follows:

Equation 2.7 $f(w) = \left|\mathrm{X}(w)\right|^2$

2.3.2 Analysis of Spiking Responses to Pulse and Ramp Current Clamp Stimuli

Instantaneous firing frequency ($iFreq(t)$) was calculated from the inverse of the interspike intervals. Adaptive instantaneous firing frequency profiles were fit with a biexponential function (Equation 2.8), where the exponential term containing the faster time constant (τ_{fast}) was the dominant term as indicated by the much larger associated amplitude term (A_{fast}). A least squares fitting method was used and profiles were considered well fit when correlation coefficients $R^2 > 0.70$ were obtained.

Equation 2.8 $iFreq(t) = A_{slow}\exp(t/\tau_{slow}) + A_{fast}\exp(t/\tau_{fast})$

A bimodal distribution in the spike frequency histogram indicated stutter spiking (Figure 3.17; Figure 3.18). The first (lower frequency mode) represent pauses between clusters of spiking. Spiking frequencies representing the limit cycle were those of the second (higher frequency) mode. These higher frequencies were used in the calculation of spike frequency gain, and only the last five instantaneous spike frequencies were used to avoid influence from spike frequency adaptation.

2.3.3 Analysis of subthreshold oscillations (STOs)

The power spectral density (PSD) was calculated using Welch's method, with 0.5 s windows, 50% overlap, and a Hamming window. Record lengths varied, such that 9-10 windows were typically used in the PSD calculation. Calculation in this manner allowed consistent frequency resolution, despite varying record length, and good quality spectral estimates afforded by the windowed averaging. The quality of the spectral estimates was indicated by reproducibility of spectral peaks despite of changes in the window size.

2.4 Modeling

Conductance based models were simulated with both Matlab and XPPAUT (version 5.85, freeware available at http://www.math.pitt.edu/~bard/xpp/xpp.html). Both methods simulation environments were used to avoid the chance of syntactic errors. Phase plane analysis was carried out with XPP, and bifurcation analysis was examined with the associated AUTO package. In all simulations the membrane voltage was calculated from the current balance equation by a fourth-order Runge-Kutta numerical method with a 0.2ms time step. Specifics of the single compartment two dimensional models presented in the introduction (Equation 1.9; Equation 1.10) are as follows:

Equation 2.9 $$m_\infty = \frac{1}{1+\exp\left(-\left(V+30\right)/7\right)}$$

Equation 2.10 $$n_\infty = \frac{1}{1+\exp\left(-\left(V+45\right)/5\right)}$$

Where $\tau_n = 1ms$, $\bar{g}_{Na} = 4mS/cm^2$, $\bar{g}_K = 4mS/cm^2$, $\bar{g}_{leak} = 1mS/cm^2$, $E_{Na} = 60mV$, $E_k = -90mV$, $E_{leak} = -78mV$, and $C = 1uF/cm^2$. These parameters and treatment is similar to that found in chapter six of (Izhikevich 2007).

A separate conductance model was used to demonstrate the sufficiency of I$_h$ in mediating a resonant response. This model was fit to recorded data and constructed as follows:

Equation 2.11 $$\frac{dV}{dt} = (I - \bar{g}_{Ih} h_{Ih}(V - E_{Ih}) - \bar{g}_{leak}(V - E_{leak}))/C$$

Equation 2.12 $$\frac{dh}{dt} = \frac{(h_\infty - h)}{\tau_h}$$

Equation 2.13 $$h_\infty = \frac{1}{1 + \exp\left(\left(V + 70\right)/5.5\right)}$$

Where $\tau_h = 600\text{ms}$, $\bar{g}_{Ih} = 0.019mS/cm^2$, $\bar{g}_{leak} = 0.04mS/cm^2$, $E_{Ih} = -20mV$, $E_{leak} = -72mV$, and $C = 1uF/cm^2$.

2.5 Histology and Fluorescence Imaging

Shortly after recording, slices were transferred to 4% paraformaldehyde and fixed for several days at 4°C. Slices were washed in 0.1 M phosphate buffer (PB) for several hours, and then placed in a solution of PB, Triton X-100 (0.1%), DMSO (0.5%) and streptavidin-Cy3 (1:1500) for three days. Neurons were imaged by obtaining z-stacks (0.5-1.0µm resolution) with a Nikon C1 confocal microscope (He/Ne 543nm laser excitation and 570–610 nm emission filter), and z-stacks were volume rendered with the accompanying EZ-C1 software.

2.6 Figures and Statistics

All figures were created in either Matlab 7.0 or Origin 7.0 (Originlab, Northampton, Massachusetts) and assembled in Adobe Illustrator 11.0 (Adobe Systems Incorporated, San Jose, California). All statistical tests were performed using GraphPad Prism 4.0 (GraphPad Software, Inc., San Diego, California), or Origin. Normality was tested with the Shapiro-Wilk test at the 5% level. Comparisons of minimum firing frequency within groups, and firing frequency gain within groups was accomplished by one way ANOVA, and Bonferroni's post hoc Multiple Comparison Test at the $P<0.05$ level. Assessment of correlations was achieved by calculating the P value for the t-test of the slope = 0 (Origin 7.0). Unless otherwise mentioned, mean and standard error are used throughout all comparisons.

Chapter Three: Firing Responses and the Governing Ion Channel Dynamics

3.1 Overview

This chapter is an investigation of firing responses observed in ICC neurons. We begin with a characterization of firing profiles in response to depolarizing current clamp pulses, which provides a basis for the separation of neuronal response into those that exhibit phasic (onset firing) responses, or only tonic (sustained firing) responses. Subsequently by treating these neurons as nonlinear dynamical systems, we attempt to understand the mechanism underlying the transition from rest to spiking by identifying the type of fixed point bifurcation, which is achieved by observing subthreshold and firing behaviours in response to a battery of current-clamp protocols. We present data in support of the hypothesis that ICC neurons exhibit a subcritical Andronov-Hopf fixed point bifurcation.

A bifurcation type is determined by fast voltage gated currents, whereas slower voltage gated currents accommodate during the firing response and determine the spike frequency acceleration or adaptation. Therefore, in addition to the bifurcation, we also attempt to identify the slow currents that contribute to different instantaneous spike frequency profiles, such as spike frequency acceleration, adaptation, and onset firing.

3.2 Results: Firing Response Profiles, and the Separation of Firing Response Types

Most neurons in the vertebrate nervous system respond to long duration depolarizing current-clamp pulses with a series of spikes with more or less continuous inter-spike intervals (ISI), or in terms of the reciprocal, a continuous instantaneous firing frequency. This response is referred to as tonic firing, and the time evolution of the instantaneous frequency may accelerate (e.g. the regular spiking cortical pyramidal neuron (Connors and Gutnick 1990)), adapt (e.g. the cortical fast spiking interneuron (Gibson et al. 1999)), or remain constant. Aside from tonic firing, less common responses include the rhythmic clustering of spikes observed during intrinsic-bursting (e.g. the cortical chattering neuron (Nowak et al. 2003)), and the single spike (phasic) response of the onset response (e.g. the brainstem mesV neuron (Izhikevich 2007)). The majority of ICC neurons exhibit either tonic accelerating or adaptive responses, which are indicated by a respective increase or decrease in the instantaneous frequency following the pulse onset (Figure 3.1; Figure 3.3). A minority exhibit an onset response (Figure 3.2; Figure 3.3). A very small proportion of neurons exhibit a constant instantaneous frequency profile with a sustained firing response devoid of any adaptation or acceleration (Figure 3.3). Nevertheless, a distinction between the tonic and onset responses is somewhat ambiguous, given that the onset response can respond with tonic firing given a pulse of sufficient amplitude (Figure 3.2A, B, and C).

3.2.1 Separation of the Onset Response from Tonic Responses

A parameter was chosen to separate neurons that responded with a phasic response from those that responded only with tonic responses. The chosen parameter was the range of current pulse amplitudes that could induce an onset firing response, and we refer to this parameter as the onset-range. We measured this parameter by plotting the number of spikes observed during a two second period in response to current clamp pulses of varying amplitudes (Figure 3.4). The onset response type responded with a single spike for a range of current pulse amplitudes, whereas the sustained response types responded with more than one spike for all current pulse amplitudes greater than the rheobase (current threshold). We define the spike threshold, as the membrane voltage

Figure 3.1 Instantaneous spike frequency adaptation and acceleration is observed in tonic firing responses to current clamp pulse stimuli.

Neuron (A) exhibits adaptive spiking, whereas spiking accelerates in neuron (B) in response to similar pulse amplitudes (i, and ii). Associated current-clamp protocols are shown in (iii). In (C), the instantaneous spike frequency profiles show a decrease in spike frequency for the adaptive response within the first 100ms of pulse onset (neuron in (A), black circles), and an increase in spike frequency in the accelerating response within a similar time scale (neuron in (B), red squares). An exponential function was fit to the adaptive profile for contrast to the accelerating responses.

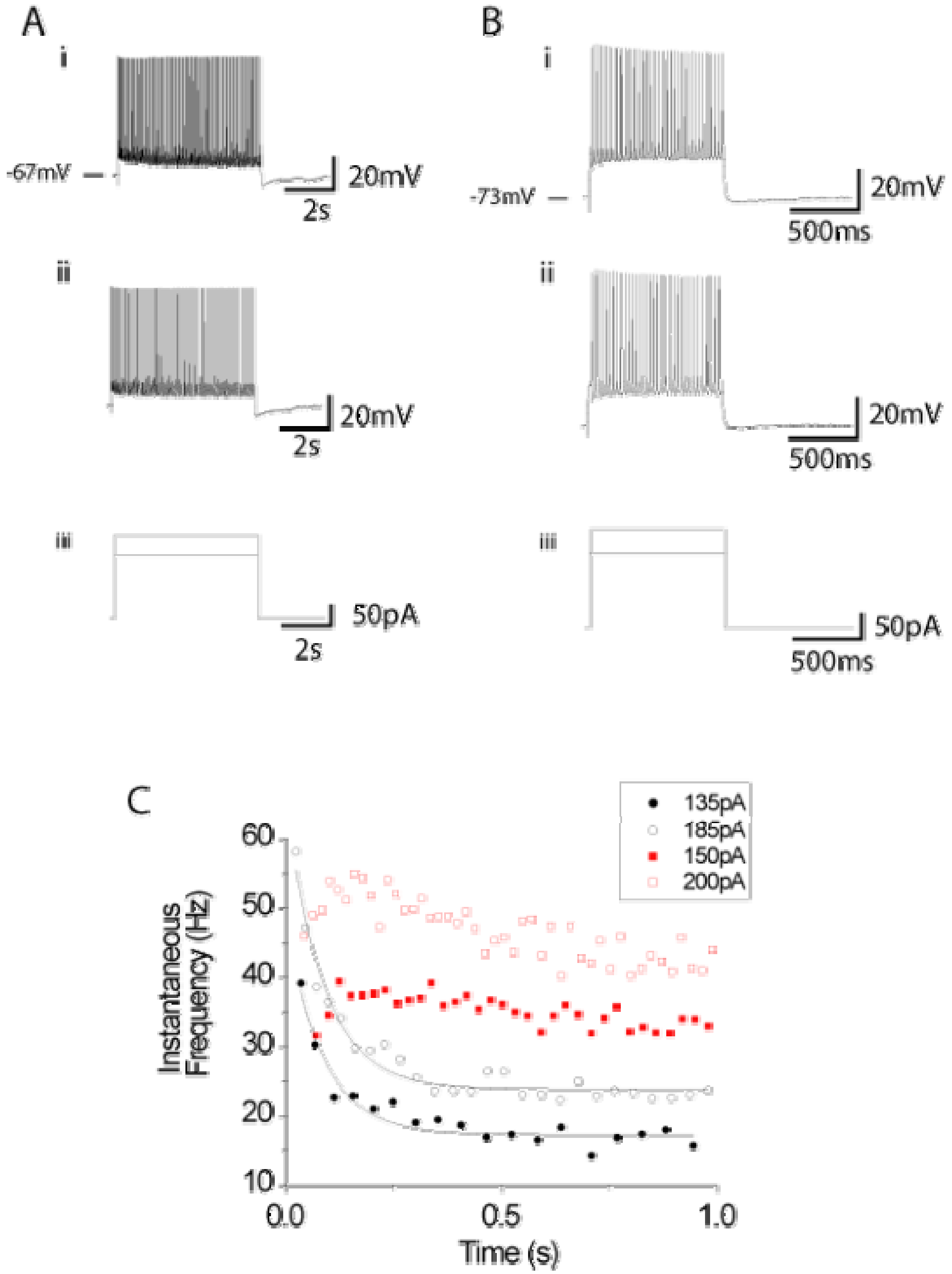
A
i
-67mV
20mV
2s
ii
20mV
2s
iii
50pA
2s
B
i
-73mV
20mV
500ms
ii
20mV
500ms
iii
50pA
500ms
C
● 135pA
○ 185pA
■ 150pA
□ 200pA
Instantaneous Frequency (Hz)
60
50
40
30
20
10
0.0
0.5
1.0
Time (s)

Figure 3.2 Phasic onset response proceeds to tonic firing with increased current pulse amplitude.

Tonic spiking is observed for large current pulse amplitudes following an onset spike, in the same neuron (A, B, and C). In (D), medium pulse amplitudes evoke a single onset response (phasic response), while small amplitudes (E) evoke an overshooting subthreshold response, instead of a spike. Associated current-clamp protocols are shown in (E) with increasing amplitude from (D) to (A). The after pulse hyperpolarization (APH), overshoot, and subthreshold oscillation are also shown.

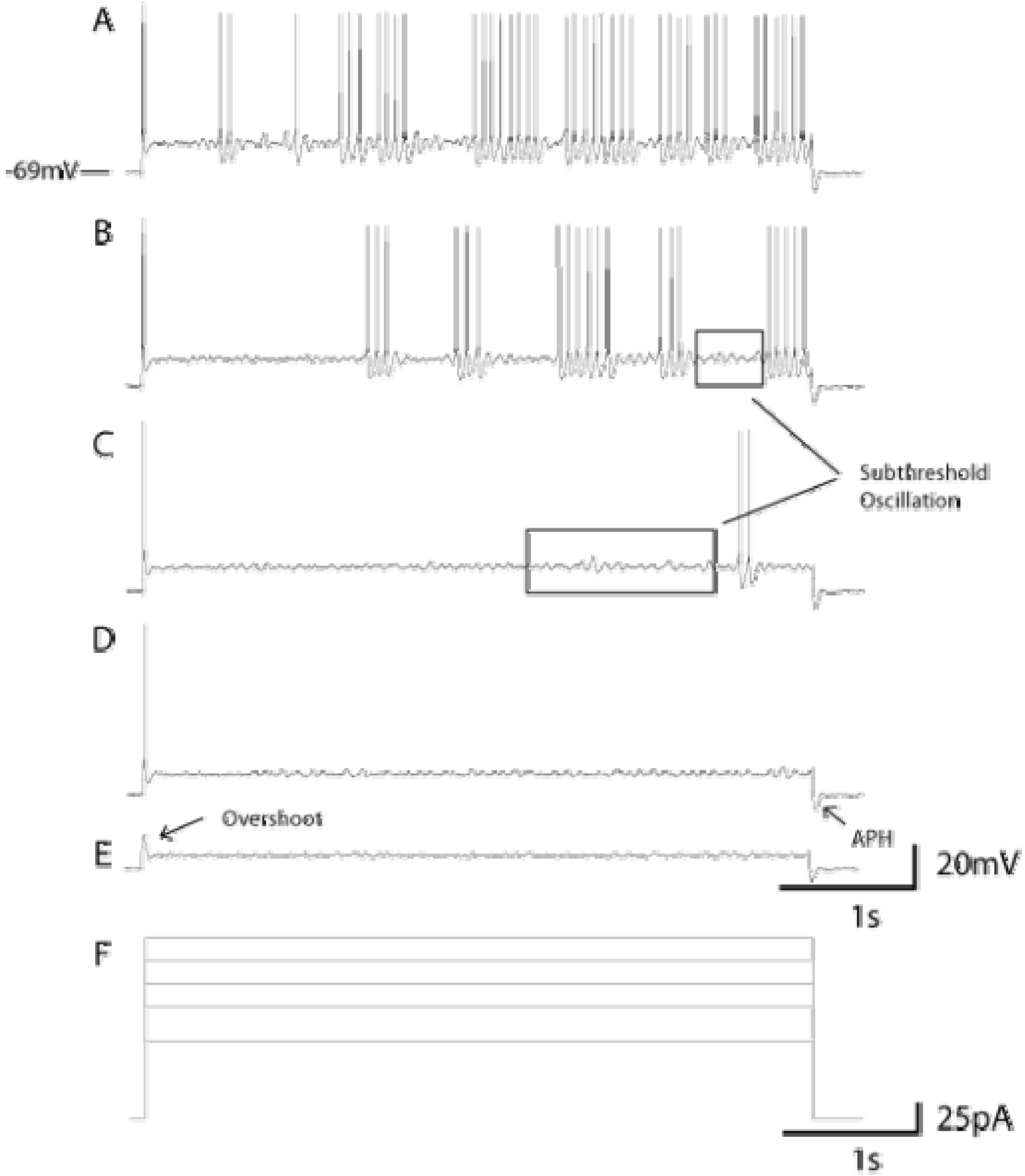
A
-69mV
B
C
Subthreshold
Oscillation
D
Overshoot
APH
E
20mV
1s
F
25pA
1s

Figure 3.3 Proportion of firing response types, according to the instantaneous firing frequency profile.

The sustained firing responses, with adaptive, accelerating, or constant instantaneous frequency profiles, are more common than the onset response. Of the sustained firing responses, the adaptive response is most common. Percent was calculated from 56 neurons.

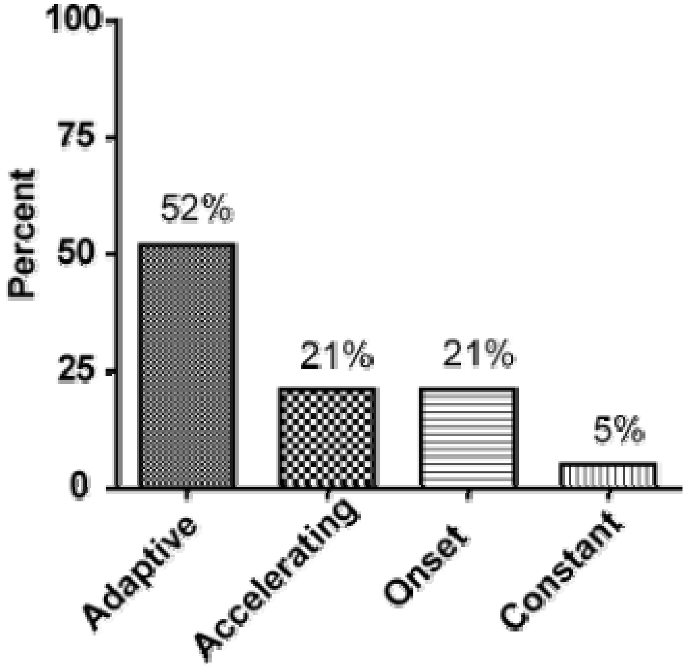
100
75
50
25
0
Percent
52%
21%
21%
5%
Adaptive
Accelerating
Onset
Constant

Figure 3.4 Phasic and tonic responses were separated by the range of current pulse amplitudes that evoke a single spike, the onset-range.

The number of spikes evoked during a two second pulse for various pulse amplitudes. Onset (phasic, single spike) responses were evoked by current-pulses of varying amplitude in some neurons (red); whereas, tonic responses were observed in others (black). The tonic response (black) is the tonic adaptive neuron presented in Figure 3.1, and the onset response neuron (red) is that of Figure 3.2.

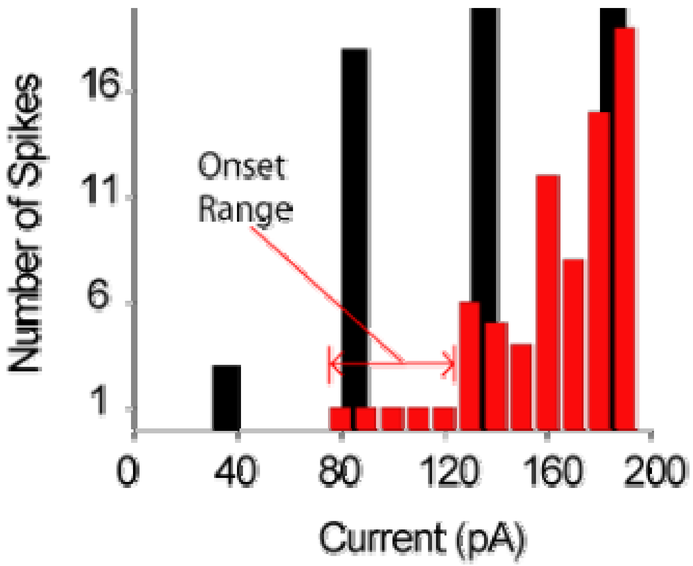
Number of Spikes
16
11
6
1
Onset
Range
0
40
80
120
160
200
Current (pA)

required to elicit a spike, and the rheobase as the minimum input current necessary to elicit spiking.

The onset-range was non-normally distributed (Shapiro-Wilk test of normality at the 5% level; Figure 3.5A). A large number of onset-range observations were made at the 25 pA level, and exclusion of these observations did not improve the test for normality. To explain this non-normality we proposed the existence of subclasses within this distribution. This possibility was explored by examining the distribution of an additional parameter of the current-pulse response. The time course of the return to rest following the after pulse hyperpolarization (APH) was chosen as the second parameter (Figure 3.6A, and Figure 3.2D), with the rationale that this parameter might provide insight into the kinetics of the accommodating current(s) that were thought to be responsible for the onset response.

We quantified the time course of the APH from the time constant (τ_{APH}) of an exponential curve fit (Figure 3.6B.ii), where τ_{APH} may represent either the inactivation of a slow outward current, and, or the activation of a slow inward current. Since a spike afterhyperpolarization has a similar time scale to that of an APH, the APH may be contaminated by conductances of spike afterhyperpolarization if a spike occurred near the end of the current pulse. To ensure that our measurement was the effect of accommodating currents only, we were careful to measure τ_{APH} only in the absence of a spike in the preceding second. To ensure maximal activation or inactivation of the accommodating current we measured τ_{APH} for the largest pulse amplitude that did not violate the first criterion concerning spiking.

Figure 3.5 Onset-range and τ_{APH} are non-normally distributed.

Histograms of the onset-range (A) and τ_{APH} (B) are shown. A large number of observations of onset-ranges were made with pulse amplitudes around 25 pA (A). Both distributions (A) and (B) failed the Shapiro-Wilk test of normality at the 5% level.

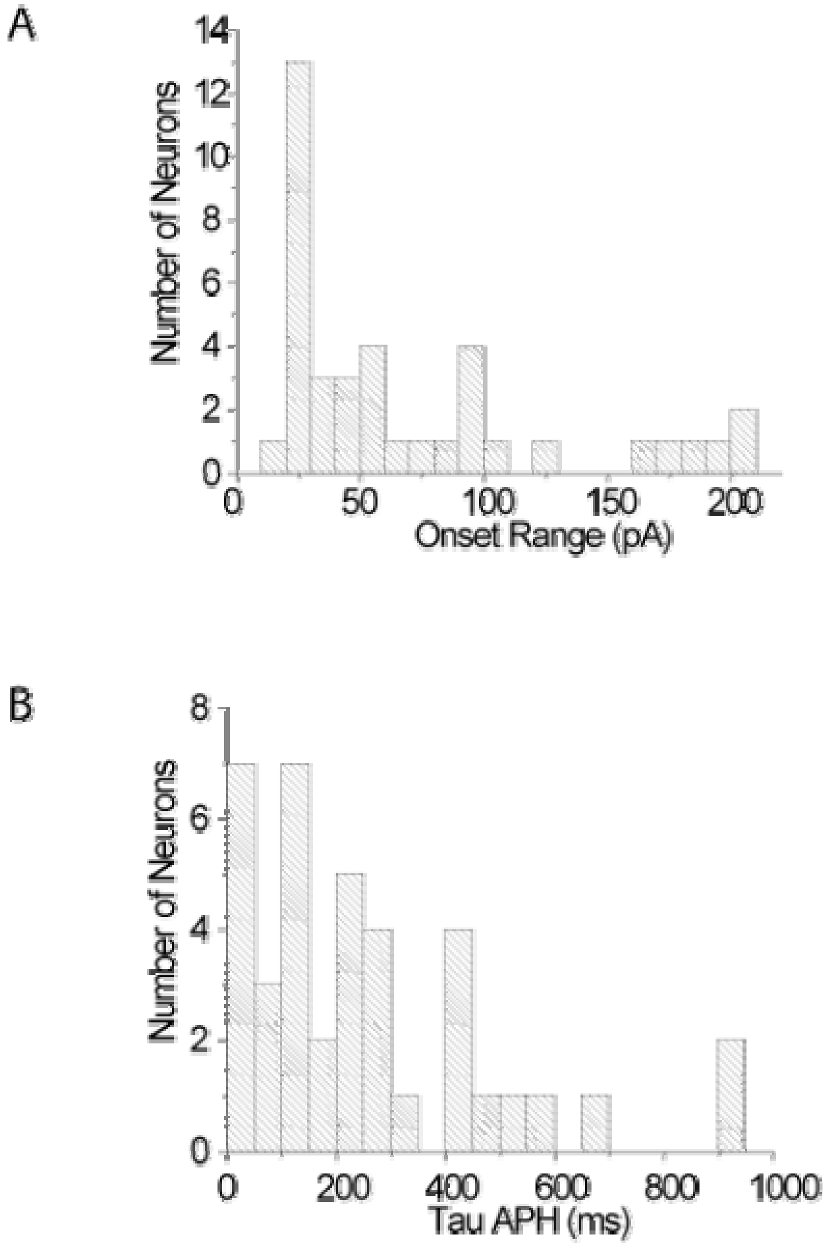
A
Number of Neurons
0
2
4
6
8
10
12
14
0
50
100
150
200
Onset Range (pA)
B
Number of Neurons
0
2
4
6
8
0
200
400
600
800
1000
Tau APH (ms)

Figure 3.6 Exponential fits of subthreshold membrane voltage responses to a current clamp pulse, quantification of the overshoot (OS) and after pulse hyperpolarization (APH).

A) The OS and APH are shown in a subthreshold response to a depolarizing current clamp pulse (green and blue respectively). B) Exponential fits are shown in red to quantify the time course of the return to rest following either an OS (τ_{OS}) (B.i), or an APH (τ_{APH}) (B.ii). The current clamp pulse amplitude was 165pA.

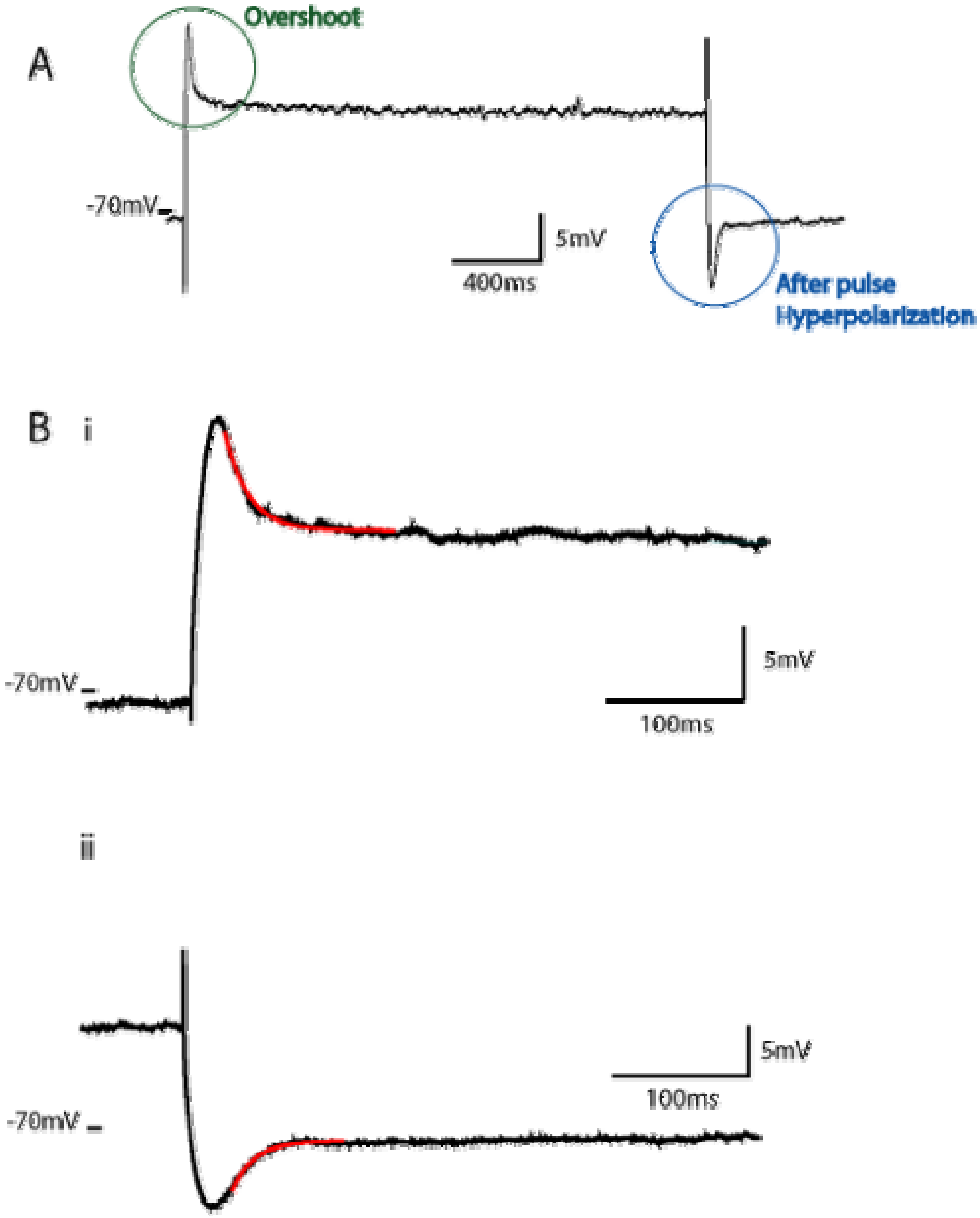
A
Overshoot
-70mV
5mV
400ms
After pulse Hyperpolarization
B
i
-70mV
5mV
100ms
ii
5mV
100ms
-70mV

The τ_{APH} measured within the population of neurons that exhibited an onset-range also proved to be non-normally distributed, further endorsing the presence of distinct classes within this distribution, or a co-distributed continuum (Figure 3.7B). Cell classification studies often rely on morphological features, and a single morphological feature is often insufficient to provide adequate separation of cell types. However, separation of cell types is improved by plotting two morphological features against one another (Sherman and Guillery 2006)[1]. We adopt this approach by plotting the onset-range and τ_{APH} parameters against each other, and in doing so we could distinguish a subpopulation of responses with τ_{APH} values <250 ms over a wide range of onset-range values from 50 to 200 pA (see * in Figure 3.7); owing to the typically larger onset-range, we refer to this subset of onset response neurons as the strong-onset response. This distinction is further supported by the typical observation of more than two onset responses for successive current pulses, of increasing amplitude (see numbering in Figure 3.7). Most of the strong onset neurons reside below a diagonal line drawn in the τ_{APH} - onset-range graph (Figure 3.7), such that we included any neurons within this space into the strong-onset response category. Neurons above this line also exhibited an onset-range, however only one or two subsequent current pulse steps elicited an onset spike (see numbering in Figure 3.7), and we refer to this subset of onset response neurons as the weak-onset response neurons. We consider these onset spikes as those arising from noisy induced spiking from a membrane that is otherwise quiescent at the membrane

---

[1] Section 2.A.2 of this reference is most pertinent, and deals with problems of cell classification in the thalamus.

Figure 3.7 An improvement of neuron response type separation is achieved by plotting the two measured parameters, τ_{APH} and onset-range, against each other.

The onset-range for each neuron that exhibited an onset response is plotted against τ_{APH}. The numeric at each point indicates the number of successive observations of onset responses as the current pulse amplitude was increased with step sizes in the range of 10 to 50 pA. A subset of neurons exhibited onset responses throughout the range of tested pulse amplitudes, up to a maximum of 200 pA (*). A distribution of neurons with τ_{APH} <250 ms was observed along the abscissa, and these neurons typically exhibited more than two successive onset responses. We considered these neurons, as those with stronger onset responses, and refer to the neurons below the diagonal line as strong-onset response neurons.

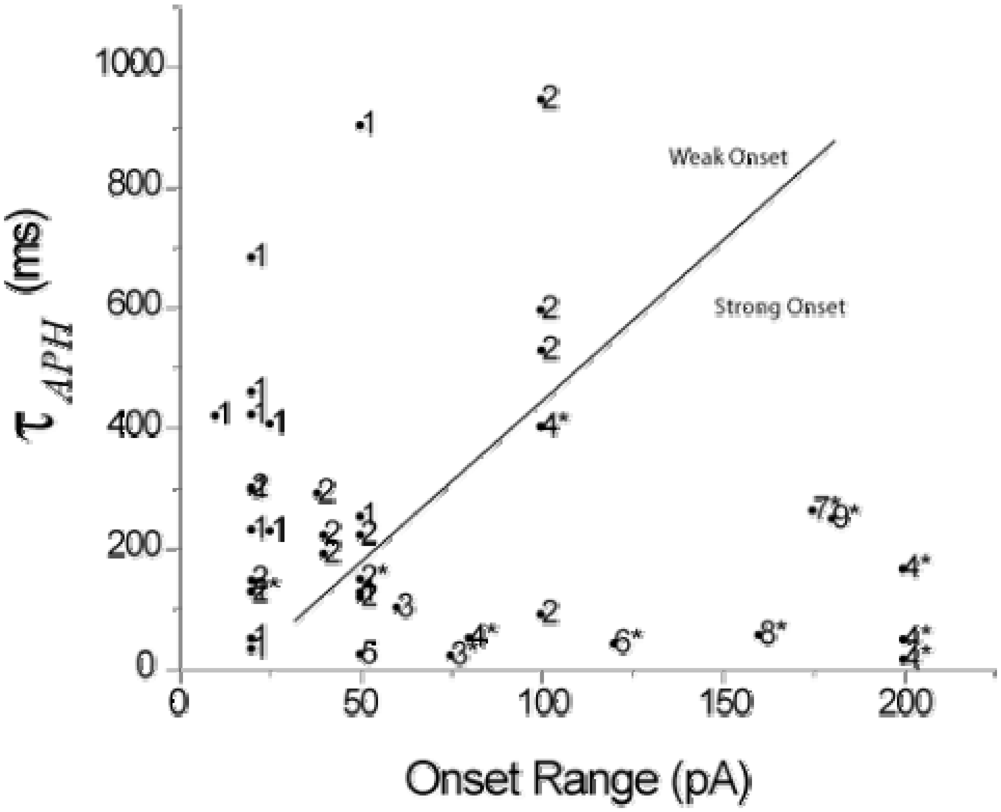
τ_{APH} (ms)
1000
800
600
400
200
0
0
50
100
150
200
Onset Range (pA)
Weak Onset
Strong Onset
2
1
1
2
2
1
1
1
4*
2
2
1
1
2
2
1
2
2
2*
4*
3
2
1
1
6
3*
4*
6*
8*
7*
8*
4*
4*
4*
4

potential determined by the current clamp pulse, and not as a result of spike arising before an accommodating current is activated or inactivated and can impede another spike. In contrast, neurons that did not exhibit an onset-range, were not included in this plot, and were classified as sustained firing neurons.

3.2.2 The Onset Response and Insight into its Mechanism

The value of τ_{APH} offers some insight into the time constants of the accommodating currents evoked by a current-clamp pulse, which by comparison are much slower, by several orders of magnitude (tens to hundreds of milliseconds), than typical time constants of the sodium or potassium currents (typically milliseconds) that underlie the action potential. I_h is a good candidate for a slow outward current that could contribute to the APH, and its expression in neurons with either an onset or an adaptive firing responses is known (Koch and Grothe 2003; Koch et al. 2004).

Strong-onset neurons exhibit a significantly smaller τ_{APH} in comparison with sustained firing neurons (Figure 3.8). Two possible reasons exist as to why τ_{APH} is smaller in onset neurons. Either the membrane time constant is considerably smaller, and, or the kinetics of the accommodating current are faster. Both of these factors appear to contribute to a smaller τ_{APH}, as the membrane time constant of onset neurons (τ_m) is approximately 50% that of sustained firing neurons (Figure 3.9), and the time constants governing I_h kinetics are faster in the onset response neurons in comparison to adaptive neuron (Koch and Grothe 2003).

The overshoot (OS) in membrane voltage shortly after the onset of the current pulse is likely the results of the same accommodating currents responsible for the APH

Figure 3.8 A comparison of τ_{APH} between strong onset and sustained firing responses.

The τ_{APH} measured for neurons exhibiting a strong-onset response, as indicated in Figure 3.6, was significantly smaller ($p<0.001$, two tailed Mann-Whitney test) than that for sustained firing neurons, which were distinct from onset neurons presented in Figure 3.7 by an absence of an onset-range.

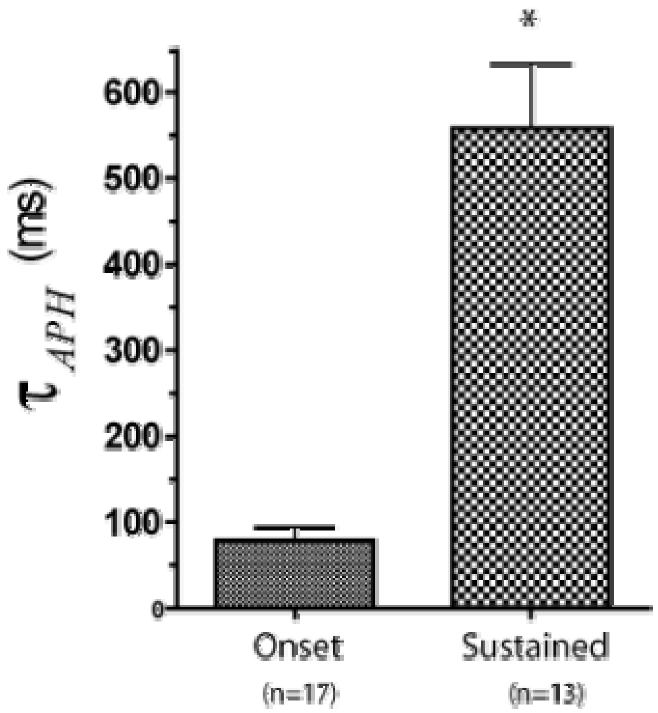
*
600
500
400
300
200
100
0
τ_{APH} (ms)
Onset
(n=17)
Sustained
(n=13)

Figure 3.9 The membrane time constant τ_m of the onset response neurons is significantly smaller than that of sustained firing neurons.

The difference in means (7.704 ± 1.497 ms) was statistically significant ($p<0.05$, two-tailed T-test).

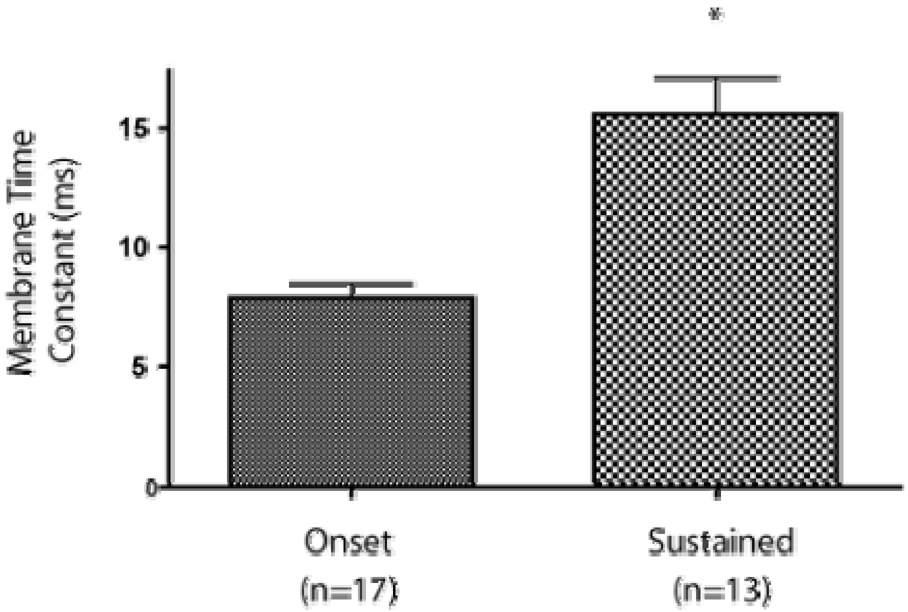
*
Membrane Time Constant (ms)
15
10
5
0
Onset (n=17)
Sustained (n=13)

(Figure 3.6A). The time course of the membrane potential following the OS was quantified in the same manner as that of the APH, with an exponential fit (Figure 3.6B.i). Measurements of τ_{OS} and τ_{APH} were similar within the same neuron, and appear to correlate close to unity (Figure 3.10); suggesting that ionic mechanisms with similar kinetics might be responsible for the OS and APH.

The presence of a faster accommodating current in the onset response neuron suggests a possible mechanism for the onset response. The overshoot provides a brief period of time when the membrane potential is above the spike threshold, and spike is fired before the activation/inactivation of the accommodating currents bring the membrane potential to a more hyperpolarized potential. In the onset neuron, the fast kinetics of the accommodating current (i.e. I_h (Koch and Grothe 2003)) keeps this superthreshold period short and allows only a single spike. Effectively the slow activation/inactivation of the accommodating currents stabilizes the membrane by returning it to its fixed point. In addition the OS in onset neurons is likely due to the greater activation of I_h at rest due to the more hyperpolarized resting membrane potential in comparison to sustained firing neurons (Figure 3.11). The identity of the major accommodating current in the onset response is likely Ih, given the ability of the I_h antagonist ZD7288 to block both the OS and APH in onset response neurons (Figure 3.12), and a previous report (Koch and Grothe 2003).

3.2.3 The Adaptive Response and Insight into its Mechanism

Slow and fast adaptation was observed in neurons exhibiting an adaptive response. A single exponential function provided an insufficient fit to the instantaneous spike frequency profile, and a bi-exponential function was required instead (Figure 3.13).

Figure 3.10 The time constants of exponential fits to the overshoot and the after pulse hyperpolarization are similar.

The time constants of exponential fits of the OS and APH (Figure 3.6) are similar and correlate close to unity, as indicated by a linear fit (slope =0.89, R^2=0.73, with the probability of the absence of correlation (slope=0) at $p<0.001$).

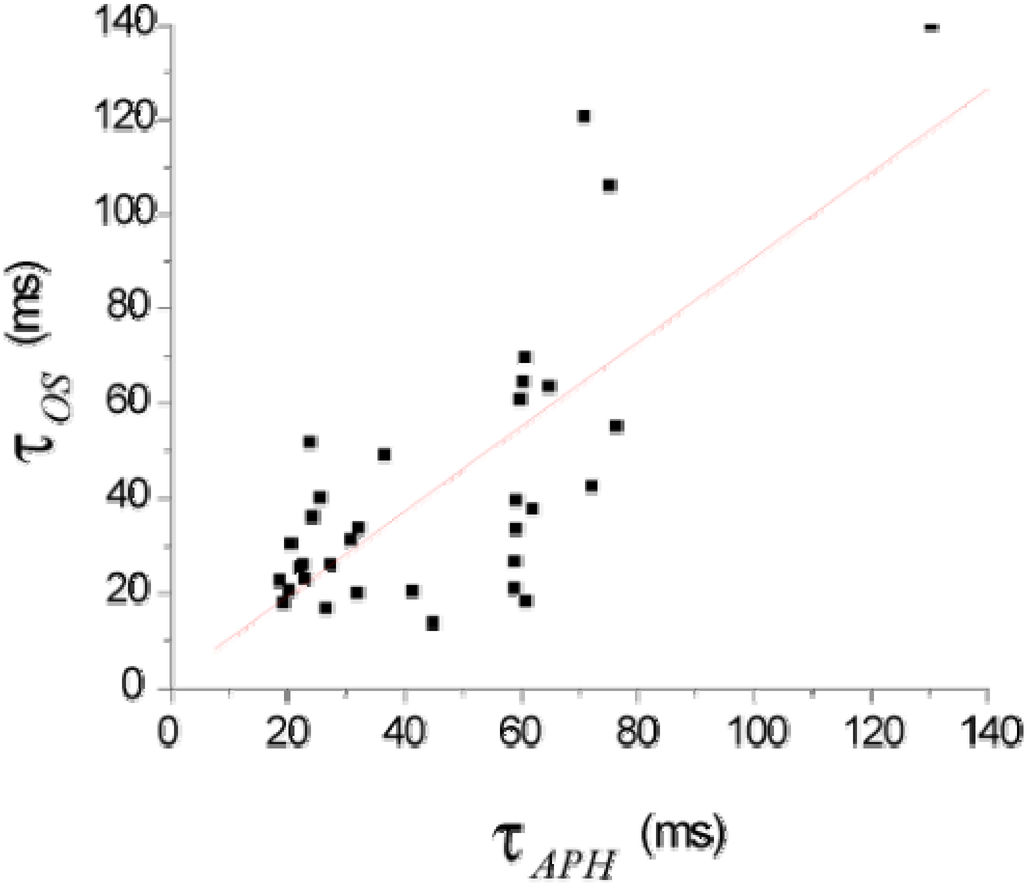
140
120
100
80
60
40
20
0
τ_{OS} (ms)
0
20
40
60
80
100
120
140
τ_{APH} (ms)

Figure 3.11 The resting membrane voltage of the onset response neuron is significantly more hyperpolarized than that of the sustained firing response neurons.

The difference in means (4.488 ± 1.749 mV) was statistically significant ($p<0.05$, two-tailed T-test).

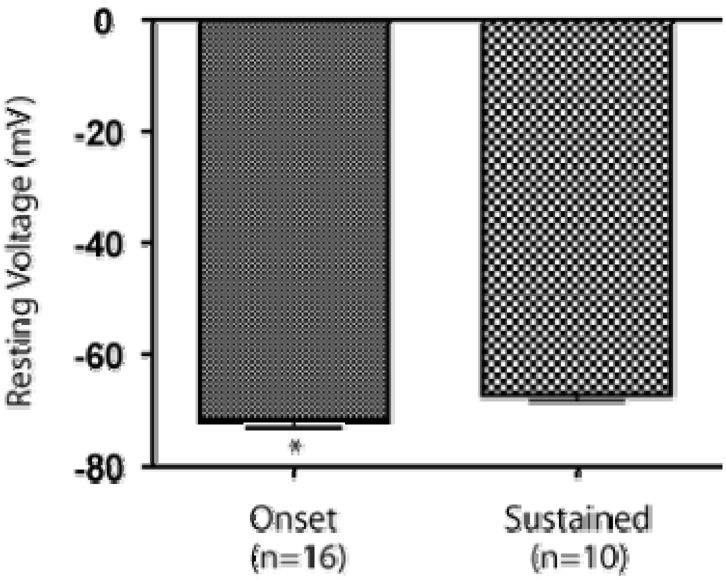
0
-20
-40
-60
-80
Resting Voltage (mV)
*
Onset
(n=16)
Sustained
(n=10)

Figure 3.12 Effect of I_h blockade by ZD7288 on the overshoot and after pulse hyperpolarization.

An overshoot at the pulse onset and an after pulse hyperpolarization at the pulse offset are observed in an onset response neuron under control conditions (black). Application of the I_h antagonist ZD7288 abolishes the OS and APH (red). Transient hyperpolarizations are also present in the control trace (indicated by *), and a description of them is presented in chapter five.

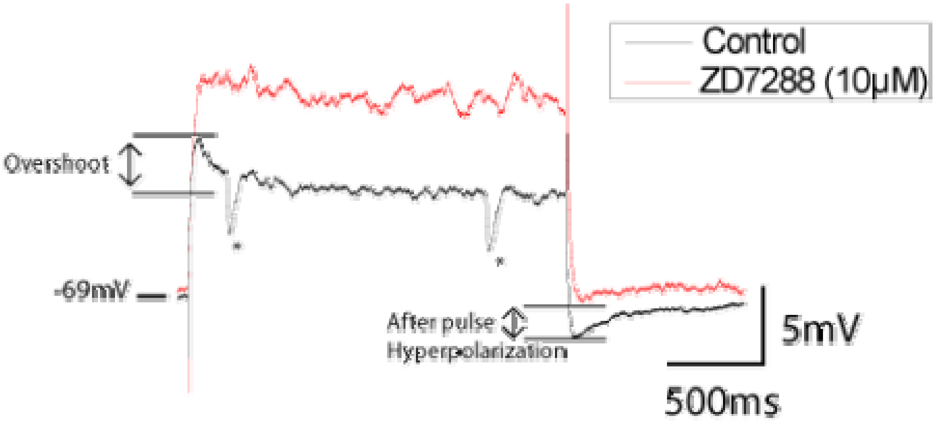
Control
ZD7288 (10µM)
Overshoot
*
*
-69mV
After pulse
Hyperpolarization
5mV
500ms

Figure 3.13 The instantaneous spike frequency profile of the adaptive response was fit with a bi-exponential function.

Spike frequency adapts very quickly at the onset of the current clamp pulse on the order of tens of milliseconds, followed by a slower adaptation on the order of seconds. The current clamp pulse amplitude was 230 pA, and the goodness of fit is indicated by R-square value. The bi-exponential equation used in the fit is shown.

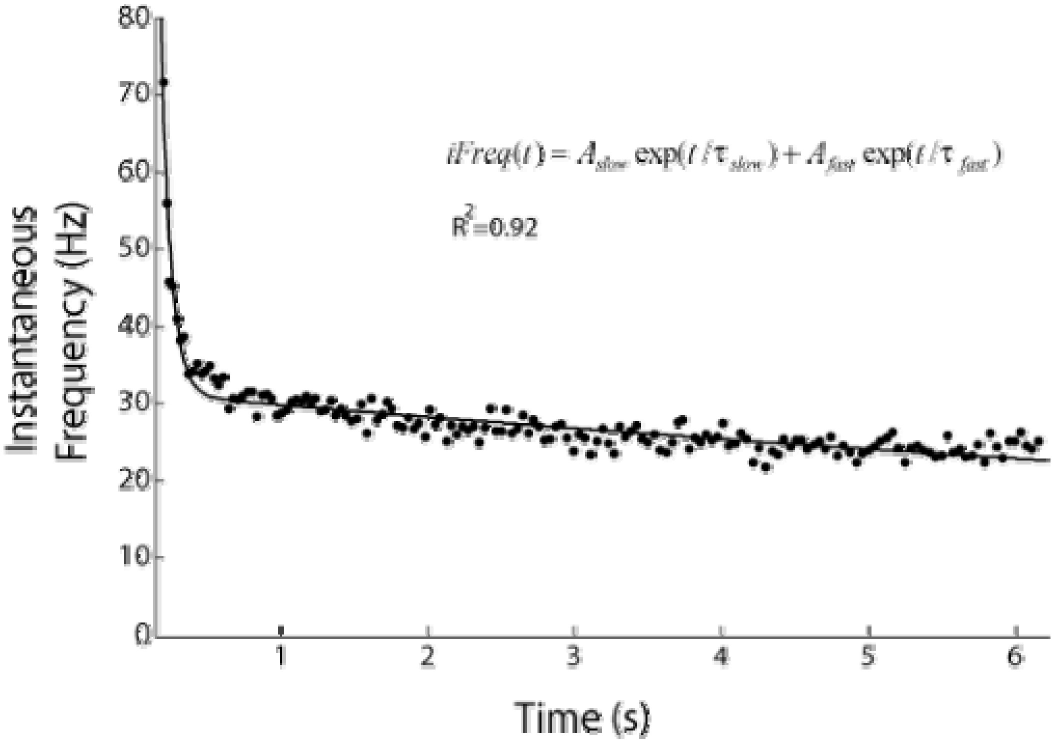
$iFreq(t) = A_{slow}\exp(t/\tau_{slow}) + A_{fast}\exp(t/\tau_{fast})$
R^2=0.92
Instantaneous Frequency (Hz)
80
70
60
50
40
30
20
10
0
1
2
3
4
5
6
Time (s)

The amplitude terms indicate the depth of adaptation, and the time constants provide insight into the time scale of the underlying accommodating currents. An increase in the amount of adaptation with increasing current pulse amplitude is apparent in both amplitude terms of the bi-exponential fit (Figure 3.14B), whereas there was no apparent trend in the time constants (Figure 3.14A). The trend in amplitude terms is also supported by reproducibility that is otherwise not observed in the time constants (see blue in Figure 3.14). The time scale of the fast time constant, in the range of 100-700 ms, suggests that adaptation might arise from a mix of activation of calcium currents, and inactivation of Ih at the onset of the pulse. The much slower time constant, in the range of tens of seconds, might represent accumulation of intracellular calcium and subsequent modulation of calcium dependent potassium channels, as proposed by the apamin sensitive adaptation observed in (Sivaramakrishnan and Oliver 2001).

3.2.4 The Accelerating Response and Insight into its Mechanism

A hyperpolarization at the pulse onset may contribute to the acceleration of spike frequency. The change in instantaneous spike frequency was less during acceleration in comparison to adaptation, with the largest accelerating difference observed between the first and second interspike interval (Figure 3.1C). Acceleration was typically observed in neurons that exhibit a hyperpolarization at the onset of a pulse response (see arrow in Figure 3.38B). This hyperpolarization is likely the result of activation and subsequent inactivation of an A-type potassium current as suggested by (Sivaramakrishnan and Oliver 2001), or the activation of calcium dependent potassium current (referred to as SK in chapter 5) by a transient influx of calcium at the onset of the pulse. Nevertheless, the time course of this hyperpolarization is uncannily similar to that of the transient

Figure 3.14 Adaptation was quantified by parameters of a bi-exponential fit to the instantaneous firing frequency profile.

Relation to current clamp pulse amplitude is shown for the four parameters of a bi-exponential fit, both fast and slow time constants (A.i, and A.ii), and both fast and slow amplitude factors (B.i and B.ii). Each colour represents a different neuron. Multiple trials of one neuron are shown to indicate reproducibility (blue).

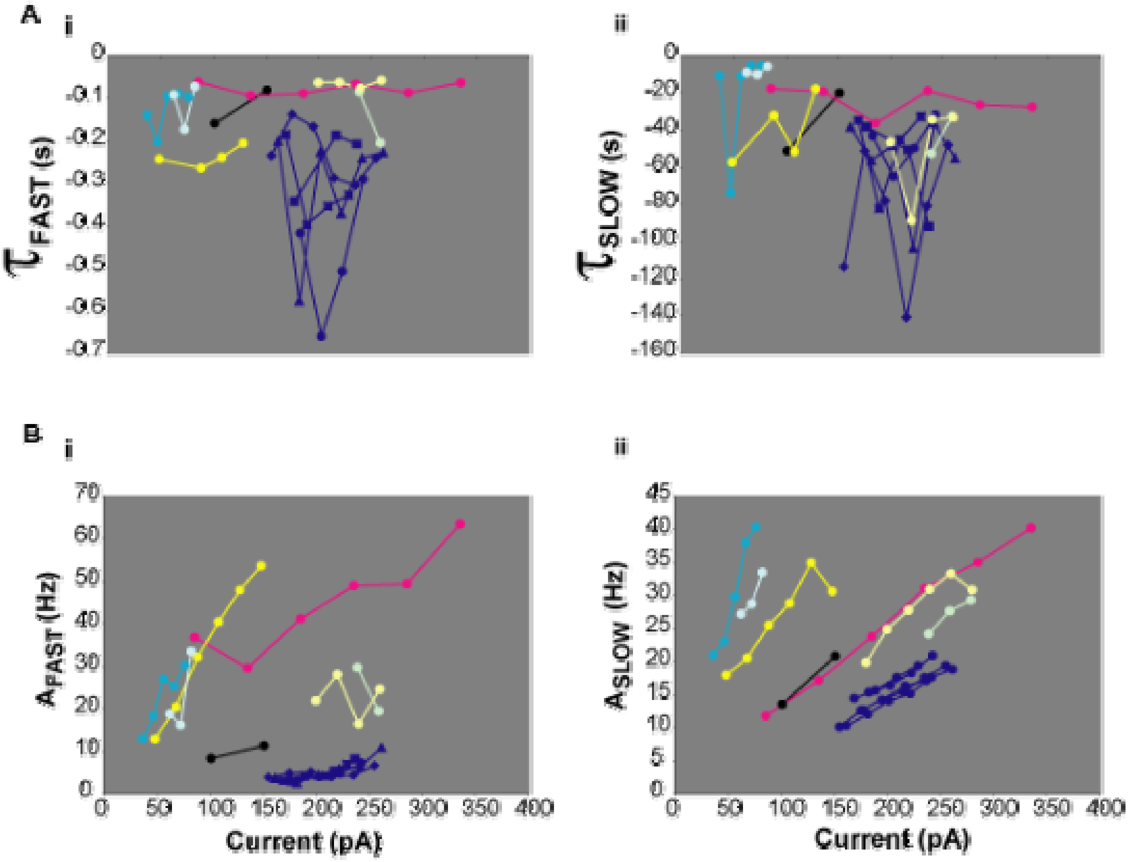
A
i
ii
τ_{FAST} (s)
0
-0.1
-0.2
-0.3
-0.4
-0.5
-0.6
-0.7
τ_{SLOW} (s)
0
-20
-40
-60
-80
-100
-120
-140
-160
B
i
ii
A_{FAST} (Hz)
70
60
50
40
30
20
10
0
A_{SLOW} (Hz)
45
40
35
30
25
20
15
10
5
0
0 50 100 150 200 250 300 350 400
Current (pA)
0 50 100 150 200 250 300 350 400
Current (pA)

hyperpolarizations that are often observed in the accelerating neuron response type, and are presented in chapter five.

3.3 Results: Subthreshold and Firing Properties for Identification of the Fixed Point Bifurcation

With adequate separation of firing response types, we investigated the current-clamp responses that offer insight into the behaviour of fast voltage gated currents, allowing identification of the bifurcation type.

3.3.1 The Steady-State Membrane Voltage Input Current Relationship

The shape of the steady-state membrane voltage and input current relationship (Iss-Vss) offers insight into the balance of steady state sodium and potassium current activation at the spike threshold. This balance of activation indicates the type of fixed point bifurcation, where greater sodium activation suggest a saddle-node bifurcation, and a concomitant activation of both sodium and potassium suggest an AH bifurcation (Fernandez et al. 2007; Izhikevich 2007). We describe the Iss-Vss relationship in the current clamp configuration, with input current below the minimum current pulse amplitude required for spiking. Voltage clamp offers a description of the Iss-Vss relationship at, and beyond, the spike threshold, unfortunately we found that ICC neurons were not amenable to voltage clamp.

In the case where a greater amount of sodium current is activated in comparison to potassium current, the Iss-Vss plot will have a point of inflection at the rheobase, with the curve bending towards the vertical (Figure 3.15B.i) (Fernandez et al. 2007; Izhikevich 2007). Bifurcations of the saddle-node type will exhibit this shape in the Iss-Vss. When the curve is monotonic, that is no change in the sign of the slope along the curve, the

Figure 3.15 The plot of steady-state membrane potential in response to steady-state input current is monotonically increasing.

A) Measured Iss-Vss relationship for both onset response (red) and tonic response neurons (black). B) Hand drawn Iss-Vss plots that correspond with non-monotonic (i), and monotonic (ii) relationships, which correspond to a saddle-node bifurcation, or an Andronov-Hopf bifurcation

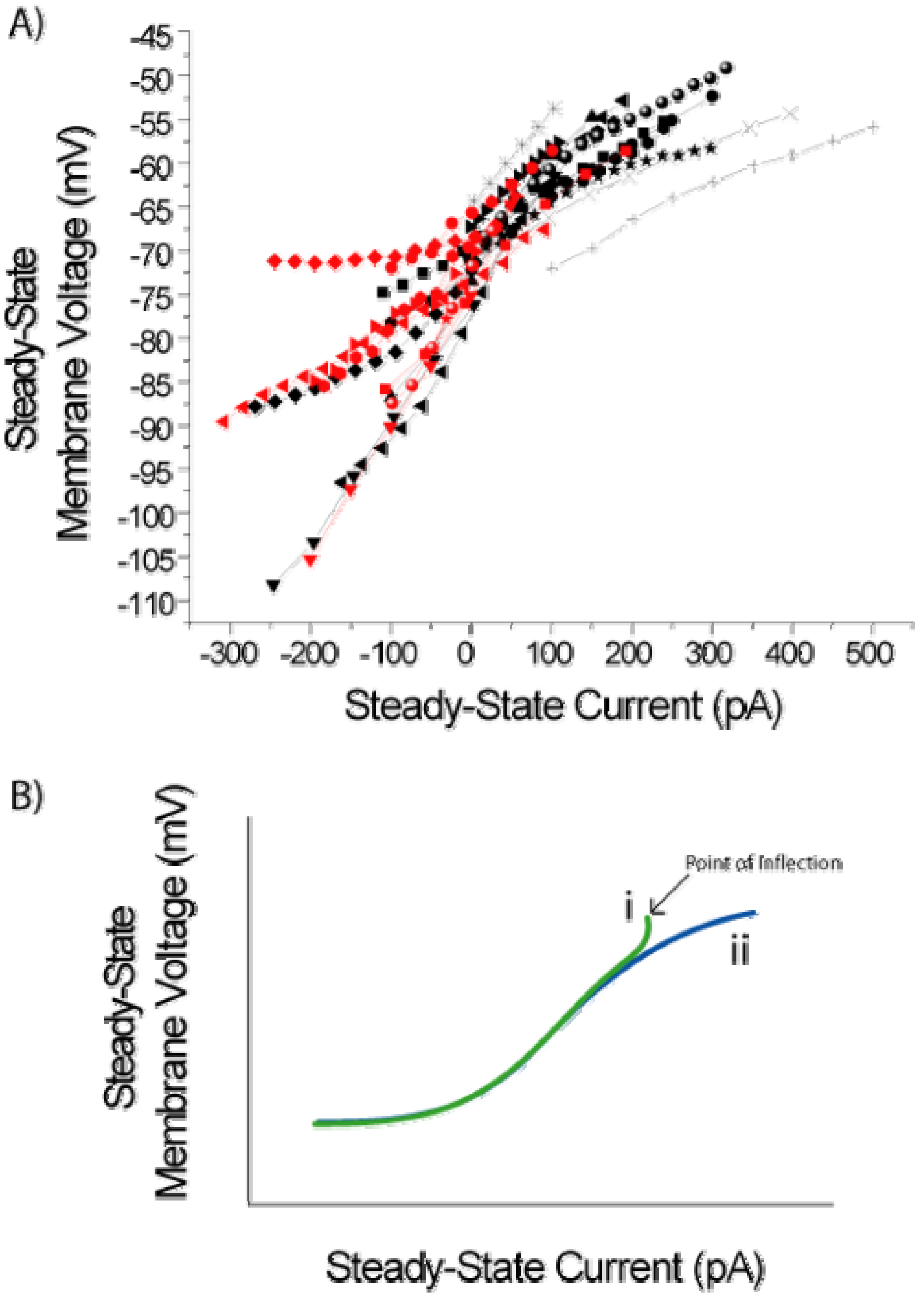
A)
Steady-State
Membrane Voltage (mV)
-45
-50
-55
-60
-65
-70
-75
-80
-85
-90
-95
-100
-105
-110
-300
-200
-100
0
100
200
300
400
500
Steady-State Current (pA)
B)
Steady-State
Membrane Voltage (mV)
Point of Inflection
i
ii
Steady-State Current (pA)

saddle-node bifurcation is ruled out in favour of the Andronov-Hopf bifurcation (Figure 3.15B.ii) (Ospeck et al. 2001; Izhikevich 2007). The monotonic curve indicates that the sodium and potassium currents activate concomitantly in rather similar quantities near the bifurcation point, and is in contrast to the predominance of sodium activation in the steady state response in the case of the saddle-node bifurcation.

The ICC onset and sustained firing neurons alike exhibit monotonic Iss-Vss relationships, which suggest an Andronov-Hopf bifurcation (Figure 3.15A). To further investigate the recruitment of voltage gated sodium near the bifurcation point, we examined the Iss-Vss relationship following blockade of voltage gated sodium by tetrodotoxin (TTX). If sodium current is active in the steady state response near threshold, its blockade should cause a downward deflection in the Iss-Vss relationship in comparison to the control condition (Figure 3.16D). This active steady state sodium current represents a window current that is possible by the overlap of sodium current's activation and inactivation profiles. This experimental condition did not support the hypothesis of a saddle-node type bifurcation in the case of the onset response neuron, as the shape of Iss-Vss near threshold remained unaltered upon TTX application (Figure 3.16A-C). Unfortunately, similar experiments with sustained firing neurons were too few and thus inconclusive. Additionally, this experiment rules out the possibility that steady-state activation of sodium is being masked by the activation of a slow outward current, as would occur if an M-current (slow potassium current) were present.

3.3.2 Bistability

Responses to current-clamp pulses near the rheobase typically elicited clusters of spikes of constant instantaneous frequency between pauses, a response referred to as

Figure 3.16 Voltage gated sodium current is not activated in the steady state response near spike threshold.

The Iss-Vss relationship of strong onset response neurons remains unchanged at membrane voltages near the bifurcation point, A) through C). Otherwise, in the hypothetical condition that the bifurcation is a saddle-node type, blockade of sodium should expose this effect by a downward deflection of the Iss-Vss relationship for membrane voltages near the spike threshold (D). The spike threshold is just above the most depolarized voltage in the control Iss-Vss relationship (black, right-most point).

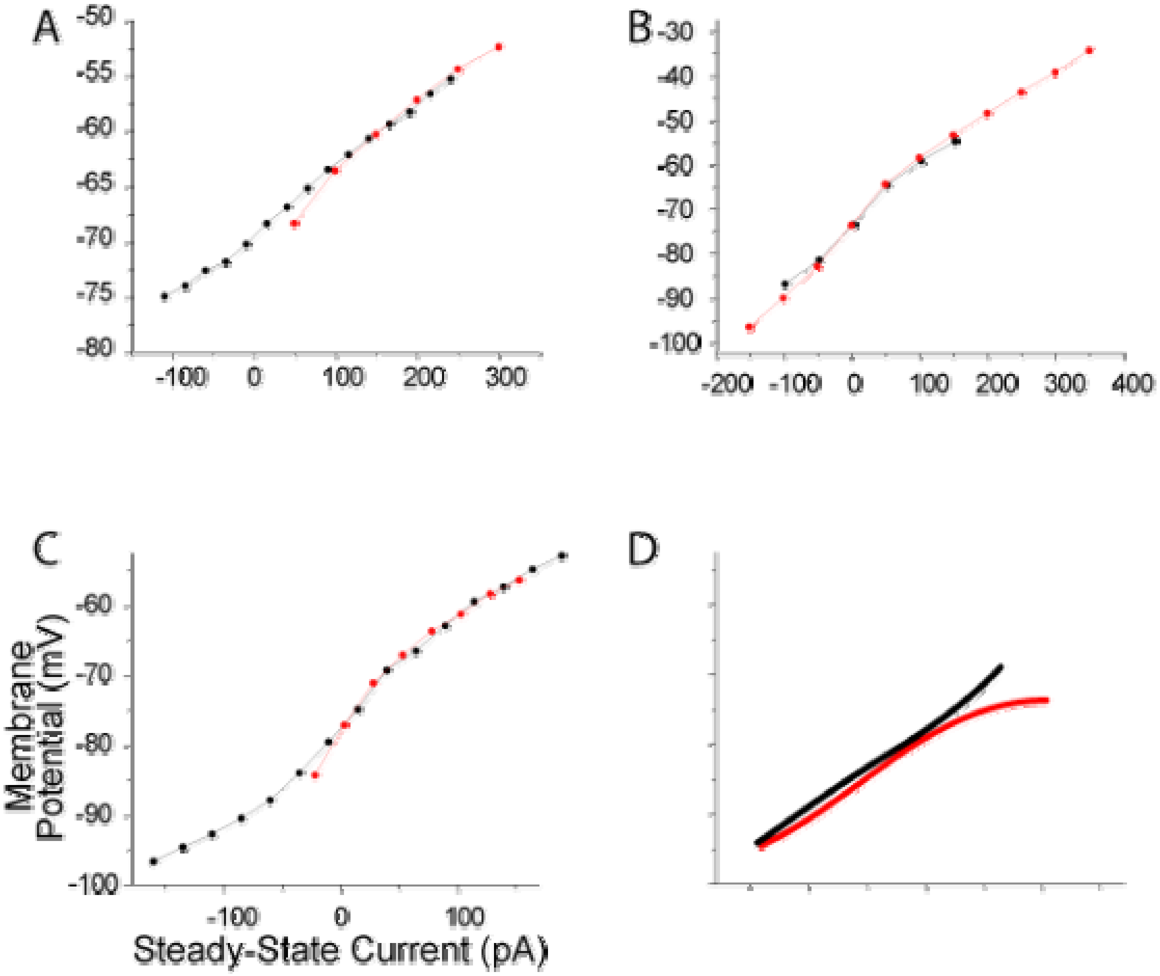
A
-50
-55
-60
-65
-70
-75
-80
-100
0
100
200
300
B
-30
-40
-50
-60
-70
-80
-90
-100
-200
-100
0
100
200
300
400
C
-60
-70
-80
-90
-100
-100
0
100
Membrane Potential (mV)
Steady-State Current (pA)
D

stuttering (Tateno et al. 2004; Izhikevich 2007). This response was observed in either sustained and onset firing neurons (Figure 3.17; Figure 3.18), and is distinct from intrinsic bursting responses, which generally have somewhat constant intervals of both spiking and quiescence (Nowak et al. 2003). The stuttering response suggests the simultaneous existence of two stable behaviours that the neuron may exhibit, either spiking or rest. The existence of two stable states is common to nonlinear systems and is referred to as bistability, where stuttering occurs as a result of the transitions between stable states afforded by small perturbations brought about by noise. Stuttering behaviours occur when the limit cycle and rest state coexist for a range of input current, where the spiking behaviour is that afforded by the limit cycle, and the quiescence by the rest state (Figure 1.4B). Both the saddle-node and AH bifurcations can exhibit bistability. More specifically, the homoclinic saddle-node bifurcation and the subcritical AH bifurcations exhibit bistability.

The stuttering behaviour was detected by the presence of a bimodal distribution in the instantaneous spike frequency histogram (Figure 3.17B; Figure 3.18B). The range of input current capable of eliciting stuttering (the bistable range) was very small, with a mean of 38 pA and standard deviation of 32 pA (from a sample of 45 sustained firing neurons), such that stuttering was often not observed when the current-clamp amplitude increment (step size) was larger than 50 pA.

Bistability can also be tested using current-clamp ramps, which permit measurement of the difference between the spike current threshold (rheobase) and the lowest current that will support firing once firing has begun, a phenomenon referred to as hysteresis (Figure 3.19) (Williams et al. 2002; Fernandez et al. 2007). This difference

Figure 3.17 Stutter firing of spikes observed in a tonic firing cell.

Clusters of spikes are observed in between pauses in firing of variable length A). The instantaneous spike frequency histogram is bimodal B), with the majority of instantaneous spike frequencies about 16 Hz within spiking clusters.

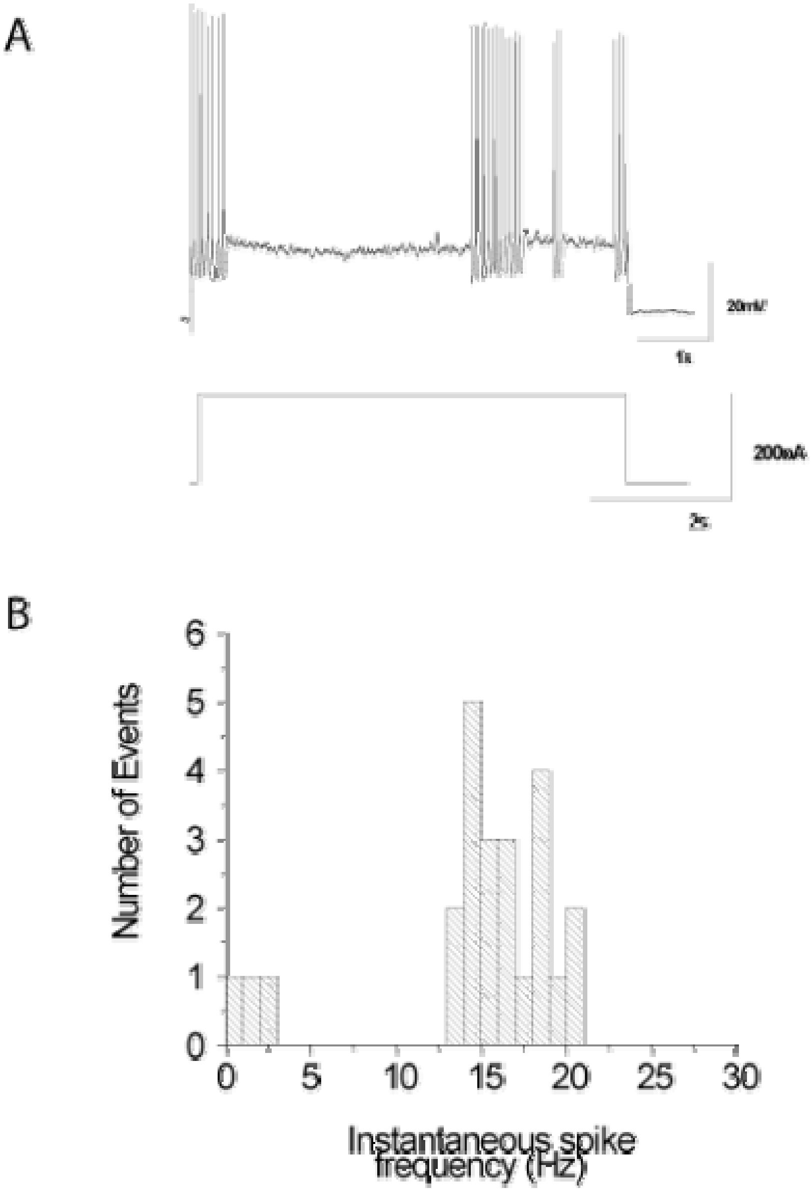
A
20mV
1s
200pA
2s
B
Number of Events
0
1
2
3
4
5
6
0
5
10
15
20
25
30
Instantaneous spike frequency (Hz)

Figure 3.18 Stutter firing of observed in a cell that also exhibits an onset-range.

Stutter firing is also observed in neurons that exhibit an onset response, and is presented in the same manner as (Figure 3.17). After removal of pauses in firing, the spiking frequency was approximately 13 Hz within spiking clusters.

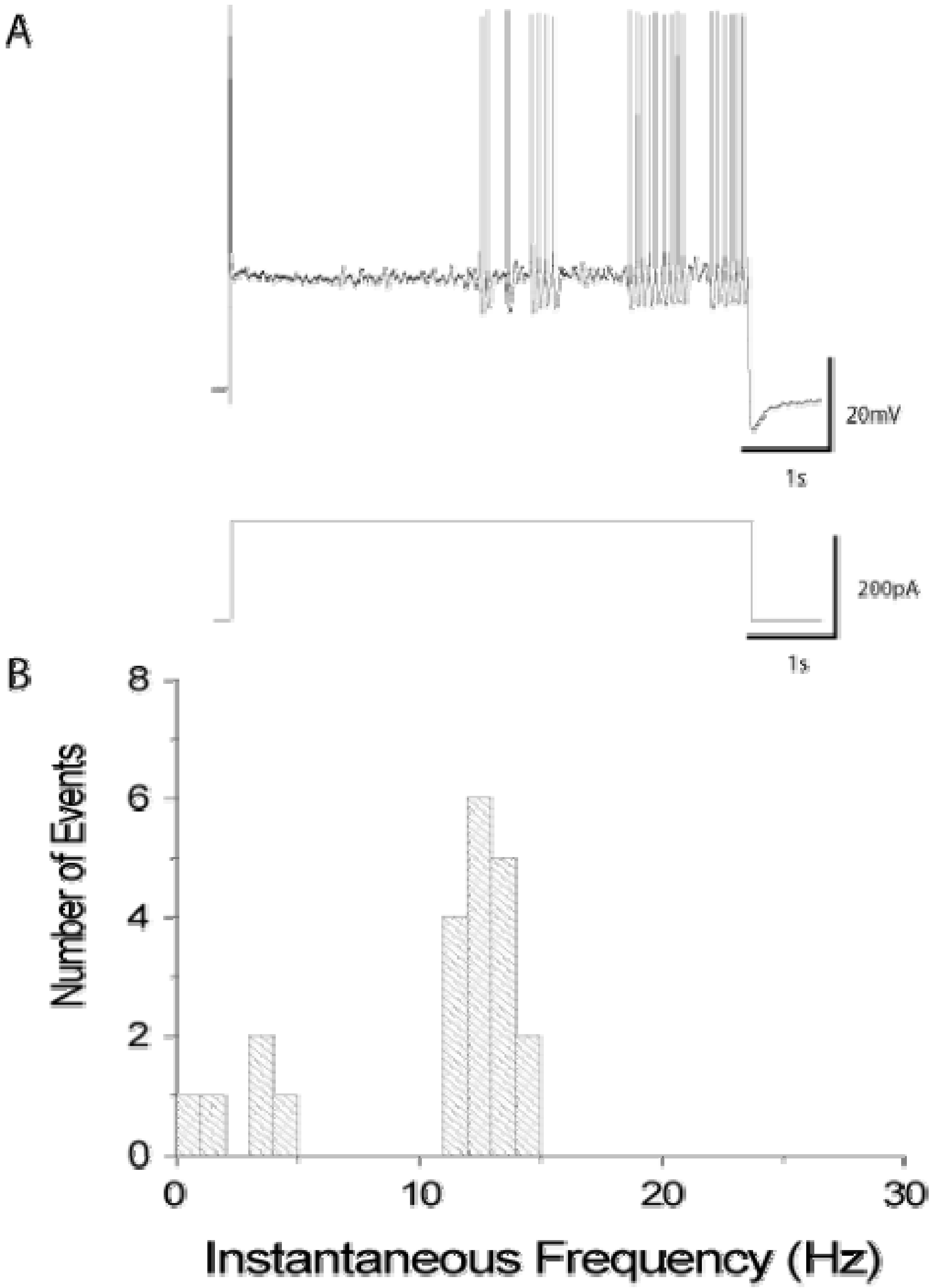
A
20mV
1s
200pA
1s
B
8
6
4
2
0
Number of Events
0
10
20
30
Instantaneous Frequency (Hz)

Figure 3.19 Test for spike hysteresis, an indication of bistability.

The difference between the current threshold for spiking (a), and the current at which spiking stops (b), indicates the degree of bistability. In this case, as with most, the spiking shuts off before the spiking threshold is reached, thereby suggesting that this neuron is not bistable. The time scale is shown by the horizontal bar to indicate five seconds.

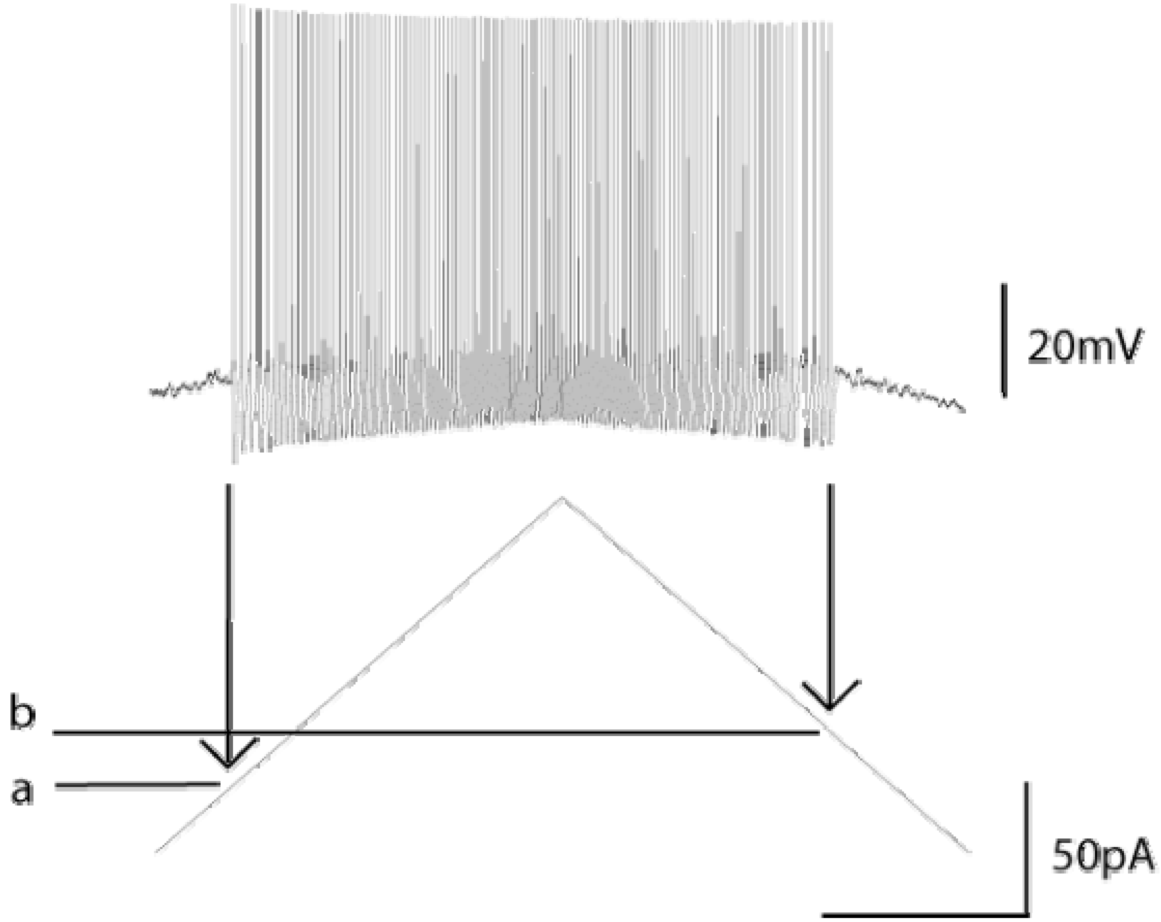
20mV
b
a
50pA

indicates the ability of the neuron to remain in the spiking state (the limit cycle), even though the input current has decreased below the current threshold. This difference was measured in response to very slow current-clamp ramp responses, and most often the spiking response turned off before the rheobase was crossed on return to rest from spiking (Figure 3.20). This observation, although failing to prove bistability, is contaminated considering the small range of bistability and the apparently large membrane voltage noise (see section 3.3.4 in regard to the presence of noise). A counterargument suggests that it is in fact consistent with the bistability. On the up-stroke of the ramp the noise can only advance the onset of the firing state, while on the down-stroke noise can only terminate the firing state. As such, the interaction between the stochastic variables and the bistable dynamics may be able to explain the tendency to fire earlier on the rising portion of the ramp stimulus and analysis of a subcritical AH bifurcation phase plane offers some suggestions. The shape of the limit cycle in the subcritical AH bifurcation is such that the voltage trajectory (purple in Figure 1.4B) passes very closely to the unstable limit cycle (blue circle in Figure 1.4B), which forms the boundary between rest and spiking phase space. Therefore when the membrane behaviour is confined by the limit cycle (the spiking state), as it is on the downstroke of the ramp, it is possible for a small amplitude noise perturbation to switch the membrane into the rest state by pushing the system into the phase space confined by the unstable limit cycle. Whereas, when the membrane behaviour is confined to the fixed point, as it is on the upstroke of the ramp, a noise induced perturbation in any direction in the phase plane will induce the system to start spiking, so long as the perturbation is of sufficient amplitude to push the system outside the unstable limit cycle. For some level of input

Figure 3.20 Representative response to current-clamp ramp stimuli.

A) Spiking in response to decreasing peak ramp current (i-vii). (B) The current-clamp protocol. Spontaneous hyperpolarizations are also observed in all traces, but most prominently in (viii) with the expanded voltage scale (one example, amongst many, is indicated with an arrow).

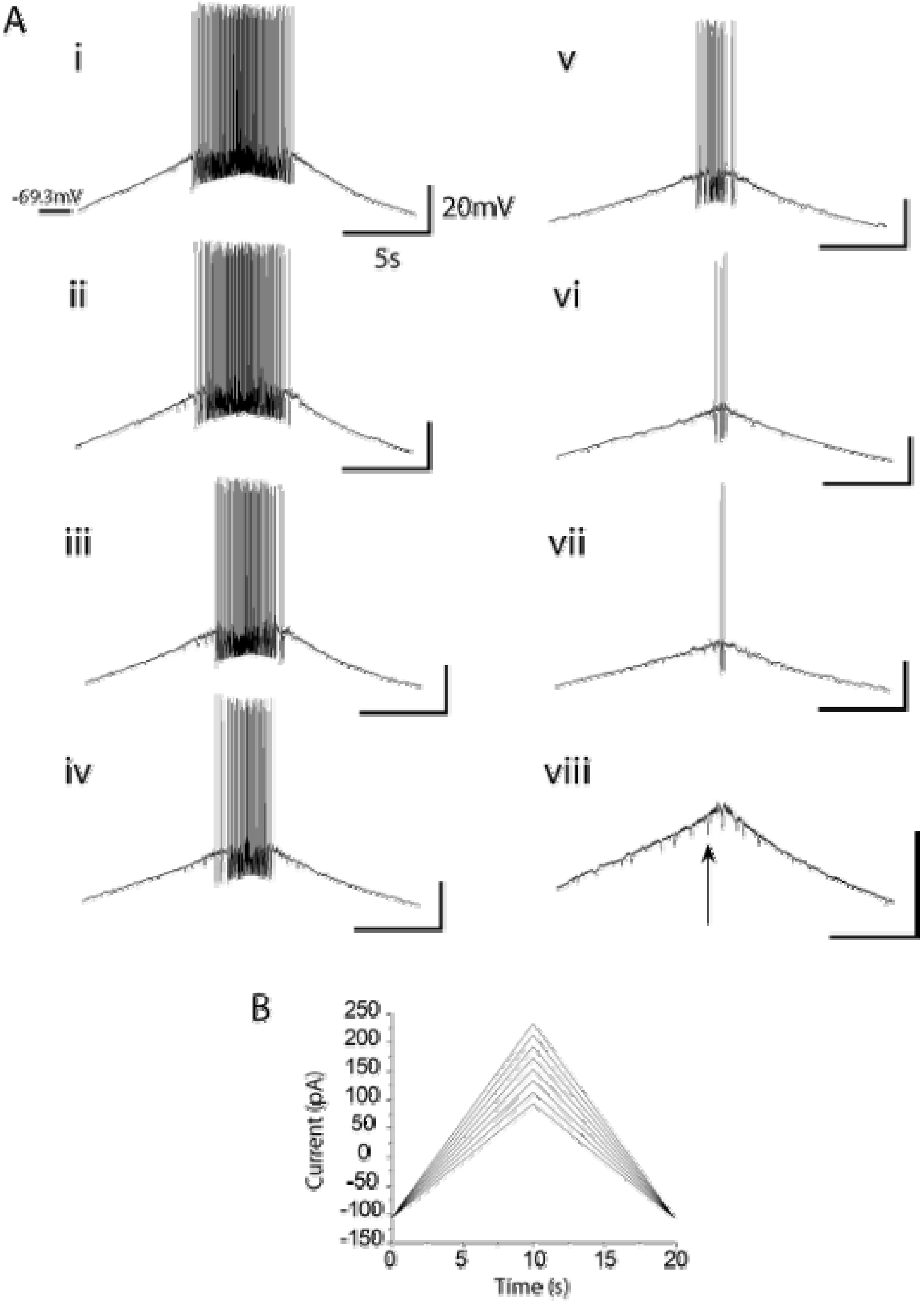
A
i
-69.3mV
20mV
5s
ii
iii
iv
v
vi
vii
viii
B
250
200
150
100
50
0
-50
-100
-150
Current (pA)
0
5
10
15
20
Time (s)

current, the phase is such that noise induced transition into spiking and out of spiking are approximately equally likely, and is the reason we do not observe bistability. Therefore, in the presence of noise the predictions of the deterministic model are not always observable. Simply put, the neuron is not a deterministic system, and requires the incorporation of stochastic influences to fully appreciate and predict its behaviours.

The observation of bistability suggest either the saddle-node homoclinic, or the subcritical AH bifurcation as possibilities for the ICC neurons. However, the AH bifurcation is in favour, in light of the monotonicity of the Iss-Vss relationship.

3.3.3 Minimum Spiking Frequency, and Gain

ICC neurons have a minimum firing frequency, and do not spike at an arbitrarily low frequency. Tonic spiking was considered synonymous with the spike clusters observed during stuttering, both of which occur with a minimum frequency. The minimum tonic spiking frequency was typically 5-20 Hz across neurons of all sustained firing response types (Figure 3.21). To ensure that low freq spiking could be observed, current-clamp pulse durations many fold longer than the period of the observed minimum firing frequency were used. Additionally, the minimum firing frequency was measured once the instantaneous spike frequency reached a steady value, after spike frequency adaptation or acceleration was exhausted.

Early studies of firing responses classified neurons according to their F-I curves as type I, II, or III (Hodgkin 1948). Type I responses do not exhibit a minimum firing frequency in response to constant current-clamp stimuli, and instead fire at an arbitrarily low frequency, type II will not fire spikes below a minimum frequency, and type III is the most distinguishable in that it will not fire tonically, and will only fire onset response

Figure 3.21 There is no difference in minimum spike frequency between response types.

The minimum firing frequency is measured from the smallest pulse amplitude response that fires more than ten spikes. The pulse durations were greater than 2 seconds, and stuttering pauses have been removed, such that the frequency is that of the limit cycle. Mean values are shown (calculated from last ten spikes), with standard error.
No significant difference was observed between firing response types (one-way ANOVA, $p>0.05$).

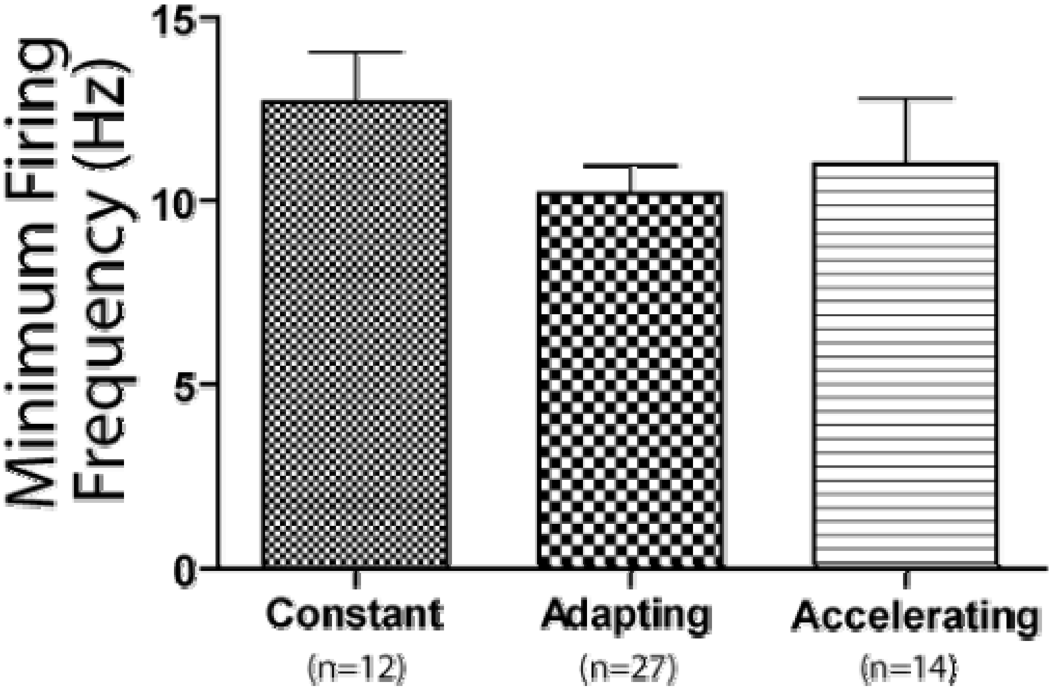
Minimum Firing Frequency (Hz)
15
10
5
0
Constant
(n=12)
Adapting
(n=27)
Accelerating
(n=14)

spikes. By the minimum firing frequency criterion the tonic firing ICC neurons fall into the type II response class, a response that is supported by either the subcritical AH or the saddle-node homoclinic bifurcation.

A linear steady-state frequency to current relationship (F-I) was obtained in response to current clamp pulses. A linear fit to the F-I permitted measurement of the spiking frequency gain (Figure 3.22). Where the gain observed for the accelerating response type neuron was significantly larger than both the onset and adapting types (Figure 3.23).

The F-I relationship was similar when a ramp current-clamp input was used (Figure 3.24). A ramp with very slow time course was used to avoid the effects of accommodating currents on the firing frequency.

3.3.4 Subthreshold Oscillations

Subthreshold oscillations (STOs) are observed in all firing response types. STOs are observed in the quiescent period after the single spike in neurons that exhibit either a strong onset response (Figure 3.2B, C), or a weak onset response (Figure 3.25A). Although the STOs are only present with appreciable amplitude at depolarized potentials near the spike threshold in the case of the weak onset response type (Figure 3.25B), they are observed over a wider range of membrane potentials in the strong onset response type (Figure 3.26). Sustained firing neurons also exhibit STOs during the pauses in stutter firing in the pulse response (Figure 3.27), or the near the spike threshold in the ramp response (Figure 3.28).

A wide range of STO frequencies were observed. These ranged from 2-16 Hz (Figure 3.29), and no difference in mean STO frequency was observed across firing

Figure 3.22 The steady-state firing frequency to current relationship is used to measure spike frequency gain.

The F-I plot of a sustained firing neuron is shown, with the mean steady-state firing frequency of the last ten spikes in the pulse response are shown with their standard deviation (open circles). A linear fit was made to the F-I (thick line), and the firing gain is measured from the slope of the linear fit, in this case 0.10 Hz/pA. The steady-state firing frequency was measured when a constant firing frequency was attained in the pulse response, to avoid the effect of spike frequency adaptation and acceleration.

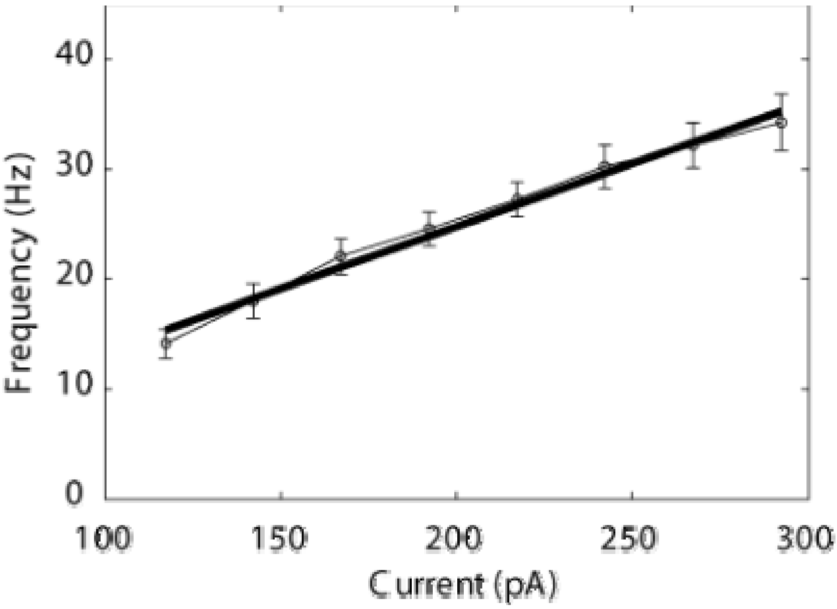
Frequency (Hz)
0
10
20
30
40
Current (pA)
100
150
200
250
300

Figure 3.23 Largest spike frequency gain is observed in the accelerating response type.

The mean spike frequency gains are shown with standard error. The accelerating response type had significantly higher gain than the other two types (one-way ANOVA, Bonferroni's post hoc Multiple Comparison Test at the $p<0.05$ level).

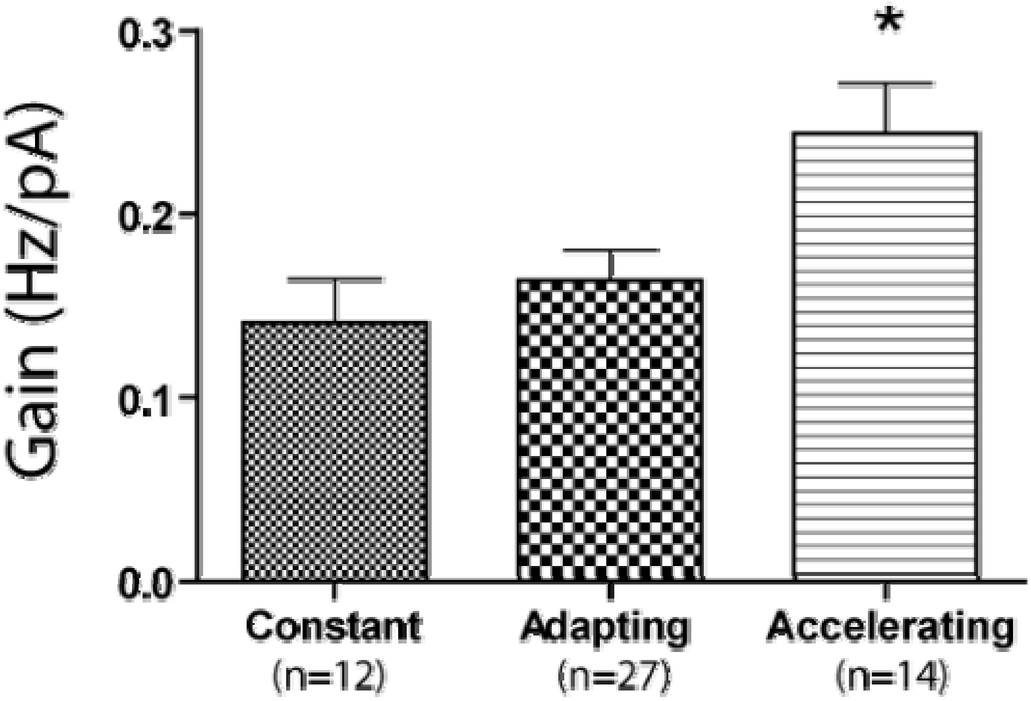
Gain (Hz/pA)
0.3
0.2
0.1
0.0
*
Constant
(n=12)
Adapting
(n=27)
Accelerating
(n=14)

Figure 3.24 The F-I relationship is similar when obtained by current clamp pulse or a slow ramp input.

The mean steady-state frequency observed during a current-clamp pulse is shown (open circles: means with standard deviations). The mean frequency was calculated from the last ten spikes in the response after the removal of stutter pauses.

Instantaneous spike frequency during a ramp current-clamp stimulus (closed circles) produced an F-I profile similar to that of the current-clamp pulse stimulus. Stuttering was observed during the first pulse used to measure the mean frequency, and instantaneous spike frequency, measured in the ramp response in the same current range, was lower than the mean frequency obtained during a pulse stimulus, suggesting that the effects of stuttering were also observed in the ramp response. The ramp was very slow (31pA/s), so as to avoid the effects of accommodating currents.

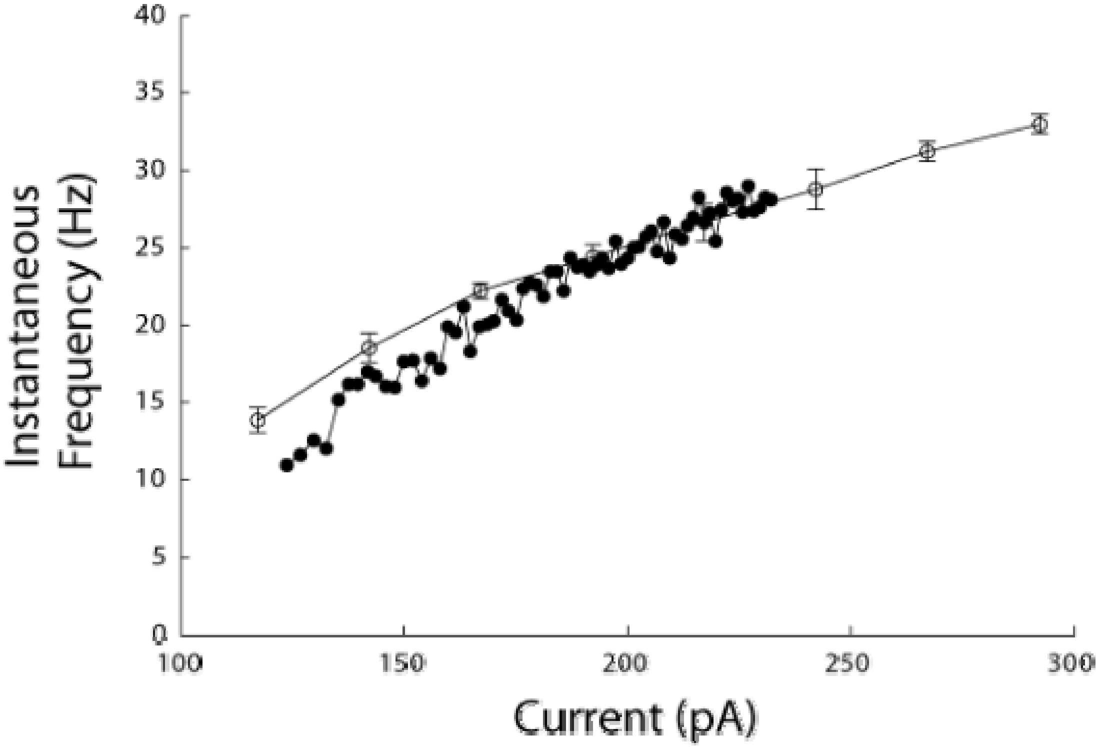
Instantaneous Frequency (Hz)
40
35
30
25
20
15
10
5
0
100
150
200
250
300
Current (pA)

Figure 3.25 Subthreshold oscillations observed in a weak onset response neuron are only present at depolarized potentials.

STO amplitude increases with mean membrane voltage (A.i-iv), as controlled by the current clamp pulse amplitude indicated in (A.v). B) The power spectral density (PSD) was calculated between time points indicated by ovals in (A.i-iv). Peak PSD amplitude (circles) increases with mean membrane voltage. A spontaneous hyperpolarization was observed amongst the STO (arrow; A.ii)

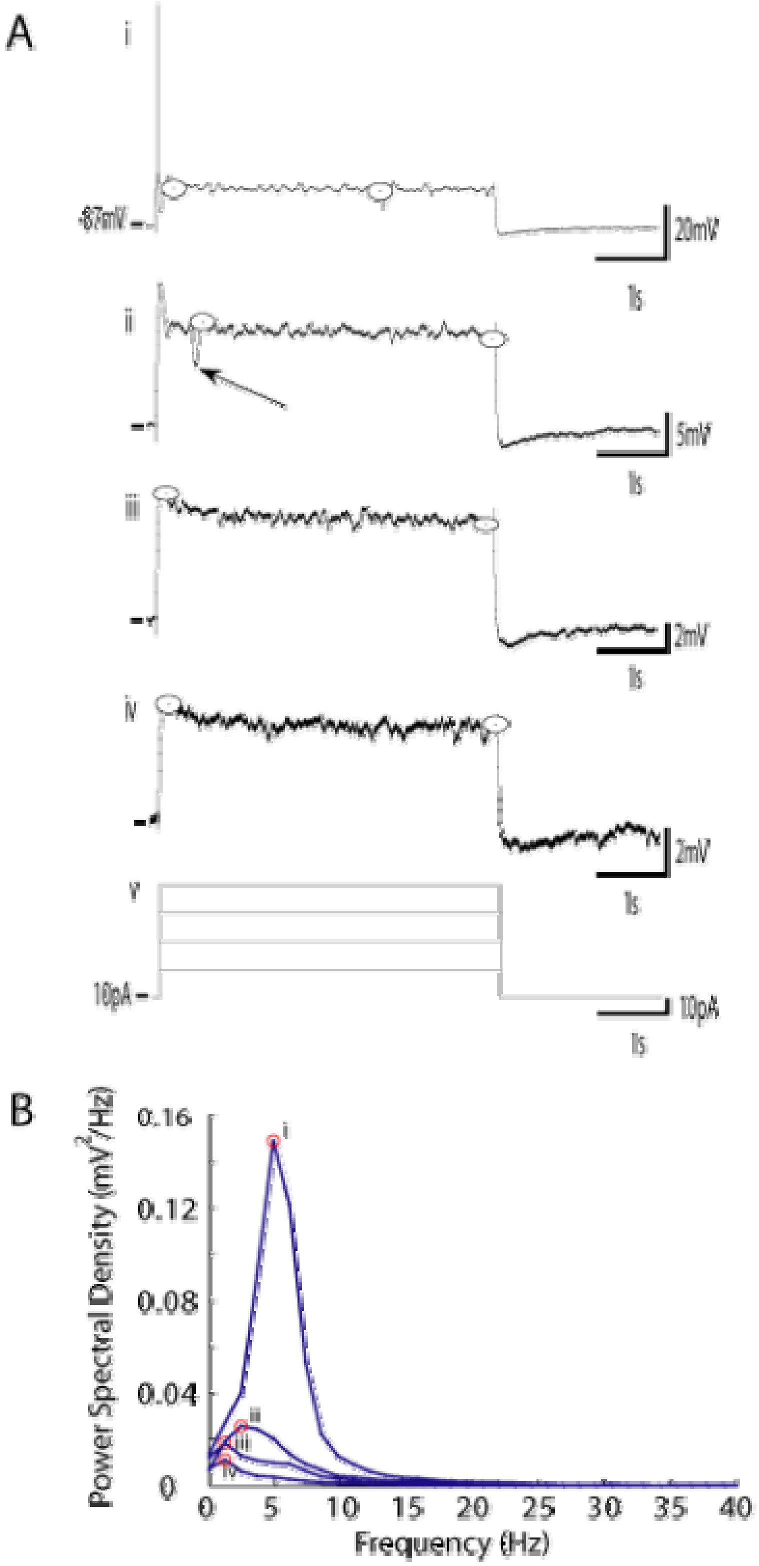
A
i
-87mV
20mV
1s
ii
5mV
1s
iii
2mV
1s
iv
2mV
1s
v
10pA
10pA
1s
B
Power Spectral Density (mV^2/Hz)
0.16
0.12
0.08
0.04
0
0
5
10
15
20
25
30
35
40
Frequency (Hz)
i
ii
iii
iv

Figure 3.26 Subthreshold oscillations observed in a strong-onset response neuron are present at resting membrane potential, and the oscillation frequency is largely invariant of the mean membrane potential.

The peak power of the STO (circle) increases with the mean membrane potential, as controlled by the amplitude of the current-clamp pulse (from 0 to 120 pA in 10 pA steps). The neuron used here is the onset neuron from Figure 3.2.

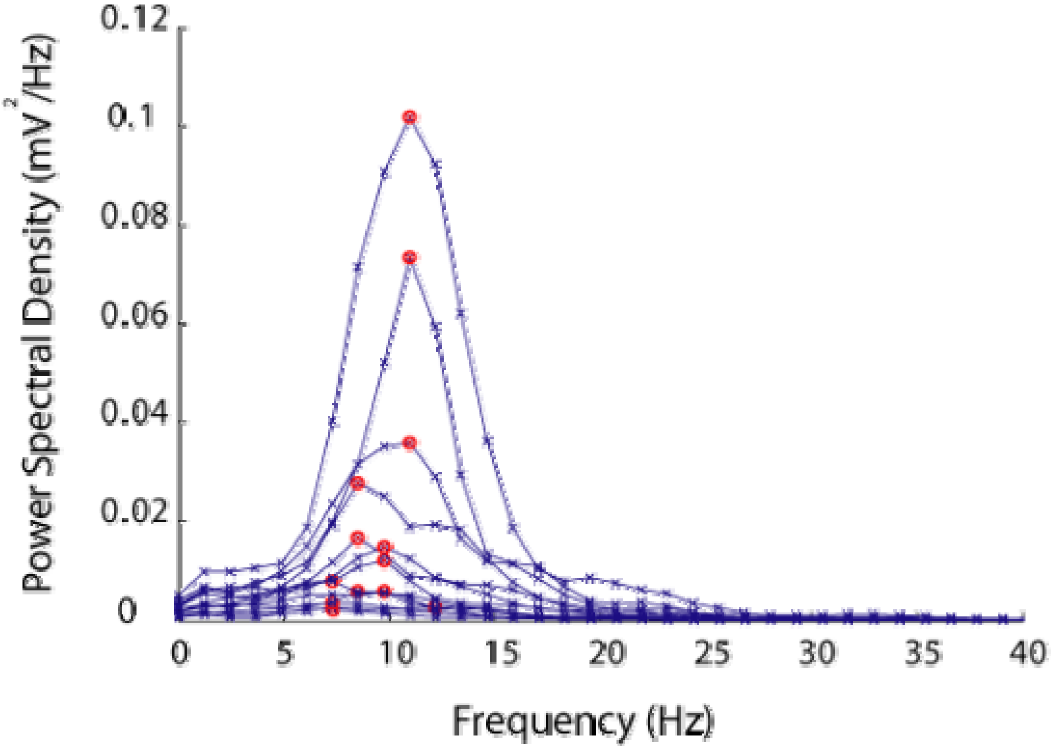
0.12
0.1
0.08
0.06
0.04
0.02
0
Power Spectral Density (mV^2/Hz)
0
5
10
15
20
25
30
35
40
Frequency (Hz)

Figure 3.27 STO observed between spikes in the sustained firing response neuron.

STO is observed in sustained firing neurons in addition to those observed in the onset response neuron. The STOs are observed during pauses in stutter firing (rectangle).

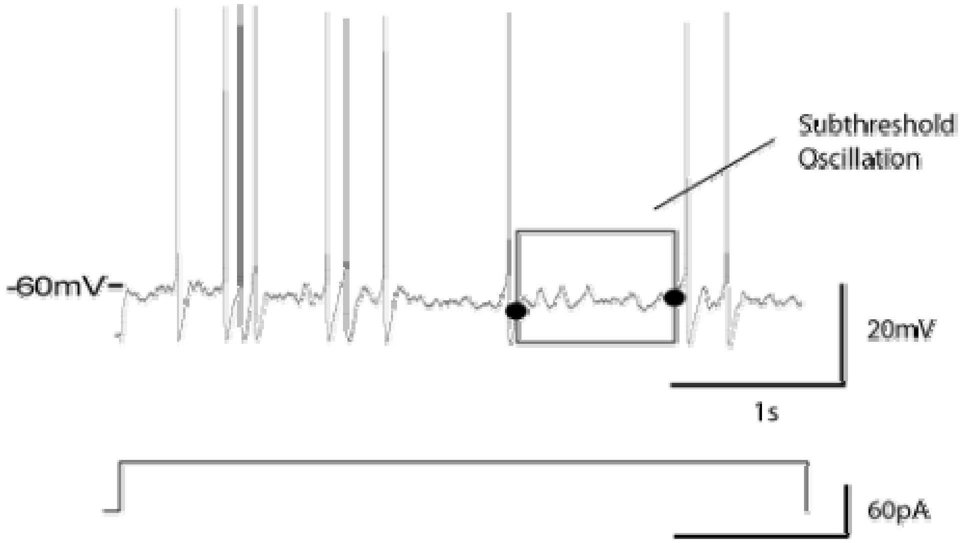
Subthreshold
Oscillation
-60mV-
20mV
1s
60pA

Figure 3.28 STOs are observed before and after spiking in response to a current-clamp ramp stimulus for a narrow range of current.

STOs are shown (see rectangles). Spikes are truncated due to re-sampling at a lower frequency during analysis. This neuron is the same as in Figure 3.27.

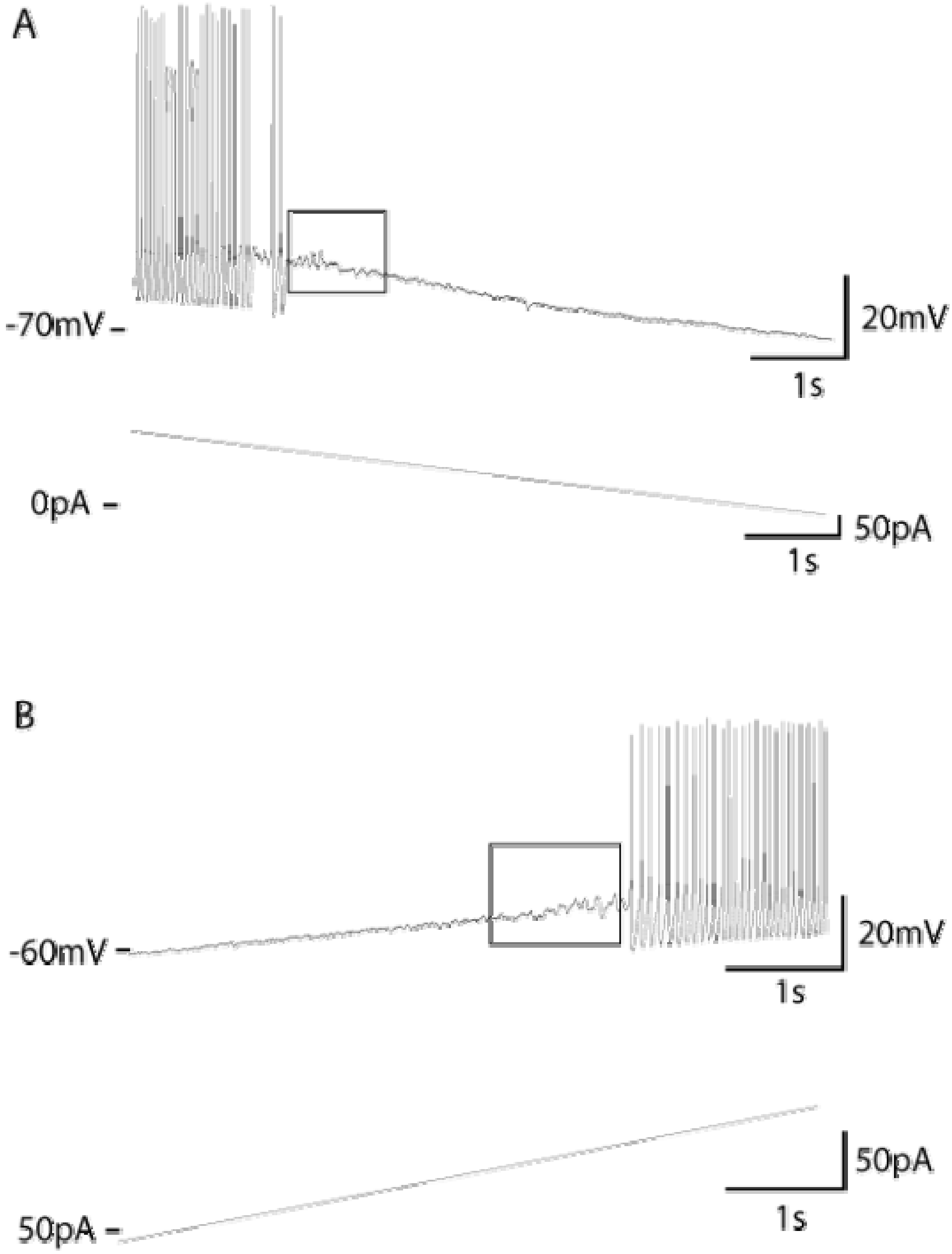
A
-70mV
20mV
1s
0pA
50pA
1s
B
-60mV
20mV
1s
50pA
1s
50pA

Figure 3.29 STO frequencies are distributed between 2 and 16 Hz.

A histogram of the STO frequencies is shown for all firing response types. The STO frequency was measured from the peak PSD from recordings with mean membrane potentials close to the spike threshold.

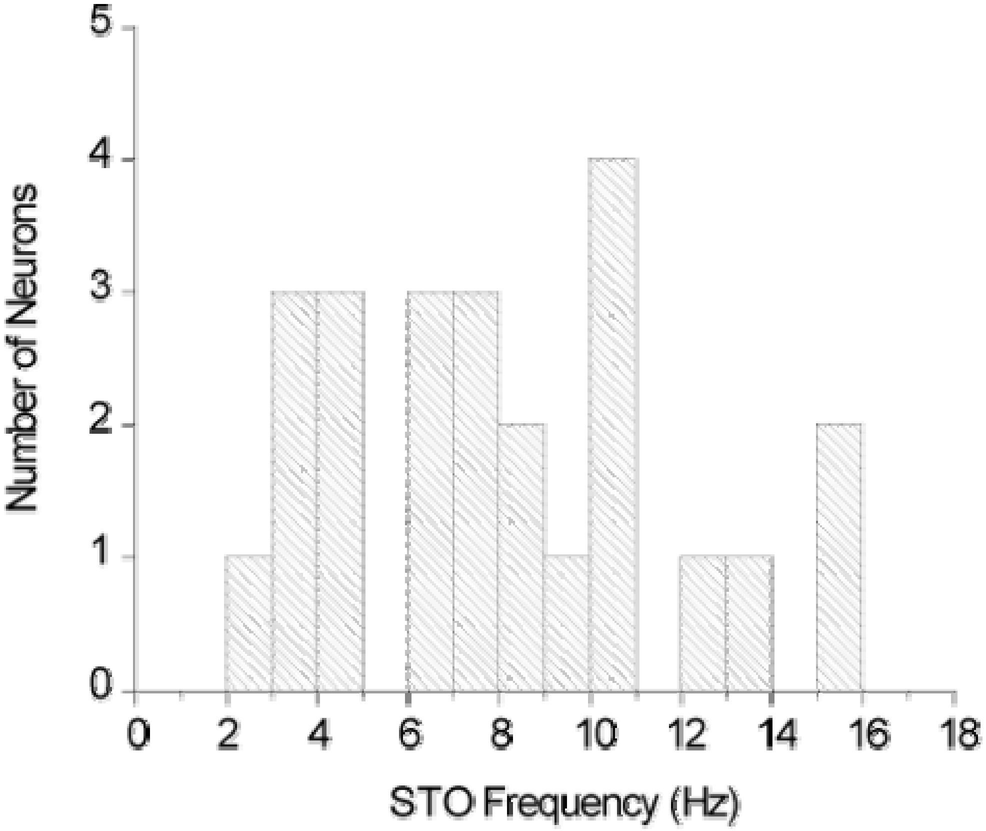
Number of Neurons
0
1
2
3
4
5
0
2
4
6
8
10
12
14
16
18
STO Frequency (Hz)

response types (Figure 3.30). STO frequency correlates well and almost in unity with the minimum firing frequencies (Figure 3.31). This correlation suggests that the oscillations and spiking may share similar kinetics and underlying ionic mechanisms, as is the case in the subcritical AH bifurcation, where the interactions between sodium and potassium currents provide the basis of both behaviours (Figure 1.4). No trend observed between the STO frequency and the mean membrane potential (Figure 3.32).

The ionic mechanism of the STOs was explored by pharmacological blockade of voltage gated ion channels. STOs were observed despite blockade of Ih current with 2 mM CsCl (Figure 3.33; Figure 3.34), whereas blockade of voltage gated sodium channels with TTX abolishes the STOs (Figure 3.35; Figure 3.36). This dependence on voltage gated sodium current suggests that these oscillations may be the result of spiralling trajectories about a fixed point, as is the case for the subcritical AH bifurcation where the fixed point is classified as a focus (Figure 1.4A, B). The manner in which sodium and potassium currents interact is responsible for the spiralling trajectory.

Also of interest is the atypical shape of the PSD profiles used in Figure 3.34. Two additional distinct peaks, other than the largest peak, were observed for the most depolarized mean membrane potentials (Figure 3.34a). After Ih blockade these additional peaks were observed at a lower mean membrane potential (CsCl treatment in Figure 3.34b). Although anecdotal, this observation suggests that Ih might be responsible for attenuation of these lower frequency oscillations at lower mean membrane potentials. Nevertheless, at these depolarized membrane potentials I_h is at the depolarized edge of its activation range.

Figure 3.30 No difference in STO frequency was observed across cell response types.

No significant difference in STO frequency was observed between response types (one-way ANOVA, $p>0.05$).

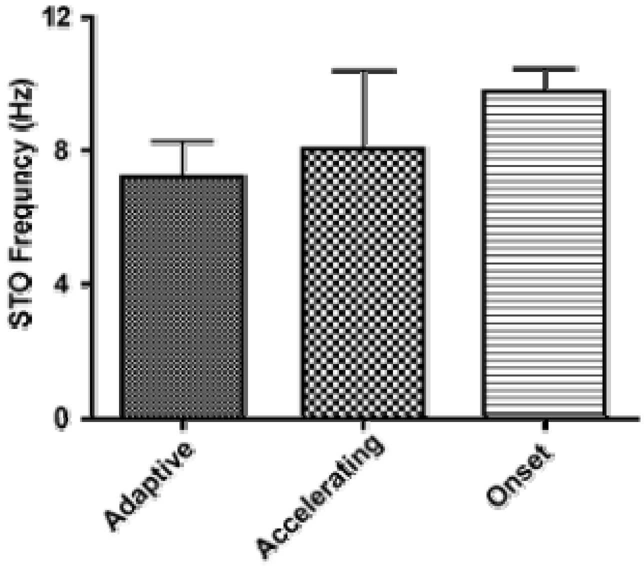
STO Frequncy (Hz)
12
8
4
0
Adaptive
Accelerating
Onset

Figure 3.31 The STO frequency correlates with the minimum firing frequency.

The correlation is approximately one-to-one, as indicated by the slope of the linear fit (solid line), and the minimum firing frequency is typically greater than the membrane potential oscillation as indicated by the y-intercept. Confidence is indicated for 95% (dotted lines), along with the correlation coefficient (R) and the probability of the absence of correlation (P).

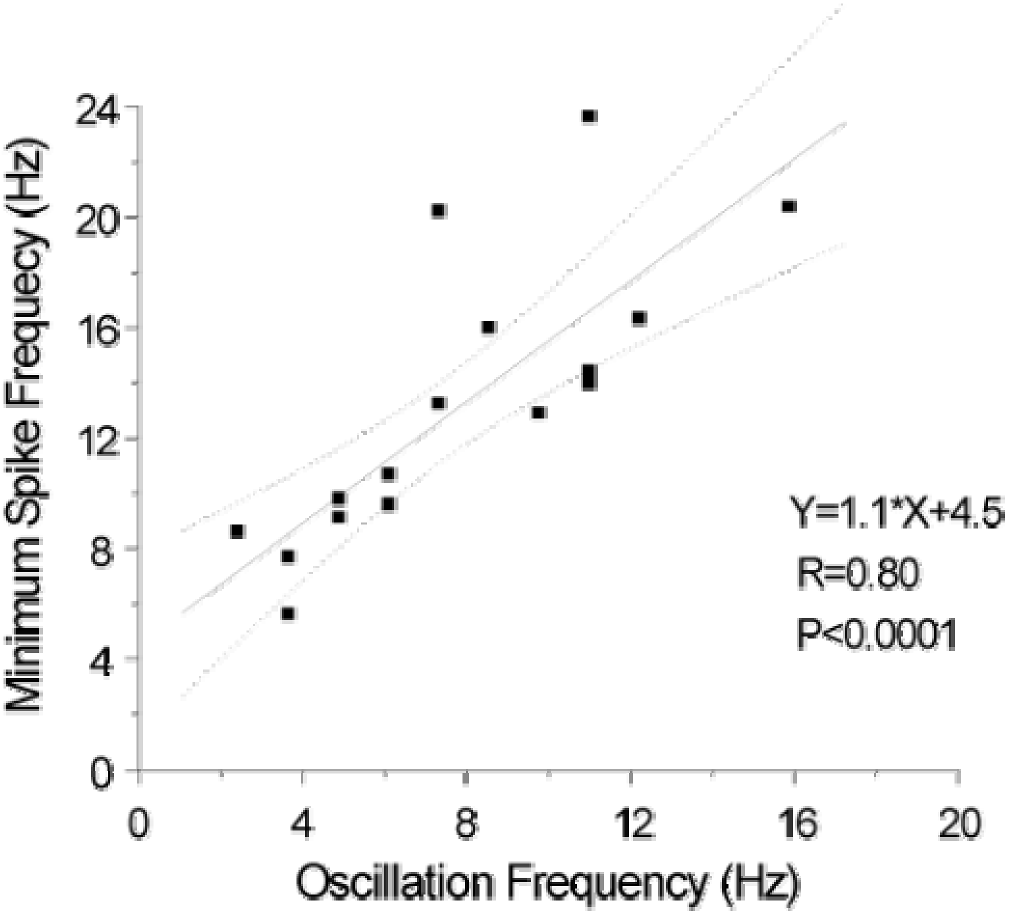
Minimum Spike Frequecy (Hz)
24
20
16
12
8
4
0
0
4
8
12
16
20
Oscillation Frequency (Hz)
Y=1.1*X+4.5
R=0.80
P<0.0001

Figure 3.32 No correlation was observed between STO frequency and the mean membrane voltage.

The effect of mean membrane voltage on the STO frequency is shown for five different neurons. No trend is observed for membrane voltages between resting membrane potential and the spike threshold.

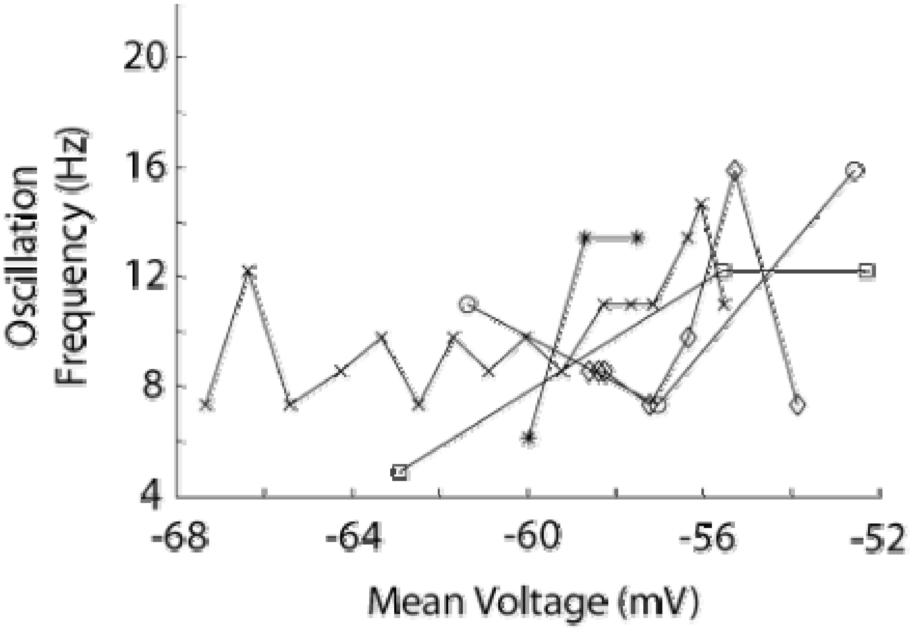

Oscillation Frequency (Hz)
20
16
12
8
4
-68
-64
-60
-56
-52
Mean Voltage (mV)

Figure 3.33 STOs are observed despite blockade of I_h current by CsCl.

Hyperpolarization induced sag (A.f) disappears after bath application of CsCl (2 mM) (B.e), indicating blockade of I_h current. While STOs are observed before spike threshold and between pauses in spiking (most obvious in A.a,b, and B.a,b). The portions of recordings used in subsequent PSD calculations (Figure 3.34) are shown by circles.

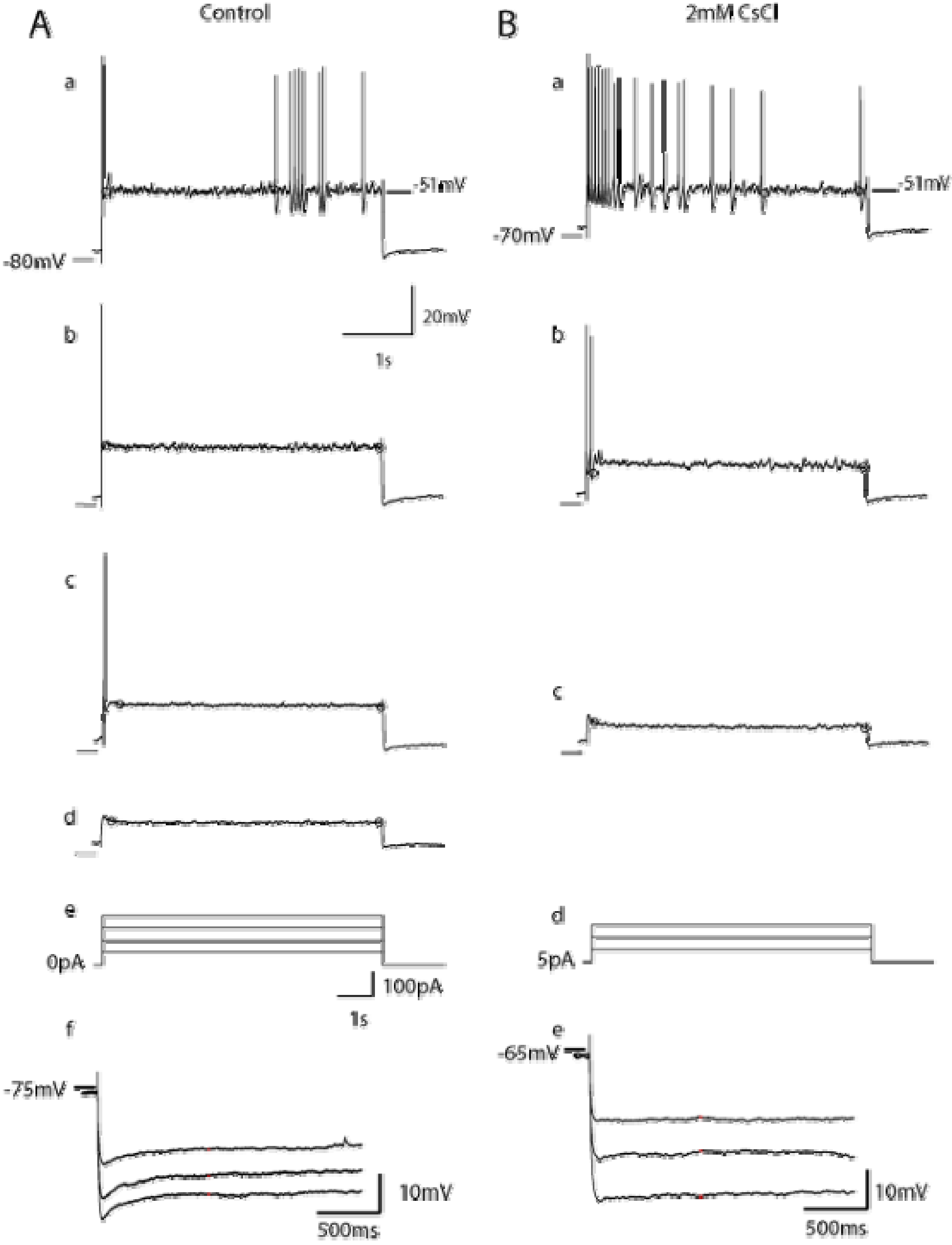
A
Control
B
2mM CsCl
a
-51mV
-80mV
a
-51mV
-70mV
20mV
1s
b
b
c
c
d
e
0pA
100pA
1s
d
5pA
f
-75mV
10mV
500ms
e
-65mV
10mV
500ms

Figure 3.34 STOs were observed despite blockade of I_h by CsCl.

PSD peaks are indicated by solid circles, and labels (letters) correspond to those of Figure 3.33. The mean membrane potential is increased from (d) through (a), under the control of the current clamp pulse amplitude (Figure 3.33e, and f). A similar mean membrane potential depolarization (-51 mV) in (a) for either the control or CsCl treated conditions permits comparison of STO freq and PSD amplitude. The peak PSD is similar between the control and the CsCl treatment conditions; however, the peak frequency appears to shift to higher frequency upon CsCl treatment (by approximately 5 Hz). The spectra shown here are atypical in comparison to other spectra (Figure 3.25B, and Figure 3.26), by the presence of two distinct peaks (arrows) in addition to the largest peak that we consider the peak of the STO.

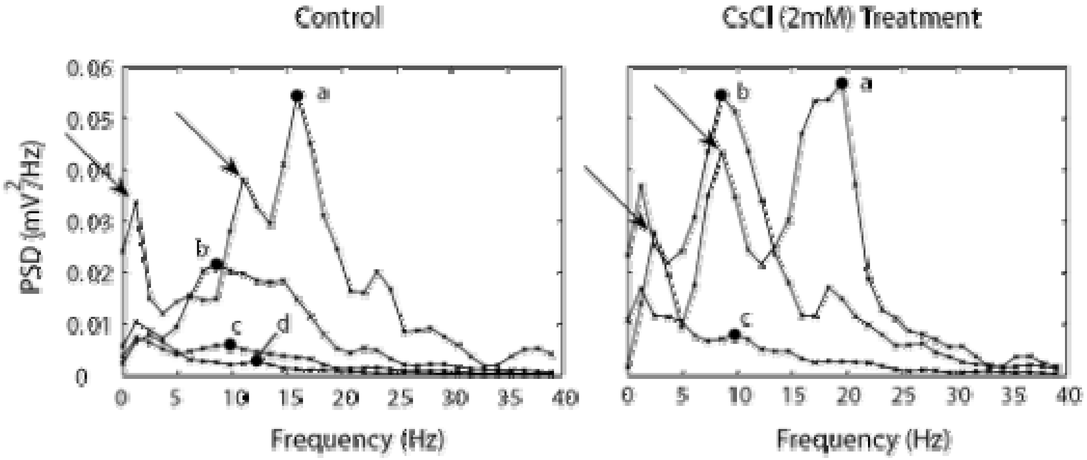
Control
CsCl (2mM) Treatment
PSD (mV²/Hz)
0.06
0.05
0.04
0.03
0.02
0.01
0
a
b
c
d
0
5
10
15
20
25
30
35
40
Frequency (Hz)
a
b
c
0
5
10
15
20
25
30
35
40
Frequency (Hz)

Figure 3.35 Blockade of voltage gated sodium channels by tetrodotoxin abolished STOs.

Application of 200nM TTX abolishes spiking and STOs at all current clamp pulse amplitudes. The portion of the records used in PSD calculations of Figure 3.36 are shown with circles.

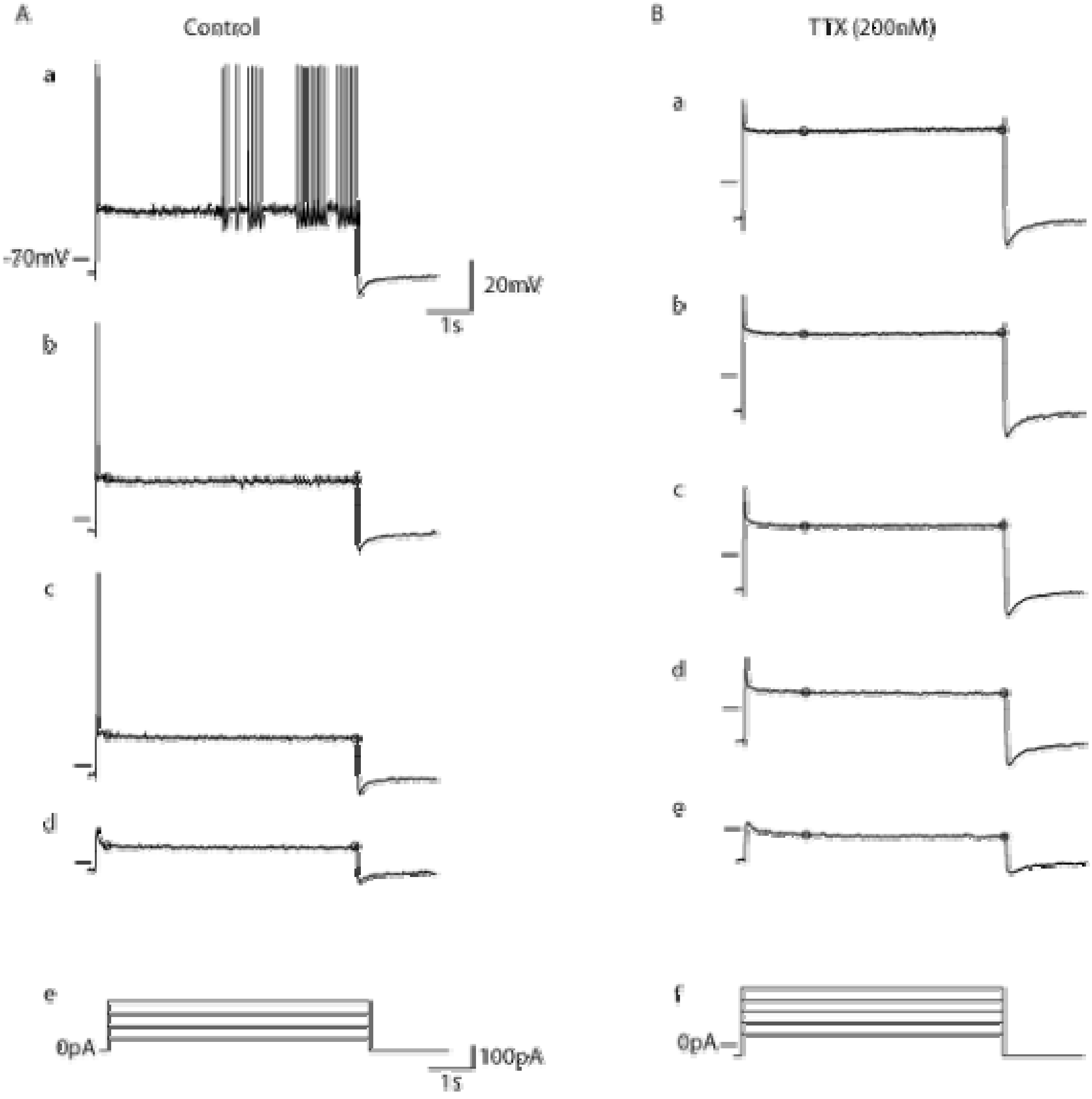
A
Control
a
-70mV
20mV
1s
b
c
d
e
0pA
100pA
1s
B
TTX (200nM)
a
b
c
d
e
f
0pA

Figure 3.36 Application of TTX abolishes STOs.

Oscillation amplitude decreases substantially after TTX application. PSD labels correspond to those of Figure 3.35, and the peaks are indicated by solid circles.

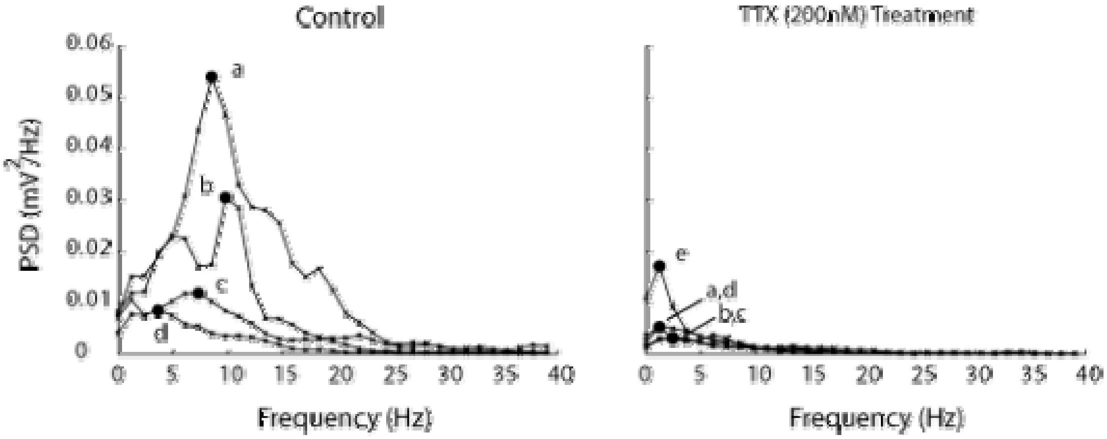
Control
TTX (200nM) Treatment
PSD (mV^2/Hz)
0.06
0.05
0.04
0.03
0.02
0.01
0
a
b
c
d
e
a,d
b,c
0
5
10
15
20
25
30
35
40
Frequency (Hz)
Frequency (Hz)

3.3.5 First Spike Latency

The minimum first spike latencies (FSL) were similar across all firing response types (Figure 3.37B), yet differences in maximum first spike latency were observed (Figure 3.37). In all response types a maximum FSL was observed when the current pulse amplitude was just above the rheobase of the neuron, and successively smaller latencies were observed with larger current-clamp pulse amplitudes. The longest maximum FSL was observed in the accelerating response type (Figure 3.37A), and was many orders of magnitude larger than the minimum latency observed at much larger current pulse amplitudes. Additionally, the voltage trajectory leading to the first spike in the long FSL response of the accelerating response type was non-monotonic and consisted of STOs (Figure 3.38A). The onset and adaptive cell response types had much smaller maximum FSL than the accelerating type, which were at most only one order of magnitude larger than their minimum FSL observed with larger current pulse amplitudes (Figure 3.37B). However the maximal FSL of the onset neuron was significantly smaller than that of the adaptive neuron (Figure 3.39), and may reflect the smaller membrane time constant of the onset neuron (Figure 3.9).

The FSL to pulse amplitude relationship was continuous for both the onset and adaptive firing response types, whereas jumps in the FSL were observed in the accelerating response type. The first of two jumps was observed between the first two observations of spikes, where the latency decreased by many orders of magnitude (Figure 3.37A (arrows), where a specific example is shown between Figure 3.38A, and Figure 3.38B). This jump in latency probably represents a switch from noise evoked spikes following accodommotion of a very slow current, to evoking spike directly after the

Figure 3.37 The maximum FSL is longest in the accelerating response type, shortest in the onset type, and jumps in the FSL were observed in the accelerating response type.

The accelerating response type (green) has a much longer maximum latency than either the onset (red) or adaptive (blue) response types (A); whereas, the onset response type has the shortest maximum latency (B, a rescaled version of A).

Two large jumps in FSL were observed for the accelerating response type. The first jump in latency was very large, on the order of 500 ms to 1 s, between the first two observations of spikes (arrows in (A)), and was followed by a graded decrease in latency. The second jump in latency was smaller, on the order of 30 to 200 ms, and was also followed by a graded decrease in latency (arrows in (B)).

The minimum latency was very similar between all response types (<20-10 ms), and whether or not this minimum was reached depended on whether or not a large enough current-pulse amplitude was applied.

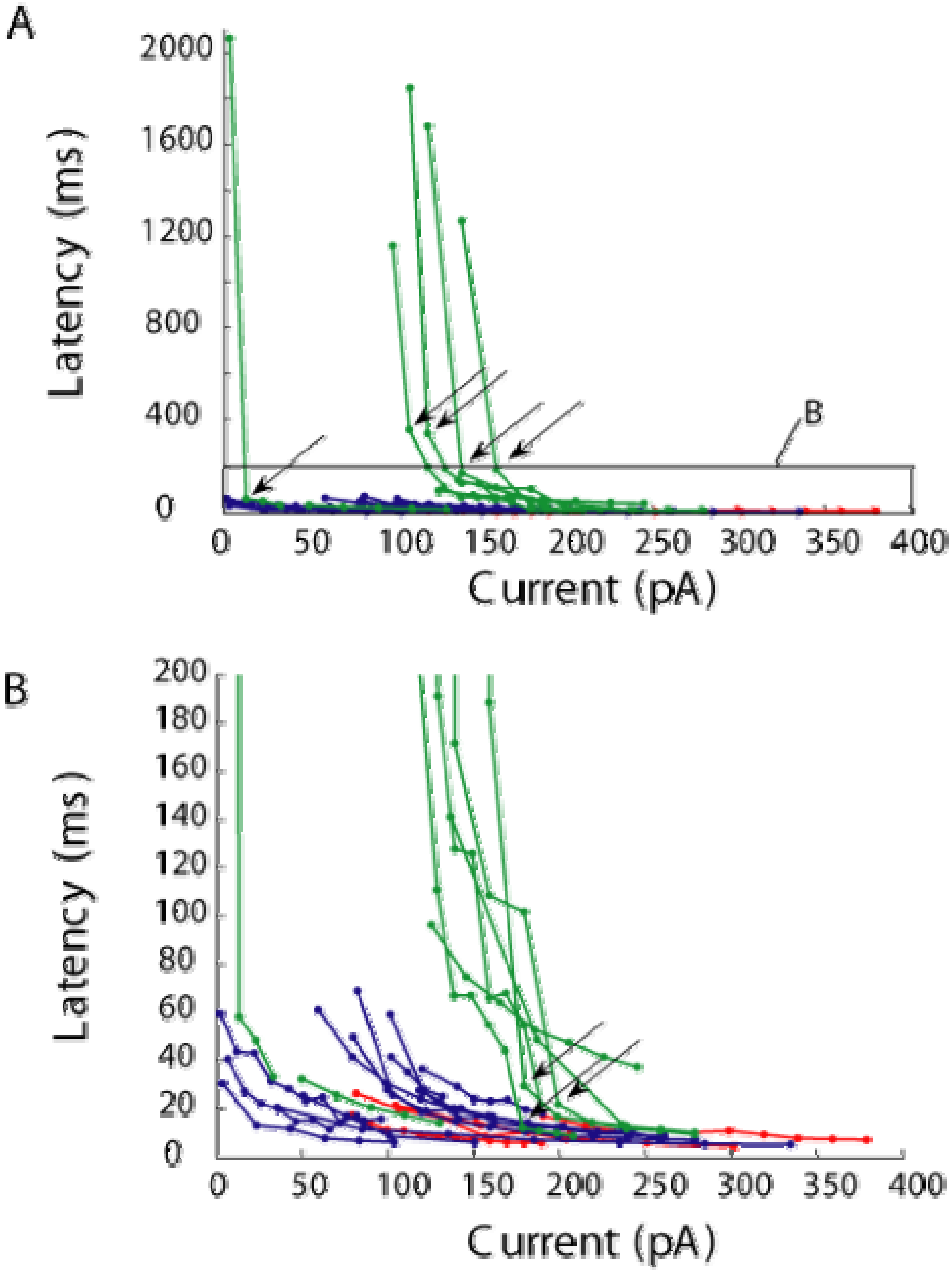
A
2000
1600
1200
800
400
0
Latency (ms)
0
50
100
150
200
250
300
350
400
Current (pA)
B
B
200
180
160
140
120
100
80
60
40
20
0
Latency (ms)
0
50
100
150
200
250
300
350
400
Current (pA)

Figure 3.38 Jumps in latency are observed in the accelerating response type.

The accelerating response type has three stages of latency. A) Small pulse amplitudes elicit spiking after a long delay with intervening STOs. B) Medium pulse amplitudes elicit spiking after a delay with a single hyperpolarization (arrow). C) Large pulse amplitudes elicit short latency to the first spike, and this spike is followed by a hyperpolarization that appears to slow the firing frequency in comparison the steady-state firing frequency. These three responses correspond to the jumps in latency observed in Figure 3.37. The current clamp pulse protocol is also shown (D).

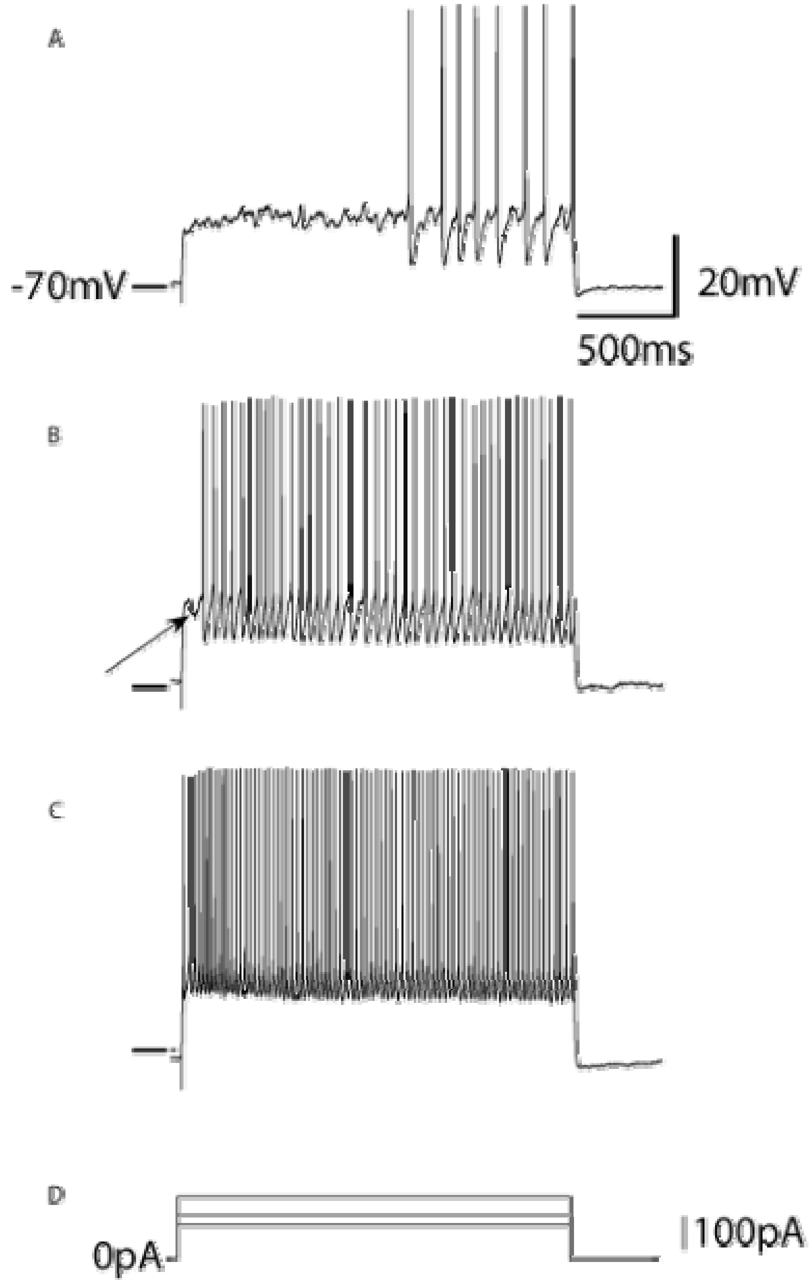
A
-70mV
20mV
500ms
B
C
D
0pA
100pA

Figure 3.39 The maximum latency of the onset response type is significantly smaller than the adaptive type.

A two tailed t-test ($p<0.05$) reveals statistical significance between the maximum latency of the onset response type in comparison with that of the adaptive response type. A comparison to the maximum latency for the accelerating is not included, and it is assumed to be significantly different because it was orders of magnitude larger than those of these two types.

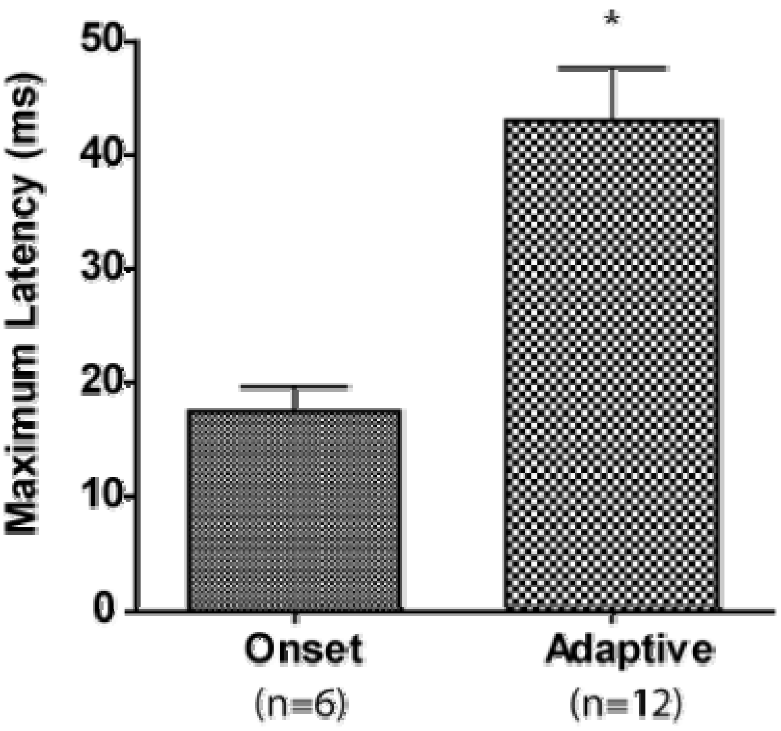
Maximum Latency (ms)
50
40
30
20
10
0
*
Onset
(n=6)
Adaptive
(n=12)

hyperpolarization at the onset current clamp pulse (arrow in Figure 3.38). The fact remains, that these long latencies were not observed in onset or adaptive responses, and indicate exclusive presence of a slowly accommodating current in the accelerating response type. Alternatively, the long latency can arise when the kinetics of the sodium and potassium currents are such that a saddle node bifurcation (SN bifurcation) is possible, however the presence of STOs on the rise to first spike negates this possibility, because STOs are only possible under the condition of an AH bifurcation. The second jump was much smaller, where the latency decreased by at most one order of magnitude (Figure 3.37B (arrows), where a specific example is shown between Figure 3.38B and Figure 3.38C). This jump in latency reflects the separation of spikes by a hyperpolarization at the onset of the pulse response (arrow in Figure 3.38).

Regardless of firing response type, the FSL is conducive of an AH bifurcation. The subcritical AH bifurcation exhibits FSLs graded to the current pulse amplitude, however the range of these latencies is within the same order of magnitude, as is the case for the adaptive and onset response neurons. Systems that exhibit a much larger range of FSL are typical of the saddle node bifurcation. Such systems also exhibit smooth monotonicity in the voltage trajectory preceding the first spike. The FSL of the accelerating type neuron can be very long, however it is unlikely that this long latency is due to a saddle node bifurcation, because the voltage trajectory to the first spike is not smooth monotonic (Figure 3.38A). Subthreshold oscillations are observed instead of a smooth monotonic trajectory on approach to the first spike (Figure 3.38A). Therefore the long FSL is likely due a slowly accommodating current. A candidate mechanism includes activation of an A-type potassium current followed by slow inactivation of a delayed rectifier potassium current, both of which are known to occur in ICC neurons (where the accelerating type is similar to the reported pause-build up neurons (Sivaramakrishnan and Oliver 2001)).

3.4 Summary of Results

ICC neurons can be separated into four major categories according to firing profiles in response to depolarizing current pulses: onset, adapting, accelerating, and constant. Additionally, the onset response can be separated into strong and weak onset responses. The strong onset response appears to reflect the effect of accommodating currents, whereas the weak onset response likely reflects a single spike induced by noise.

To determine the type of fixed point bifurcation in each of the firing response types, we examined several membrane response properties in current-clamp. These include: tonic firing response, the Iss-Vss relationship, bistability, STOs, and FSL. All firing response types exhibited a monotonic Iss-Vss relationship, and no active sodium current was present in the steady state response at the subthreshold membrane potentials leading up to the bifurcation point (the input current where the fixed point looses stability), at least in the case of the onset response neuron as indicated by TTX application. Bistability between spiking and the rest state was observed for current pulse amplitudes near the bifurcation value; however this bistable range was small, and no hysteresis was observed in the spiking response to ramp current-clamp stimuli. Regardless of the firing response type, all ICC neurons have a minimum firing frequency, and the gain of the spiking response is higher in the accelerating response type. STO is another property shared amongst all firing response types, and TTX application demonstrates the requirement of sodium current in STOs. First spike latency was largest in the accelerating response type, where the voltage trajectory preceding the first spike was non-monotonic.

3.5 Discussion

3.5.1 Firing Response Types in the ICC

We hypothesized that differences in the fixed point bifurcation exist across different firing response types. This hypothesis served as the motivation for separating firing response types, which were separated according to the instantaneous firing frequency profile generated in response to depolarizing current pulses. Our classification into four categories—onset, adapting, accelerating, and constant—is slightly more simplistic than that reported elsewhere (Wagner et al. 1987; Li et al. 1998; Reetz and Ehret 1999; Peruzzi et al. 2000; Sivaramakrishnan and Oliver 2001; Wu et al. 2002; Tan et al. 2007). Previous studies of ICC spiking properties employing *in vitro* brain slice intracellular recordings (whole cell, and microelectrode) classify ICC neurons into six different firing response types (Peruzzi et al. 2000; Sivaramakrishnan and Oliver 2001). The biggest difference in this previous classification scheme, in comparison to that of our own, was the inclusion of a subthreshold rebound response as a parameter by which to further separate response types. We found that most ICC neurons can exhibit a subthreshold rebound, given a large amplitude hyperpolarizing current-clamp pulse, and we attribute this response to activation of both the mixed cation current I_h, and possibly the low voltage activated calcium current I_{CaLVA} at hyperpolarized membrane potential (Sivaramakrishnan and Oliver 2001; Koch and Grothe 2003), although the latter is expressed in small quantity (N'Gouemo and Morad 2003). Since we are primarily interested in responses to small perturbations of the membrane potential, we did not separate neurons according to this rebound response. Nevertheless, we share the definition of the onset response type; yet, we disagree with the classification of the five sustained firing response types, and opted for a simpler classification. We have concerns over the validity of the rebound-transient response type, and suggest that it represents an unhealthy neuron. In our hands, this response type was observed only after the neuron had been held in the whole cell configuration for an extended amount of time, while a sustained firing response was observed shortly after the whole cell configuration was achieved. The accelerating response type category used here is similar to the reported buildup-pause category, as is the constant response type to the reported sustained-regular response type. The adapting response type category used here encompasses the remaining two response types, the rebound-regular and the rebound-adapting, both of which have adaptive profiles, regardless of the reported conclusions by Sivaramakrishnan and Oliver (Sivaramakrishnan and Oliver 2001).

Recent reports of *in vivo* whole cell recordings of ICC neurons have classified firing responses into yet another set of categories (Tan et al. 2007). The experimental procedure used to classify firing response types differ from ours in two ways. First, some variability is observed in the firing profile because synaptic blockers were not used. Second, exclusively large magnitude current-clamp pulse amplitudes were used to classify the neuron firing response type, where we make our conclusions of firing response type from much smaller pulse amplitudes. The large amplitude current pulses served largely to establish the existence of spikes, but provided little information about the subthreshold and threshold dynamics vital to spike generation.

Fortunately, only two new response types were identified in the *in vivo* study, and were formed by including burst firing as a parameter for response type classification. These two categories are: the burst-onset and burst-sustained responses. Burst spiking is transient fast spiking (in the range of 200-300 Hz), at frequencies that exceed the maximum tonic firing rate four to five fold in ICC neurons. The burst-sustained response is an example of rhythmic bursting in response to a constant current-clamp pulse, similar to the chattering firing response in neurons of the visual cortex (Nowak et al. 2003). This response was not observed under *in vitro* conditions. Since synaptic blockade was not used in the *in vitro* conditions we cannot rule out the possibility that the bursting rhythm was due to do an extrinsic synaptic signal. However, because the duration of the burst is large and faster than the maximal tonic firing, we suspect that a slower intrinsic conductance might be responsible for the burst-sustained response, and this conductance might not be present *in vitro*. Otherwise the burst-onset response observed *in vivo* is similar to the bursting we observed in the onset and strongly adaptive neurons in response to fast large amplitude deflections of the membrane potential, either with current-clamp pulses, or with low pass filtered Gaussian white noise (see LPFGWN in chapter four). In this study we do not investigate burst firing; instead we restrict our study to small deflections of the membrane potential. Without any doubt, bursting plays an important role in auditory processing, as it is readily observed during afferent auditory stimulation (D'Angelo et al. 2003; Sterbing et al. 2003; Tan and Borst 2007). Additionally, the ability of a neuron to encode the sensory environment with either a tonic or a burst code can provide separation of specific stimulus components (Oswald et al. 2004); whether or not

ICC neurons are capable of doing so, and which response types are best suited to do so, remain unknown.

Experimental conditions employed during intracellular recordings are important in determining the accuracy with which recordings approximate the true response of the intact neuron. In the brain slice preparation, intracellular and extracellular electrolyte concentrations are entirely under the control of the experimenter. It is important to consider that during the whole cell recording procedure the neuron's intracellular space becomes dialyzed by the internal solution on the patch electrode, such that the intracellular electrolyte concentrations become those of the internal solution. The choice of electrolyte concentrations is very important, as they control not only the reversal potentials of various ligand and voltage gated conductances, but often the activation profiles of the latter. Arguably the most important of these electrolytes to consider is calcium, as the intracellular calcium concentration and rate of buffering controls many, often non-linear and unpredictable, cellular properties, such as regulation of I_h current via cyclic adenosine monophosphate (cAMP) production (Luthi and McCormick 1999), or regulation of calcium and voltage activated potassium conductances (Sah 1996; Sah and Faber 2002).

Typical free intracellular calcium concentration are on the order of 50 nM to at most 1 μM (Morris et al. 1987; Morris et al. 1987; Bleakman et al. 1993), and we are therefore sceptical of findings reported by Sivaramakrishnan and Oliver because of their use of an extremely high calcium concentration in their internal pipette solution at 1 mM (Sivaramakrishnan and Oliver 2001). Since abnormally high concentrations of internal calcium lead cellular cascades like apoptosis (Mattson et al. 2000), the only reason that these cell remained viable in that study was the abnormally high concentration of calcium buffer in their internal pipette solution (11 mM, ethylene glycol tetraacetic acid (EGTA)). However the use of high concentration calcium buffer is not an adequate compensation for a poor choice of intracellular calcium concentration, as it most likely disrupts the time course of the buffering of free calcium following calcium influx. In other studies, calcium buffering was more reasonable with 0.2-1 mM EGTA concentrations, and no internal calcium was added to the internal pipette solution (Koch and Grothe 2003; Vale et al. 2003; Tan et al. 2007). Additionally, the extracellular calcium concentration was also larger than reasonable at 2.4 mM, which is almost two-fold larger than the external calcium concentration in cerebral spinal fluid at 1.4 mM (Brown et al. 2004). On another note, the voltage clamp experiments reported by Sivaramakrishnan and Oliver are also troublesome. Control of the membrane potential was poor, as indicated by unclamped action potential generation. The application of TTX to block action potential generation does not rectify this problem, as suggested by the authors, instead proper characterization of voltage gated ion channel expression should be carried out on smaller patches of membrane like outside-outs, or possibly dissociated neurons, where proper control over the membrane potential achieved (Rothman and Manis 2003; Fernandez et al. 2007). The error introduced by inadequate voltage clamp provide inaccurate estimates of the half maximal activation potentials, and is likely the reason that the authors did not make an attempt to identify voltage gated currents by their kinetics.

In the recent *in vivo* ICC study, proper electrolyte concentrations were used for the most part (Tan et al. 2007). The exception being the intracellular chloride concentration, which is very high (20 mM) in this study, such that the chloride reversal potential is around -50 mV, assuming that the external chloride concentration (in the endogenous cerebral spinal fluid) is approximately 133 mM as reported elsewhere (Brown et al. 2004). Therefore, at resting membrane potential around -70 +/-5 mV, either $GABA_A$ or glycine receptor activation will cause depolarization of the membrane, and appear as an EPSPs. In reality, activation of $GABA_A$ or glycine receptors at this membrane potential produces IPSPs, because the true IPSP reversal potential (E_{IPSP}) in ICC neurons is -73.1 +/-2.1 mV, as determined using gramicidin-perforated-patch recordings (Vale et al. 2003). The improper internal chloride concentration probably has no bearing on the firing response type; the linear leak has minimal qualitative effects on the underlying bifurcations, however the resulting upset of the reversal potential, negates any efforts to investigate the contribution of inhibitory synaptic input to the ICC neurons during afferent stimulation.

3.5.2 Identity of the Fixed Point Bifurcation

Following this review and comparison of firing response types observed in our recordings and those reported elsewhere, we return to a discussion of our hypothesis. Across response types there does not appear to be any difference in the fixed point bifurcation, and all response types exhibit spiking and subthreshold responses that are indicative of an Andronov-Hopf fixed point bifurcation. The different firing responses observed in ICC neurons are likely brought about by the expression of different slow accommodating currents. As a summary, different categories of evidence suggest an AH bifurcation and include: the tonic firing response, the Iss-Vss relationship, bistability, STOs, and FSL.

Tonic spiking does not occur at an arbitrarily low frequency in any of the ICC neuron response types. Instead a minimum tonic firing frequency is observed in ICC neurons, which is conducive of an AH bifurcation. This response rules out the saddle node on invariant circle bifurcation in which spiking can occur at an arbitrarily low frequency; however it does not rule out other codimensional-1 fixed point bifurcations. The entorhinal cortex layer 2 stellate neuron is an example of a system that also exhibits a minimum firing frequency (Dickson et al. 1997), and this neuron also appears to exhibit a subcritical AH bifurcation (Rotstein et al. 2006). Similarly, a neuron that exhibits a saddle homoclinic bifurcation can also exhibit a minimum firing frequency, as in the case of the cerebellar purkinje cell (Fernandez et al. 2007). In contrast to a minimum firing frequency, the layer 5 pyramidal neuron in the rat visual cortex can exhibit an arbitrarily low firing frequency, and appears to exhibit the saddle node on invariant circle bifurcation (Izhikevich 2007). A neuronal example does not exist for a supercritical AH bifurcation, in which the amplitude of the oscillation (e.g. action potential amplitude) will increase with input current (Longtin and Milton 1989; Izhikevich 2007).

The relationship between the steady state membrane potential in response to a constant input current (Iss-Vss) provides a description of the steady-state activation of sodium and potassium current. The monotonicity of the Iss-Vss relationship indicates a lack of active sodium in the steady state response. By comparison, the purkinje cell exhibits a non-monotonic Iss-Vss relationship, with an upward deflection near the bifurcation value (the input current required for fixed point to loose stability), which indicates the recruitment of sodium current in the steady state response (Fernandez et al. 2007). This active sodium current is present in the steady state response because the activation and inactivation profiles have a large overlap, and hence a large window current. By comparison, a neuronal system that exhibits an AH bifurcation has a smaller amount of overlap between the activation and inactivation profiles, such that the sodium current is inactivated in the steady state response, and sodium is only activated in response to fast transient inputs. The monotonic Iss-Vss relationship of all ICC neuron response types is conducive of an AH bifurcation (Izhikevich 2007). However, the presence of active sodium current in the steady state response can be masked at steady-state by recruitment of a slow outward current such as an M-current. Unlike the fast potassium current responsible for repolarization following the action potential, this current is too slow to contribute to the bifurcation. The blockade of voltage gated sodium channels with TTX did not, however, unmask the recruitment of active sodium current in the steady state response.

Subthreshold oscillations have been observed in many neuronal systems, such as the pyramidal neurons of the dorsal cochlear nucleus (Manis et al. 2003), the layer 2 stellate neurons of the entorhinal cortex (Fransen et al. 2004; Rotstein et al. 2006), and the mesencephalic trigeminal sensory neurons (Wu et al. 2005). The presence or absence of oscillations is also indicative of the type of bifurcation. Subthreshold oscillations are restricted to the AH bifurcation (Strogatz 2000; Izhikevich 2007). The fact that oscillations were observed across all ICC firing response types provides additional evidence to suggest that ICC neurons exhibit an AH bifurcation. The sensitivity to voltage gated sodium channel blockade by TTX indicates that the bifurcation underlying the transition to spiking is necessary for the subthreshold oscillations to occur. The spiralling trajectories present in the phase plane of the AH bifurcation determine the frequency with which the oscillations occur, and perturbations of the membrane into these trajectories are likely the result of noise generated by ion channel fluctuations (White et al. 1998; White et al. 2000; Dorval and White 2005). The oscillation's insensitivity to I_h blockade by Cs^+ indicates that the interaction between sodium and potassium currents is sufficient for the oscillations to occur, both of which are necessary elements of the AH bifurcation. The range of observed oscillation frequencies and the mechanism of ICC neurons is very similar to that of the layer 2 entorhinal cortex neurons (Haas et al. 2007). Although both subtypes of the AH bifurcation can exhibit subthreshold oscillations, we do not entertain the possibility of a supercritical AH bifurcation because the hallmark feature of the supercritical subtype of increasing action potential amplitude with input current was not observed (Strogatz 2000; Izhikevich 2007).

Bistability is a less obvious neuronal response property, which arises when two attractive regions exist in the phase plane for a given input current value. Bistability between different resting membrane potentials (fixed points) can be observed in some neurons, such as a small proportion of thalamocortical neurons (Hughes et al. 1999), and mitral neurons of the olfactory bulb (Heyward et al. 2001). However, our primary interest in determining the identity of the fixed point bifurcation requires the detection of bistability between the spiking state (the limit cycle), and the resting membrane potential (the fixed point). To avoid confusion we refer to this bistability as spiking bistability. In this bistable system, the spiking state and the resting membrane potential are the stable attractors of the phase plane, where the trajectory starting at any point on the phase plane will arrive at one of these attractors given sufficient elapsed time (for an example of a bistable phase plane in the AH bifurcation: Figure 1.4). This bistability is only observed for a finite range of input current. ICC neurons exhibit spiking bistability, albeit for a very small range of input current. This was observed in histograms of the instantaneous spike frequency in response to current-clamp pulses. Spiking bistability suggests either a saddle node homoclinic bifurcation, or a subcritical Andronov-Hopf bifurcation (Strogatz 2000; Izhikevich 2007); however, oscillations observed during the pauses between stutter spiking, as well as during subthreshold depolarizations, exclude the saddle node bifurcation. Another phenomenon associated with firing bistability is hysteresis, which for a bistable neuron usually presents itself in response to ramp current-clamp stimuli as a resilience to stay in the spiking state on return of the input current to a value below that required for spiking on the increasing portion of the current ramp (Fernandez et al. 2007; Shapiro and Lee 2007). However, the ramp test proved inadequate in detecting spike bistability in the case of the ICC neuron, possibly due to the very small input current range over which bistability is observed. Additionally, the interaction between the stochastic variables and the phase plane may be able to explain the tendency to fire earlier on the rising portion of the ramp stimulus, before the fixed point looses its stability. The mechanism underlying this very small bistable range is not known, however the presence of the slow accommodating currents can influence the size of the bistable range. For example, the expression of I_h has been implicated in decreasing the bistable range in the purkinje cell, which undergoes a saddle node bifurcation (Williams et al. 2002; Fernandez et al. 2007). Nevertheless, the small range of bistability in ICC neurons suggests that these neurons are very responsible to synaptic input.

First spike latency in response to current clamp pulses also offers some suggestion as to the identity of the bifurcation. Indicative of a SN bifurcation are long first spike latencies that are graded over several orders of magnitude with respect to the pulse amplitude; however most ICC neurons, specifically the onset and adaptive response types, exhibited short first latency with values within an order of magnitude. The exception being the accelerating response type, in which long latencies to first spike were observed. However these latencies were not indicative of a SN bifurcation due to the presence of jumps in the FSL to pulse amplitude relationship, and presence of oscillations between the onset of the pulse and the first spike. As mentioned previously, the presence of oscillations alone exclude the possibility of a SN bifurcation (Strogatz 2000; Izhikevich 2007).

3.5.3 Why is the Identity of the Fixed Point Bifurcation Important?

The identity of the fixed point bifurcation determines the neuronal computational properties of the neuron, and serves as the motivation for collecting the aforementioned evidence. Our hypothesis that different firing response types exhibit different fixed point bifurcations was made in light of an apparent dual strategy of encoding amplitude modulations with both temporal and rate level in the IC (Joris et al. 2004). More specifically, we hypothesized that the subset of ICC neurons that encode amplitude modulation with a rate level code might exhibit a SN on invariant circle bifurcation, which would confer a greater range of spiking frequency over which to encode amplitude modulation. Conversely, the temporal coding might occur in neurons that exhibit AH bifurcations. We continue with a discussion of computational features intrinsic to the AH bifurcation, and compare it to those of the other bifurcations. The computational features of the AH bifurcation include: frequency selectivity, an undefined spike threshold, and a bi-directional phase reset curve.

The AH bifurcation confers frequency selectivity. About the fixed point of a SN bifucation, perturbations of the membrane potential lead straight to the fixed point; whereas perturbations about the fixed point of the AH bifurcation return to the fixed point via a spiralling trajectory (Figure 1.4A, B), and the period of the spiral is determined from the eigenvalues of the system at the fixed point. If the perturbations are spaced in time on the same order as the period of the spiralling trajectory, then a larger membrane potential response will be observed than is otherwise possible for perturbations with either higher or lower frequency content than the frequency of the spiral. The spiralling trajectory confers frequency selectivity, and is the mechanism underlying a subthreshold band pass response. In contrast, such a response is not present in SN bifurcations, where the subthreshold response is that of a low pass filter (Strogatz 2000; Fernandez et al. 2007; Izhikevich 2007). Subthreshold oscillations are a product of the band pass response, where noisy inputs from fluctuations of voltage gated ion channels provide perturbations of the membrane, and the spiralling trajectories serve to select for a certain frequency band within this broad band source. In effect, STOs are the filtered output of intrinsic membrane noise.

Spike threshold is undefined in the AH bifurcation. In a system with a SN bifurcation, a spike is observed following a perturbation of the membrane potential beyond a certain voltage value, the spike threshold. A separation of the phase plane into subthreshold, and superthreshold values arises in the SN bifucation and is referred to as the separatrix (Fernandez et al. 2007; Izhikevich 2007). In contrast, in a system with an

AH bifurcation, perturbation induced spiking does not depend solely on membrane voltage, but also on the state of the other dynamic variables. At the fixed point of an AH bifurcation, spiking can be achieved by moving the system outside of the phase plane area contained by the unstable limit cycle (Figure 1.4B), and this is possible by either a perturbation of the membrane potential (in either the positive or negative direction), or a perturbation of the gating variable (also in either the positive or negative direction); this contrasts to the situation of the SN bifurcation, where the criteria for spiking requires a perturbation of the membrane voltage in the positive direction beyond the threshold voltage. Therefore the transition from rest to spiking is very different, depending on the bifurcation of the system. From the resting membrane potential of a SN system, the transition to spiking depends on the resting membrane potential and the size of the perturbation; whereas a more complicated criteria for spiking occurs in the AH bifurcation, where the states of the dynamic variables determines both the amplitude and direction of the perturbation necessary to elicit spiking. A special feature of this undefined spike threshold is anode break excitation, where the return from a strong hyperpolarization, such as a hyperpolarizing current pulse, will elicit a spike on return to the fixed point. Likewise, a smaller hyperpolarization can facilitate spiking in response to a subsequent depolarization, a phenomenon referred to as post-inhibitory facilitation (Dodla et al. 2006). Slow accommodating currents, such as I_h and I_{CaLVA} may also contribute to spiking following a strong hyperpolarization; in fact, they may confer this response in a system that exhibits a SN bifurcation, where this response is not otherwise possible. Therefore, whether or not a spike is elicited following a perturbation in a neuron exhibiting an AH bifurcation depends greatly on the previous history of the neuron. In contrast, a neuron that exhibits a SN bifurcation requires only that a voltage threshold is exceeded. We continue to implement the term spike threshold throughout this manuscript, all the while keeping in mind that it is not an absolute value in the context of neurons that exhibit AH bifurcations.

Perturbations affect spiking intervals differently depending on the type of bifurcation. Under the condition of tonic spiking, a small perturbation of the membrane potential may advance or delay the phase of the next spike, depending on when the perturbation was made in relation to the spiking cycle. For a system with type I spiking, that is a SN on invariant circle bifurcation, the perturbation can only advance the phase of the next spike (Ermentrout 1996; Izhikevich 2007), as demonstrated in the cat layer 5 sensorimotor cortex (Reyes and Fetz 1993). In contrast, perturbations in the AH bifurcation will delay or advance the next spike depending on when the perturbation is delivered with respect to phase of the spiking cycle (Hansel et al. 1995; Izhikevich 2007). Specifically, a perturbation delivered early in the spike cycle will delay the next spike, and a perturbation nearer the end of the cycle will advance the next spike. These two examples indicate how two different strategies might exist to encode the arrival time of a perturbation, such as a synaptic input, in relation to a previous spike.

Identification of the bifurcation type provides insight necessary to build accurate neuronal conductance models. The bifurcation type alone offers much insight into the relation between the activation and inactivation curves and the time scales of the current, which in return indicate the behaviour of the nullclines. As an example, the SN bifurcation requires a large sodium window current. Furthermore, if the neuron exhibits a SN on invariant circle subtype, then the recovery variable must have slower kinetics than those necessary for a homoclinic SN bifurcation. Likewise, if one wishes to model an apparent AH bifurcation, then there must be very little sodium window current, and the eigenvalues at the fixed point must be complex valued. In essence, knowledge of the bifurcation type provides more constraints on the multi-parameter model, which is always helpful, given that the number of parameters that need to be specified can be quite large. A model build around the bifurcation type serves as a base onto which slower accommodating current can be added to achieve the full response of the neuron.

As contrast, it is worth mentioning that the original Hodgkin Huxley model (HH-model) for action potential generation in the squid giant axon exhibits an AH bifurcation (Fitzhugh 1960; Koch and Segev 1998; Izhikevich 2007). Therefore the application of this model is appropriate only for neurons that exhibit such a bifurcation. The HH-model is only one instance of the conductance based model, and any of the co-dimensional-1 bifurcations are possible by modification of the model parameters. As an example, a leftward (hyperpolarizing) shift of the steady-state activation profile will transform will transform the fixed point bifurcation of the HH-model into a saddle-node bifurcation (Guckenheimer and Labouriau 1992; Fernandez et al. 2007; Izhikevich 2007).

Chapter Four: Temporal Filtering and Resonance.

4.1 Overview

This chapter is an investigation of the ability of ICC neurons to act as temporal filters of time-varying synaptic current, and whether their filtering characteristics are different across cell types as distinguished by firing response. This was realized by observing the membrane potential response to broadband stimuli applied via a patch electrode in current clamp configuration. An impedance profile was generated from this response, and allows a comparison of membrane responses across input frequencies.

We show that ICC neurons can exhibit a band-pass filtering response to small perturbations of the membrane potential. This band-pass feature is more pronounced in neurons that exhibit an onset response to a current clamp pulse, and less so in neurons exhibiting sustained tonic firing responses. The voltage gated hyperpolarization activated cyclic nucleotide dependent current (I_h) appears to be primarily responsible for this resonance response, in addition to smaller contributions by low voltage activated calcium current (I_{CaLVA}), and voltage gated sodium current (I_{Na}). A simple conductance model was fit to a recorded subthreshold response, and used to demonstrate the sufficiency of I_h in attenuation of low frequency inputs required for the resonance response.

In the previous chapter, we presented evidence suggesting that ICC neurons undergo an Andronov-Hopf (AH bifurcation) fixed point bifurcation. This bifurcation exhibits membrane potential oscillations in the presence of a noise source, because the voltage trajectories are confined to spiralling trajectories on their return to the fixed point (resting membrane potential). These spiralling trajectories exist due to interactions between fast dynamics of voltage gated sodium and potassium currents. The resonant response examined here is a continuation on this theme, where other slower currents activated at more hyperpolarized membrane voltages serve to attenuate and amplify inputs depending on the spectral content of the input.

4.2 Results

4.2.1 Calculation of the Impedance Profile

Two different inputs were used to probe the filtering characteristics of ICC neurons in response to current sources. Our first approach employed the ZAP protocol, which is a time varying current clamp protocol consisting of a frequency modulated sinusoid (Equation 2.1; Equation 2.2; Figure 4.1A). By applying this protocol in whole cell current clamp configuration, a resonant response could be observed qualitatively by a maximal response in the membrane potential output at the point in time when the modulation frequency approaches that of the resonant frequency of the neuron (Figure 4.1B). The impedance amplitude profile (Figure 4.1D) was calculated as the magnitude of the ratio of the spectral content of the membrane potential output over the spectral content of the input stimulus (Figure 4.1C). The peak in the impedance profile indicates the maximal impedance, and the resonant frequency at which it occurs.

Our second approach employed a low-pass filtered Gaussian white noise (LPFGWN) input, instead of the ZAP protocol (Figure 4.2A). The longer signal duration permitted the use of a window averaging spectral technique (Welch’s method) to improve the spectral estimates (Figure 4.2). To demonstrate the improvements in the spectral estimates, their confidence intervals were calculated under the assumption of a Chi-square distribution (see chapter two for method).

Figure 4.1 Impedance profile calculated from a ZAP input protocol.

A) The ZAP current clamp protocol with a frequency sweep of 0 to 15 Hz over a duration of thirty seconds, and (B) the associated membrane potential response is shown. C) Amplitude spectra were generated by the fast Fourier transforms of both the current clamp input (A) and membrane voltage output (B). D) The impedance magnitude calculated from the ratio of spectra in (C), with maximal impedance Z_{max} at a resonant frequency F_r, and an input resistance R_{in}. This recording belongs to the strong onset neuron of Figure 3.2.

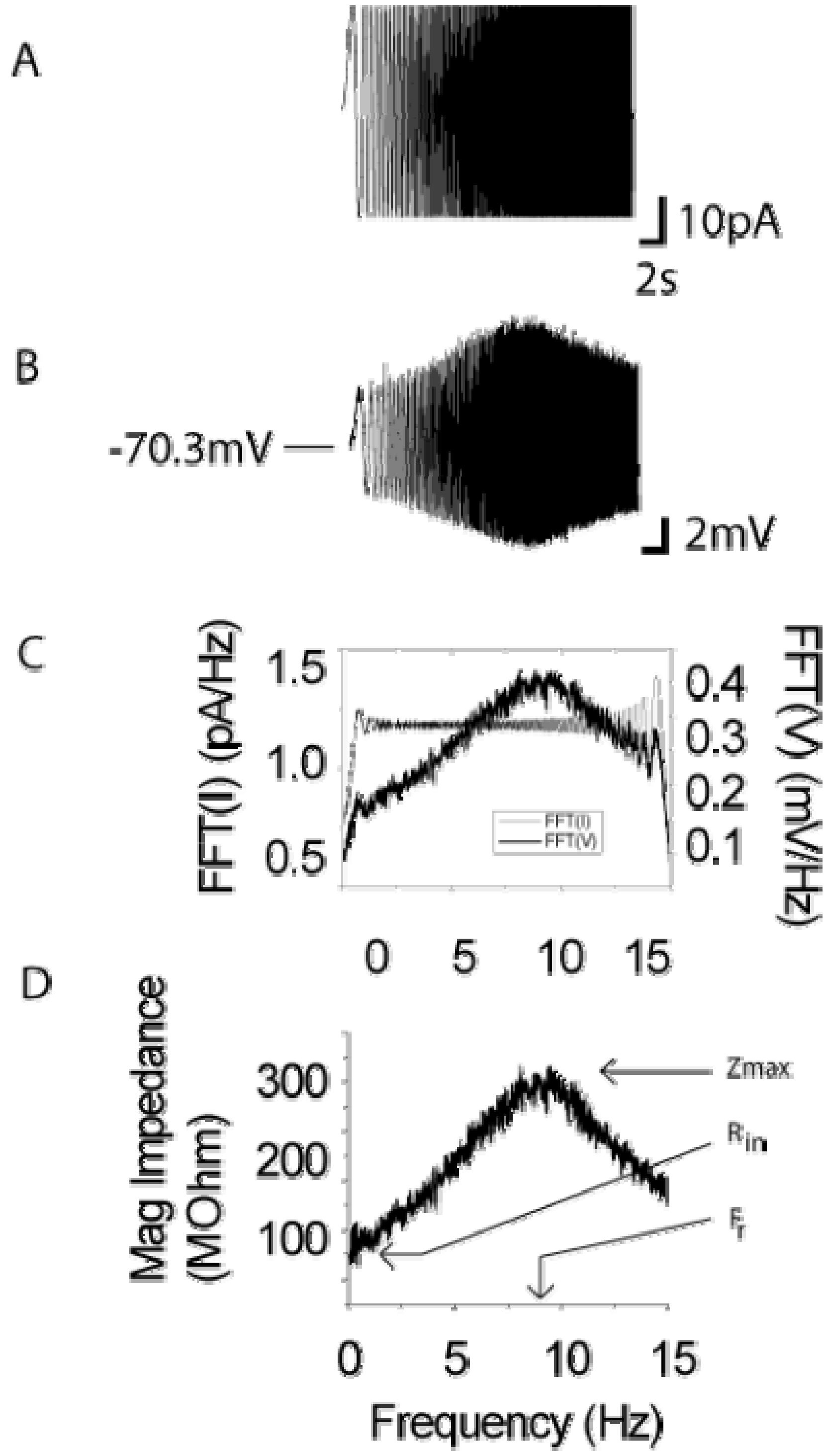
A
10pA
2s
B
-70.3mV
2mV
C
FFT(I) (pA/Hz)
1.5
1.0
0.5
FFT(V) (mV/Hz)
0.4
0.3
0.2
0.1
FFT(I)
FFT(V)
0
5
10
15
D
Mag Impedance (MOhm)
300
200
100
Zmax
R_in
F_r
0
5
10
15
Frequency (Hz)

Figure 4.2 Impedance profile calculated from a LPFGWN input protocol.

A) The LPFGWN current clamp protocol filtered with a 40 Hz cut-off frequency and duration of 100 seconds (only 30 seconds is shown), and (B) the associated membrane voltage response are shown. C) Power spectral density estimates of the input (A) and output (B) were generated by Welch's method (see chapter two for details). D) The impedance magnitude was calculated from the ratio of spectra in (C), with maximal impedance Z_{max} at a resonant frequency F_r, and input resistance R_{in}. This recording belongs to the strong onset neuron of Figure 3.2.

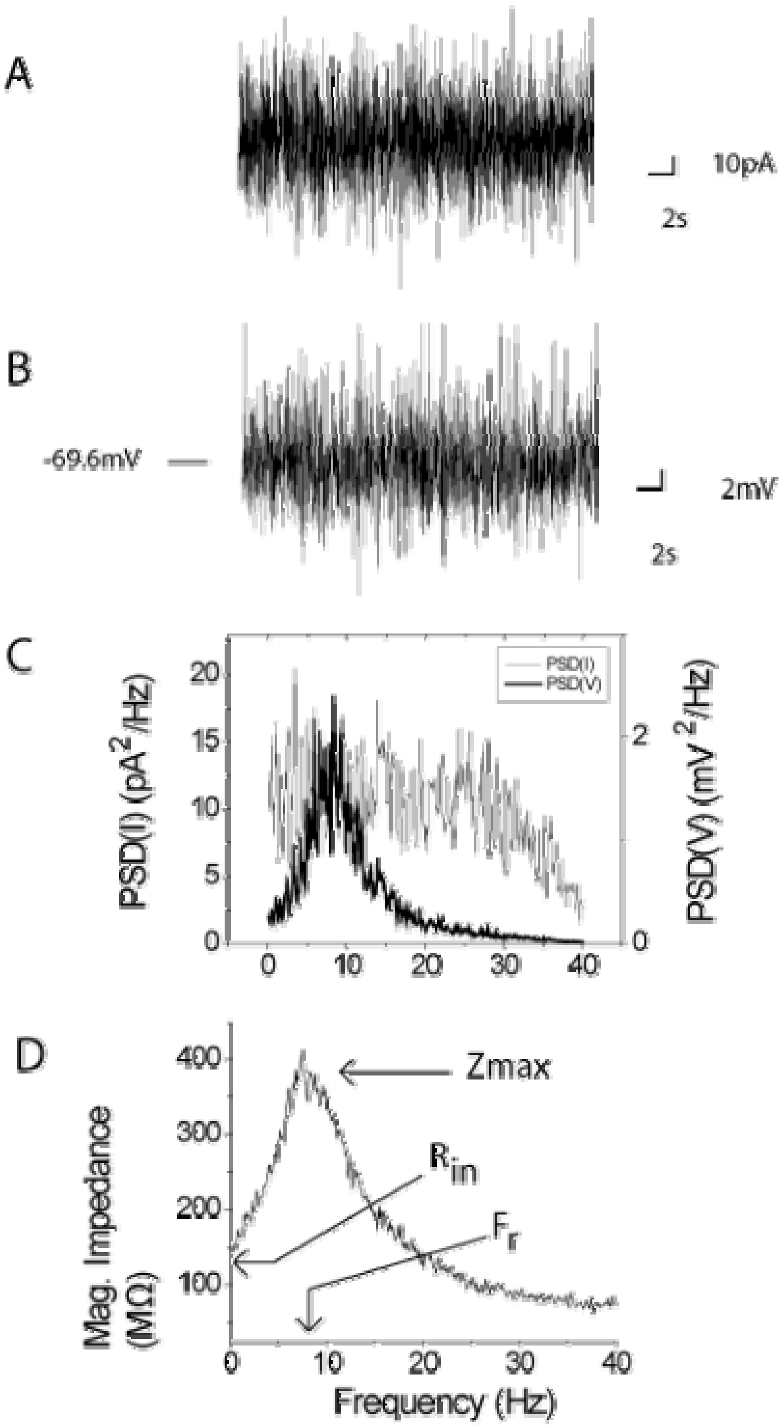
A
10pA
2s
B
-69.6mV
2mV
2s
C
PSD(I)
PSD(V)
PSD(I) (pA^2/Hz)
PSD(V) (mV^2/Hz)
0
5
10
15
20
0
2
0
10
20
30
40
D
Zmax
R_{in}
F_r
Mag. Impedance (MΩ)
100
200
300
400
0
10
20
30
40
Frequency (Hz)

Figure 4.3 Spectral estimates calculated for the LPFGWN stimulus are superior to those calculated for the ZAP stimulus, as indicated by their confidence intervals.

Power spectral density estimates of the membrane potential response are shown in blue for both the ZAP stimulus (A), and the LPFGWN stimulus (B). The 90% confidence intervals are shown in red, and are much improved for the LPFGWN stimulus. The recordings used in (A) and (B) are those of Figure 4.1, and Figure 4.2, respectively.

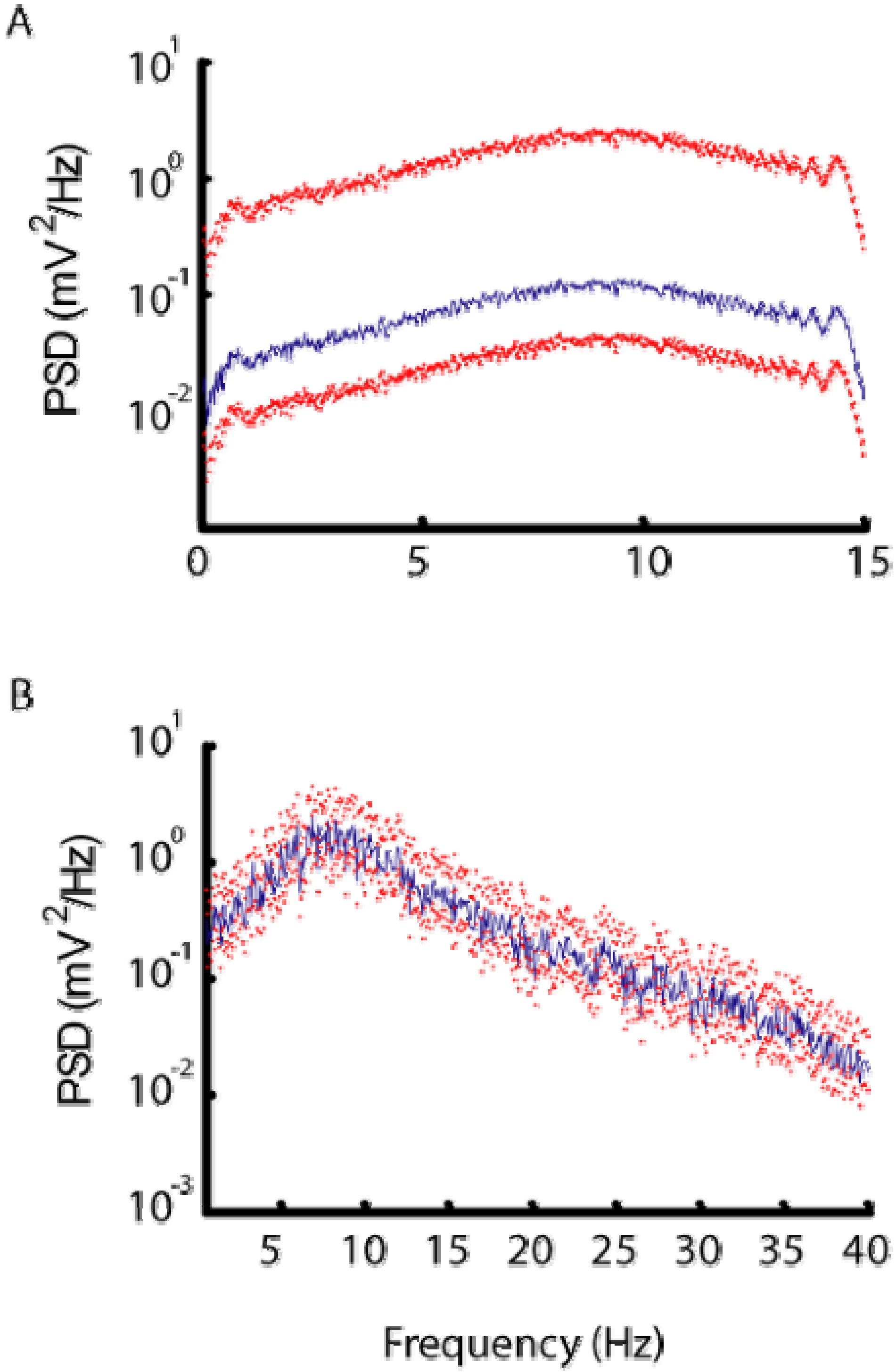
A
10^1
10^0
10^-1
10^-2
PSD (mV^2/Hz)
0
5
10
15
B
10^1
10^0
10^-1
10^-2
10^-3
PSD (mV^2/Hz)
5
10
15
20
25
30
35
40
Frequency (Hz)

These confidence intervals are compared in Figure 4.3, and demonstrate superior confidence when the LPFGWN protocol was used in comparison to the ZAP protocol. The impedance profiles generated with either a ZAP or LPFGWN were similar in shape, but smoother in the case of the latter (Figure 4.4). Therefore in subsequent analyses, the impedance profile generated with the LPFGWN stimulus was favoured over that generated with the ZAP stimulus.

In order to validate the use of window averaging, a proof of stationarity is required. This was obtained by calculating the Fano factor for both the input and output signals for increasing window size (Figure 4.5), where the Fano factor is the ratio of sample variance over the sample mean as described in (Equation 2.3). The Fano factor approaches a steady state value with increasing window size. The window size used in Welch's method was chosen greater than the number of samples required for the Fano factor to reach this steady state, as indicated on the abscissa at 100% in Figure 4.5.

4.2.2 Parameters of the Impedance Profiles

The observed impedance profiles varied considerably between neurons, and neurons were separated based on the presence or absence of a resonant peak. The resonant responses were characterized by parameters including the maximum impedance (Z_{max}), the resonant frequency (F_r), the degree of low frequency attenuation as indicated by the Q-value (Q), and the width of the resonance peak as indicated by the W-value (W) (Figure 4.6).

An impedance profile was considered resonant when a defined peak was observed, with a maximum impedance (Z_{max}) which exceeded that of the input resistance

Figure 4.4 Impedance spectra are similar when obtained from either ZAP, or LPFGWN stimuli.

The impedance spectra obtained from either a ZAP (blue) or LPFGWN (green) stimuli were similar in shape, and more specifically in F_r and Z_{max} parameters (table inset). These impedance profiles belong to an adaptive response neuron that exhibited a small onset-range.

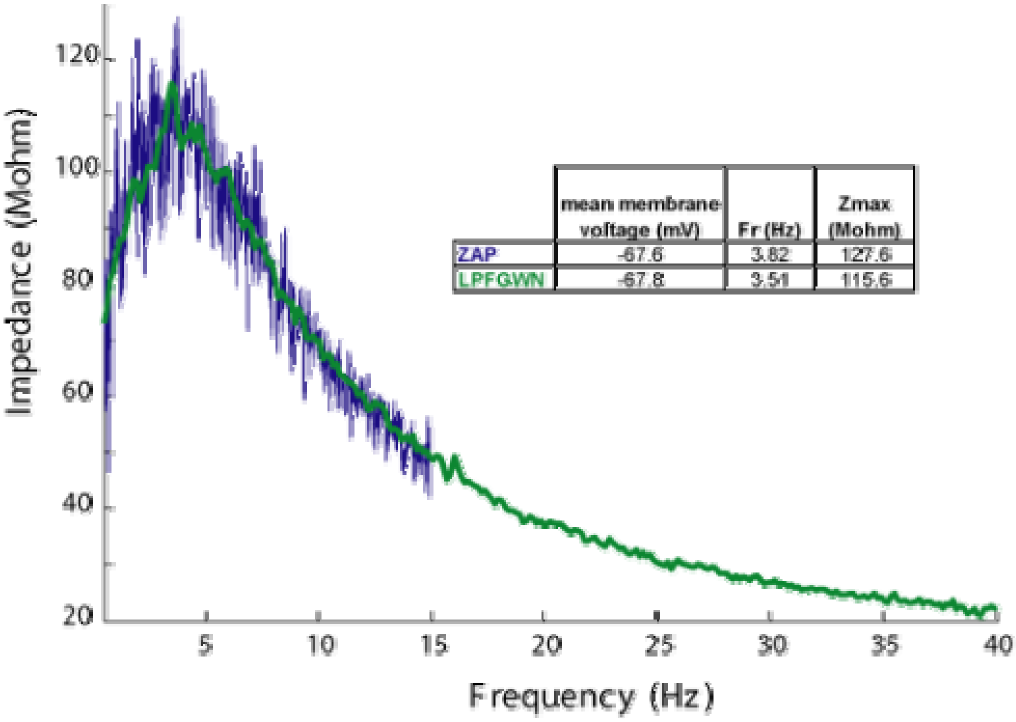

	mean membrane voltage (mV)	Fr (Hz)	Zmax (Mohm)
ZAP	-67.6	3.82	127.6
LPFGWN	-67.8	3.51	115.6

Figure 4.5 An optimal window size was obtained by calculating the Fano factor for increasing window sizes.

The Fano factor, calculated for increasing window sizes, is shown as a function of the fraction of the window size used in the windowed averaging spectral technique (Welch's method), for both (A) the input LPFGWN current clamp protocol, and (B) the output membrane voltage response. The window selected for Welch's method was larger than the number of samples necessary for the Fano factor to reach a steady state value, and is the 100% point on the abscissa (2.5×10^5 samples, or 12.5 seconds at the 20 kHz sampling frequency). The recording used here belongs to the strong onset neuron of Figure 3.2.

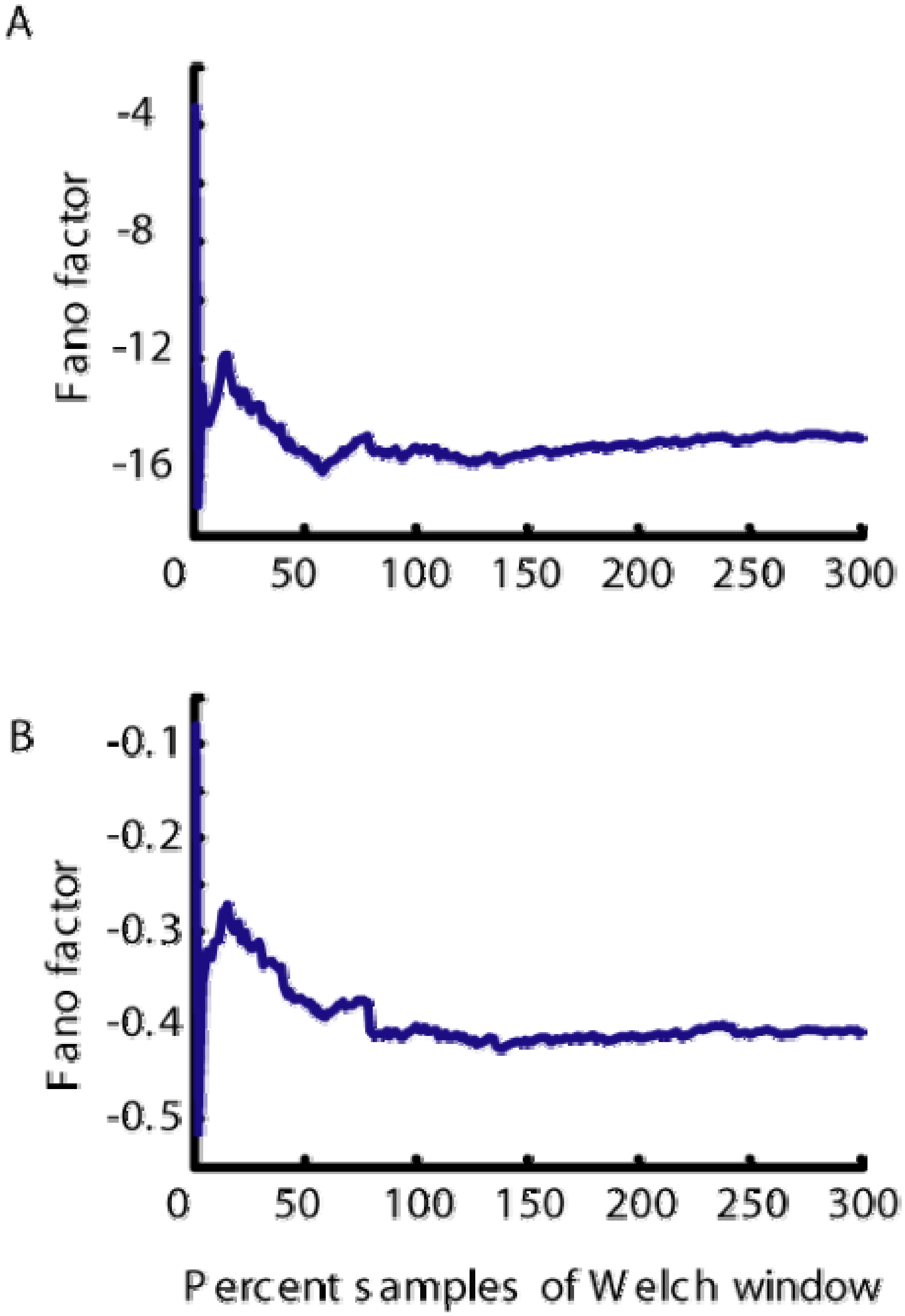
A
-4
-8
-12
-16
Fano factor
0
50
100
150
200
250
300
B
-0.1
-0.2
-0.3
-0.4
-0.5
Fano factor
0
50
100
150
200
250
300
Percent samples of Welch window

Figure 4.6 A representative impedance profile with the measured parameters indicated.

The resonance frequency (F_r) and maximum impedance (Z_{max}) were measured from the impedance profile peak. The input resistance (R_{in}) was measured from a current-clamp pulse response (not shown), with amplitude equal to the RMS value of the LPGWN stimulus, or the peak amplitude of the ZAP stimulus. The Q-value (Q) provided a measure of the degree of low frequency attenuation, as the ratio of Z_{max} over R_{in}. The W-value (W) provided a measurement of the width of the resonant peak, as the frequency range for which the magnitude of the impedance was larger than R_{in}. The recording used here is that of a strong onset neuron.

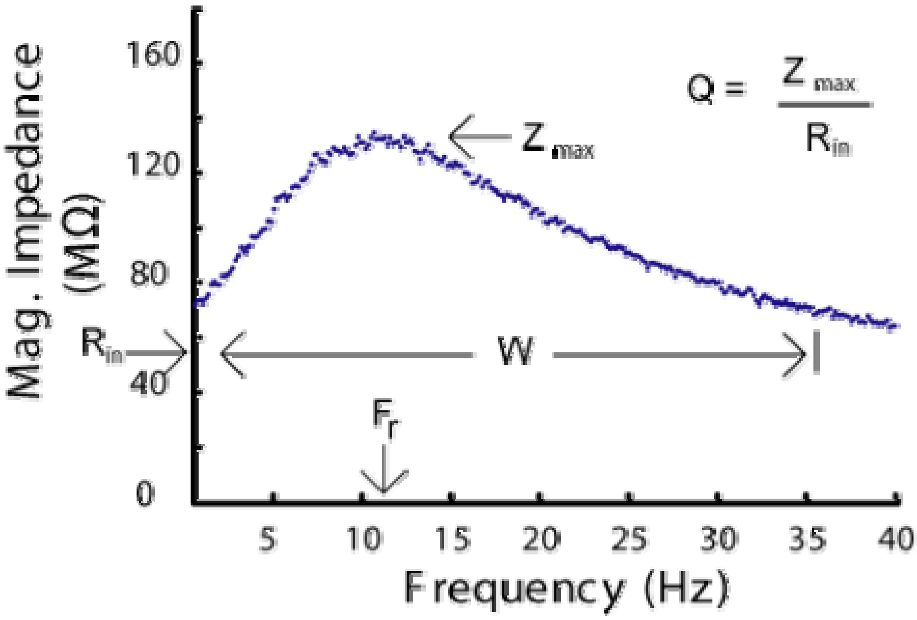
Mag. Impedance (MΩ)
160
120
80
40
0
R_{in}
W
F_r
Z_{max}
$Q = \frac{Z_{max}}{R_{in}}$
5
10
15
20
25
30
35
40
Frequency (Hz)

(R_{in}) as indicated by a $Q>1.3$ (Figure 4.6). A peak is observed in a resonant response as a result of attenuation of low frequency input, whereas a non-resonant response does not. A comparison of impedance profiles demonstrates this difference, where R_{in} and Z_{max} are very similar in the case of the non-resonant impedance profile and coincide at zero frequency, where R_{in} is much less than Z_{max} in the case of the resonant impedance profile (Figure 4.7). This criterion is identical to that used elsewhere but stricter in both numerical value, and the improved spectral estimates afforded by window averaging (Puil et al. 1986; Puil et al. 1987; Puil et al. 1994; Hu et al. 2002; Erchova et al. 2004; Schreiber et al. 2004). Given the finite length of the recording, the accuracy of spectral estimates at low frequencies was of concern. We chose to exclude spectral estimates for frequencies lower than those that do not have at least one cycle present in the record or window (Chatfield 2004). Thus, in addition to the Q-value criterion, an impedance profile was considered resonant when the F_r exceeded the reciprocal of the time window used in the spectral technique. Using these criteria we found 35 (40%) neurons that exhibit resonance about their resting membrane potential amongst 86 tested neurons (20 resonators were observed with a LPFGWN stimulus, and an additional 15 resonators were observed with a ZAP stimulus). The proportion of resonators is biased, in the sense that we began testing for resonance only in neurons that exhibited firing profiles that we had previously associated with resonance responses, such that this proportion is an overestimation and does not represent the true proportion amongst all neurons.

A comparison of the number of resonators in each firing response type suggests that resonance is most often observed in onset response type neurons (Figure 4.8). Specifically, of the onset response neurons, resonance was typically observed in the subset of strong-onset response neurons (Figure 4.9). Histograms indicate the distribution of impedance profile parameters for resonant responses (Figure 4.10). The resonance parameters of the strong onset response neurons, a subset of onset response neurons, typically exhibited a strong resonance response with larger F_r and Q (Figure 4.10).

The presence of additional peaks in the impedance profile, at higher frequencies, was investigated with larger bandwidth input signals. No additional peaks were observed, even with the increase in bandwidth to 160 Hz (Figure 4.11).

4.2.3 Effect of Mean Membrane Voltage on Resonance

In an attempt to determine which currents contribute to the resonance response, we investigated the range of voltage over which resonance was observed by varying the mean membrane voltage. The mean membrane voltage was manipulated by adding a bias current to the LPFGWN stimulus.

The resonance response remained despite hyperpolarization and depolarization of the mean membrane voltage in either onset response or adaptive firing neurons (Figure 4.12, and Figure 4.14). This suggests that if a single resonant current underlies the resonant response it must have a large activation range, otherwise multiple overlapping activation profiles from multiple voltage gated currents may be responsible.

One strong-onset response type neuron exhibited a larger maximum impedance (Z_{max}) at resting membrane potential, larger than that observed at a more hyperpolarized potential (Figure 4.12, and Figure 4.13a). A larger Q-value was also observed at resting membrane potential (Figure 4.13a), suggesting that this larger Z_{max} reflects an increased selectivity for input at the resonance frequency (F_r). In this example F_r also decreased considerably (Figure 4.13a). This increased selectivity, or in other words sharper

Figure 4.7 A peak in the impedance profile is observed for neurons that exhibit resonance.

The impedance profile of a non-resonant response is shown (A), with monotonically decreasing impedance as a function of frequency, in contrast with a resonant response (B), which has maximal impedance at a non-zero frequency. The impedance profile for the resonant response is that of Figure 4.6, and the non-resonant profile was obtained from a sustained firing neuron that exhibited neither adaptation nor acceleration of the spike frequency.

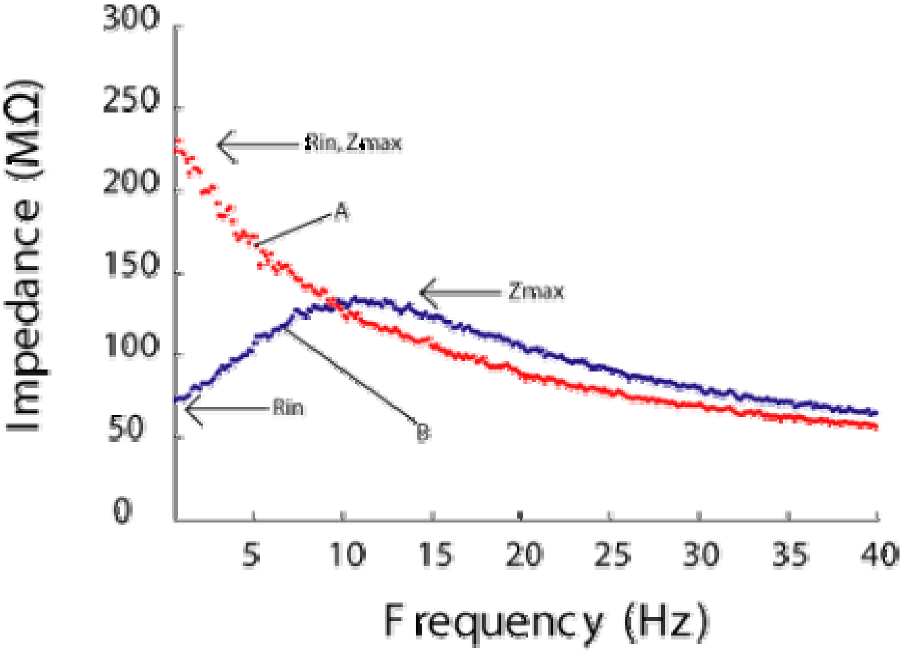
300
250
200
150
100
50
0
Impedance (MΩ)
5
10
15
20
25
30
35
40
Frequency (Hz)
Rin, Zmax
A
Zmax
Rin
B

Figure 4.8 Resonance was observed across different firing response types, and was most common to the onset response type.

A histogram of firing response types that exhibited resonance about the resting membrane potential is shown.

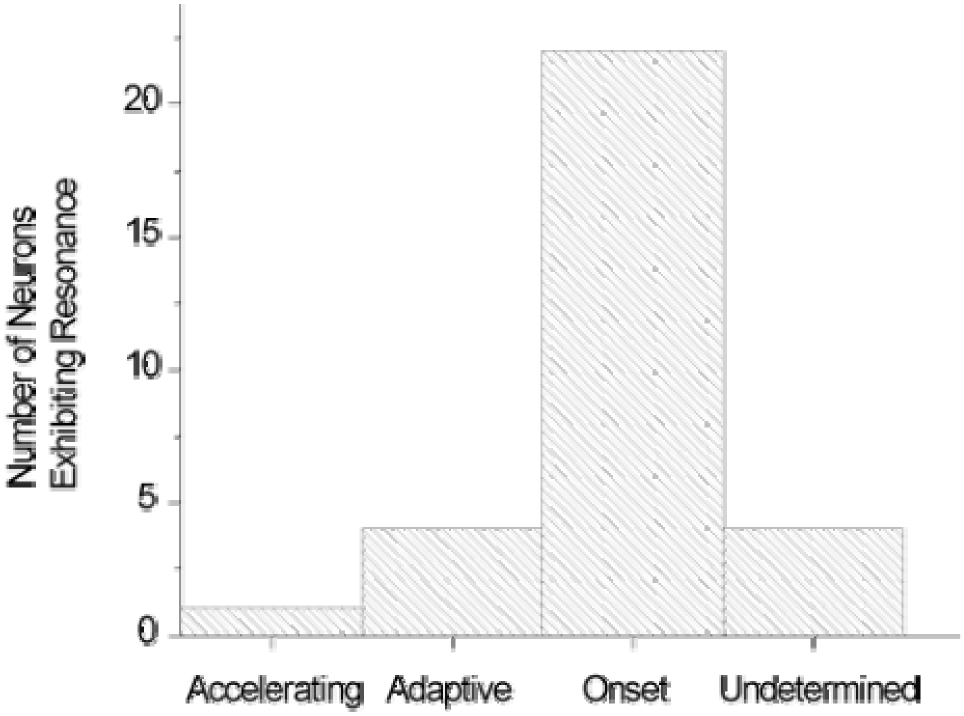
Number of Neurons
Exhibiting Resonance
0
5
10
15
20
Accelerating
Adaptive
Onset
Undetermined

Figure 4.9 Resonance is most often observed amongst neurons of the strong-onset response category.

The onset-range versus τ_{APH} relationship for neurons that exhibited an onset-range is reproduced here, to indicate the common occurrence of resonance in strong-onset response neurons (✳). All labels are those used in Figure 3.7, except (✳). Resonance was exclusive to neurons with τ_{APH} smaller than ≈400 ms.

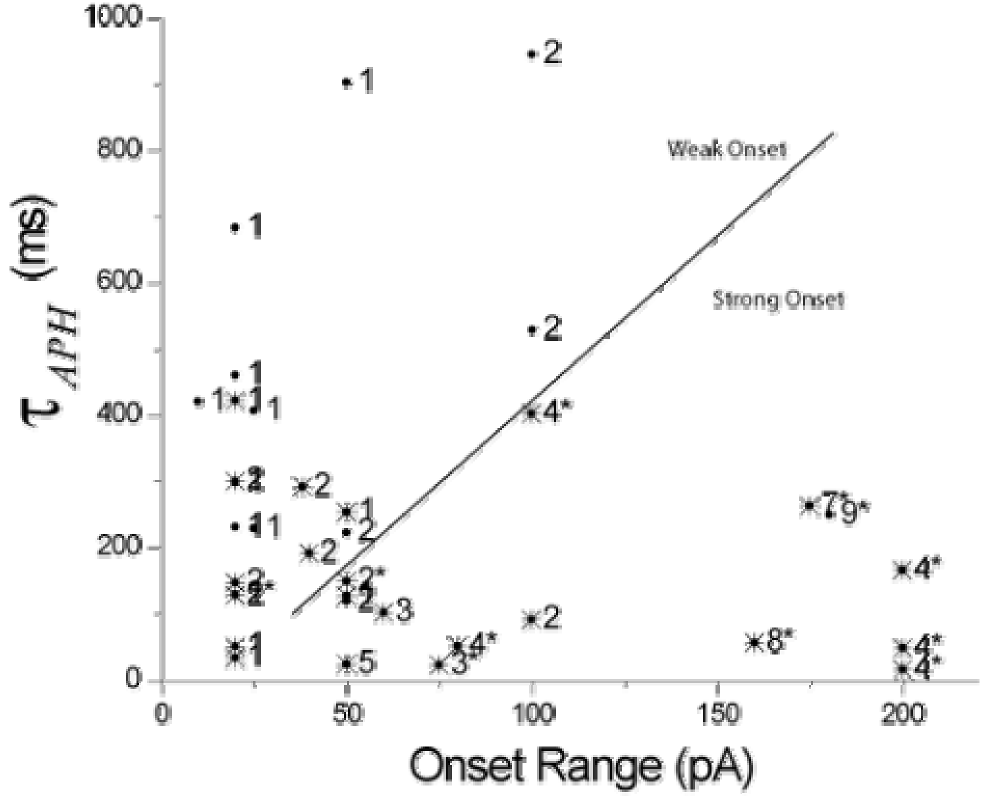

τ_{APH} (ms)
Onset Range (pA)
Weak Onset
Strong Onset
0
200
400
600
800
1000
0
50
100
150
200
1
2
1
1
2
1
1
1
2
4*
2
1
2
1
2
7*
9*
4*
2
2*
2
3
2
8*
4*
1
1
5
3*
4*
4*
4*

Figure 4.10 Strong-onset response neurons exhibit stronger resonance behaviour.

Histograms of resonance parameters for all neurons that exhibited a resonant response are shown (single-hatched). The strong-onset responses (cross-hatched) exhibited larger F_r and Q than other cell response types.

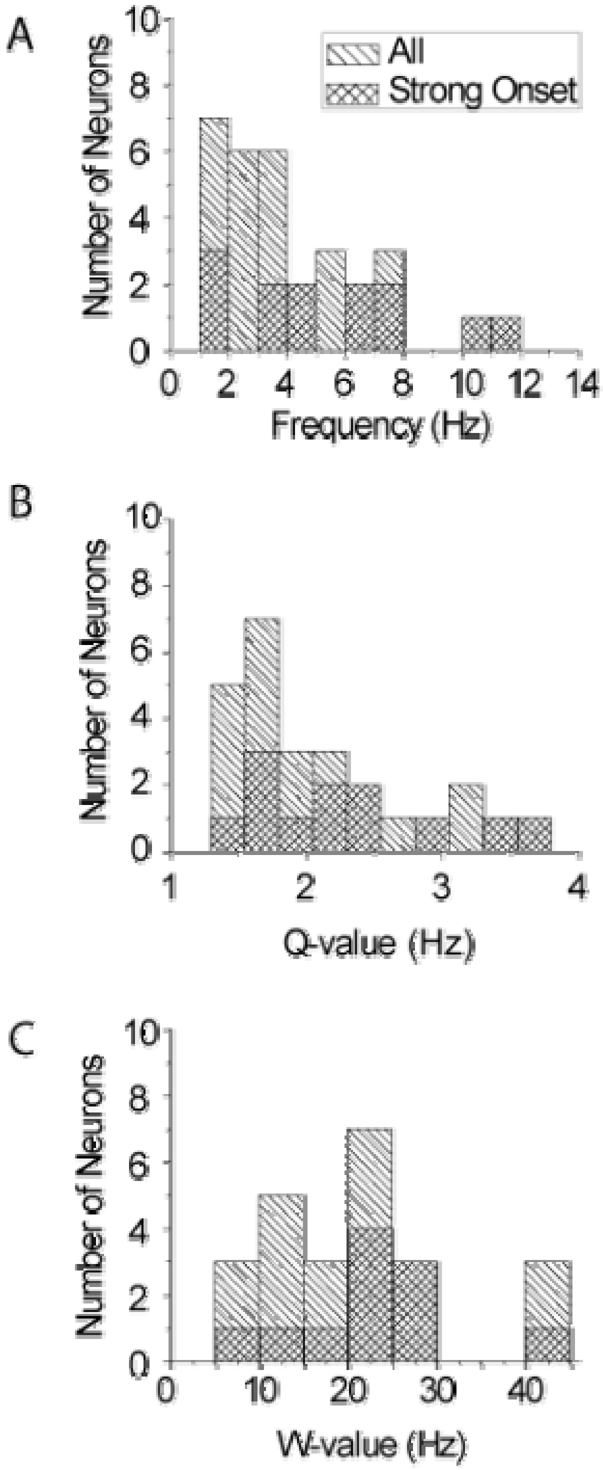
A
All
Strong Onset
Number of Neurons
0
2
4
6
8
10
0
2
4
6
8
10
12
14
Frequency (Hz)
B
Number of Neurons
0
2
4
6
8
10
1
2
3
4
Q-value (Hz)
C
Number of Neurons
0
2
4
6
8
10
0
10
20
30
40
W-value (Hz)

resonance, is likely the result of a shift between two different mechanisms of resonance. At the hyperpolarized potential, the primary mechanism of resonance might involve a single resonant current like I_h. At rest, the spiralling trajectories about the fixed point that result from the AH bifurcation are likely the mechanism for frequency selectivity, because the resting membrane potential is at the edge of the I_h activation profile (McCormick and Pape 1990; Koch and Grothe 2003). In two examples, depolarization from rest by 10mV had little effect on the impedance profiles (Figure 4.12, and the control condition in Figure 4.16B), or the measured impedance profile parameters (Figure 4.13b), which indicates the conservation of frequency selectivity over a wide range of membrane potential. In a fourth example, hyperpolarization from rest increased the sharpness of the resonance response, as indicated by a larger Q-value at the hyperpolarized potentials (Figure 4.13c), which might be caused by an increased recruitment of I_h at hyperpolarized potentials.

Like the onset response neuron, the adaptive response neuron exhibited both increased and decreased frequency selectivity were observed at hyperpolarized potentials, in comparison to resting membrane potential. In one example, both the Z_{max} and Q were larger at the resting membrane potential in comparison to those at a more hyperpolarized potential (Figure 4.14A; Figure 4.15a), and as suggested for the onset response neuron, might indicate better frequency selectivity brought about by the AH bifucation in comparison to a single resonant current like I_h. Otherwise, in another example the larger Z_{max} at rest is not accompanied by a larger Q (Figure 4.14B; Figure 4.15b), indicating reduced frequency selectivity at rest in comparison with that observed at more hyperpolarized potentials.

Figure 4.11 The impedance profile is independent of the low pass filter cut-off frequency.

At resting potential, three LPFGWN stimuli with different low pass cut-off frequencies (40, 80, and 160 Hz) were used to generate the impedance profiles. In this example of a strong-onset neuron, a single resonance peak was observed around 3.2 to 3.4 Hz, with somewhat indifferent Q-values and W-values. Despite the increase in bandwidth, no additional peaks were observed. The mean membrane voltages were within +/-1 mV across all trials.

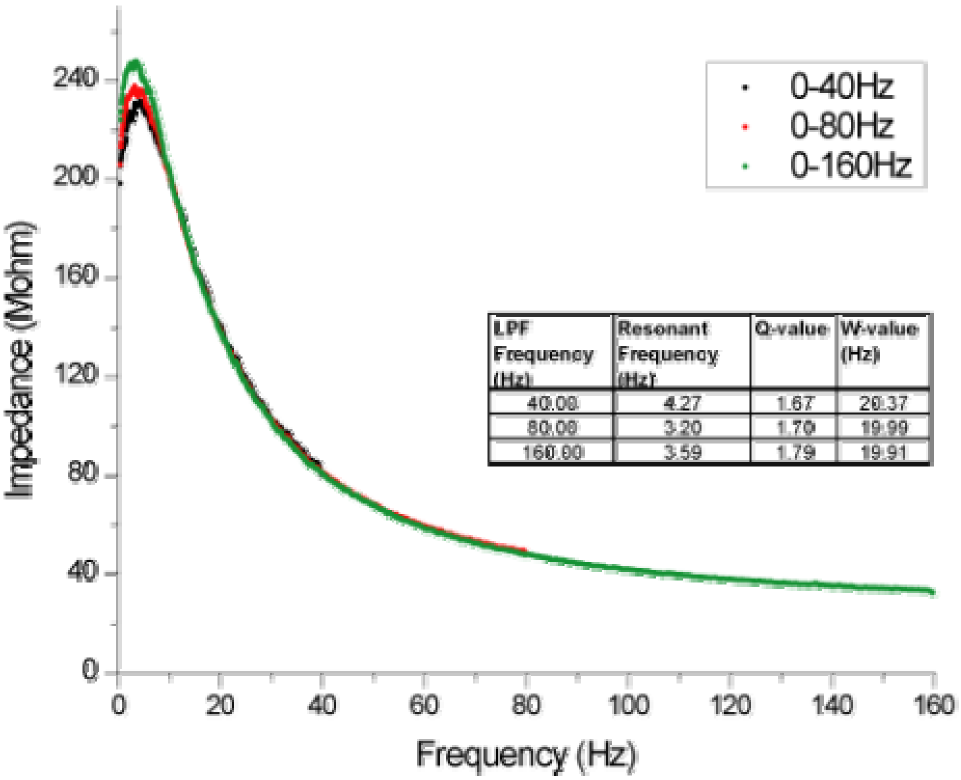

LPF Frequency (Hz)	Resonant Frequency (Hz)	Q-value	W-value (Hz)
40.00	4.27	1.67	20.37
80.00	3.20	1.70	19.99
160.00	3.59	1.79	19.91

Figure 4.12 Resonance was observed in impedance profiles of strong-onset response type neurons despite manipulation of the mean membrane potential.

The impedance profiles of three different strong-onset neurons were calculated at different mean membrane voltages with LPFGWN as the stimulus (A-C). The mean membrane voltage, as indicated in the legends, was manipulated by applying a bias current.

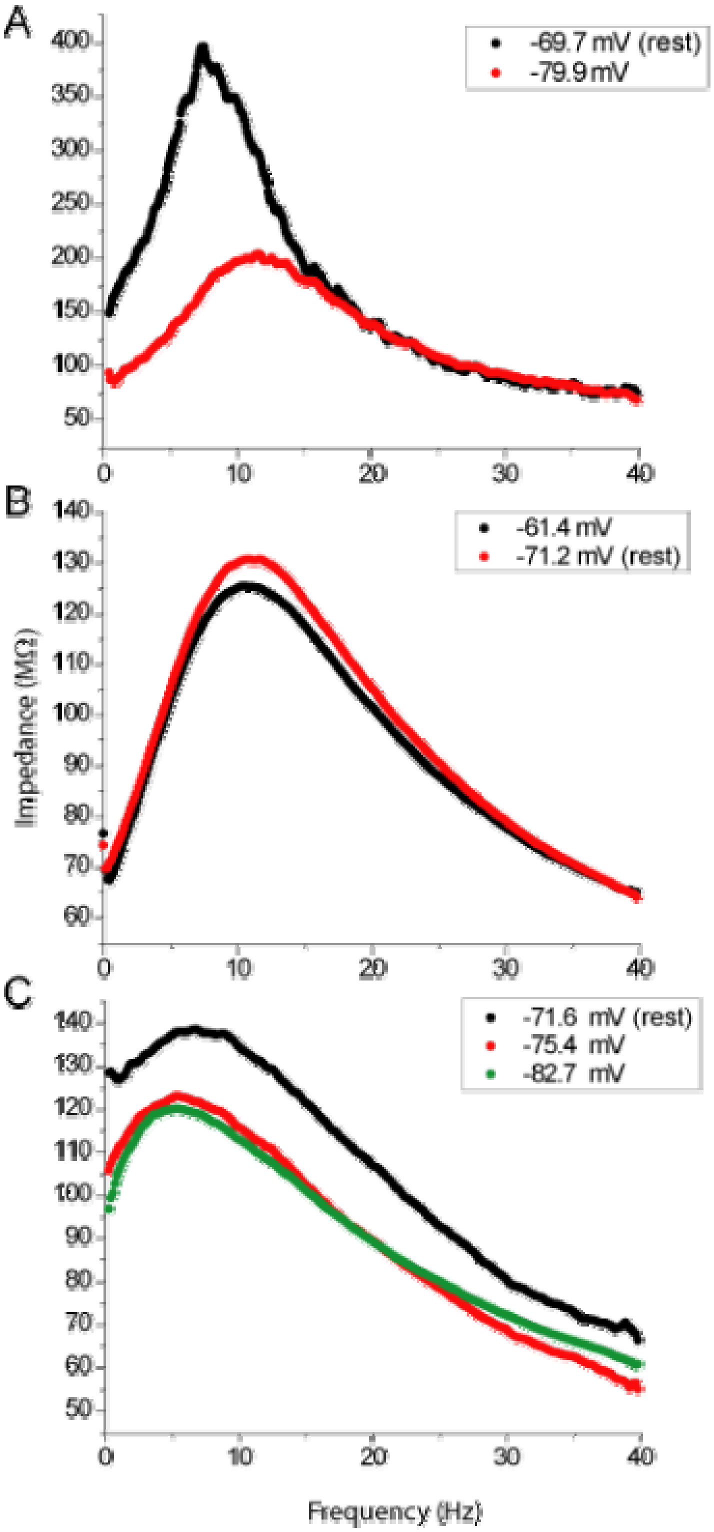
A
400
350
300
250
200
150
100
50
0
10
20
30
40
● -69.7 mV (rest)
● -79.9 mV
B
140
130
120
110
100
90
80
70
60
0
10
20
30
40
● -61.4 mV
● -71.2 mV (rest)
Impedance (MΩ)
C
140
130
120
110
100
90
80
70
60
50
0
10
20
30
40
● -71.6 mV (rest)
● -75.4 mV
● -82.7 mV
Frequency (Hz)

Figure 4.13 Strong onset response neurons did not exhibited any trend with respect to the mean membrane potential for the four impedance profile measurements (F_r, Q, W, and Zmax).

Impedance profile measurements of the strong-onset neurons, from Figure 4.12, are shown. Labels in the legend correspond with those the in previous figure.

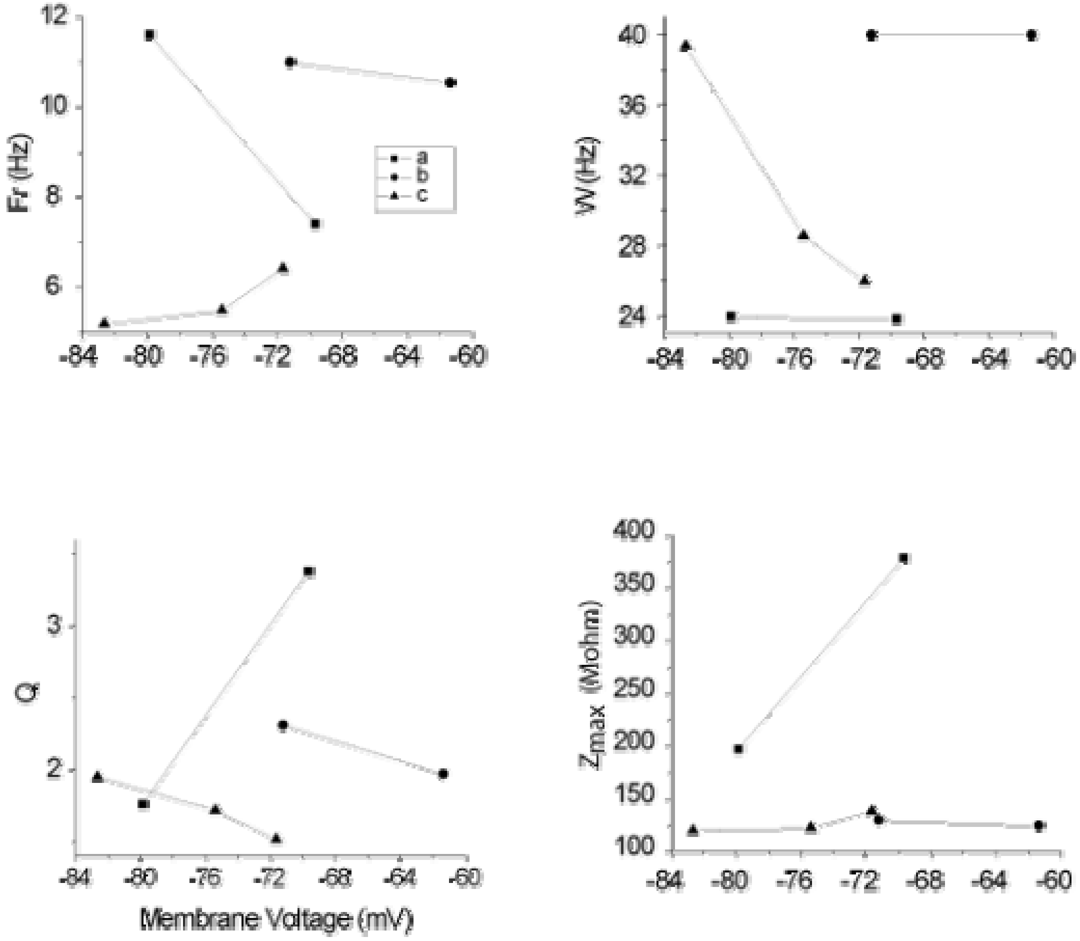
Fr (Hz)
12
10
8
6
■ a
● b
▲ c
-84
-80
-76
-72
-68
-64
-60
W (Hz)
40
36
32
28
24
Q
3
2
Membrane Voltage (mV)
Zmax (Mohm)
400
350
300
250
200
150
100

Figure 4.14 Resonance was observed in impedance profiles of adaptive response type neurons despite manipulation of the mean membrane potential.

The impedance profiles of two different adaptive firing neurons were calculated at different mean membrane voltages, with LPFGWN as the stimulus (A, and B). The mean membrane voltage, as indicated in the legends, was manipulated by applying a bias current. Larger maximum impedance was typically observed at the more depolarized voltage.

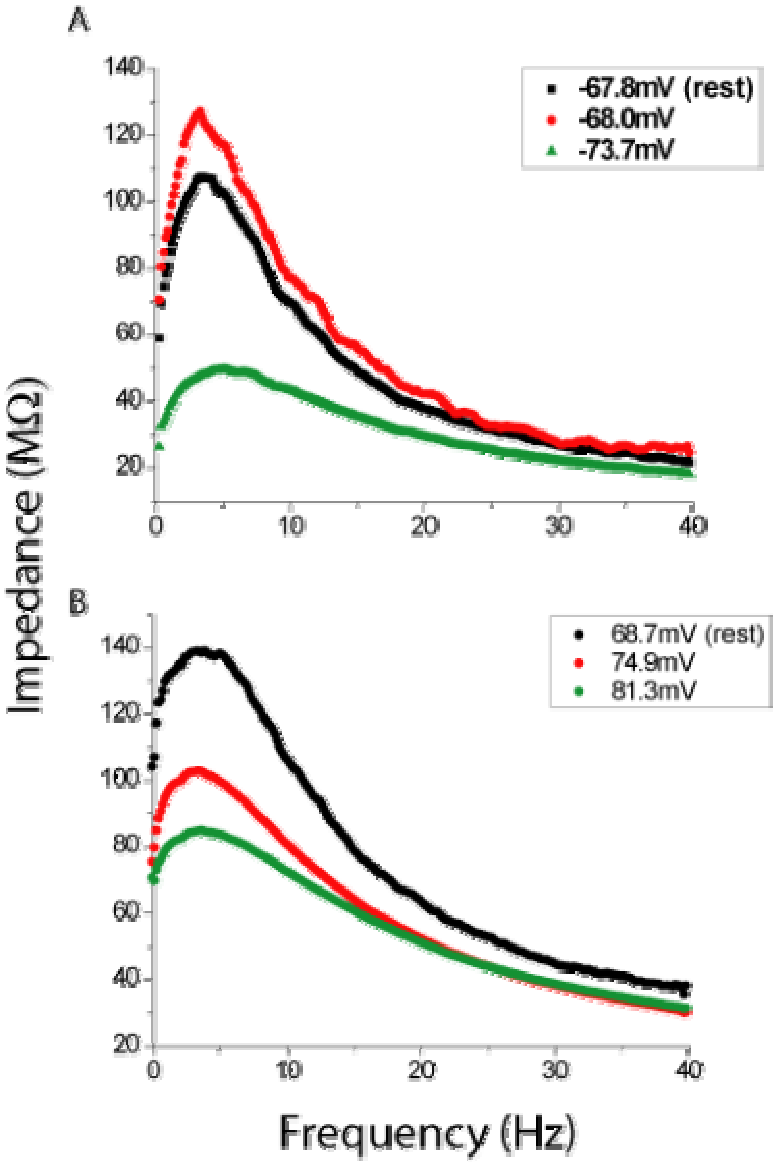
A
140
120
100
80
60
40
20
0
10
20
30
40
-67.8mV (rest)
-68.0mV
-73.7mV
B
140
120
100
80
60
40
20
0
10
20
30
40
68.7mV (rest)
74.9mV
81.3mV
Impedance (MΩ)
Frequency (Hz)

Figure 4.15 No trends were observed with respect to the mean membrane potential for the four impedance profile measurements (F_r, Q, W, and Zmax) in the adaptive firing response neurons.

Impedance profile measurements of the impedance profiles of the adaptive firing neurons, from Figure 4.14 are shown. A trend in mean membrane potential was observed only for Z_{max} (D). Labels in the legend correspond with those the in previous figure.

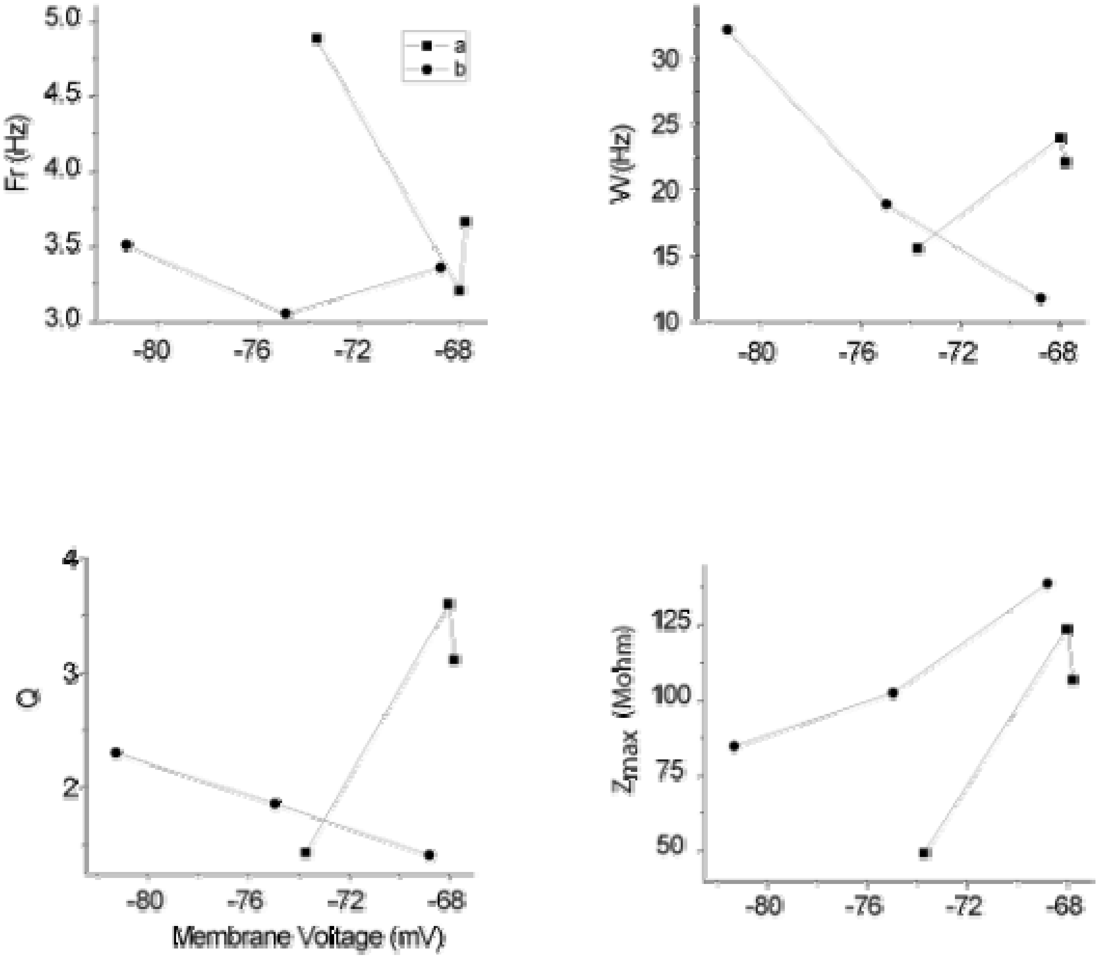
Fr (Hz)
5.0
4.5
4.0
3.5
3.0
a
b
-80
-76
-72
-68
W(Hz)
30
25
20
15
10
-80
-76
-72
-68
Q
4
3
2
-80
-76
-72
-68
Membrane Voltage (mV)
Zmax (Mohm)
125
100
75
50
-80
-76
-72
-68

Figure 4.16 I_h blockade reduces the resonance response, as observed in the impedance profile.

The impedance profiles of three different resonance response neurons are shown before (solid circles) and after I_h blockade (open circles), and with varying mean membrane potential, as indicated in the legends (A-C). A left and upward shift in the impedance profile was observed following blockade of I_h with 2 mM CsCl. The peak in the impedance profile was not completely abolished, suggesting the presence an additional mechanism of low frequency attenuation. An adaptive response type is shown in (A), whereas (B) and (C) are strong-onset response types. The impedance profiles for the control conditions in (A) and (C), are those of Figure 4.12A, and Figure 4.14C respectively.

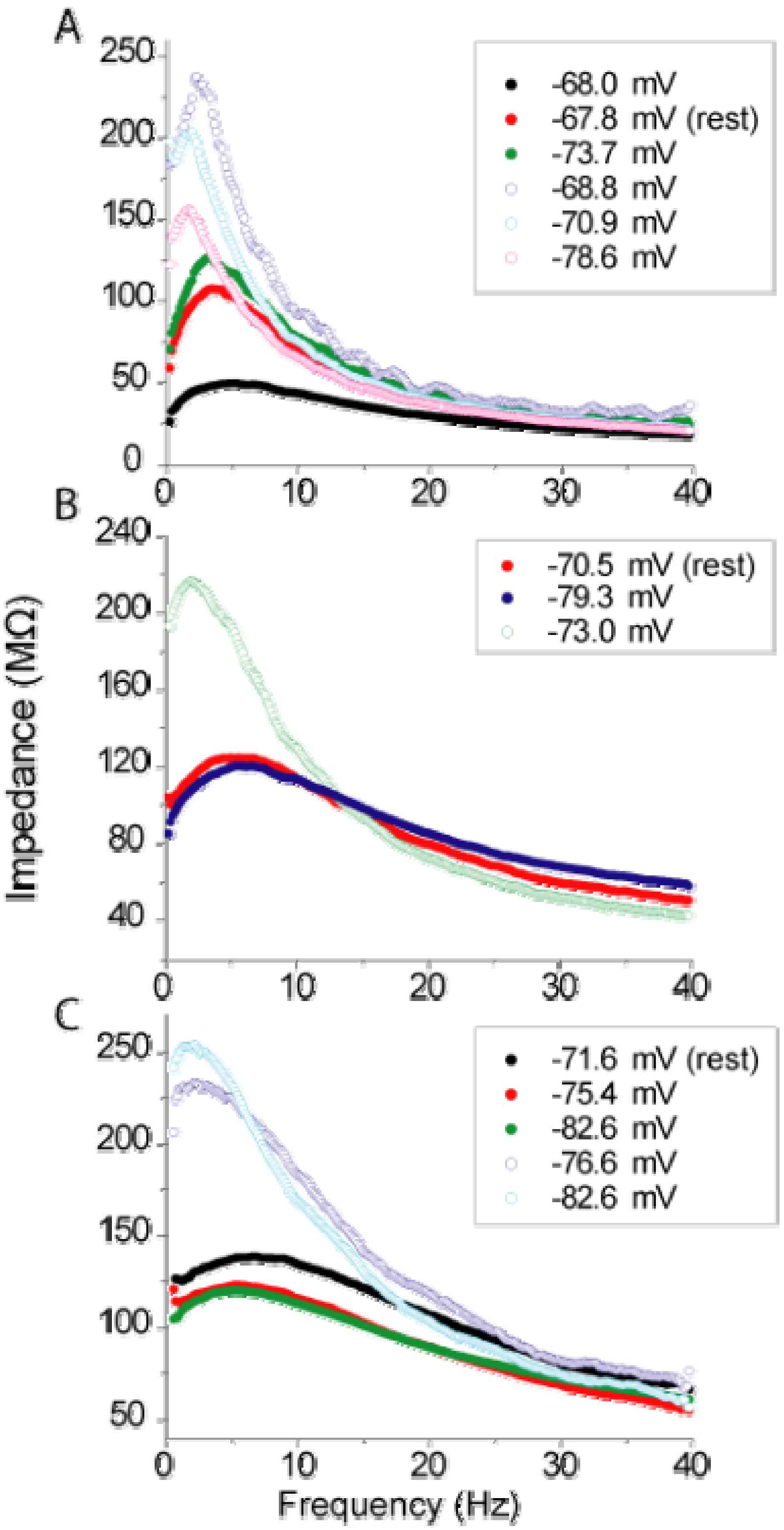
A
250
200
150
100
50
0
0
10
20
30
40
● -68.0 mV
● -67.8 mV (rest)
● -73.7 mV
○ -68.8 mV
○ -70.9 mV
○ -78.6 mV
B
240
200
160
120
80
40
0
10
20
30
40
● -70.5 mV (rest)
● -79.3 mV
○ -73.0 mV
Impedance (MΩ)
C
250
200
150
100
50
0
10
20
30
40
● -71.6 mV (rest)
● -75.4 mV
● -82.6 mV
○ -76.6 mV
○ -82.6 mV
Frequency (Hz)

Regardless of the effect of mean membrane potential on resonance, it appears that resonance occurs in ICC neurons over a wide range of membrane potentials, at least in the case of the onset response, and adaptive response neurons.

4.2.4 Mechanism of Resonance: Voltage Gated Ion Channels.

Given the large range of mean membrane potentials over which resonance could be observed, we investigated the possibility that more than one ionic mechanism may contribute to the resonance response. To investigate this, we compared impedance profiles with various mean membrane voltages before and after the application of ion channel blockers. Our working hypothesis being that resonance at hyperpolarized potentials was largely attributed to I_h current, whereas the spiralling voltage trajectories of the AH bifurcation contribute to resonance at more depolarized potentials. Respectively, evidence in support of this hypothesis includes a hyperpolarization induced depolarizing sag in the step response, and the AH bifurcation identified in chapter three.

4.2.4.1 The Role of I_h Current in the Resonance Response

I_h current is classified as a resonant current by its ability to counteract deflections of the membrane potential. Expression of I_h in ICC neurons is known in onset and adaptive response type neurons (Koch and Grothe 2003), and readily observed as voltage sag in response to hyperpolarization (Figure 4.18). The ability of I_h to attenuate slow deflections of the membrane voltage offers a mechanism for low frequency attenuation required to explain the resonance response (Haas et al. 2007).

Blockade of I_h decreases low frequency attenuation. A left-upward shift in the impedance profiles is observed after blockade of I_h (Figure 4.16). The measured impedance profile parameters were conducive with this decrease in low frequency attenuation, with an increase in Zmax, and decreases in F_r, Q, and W (Figure 4.17). The decrease in Q value demonstrates a decrease in frequency selectivity despite an increase in Z_{max}, because it is accompanied by an increase in R_{in}. Despite blockade of I_h by caesium (Cs^+) treatment some degree of frequency selectivity remains, as a residual peak in the impedance spectrum is observed and Q remains greater than unity. This observation suggests the presence of other ionic mechanisms in the resonance response, and is supported by a caesium (Cs^+) insensitive depolarizing rebound observed at the offset of a hyperpolarizing current pulse (Figure 4.18), which may reflect either T-type calcium current expression, or a subthreshold anode break response mediated by sodium and potassium currents (graded action potentials in chapter three). As expected an increase in input resistance is also observed upon Cs^+ treatment, because I_h is active at subthreshold voltage.

In order to demonstrate the possibility that I_h is sufficient for a resonant response, we fit a conductance model with I_h and leak current to the subthreshold response of a hyperpolarizing current pulse (Figure 4.19A; see chapter two for details of model). The impedance profiles, generated with the LPFGWN stimulus, were similar in shape between the neuron and the model (Figure 4.19B, and C). Additionally, the relationship between Z_{max} and R_{in}, that is the Q-value, were similar between these two impedance profiles. Upon removal of I_h in the model, the resonance response disappears, and an integrator impedance profile is observed instead (Figure 4.19D), where R_{in} and Z_{max} assume the same value.

Figure 4.17 Effect of I_h blockade on the impedance profile measurements.

The impedance profile measurements before and after I_h blockade (2 mM) are shown at varying mean voltage. Increase in F_r, and W were observed, while Z_{max} increased and little change was observed in Q. Labels in the legend correspond with those in the previous figure.

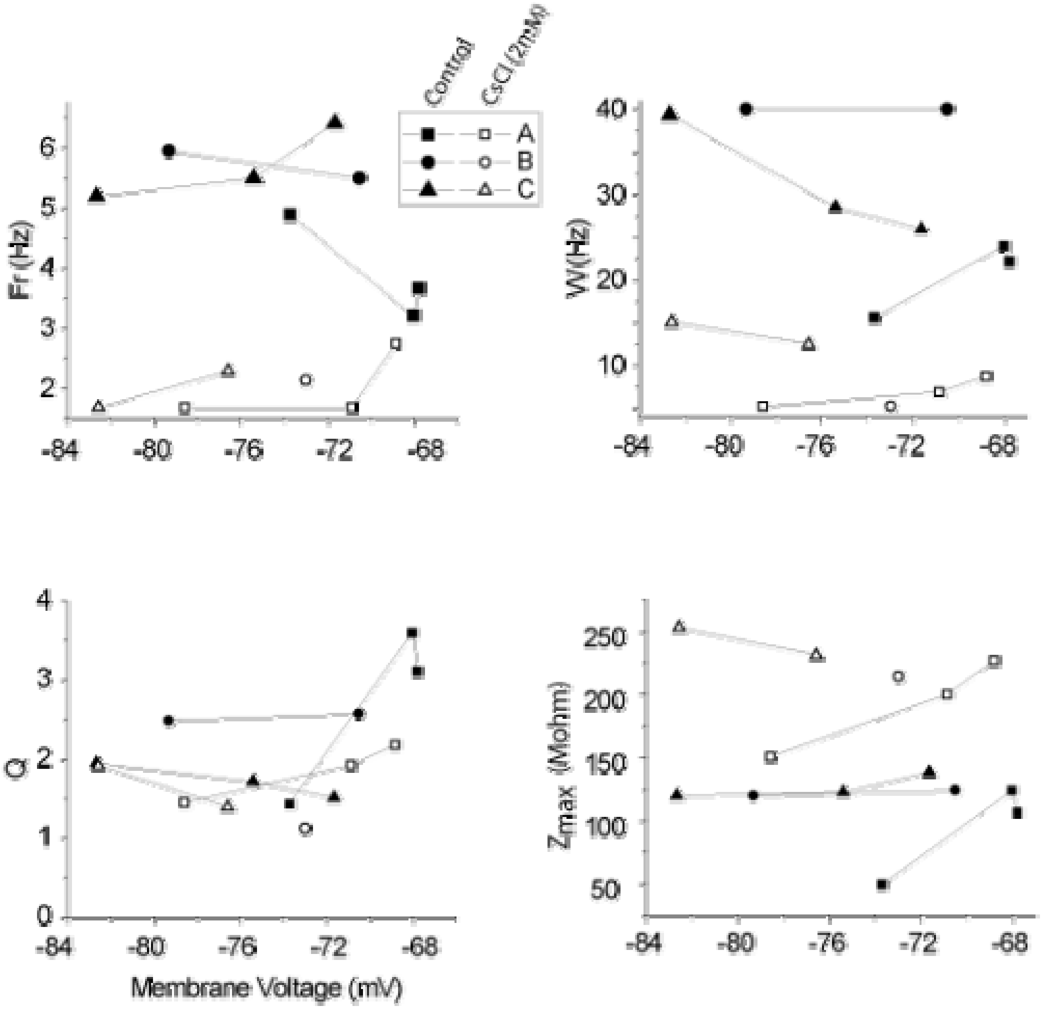
Control
CsCl (2mM)
A
B
C
Fr (Hz)
6
5
4
3
2
W(Hz)
40
30
20
10
Q
4
3
2
1
0
Zmax (Mohm)
250
200
150
100
50
-84
-80
-76
-72
-68
Membrane Voltage (mV)

Figure 4.18 Blockade of I_h reduces hyperpolarization induced sag, yet a rebound depolarization remains.

In the control condition, a hyperpolarizing current pulse elicits a hyperpolarization sag (A, black), which is reduced in amplitude by I_h blockade (2 mM CsCl) (A, red). At pulse offset, a depolarizing rebound is observed, and persists despite I_h blockade. The Cs^+ insensitive rebound may represent either T-type calcium current, or a subthreshold anode break excitation mediated by sodium and potassium currents. The current clamp protocol is shown for control (B, black), and I_h blockade (B, red) recordings.

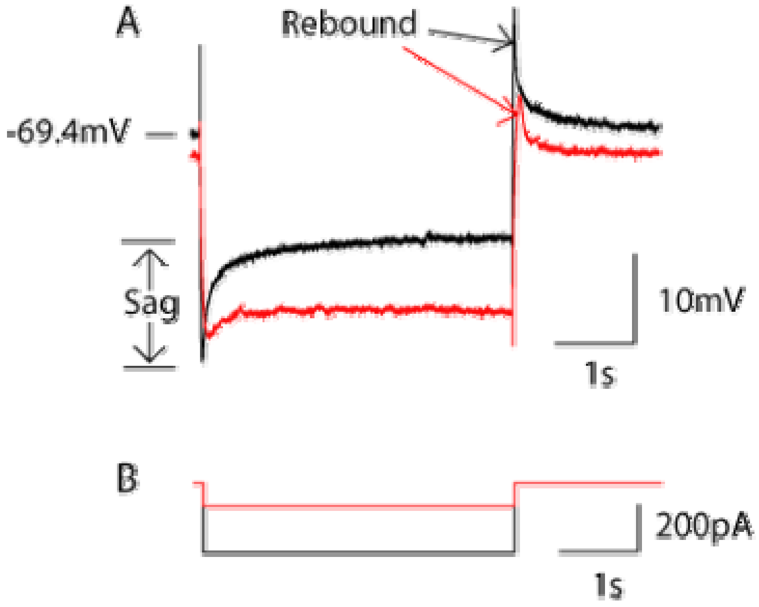
A
Rebound
-69.4mV
Sag
10mV
1s
B
200pA
1s

Figure 4.19 Resonance observed in a conductance model with leak and I_h current.

A conductance model consisting of I_h and leak current was fit to the subthreshold response of an adaptive response type neuron that exhibited resonance (A). A similar impedance profile was observed for either the model or the neuron, with a resonant peak in each (B, and D), with LPGWN used as the stimulus. Removal of I_h from the model abolished the resonance peak (C). A current-pulse amplitude of 100 pA was used in the neuron, a 0.454 $\mu A/cm^2$ conductance pulse was used in the model; likewise the amplitudes of the LPFGWN stimuli were scaled relative to each other in the same manner to achieve approximately 10 mV deflection in the membrane voltage.

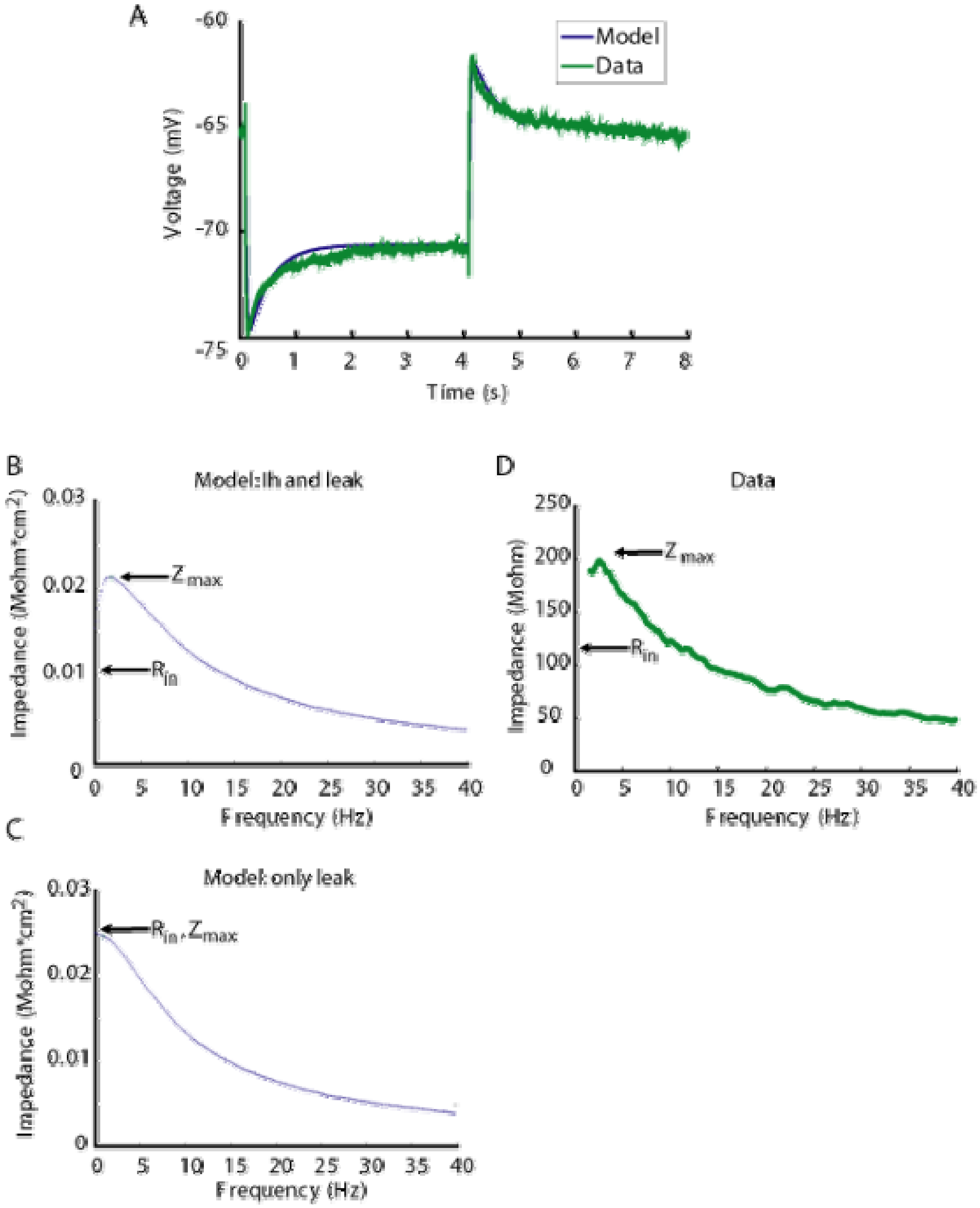
A
-60
-65
-70
-75
Voltage (mV)
Model
Data
0
1
2
3
4
5
6
7
8
Time (s)
B
Model:Ih and leak
Impedance (Mohm*cm^2)
0.03
0.02
0.01
0
Z_{max}
R_{in}
0
5
10
15
20
25
30
35
40
Frequency (Hz)
D
Data
Impedance (Mohm)
250
200
150
100
50
0
Z_{max}
R_{in}
0
5
10
15
20
25
30
35
40
Frequency (Hz)
C
Model: only leak
Impedance (Mohm*cm^2)
0.03
0.02
0.01
0
R_{in}, Z_{max}
0
5
10
15
20
25
30
35
40
Frequency (Hz)

4.2.4.2 The Role of Voltage Gated Calcium Current in the Resonance Response

The conductance of low voltage activated calcium channels (the basis of T-type calcium current) is controlled by both an activation and inactivation gate. This combination of gates in an inward current permits both amplification and attenuation of low frequency deflections of the membrane potential. The activation gate is responsible for a negative conductance region (like that of voltage gated sodium current: Figure 1.7) that provides amplification of inputs at frequencies lower than the inverse of the time constant of the activation gate, whereas attenuation is achieved by the inactivation gate that provides a positive conductance region (like that of delayed rectifier potassium current: Figure 1.6), and attenuates inputs with frequencies lower than the inverse of the time constant of the inactivation gate. Because the half maximal activation voltage ($V_{1/2}$) of the activation gate is more hyperpolarized than the $V_{1/2}$ of the inactivation gate, amplification should dominate at hyperpolarized potentials, whereas attenuation should dominate at more depolarized potentials. Expression of low I_{CaLVA} is suggested by the sensitivity of the hyperpolarization induced rebound depolarization to 2 mM $NiCl_2$ (Figure 4.20A), and described elsewhere (N'Gouemo and Morad 2003). Neurons that exhibit this rebound depolarization also exhibit a resonance response with a low resonance frequency in the range of 2-4 Hz (Figure 4.20B). Similar low-frequency resonance has been observed elsewhere in the avian auditory thalamus, and I_{CaLVA} is thought to be responsible (Strohmann et al. 1994). Blocking I_{CaLVA} by application of $NiCl_2$ reduced the resonance response (Figure 4.20B; Figure 4.21), in addition to blocking the rebound depolarization (Figure 4.20A).

Figure 4.20 I_{CaLVA} blockade reduces the resonance response, as observed in the impedance profile of a strong-onset response neuron.

Hyperpolarizing current pulses were used to investigate the contribution of low voltage activated calcium current to the hyperpolarization induced rebound depolarization. A) Blockade of low voltage activated calcium (I_{CaLVA}) by $NiCl_2$ (2 mM) decreases the hyperpolarization induced rebound. B) Ni application causes a leftward shift in the impedance profile, suggesting that LT-Ca may act to amplify low frequency input. The current-clamp pulse amplitude in (A) was 100 pA, and the mean membrane potentials of (B) are hyperpolarized from the resting membrane potential at -70 mV.

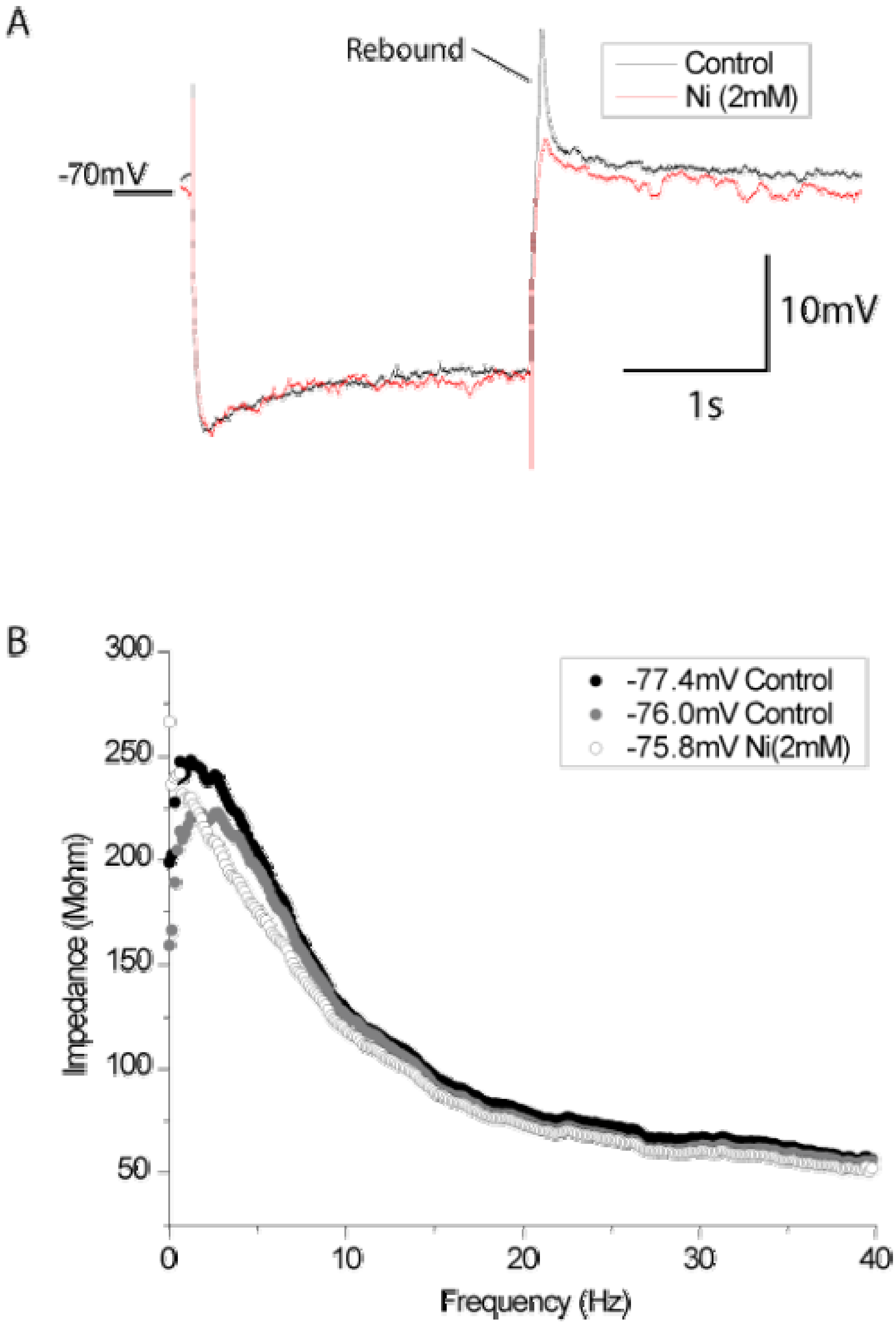
A
Rebound
Control
Ni (2mM)
-70mV
10mV
1s
B
300
250
200
150
100
50
Impedance (Mohm)
0
10
20
30
40
Frequency (Hz)
-77.4mV Control
-76.0mV Control
-75.8mV Ni(2mM)

Figure 4.21 Effect of I_{CaLVA} blockade on the impedance profile measurements of a strong-onset response neuron.

Impedance profile measurements from the impedance profiles of the previous figure are shown. The impedance profile observed after I_{CaLVA} blockade by 2 mM $NiCl_2$ exhibits less frequency selectivity (less resonance), than the impedance profile observed at a similar mean membrane voltage (around -76 mV), with increased Z_{max} despite decreases in Q, W, and F_r.

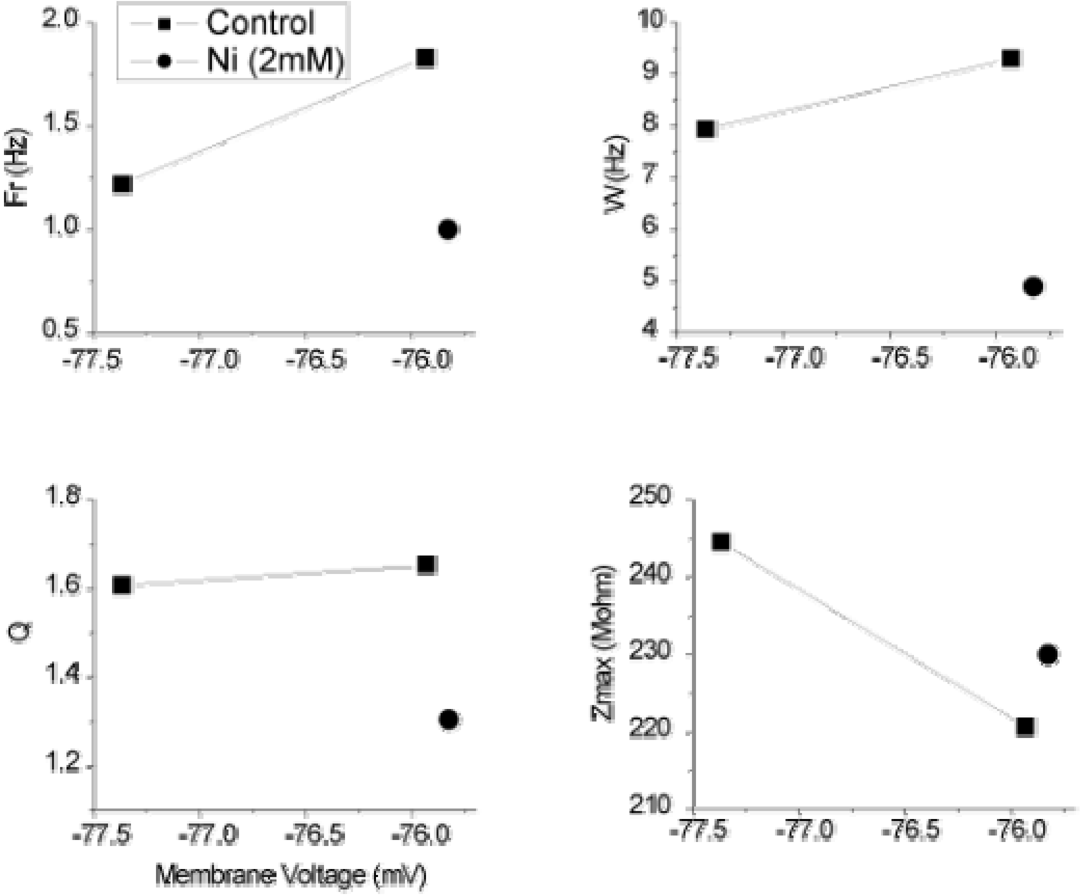
Control
Ni (2mM)
Fr (Hz)
2.0
1.5
1.0
0.5
-77.5
-77.0
-76.5
-76.0
W (Hz)
10
9
8
7
6
5
4
-77.5
-77.0
-76.5
-76.0
Q
1.8
1.6
1.4
1.2
-77.5
-77.0
-76.5
-76.0
Membrane Voltage (mV)
Zmax (Mohm)
250
240
230
220
210
-77.5
-77.0
-76.5
-76.0

4.2.4.3 The Role of Voltage Gated Sodium Current in the Resonance Response

Identification of the fixed point bifurcation of ICC neurons in chapter three suggests the presence of spiralling voltage trajectories at resting membrane potential, or at least when the membrane is slightly depolarized yet subthreshold. These trajectories should facilitate a resonance response that would disappear upon blockade of either the voltage gated sodium or potassium current. This type of resonance is different from that achieved by the slow accommodating current (e.g. I_h), because the time constants of the currents involved in the bifurcation are faster than the time constant of the membrane. Further, as discussed in chapter three, these faster currents are able to create observable (self generating) oscillations in the subthreshold membrane voltage, rather than acting primarily to filter incoming signals.

We examined the ability of the bifurcation to contribute to the resonant response by comparing impedance profiles before and after blockade of voltage gated sodium current with TTX. Resonance was observed at the resting membrane potential and at depolarized potentials upon application of a depolarizing bias current (Figure 4.22). At resting membrane potential, application of TTX had little effect on the impedance profile (Figure 4.22A, and C), whereas, TTX application decreased the resonance response when the mean membrane potential was depolarized from rest (Figure 4.22B, and C). Specifically, at depolarized potentials the application of TTX decreased Z_{max}. This suggests the involvement of voltage gated sodium currents in the resonance response, which by the concerted interaction with voltage gated potassium current leads to an amplification of inputs within a specific frequency band. Hence different currents are involved in the resonance response at different membrane voltages, where I_h is responsible at

Figure 4.22 Blockade of voltage gated sodium channels attenuates resonance at depolarized, but not hyperpolarized voltages.

Impedance profiles for three different neurons were calculated before and after blockade of voltage gated sodium channels by TTX (200nM) (A-C). When the mean membrane voltages were depolarized with respect to rest, TTX application caused a reduction in the maximum impedance (B, and red in C), whereas little change in the impedance profile was observed at hyperpolarized voltages (A, and black in C). Three firing response types are shown, with (A) a strong onset response, (B) an adaptive response, and (C) and accelerating response.

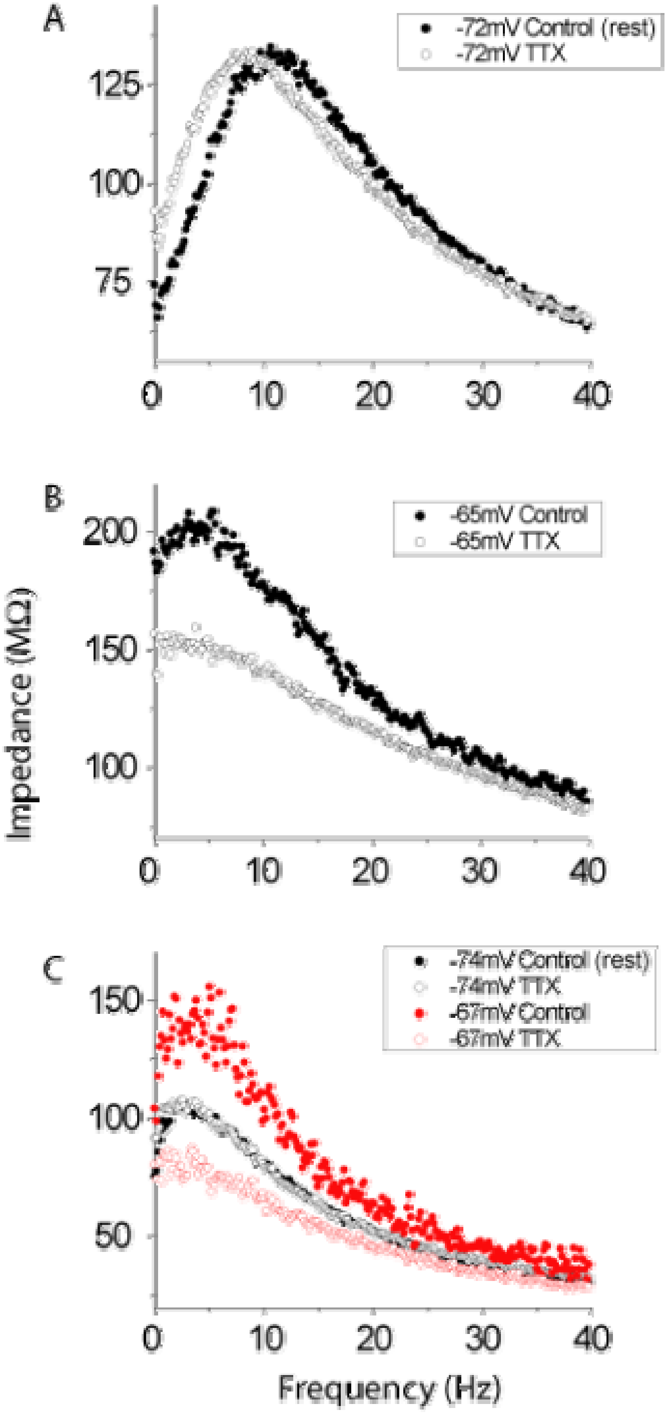
A
-72mV Control (rest)
-72mV TTX
125
100
75
0
10
20
30
40
B
-65mV Control
-65mV TTX
200
150
100
0
10
20
30
40
Impedance (MΩ)
C
-74mV Control (rest)
-74mV TTX
-67mV Control
-67mV TTX
150
100
50
0
10
20
30
40
Frequency (Hz)

hyperpolarized potentials, and sodium and potassium currents are responsible at depolarized potentials. The combination of these two mechanisms may explain the wide range in membrane potential over which resonance is observed.

4.3 Summary of Results

Frequency selectivity, as indicated by a resonant frequency, was observed within a range of frequencies (1.5-12 Hz) similar to those of the STOs in chapter three (2-16 Hz). No apparent trend was observed between the degree of frequency selectivity with mean membrane potential; however on occasion, frequency selectivity increased upon depolarization of the membrane, suggesting that more than one ionic mechanism might be contributing to the resonance response given that the membrane was depolarized beyond the activation profile of I_h. The contribution of I_h to the resonance response at rest and at hyperpolarized potentials was demonstrated by blockade with CsCl. In contrast, the mechanism underlying resonance at membrane potentials depolarized from rest involves I_{Na}, as indicated by blockade of I_{Na} by TTX. These two different mechanisms indicate how both an accommodating current and the type of fixed point bifucation (as determined by I_{Na} and I_K) work synergistically in ICC neurons to provide frequency selectivity over a wide range of membrane potential. Additionally, I_{CaLVA} is thought to play a role in the resonance response, albeit a smaller one, and only for low frequencies.

4.4 Discussion

A proportion of ICC neurons exhibit subthreshold frequency selectivity in response to broadband current-clamp stimuli, as indicated by a measurable resonance response, which is most prominent in strong-onset response neurons. Frequency selectivity was detected by the presence of a distinct peak in the impedance spectrum, and the Q-value serves to indicate the specificity of frequency selectivity by comparing the peak impedance with the steady state impedance (i.e. the input resistance). Resonance indicates a preferential response to periodic inputs of a specific frequency. This behaviour could be interpolated from a previous study that investigated the contribution of I_h current to temporal processing in the ICC (Koch and Grothe 2003). In this study, I_h was shown to attenuate consecutive overlapping postsynaptic potentials. Although not specifically addressed, Koch and Grothe indirectly suggest I_h's ability to attenuate low frequency deflections of the membrane potential through filtering of synaptic inputs. In light of the low frequency attenuation provided by I_h and the high frequency attenuation provided by the membrane capacitance, we hypothesized that ICC neurons exhibit a preferred response to inputs of a specific frequency. Further, the spiralling trajectories in the phase plane near the AH bifurcation identified in chapter three, suggest another possible mechanism for frequency selectivity. Membrane resonance was observed over a wide range of mean membrane potentials, at least 5 mV above and below resting membrane potential, and resonance frequency at resting membrane potential varied between 1.5-12 Hz depending on the neuron.

A slow accommodating resonant current can provide frequency selectivity. A peak in the impedance profile may not be observed despite expression of I_h, or another slow resonant current, if the time constant of the membrane is larger (effectively slower) than the time constant governing the I_h kinetics. When I_h, or any other resonant current, is expressed, the membrane response to input current is the output of a combined high pass filter and low pass filter. The high pass filter arises from the low frequency attenuation provided by the I_h kinetics, and the low pass filter from the capacitive properties of the membrane. However, a distinct peak in the impedance spectrum is observed only when the corner frequency of the low pass filter (the inverse of the membrane time constant) is considerably larger than that of the high pass filter (the inverse of the I_h time constant). Otherwise, I_h current cannot act to provide frequency selectivity, but can still serve to decrease the input resistance.

Frequency selectivity can be achieved independent of expression of a slow resonant current. Instead, the dynamic interaction between the fast currents, sodium and potassium, can facilitate frequency selective spiral trajectories in the phase plane where perturbations return to the fixed point through a damped oscillation of the membrane potential. These trajectories occur on the condition of an AH bifurcation, as discussed in chapter three. In comparison to the intuitive frequency selectivity provided by a slow resonant current, the frequency of the spiral trajectory is determined by many factors. These include the steady state values of the activation and inactivation gates and their derivatives with respect to membrane potential, the time constants on the activation and inactivation gates and their derivatives with respect to membrane potential, the maximal conductance values of each current, and the membrane capacitance. When this information is known a conductance model can be constructed, from which the eigenvalues of the Jacobian at the fixed point can be calculated. The spiral frequency is the complex valued portion of the eigenvalues (Strogatz 2000; Izhikevich 2007).

We collected evidence indicating that both mechanisms of resonance are at play in ICC neurons. A decrease in the resonant response was observed upon blockade of I_h with Cs^+, indicating the contribution of this slow resonant current to frequency selectivity. I_h can only contribute to resonance at relatively hyperpolarized potentials, as indicated by its activation curve; however the range of membrane potentials at which frequency selectivity can be observed is extended beyond the activation profile of I_h. In comparison, the higher-frequency resonance observed at more depolarize membrane potentials is sensitive to voltage gated sodium channel blockade by TTX. The contribution of sodium to the resonant response is provided by the oscillatory trajectories of the AH bifurcation, and is the same mechanism responsible for I_h independent STOs of chapter three. Additionally, the frequency selectivity provided by these two mechanisms appears to transition gradually with membrane potential, given the absence of any large shift in the resonant frequency with changes in the mean membrane potential. We propose that frequency selectivity might also be provided by I_{CaLVA} in ICC neurons. However, the expression of I_{CaLVA} is not very strong, as indicated either by whole cell recordings (N'Gouemo and Morad 2003), or in situ hybridization (Talley et al. 1999).

These three mechanisms of resonance are known in other neurons. Although resonance was first observed in the turtle auditory hair cell (Crawford and Fettiplace 1981), neuronal resonance was first observed in the guinea pig trigeminal root ganglion, with a resonant frequency in the 50 to 250 Hz range (Puil et al. 1986). Hyperpolarization of the membrane below resting membrane potential abolished the resonant peak, suggesting that recruitment of voltage gated sodium and or potassium are necessary for resonance (Puil et al. 1987). Pharmacological blockade of voltage gated potassium channels with tetraethylammonium (TEA) abolished the resonance response (Puil et al. 1988). Likewise, subthreshold oscillations were also blocked by TEA (Puil et al. 1989). However, blockade of voltage gated sodium channels with TTX had little effect on the impedance profile, possibly due to the expression of TTX resistant I_{Na} (Kim and Chung

1999). We propose that the resonance response observed in the trigeminal root ganglion is due to an AH bifurcation like mechanism, similar to the TTX sensitive mechanism proposed for ICC neurons. Mesencephalic trigeminal sensory neurons (Mes V) also exhibit resonance with a frequency similar to that of the trigeminal root ganglion neurons. It is also likely that the AH bifurcation is the mechanism of resonance in Mes V, as suggested by TTX sensitivity (Wu et al. 2005).

Like ICC neurons, many neurons employ more than one mechanism of resonance. Neurons of the avian thalamus were the first neurons identified which exhibit more than one mechanism of resonance, where the involvement of voltage gated sodium current, low-threshold calcium current, and I_h has be shown (Strohmann et al. 1994). Similarly, in the case of the ICC, we suggest that the involvement of sodium current indicates the AH bifurcation mechanism or resonance, and the involvement of I_h and indicates the slow resonant current mechanism of resonance. Additionally, these dual mechanisms of resonance are observed in neocortical intrinsic bursting and regular spiking neurons (Hutcheon et al. 1996; Ulrich 2002), layer 2 entorhinal cortex stellate neurons (White et al. 1998; Dickson et al. 2000; Haas et al. 2007), and pyramidal neurons of the subiculum (Wang et al. 2006). Similarly, CA1 hippocampal pyramidal neurons express two resonant currents, I_h and M-type current (a slow potassium current, I_M), which facilitate resonance at hyperpolarized and depolarized membrane potentials respectively, in addition to I_{Na} involvement at depolarized potentials (Leung and Yu 1998; Hu et al. 2002).

We propose that frequency selectivity might also be provided by I_{CaLVA} (i.e. T-type calcium current) in ICC neurons. However our evidence for this is anecdotal and we further suggest that I_{CaLVA} dependent resonance might arise from larger amplitude membrane potential deflections. The low-threshold calcium mechanism of resonance is similar to the AH bifurcation mechanism, in that antagonistic action of two gating variables (which are dynamic variables) are responsible for the frequency selectivity. The activation and inactivation gates of I_{CaLVA} provide amplification of high frequency inputs and attenuation of low frequency inputs. Specifically, fast inputs are amplified, but the ability of the activation gate to keep up with the input is constrained by the kinetics of the activation gate, and input amplification is only possible up to a certain frequency; whereas, low frequency inputs are not amplified because the inactivation gate can track low frequency inputs, effectively shutting off the otherwise amplifying effect of I_{CaLVA}. In addition to the already mentioned mechanisms, the involvement of I_{CaLVA} in the resonance response of mammalian and avian thalamus is indicated by sensitivity to I_{CaLVA} blockade with Ni (Puil et al. 1994; Strohmann et al. 1994).

4.4.1 Functional Role of Subthreshold Frequency Selectivity

Resonance is observed in many different types of neurons; yet there is currently no clearly established functional role. A comparison of the resonance responses across stations of the avian auditory pathway shows a decreasing resonance frequency with ascending stations (Strohmann et al. 1995). The mammalian auditory pathway demonstrates a similar trend. At the more peripheral stage of the cochlear nucleus, high frequency membrane potential oscillations are observed in the dorsal cochlear nucleus pyramidal neurons (50-100 Hz) (Manis et al. 2003); whereas, the more central ICC exhibits much lower frequency membrane potential oscillations. Nevertheless, the relevance of this trend is unknown. Similarly, a resonance frequency gradient is also observed within the same neuron type in the entorhinal cortex, with a decrease along the dorsal-to-ventral axis (Giocomo et al. 2007). The existence of membrane resonance in multi-modal high order cortical neurons suggests that resonance may play a broader role beyond early sensory signal processing.

In a neuron with a minimal firing frequency different from the subthreshold resonance frequency, noise intensity appears to modulate action potential firing rate. At low noise intensity, the neuron will preferentially fire action potentials at the minimum firing frequency. In contrast, a higher noise intensity will shift the firing rate to that of the resonant frequency (Richardson et al. 2003). The application of this phenomenon to ICC neurons is questionable, given the close similarity between resonant frequency and the minimal firing frequency.

Regardless, the attenuation of low frequency inputs in ICC neurons is clear. We suggest that the specific role of this low frequency attenuation is to reduce the summation of temporally overlapping inputs, as reported in the context of the role of I_h in temporal processing (Koch and Grothe 2003). The selectivity for temporally coincident inputs, suggests that resonant neurons might serve to process binaural inputs. Nevertheless, we have here established that resonance can be observed if the neuron is driven by a current source. In reality, the neuron is driven by conductances, and these synaptic events modulate membrane impedance. On the condition that the synaptic inputs impinge on dendrites and not the soma, these inputs might be well approximated by currents (Vogels and Abbott 2005). The ability of small conductance changes to dampen a subthreshold oscillation has been demonstrated with the use of conductance clamp in entorhinal cortex layer 2 stellate neurons (FR Fernandez, personal communication).

Chapter Five: Spontaneous Stochastic Events in ICC Neurons (Transient Hyperpolarizations, and Spikelets)

5.1 Overview

While observing the largely stochastic subthreshold responses, numerous near identically shaped transient hyperpolarizations (THs) of the membrane potential were observed, occasionally with nearly regular periods. Further, there was a positive correlation between the TH event frequency and the mean membrane potential. Unfortunately, sufficient time was not available to fully explore the mechanism underlying THs, and they proved resistant to many pharmacological manipulations. Instead we briefly characterized these events, and carried out experiments that served to rule out possible underlying mechanisms.

In addition to THs, we observed spikelets like those observed in vivo (Tan et al. 2007). Very few neurons exhibited spikelets. Nevertheless, spikelets exhibited a positive correlation between event frequency and membrane potential, like that observed for THs. In contrast, spikelets appear to be sensitive to voltage gated sodium channel blockade by TTX.

5.2 Results

5.2.1 Characteristics of Transient Hyperpolarizations

5.2.1.1 The Transient Hyperpolarization Waveform

The TH waveform was uniform amongst observations at a given holding current. An average of ten events observed at the same membrane voltage demonstrates the initial steep negative deflection for approximately 20 ms, followed by a slow return to the resting membrane potential over approximately 80 ms (Figure 5.1). This uniform shape and its sparseness distinguish THs from the subthreshold oscillations, both of which coexist at the same mean membrane potential (Figure 3.25).

The time course of the TH is too fast to be due to a slow synaptic current mediated by the $GABA_B$ receptor (Sodickson and Bean 1996). However, the kinetics of the glycine receptor (Harty and Manis 1998), and, or the $GABA_A$ receptor are (Sivaramakrishnan and Oliver 2006) sufficiently fast, particularly when the relatively high input resistance, and therefore RC properties, are taken into account. Therefore they are plausible candidate mechanisms of THs. Under the assumption of an ionotropic synaptic mechanism, we expected to see quanta in either distributions of amplitude or initial slope (Kuno and Weakly 1972). Quanta should appear as a multimodal distribution of either metric, and are the result of coincident release of more than one synaptic vesicle. However, the presence of quanta was not confirmed in either the TH amplitude, or the TH minimum slope, as indicated by their distributions (Figure 5.2).

One hint was provided by the TH waveform, which had a time course similar to that of the after hyperpolarization (AHP) following an action potential (Figure 5.3). In many neurons throughout the mammalian brain, the AHP is caused by activation of small conductance calcium and voltage-activated potassium channels (SK) following influx of calcium through voltage gated calcium channel during the depolarized phase of the action potential (Sah 1996; Aizenman and Linden 1999; Sah and Faber 2002; Vogalis et al. 2003; Stocker 2004; Pedarzani et al. 2005). The kinetics of the SK channel are much slower than those of the other currents activated during the action potential, and the time constant of deactivation can range from 60 to 200 ms (Sah 1996; Sah and Faber 2002), which coincides well with the amount of time required for the return to rest during the

Figure 5.1 The uniform waveform of transient hyperpolarizations.

A) Five superimposed, randomly selected events from Figure 5.4A. B) An average was obtained using ten events.

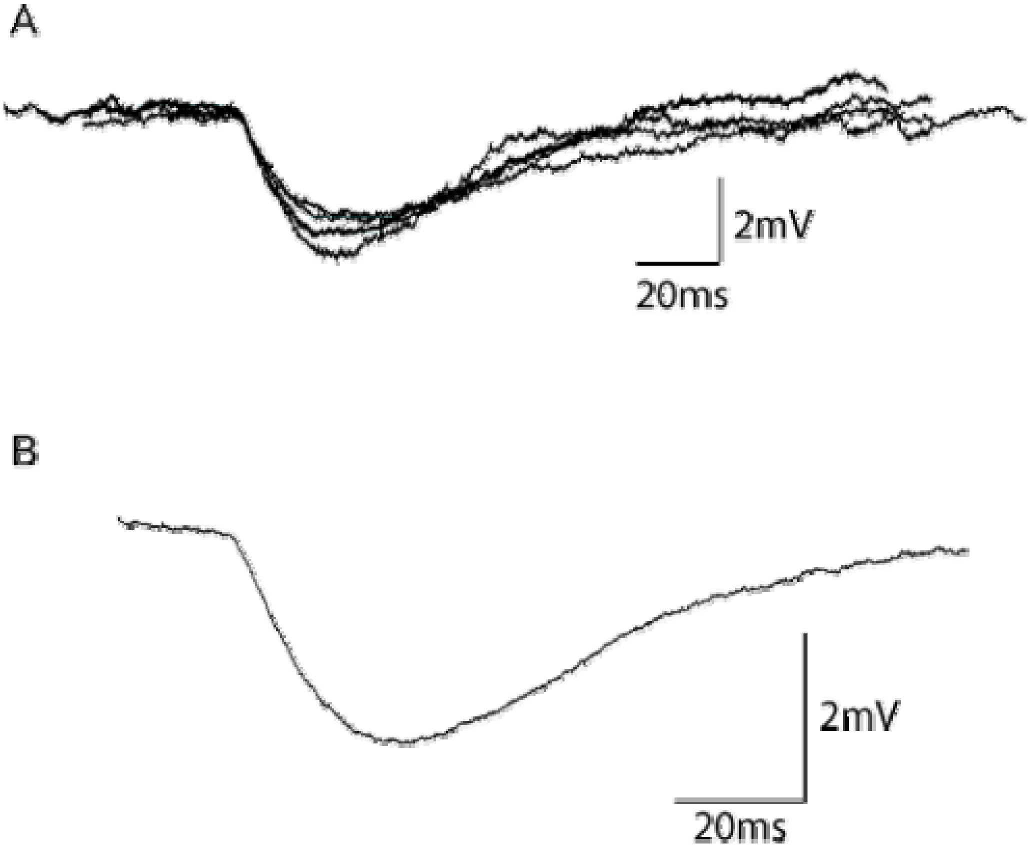
A
2mV
20ms
B
2mV
20ms

Figure 5.2 Quanta were not observed in either the distribution of transient hyperpolarization amplitude or minimum slope.

The presence of quanta in SP amplitude or minimum slope values was investigated by plotting histograms for current-clamp responses in which THs were observed (A, and B). All distributions appear unimodal, and do not have a second or third peak at the respective two or three times the value of the main peak, which represent coincident release of respective two or three synaptic vesicles.

The two trials shown here are those of Figure 5.4A and Figure 5.4B, and correspond to (A) and (B) respectively. The minimum slope refers to the downward slope observed during the downward deflection in membrane potential during TH (at the onset of the waveform), and the amplitude was measured with respect to the voltage at the start of this downward deflection.

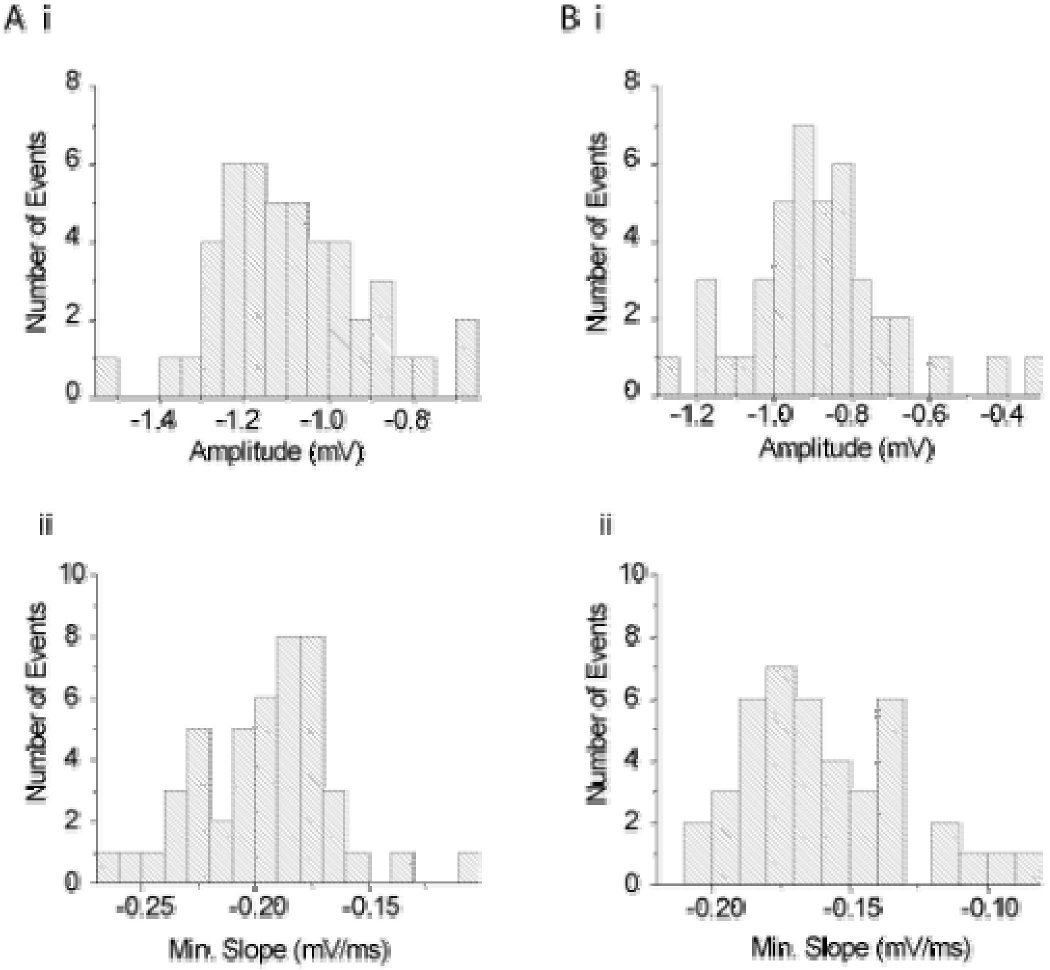
A i
Number of Events
8
6
4
2
0
-1.4
-1.2
-1.0
-0.8
Amplitude (mV)
B i
Number of Events
8
6
4
2
0
-1.2
-1.0
-0.8
-0.6
-0.4
Amplitude (mV)
ii
Number of Events
10
8
6
4
2
0
-0.25
-0.20
-0.15
Min. Slope (mV/ms)
ii
Number of Events
10
8
6
4
2
0
-0.20
-0.15
-0.10
Min. Slope (mV/ms)

Figure 5.3 The time course of the waveform is similar between the after hyperpolarization and the transient hyperpolarization.

A) Stutter firing of adaptive neuron in response to a depolarizing current-clamp pulse (130 pA) is shown, with two THs (circles). B) A sAHP (grey trace) (from A; see arrow) was overlaid on top of the average TH from Figure 5.1B (black trace), in order to demonstrate the similarity of time course between the two.

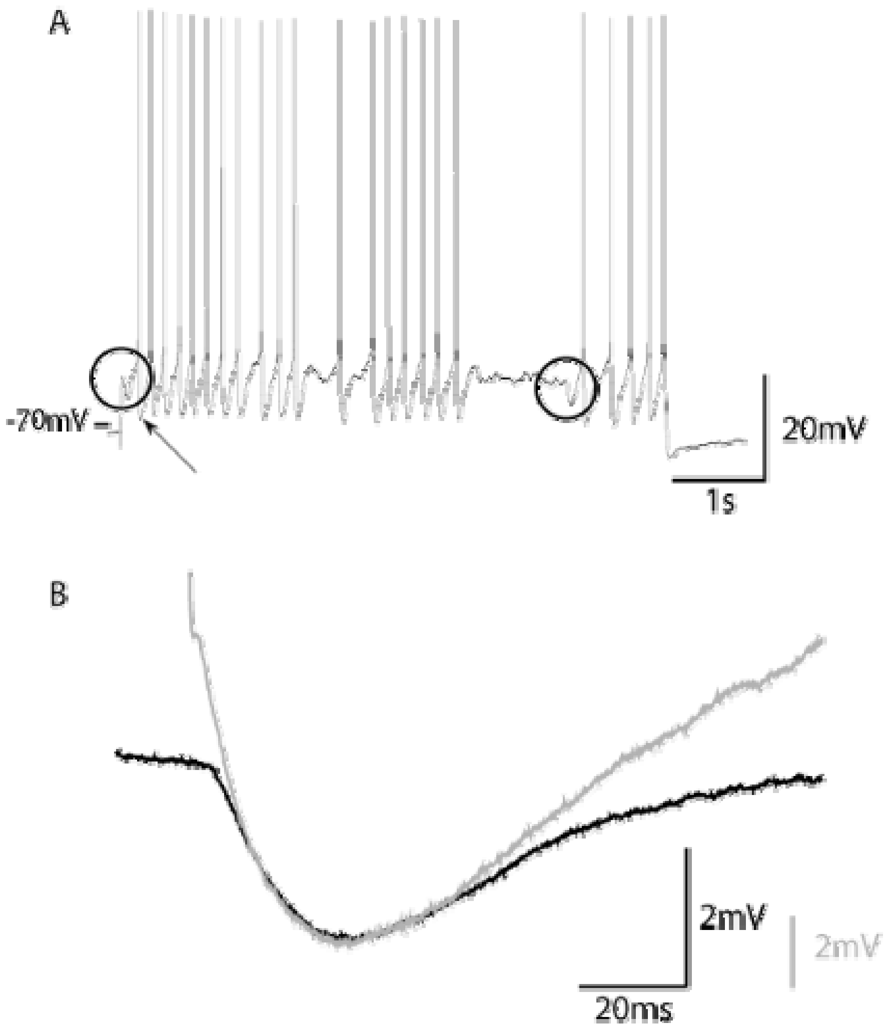
A
-70mV
20mV
1s
B
2mV
2mV
20ms

TH (Figure 5.1). Therefore, based on this similarity of time course, we suggest that transient SK activation is a possible mechanism underlying THs. Additionally, spiking was never interrupted by THs, nor was a TH observed during the AHP, further suggesting that the same mechanism contributes to both the TH and the AHP. The putative source of calcium in the absence of a spike remains to be determined however.

5.2.1.2 Voltage Dependence

Transient hyperpolarizations were most frequently observed during depolarized subthreshold responses to current-clamp pulses. Strong voltage dependence was often observed, where the appearance of THs could be switched on or off following a 3-4 mV manipulation of the mean membrane voltage (Figure 5.4). Additionally, voltage dependence was apparent by a positive correlation between the event frequency and the mean membrane potential, where a difference in 6 mV could more than double the average event frequency (Figure 5.5). This positive correlation was ubiquitous in all neurons that exhibited THs.

The voltage dependence of TH event frequency was also observed in voltage clamp. Small transient outward currents were observed under the voltage clamp configuration in neurons that also exhibited THs in current-clamp (Figure 5.6A). Given that we observed unclamped sodium spikes during voltage clamp, we do not believe that control of the membrane voltage was achieved throughout the neuron. Nevertheless, our control was sufficient to observe a positive correlation between the average event frequency and the membrane potential (Figure 5.6D), like that observed in current-clamp (Figure 5.5B). Such voltage dependence is unlikely to be due to synaptic events, which should be largely independent of postsynaptic membrane voltage on this scale.

Figure 5.4 Transient hyperpolarizations exhibit strong voltage dependence.

A) THs were observed when the membrane voltage is held depolarized (one example is shown with arrow), yet subthreshold to spiking at -59 mV with a current pulse of 130 pA. B) No hyperpolarizations are observed when the membrane is held at -62.5 mV with a 90 pA pulse. C) THs are observed again upon return to the -59 mV potential with a 120 pA current pulse (one example is shown with arrow).

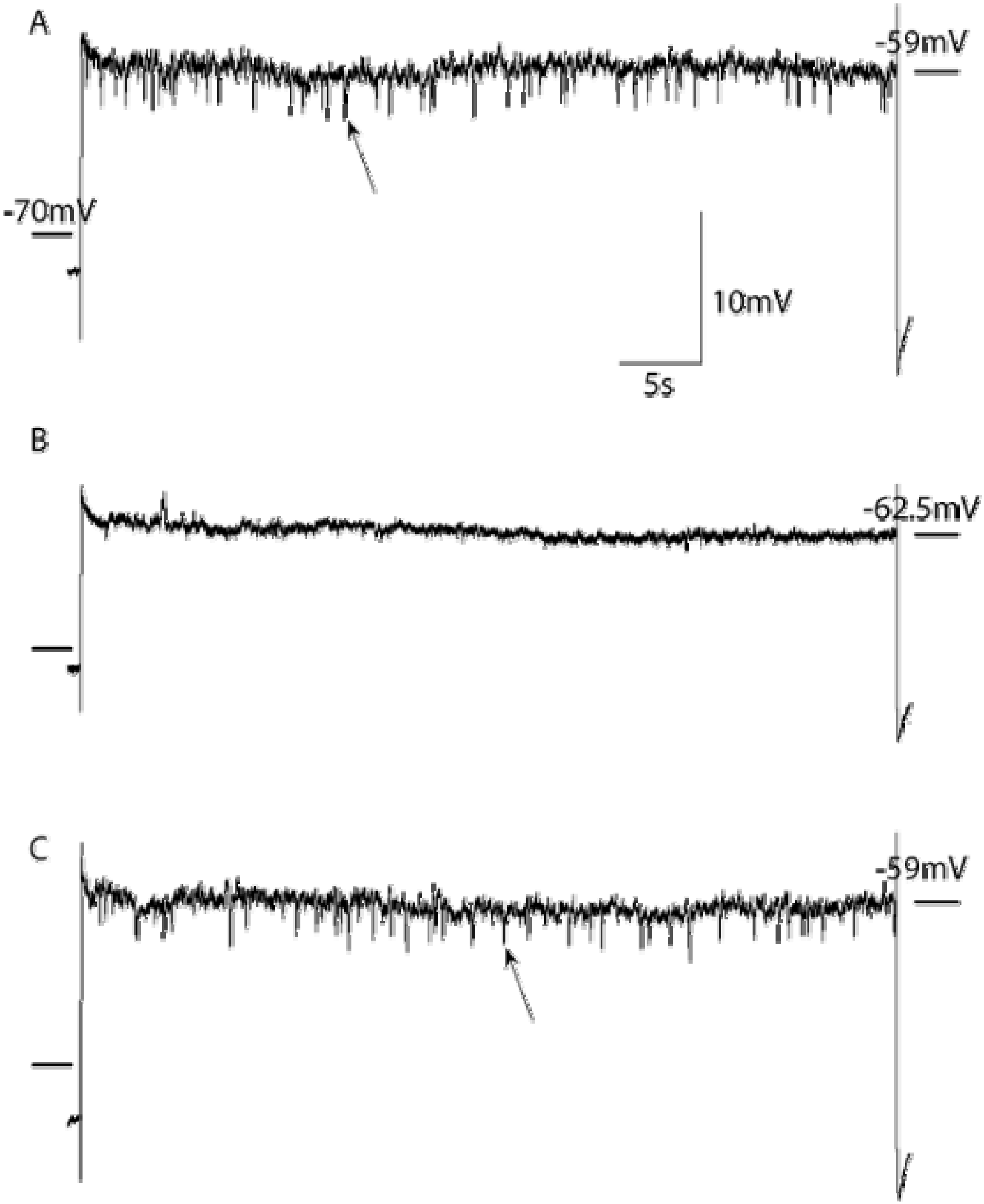
A
-59mV
-70mV
10mV
5s
B
-62.5mV
C
-59mV

Figure 5.5 Transient hyperpolarization event frequency correlates positively with the mean membrane potential.

A) Event frequency is higher when the membrane is depolarized by a 50 pA current-clamp step. The events are less frequent at rest (-70 mV), and sufficient driving force is still available at this potential despite its proximity to the chloride equilibrium potential (-74.2 mV). B) The average event frequency correlates with the mean membrane potential, and the difference in mean event frequencies are statistically significant (two-tailed T-test, $p<0.05$).

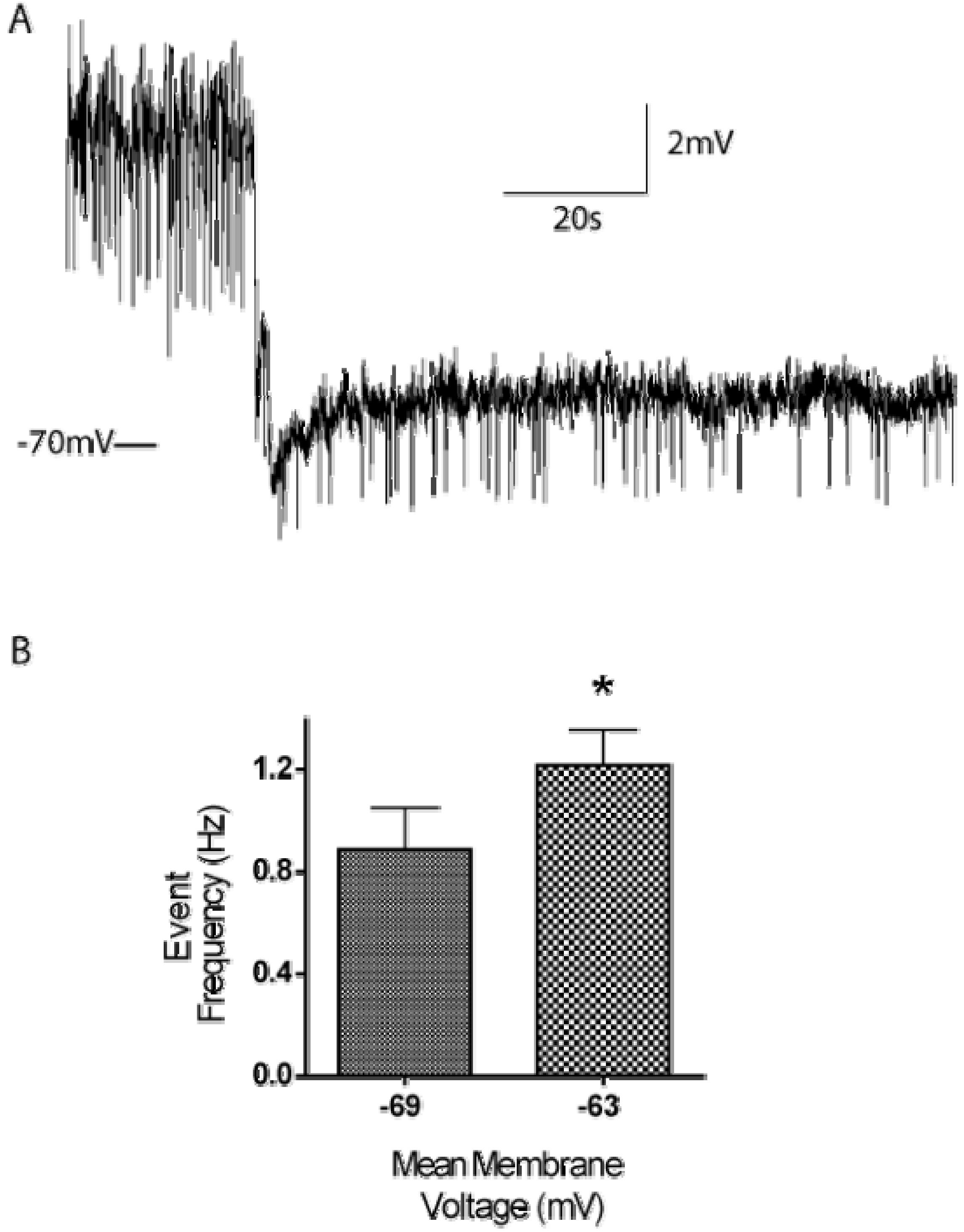
A
2mV
20s
-70mV
B
*
Event Frequency (Hz)
1.2
0.8
0.4
0.0
-69
-63
Mean Membrane Voltage (mV)

Figure 5.6 Transient hyperpolarizations were also observed in voltage clamp.

A) Transient hyperpolarizations observed in current-clamp were observed as outward currents in voltage clamp, with the voltage clamp protocol is show in (B). One TH example is shown with arrow, and reproduced in (C). The average event frequency correlated with the membrane potential (D), similar to that observed in current-clamp. The difference in event mean frequencies (D) is statistically significant (two-tailed T-test, $p<0.05$).

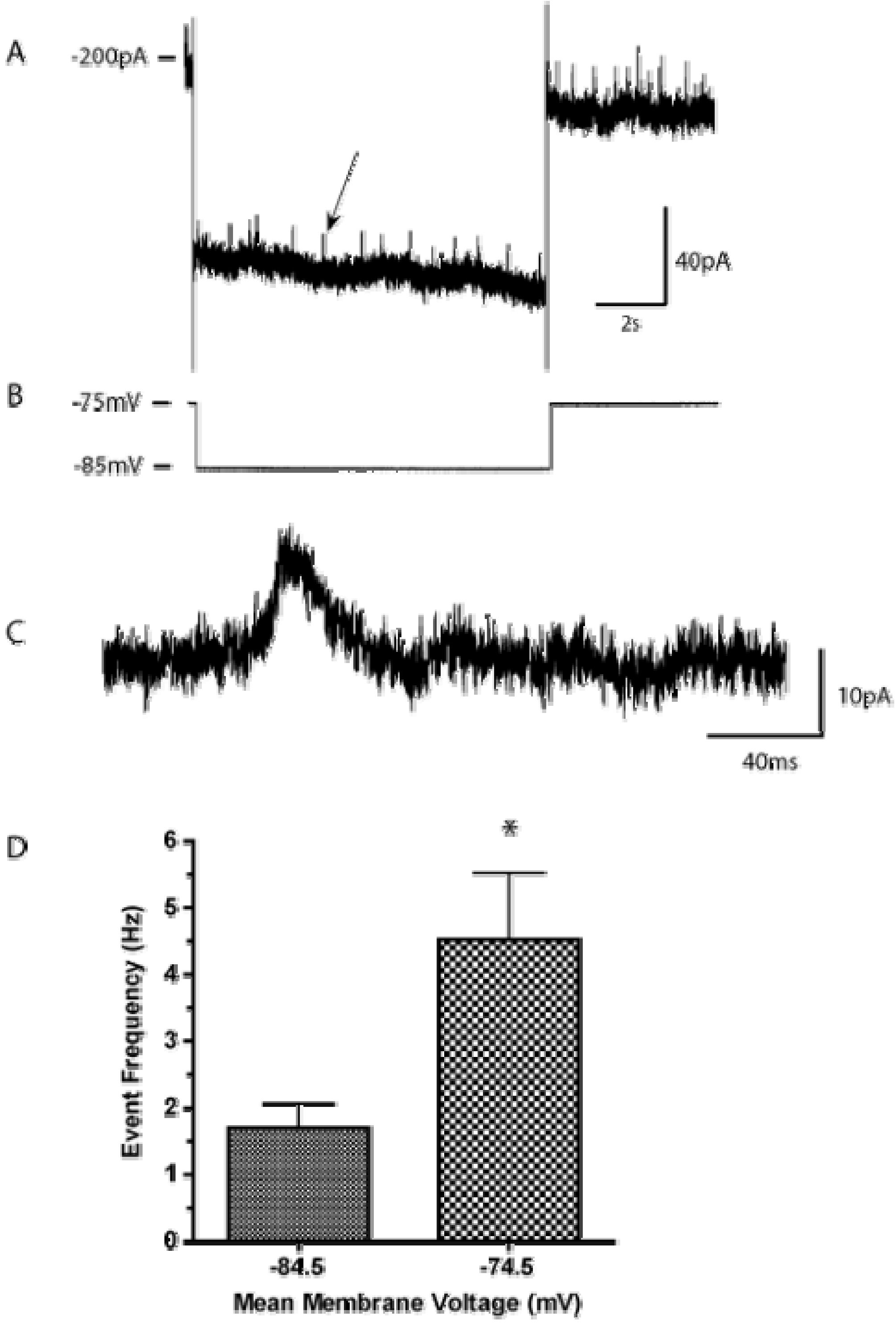
A
-200pA
40pA
2s
B
-75mV
-85mV
C
10pA
40ms
D
*
6
5
4
3
2
1
0
Event Frequency (Hz)
-84.5
-74.5
Mean Membrane Voltage (mV)

We gave further consideration to the idea of a synaptic mechanism however, and we made an attempt to determine the reversal potential of the putative synaptic current, which should provide insight into the ionic identity of the current responsible for THs. Upon plotting the relationship between TH amplitude and membrane voltage, it was apparent that the TH amplitude increases approximately linearly in accordance with depolarization of the membrane potential, and a linear fit was used to describe this relationship. The TH reversal potential was estimated as the intersection of this linear fit with the abscissa (the mean membrane potential axis) (Figure 5.7) (Arima et al. 2001). Chloride does not appear to be the ion involved in the current underlying the TH because the estimated reversal potentials are typically more hyperpolarized than the calculated chloride equilibrium potential (E_{Cl}=-74.2 mV, Figure 5.7), and TH events were often observed below E_{Cl} (Figure 5.7; Figure 5.6; Figure 5.12B; Figure 5.13B). More specifically, this suggests that neither chloride ionotropic receptors, the $GABA_A$ (type A gamma-aminobutyric acid) receptor nor the glycine receptor, is involved in the generation of THs. Alternatively, potassium might be involved because its calculated equilibrium potential (E_K=-96.8 mV) is lower than that of chloride.

5.2.1.3 Transient Hyperpolarizations Observed in Firing Response Types

Approximately 50% of all neurons exhibited THs to a varying degree. The TH response was more common in neurons that exhibit an accelerating firing response and least common in the onset and adaptive response types (Figure 5.8).

5.2.2 Characteristics of Spikelets

Spikelets have characteristics in common with THs. Like THs, spikelet events are more common at depolarized potentials than at hyperpolarized potentials (Figure 5.9). An

Figure 5.7 The estimated TH reversal potential is lower than the chloride equilibrium potential.

The mean TH amplitude observed during current-clamp pulses was plotted against the mean membrane potential for three separate neurons. The TH amplitude decreased with hyperpolarization of the membrane, and the TH reversal potential was estimated for each neuron as the intersection of the linear fit with the abscissa. The trace used in (A) was obtained from the recording presented in Figure 5.5A.

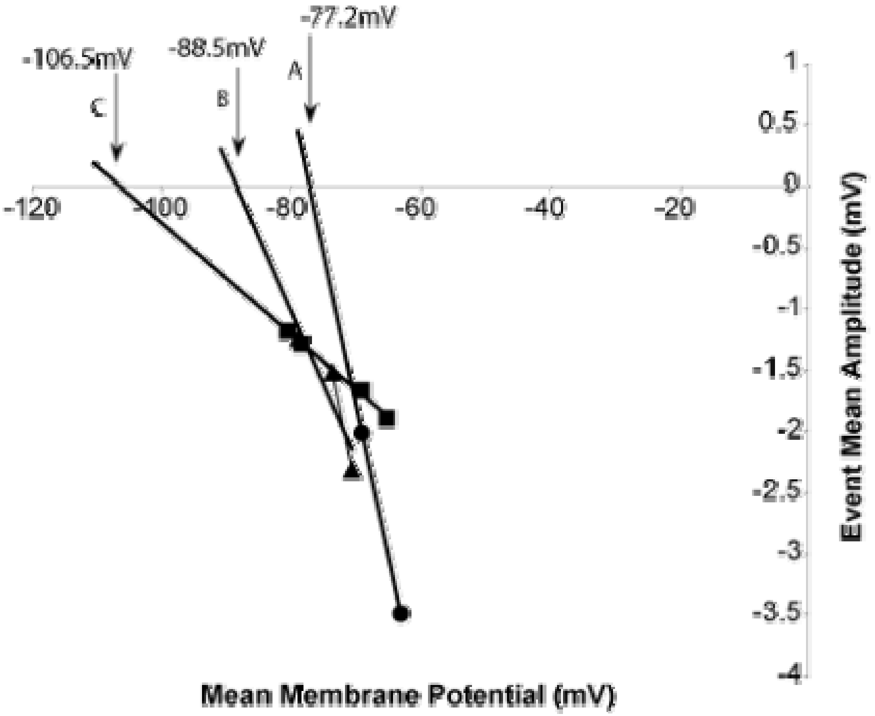
-77.2mV
-88.5mV
-106.5mV
A
B
C
-120
-100
-80
-60
-40
-20
1
0.5
0
-0.5
-1
-1.5
-2
-2.5
-3
-3.5
-4
Event Mean Amplitude (mV)
Mean Membrane Potential (mV)

Figure 5.8 TH were most often observed in the accelerating response type, and less so in adaptive and onset response types.

The percentage of response types that exhibited THs is shown. From a total of seventeen neurons, 70% were of the accelerating response type, and the remaining 30% were of the adaptive or onset response type.

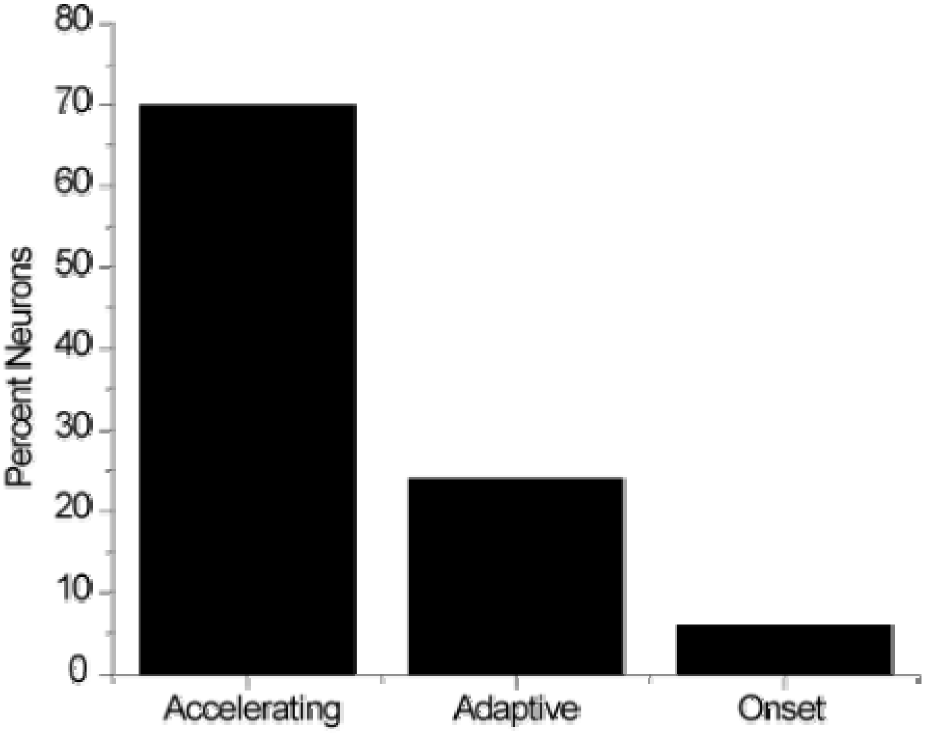

Percent Neurons
80
70
60
50
40
30
20
10
0
Accelerating
Adaptive
Onset

Figure 5.9 Spikelet event frequency correlates positively with the mean membrane potential.

A) Spikelets were observed at resting membrane potential (one example shown with arrow), and their frequency decreased with hyperpolarization. B) A positive correlation is observed between the average event frequency and the mean membrane potential.

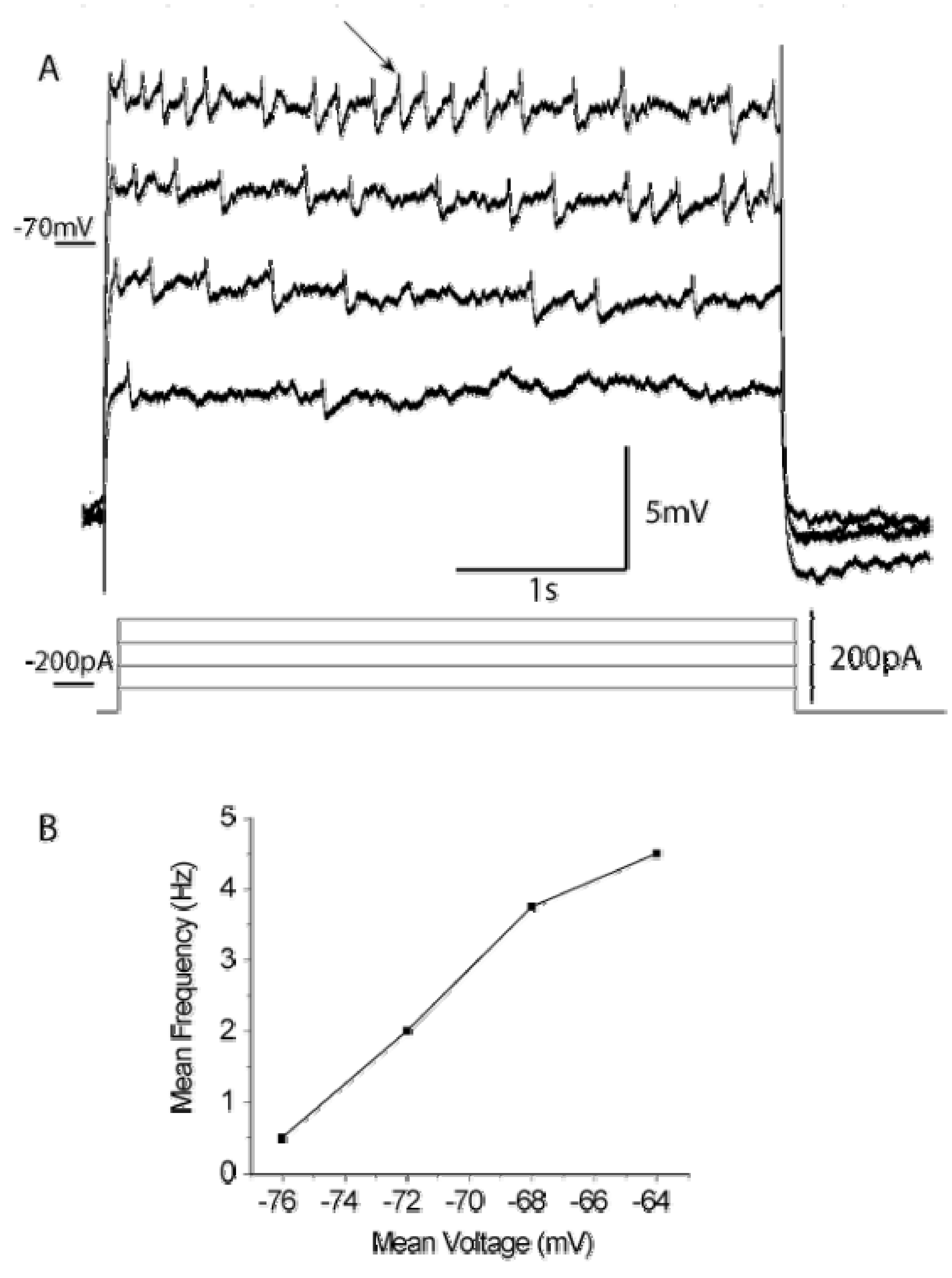
A
-70mV
5mV
1s
-200pA
200pA
B
Mean Frequency (Hz)
0
1
2
3
4
5
-76
-74
-72
-70
-68
-66
-64
Mean Voltage (mV)

additional similarity is the positive correlation between average event frequency and membrane voltage (Figure 5.9B). Spikelets are distinguished from THs by an initial upward depolarization, in contrast to the initial downward hyperpolarization observed in THs. This small amplitude fast depolarization is followed by the slower hyperpolarization with a similar time course as that observed in the TH (Figure 5.10B). Both THs and spikelets could be observed at the same mean membrane potential sufficient to observe spiking (Figure 5.3A; Figure 5.10A). Neurons that exhibited spikelets were rare, appearing in only two neurons out of a sample of sixty-eight neurons, and is far rarer than the 18% observed in vivo (Tan et al. 2007). Both of these neurons were of the adaptive spiking response type.

5.2.3 Mechanism of Transient Hyperpolarizations

A synaptic mechanism does not appear to be responsible for THs, as indicated by TH characteristics. We chose to investigate this mechanism by response to pharmacological blockade of ionotropic synaptic receptors, and voltage gated ion channels.

5.2.3.1 Synaptic Receptors: A Mechanism for Transient Hyperpolarizations?

Despite indications that the mechanism underlying the TH is not a postsynaptic ionotropic receptor, such as the reversal potential below the chloride equilibrium potential indicative of $GABA_A$ or glycinergic current, as well as the lack of defined quanta, we conducted further experiments to ensure that THs were not simply a result of inadequate blockade of post-synaptic receptors.

Of concern was inadequate blockade of inhibitory synaptic currents. In all experiments the $GABA_A$ receptor was antagonized by (10 μM) picrotoxin, and the

Figure 5.10 The time course of the waveform is similar between the spikelet and the TH.

A) Spiking is observed along with spikelets in response to a depolarizing current pulse. B) A spikelet (grey trace) (from A; see arrow) was overlaid on top of the average TH from Figure 5.1B (black trace), to demonstrate similarity of time course.

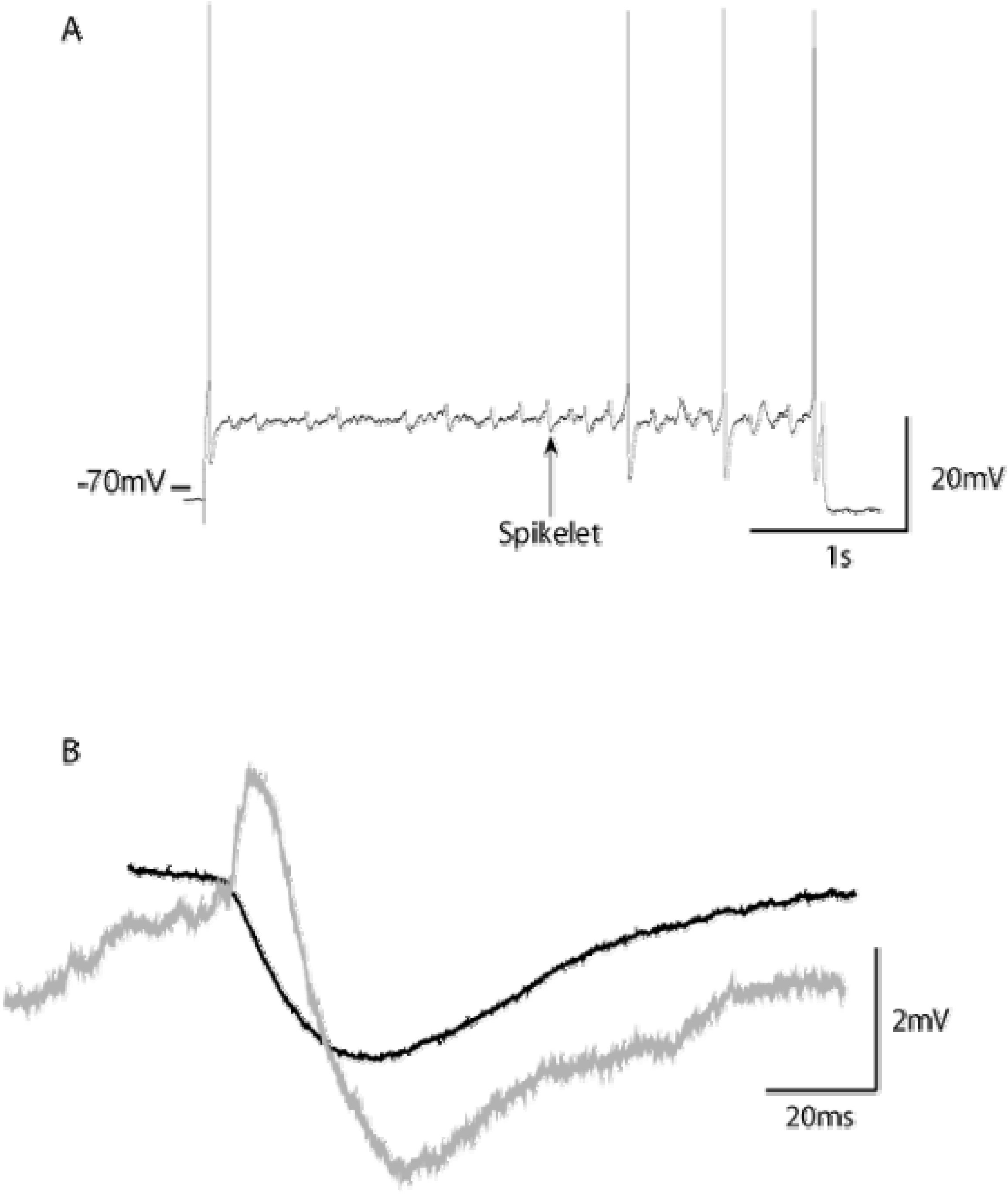
A
-70mV
Spikelet
20mV
1s
B
2mV
20ms

glycine receptor was antagonized by (5 μM) strychnine. The strychnine concentration is ten fold greater than that necessary for blockade of evoked glycine receptor mediated inhibitory potentials in the IC, and the picrotoxin concentration is sufficient for blockade of evoked $GABA_A$ receptor mediated inhibitory potentials in the IC (Wu et al. 2002). Nevertheless, we chose to examine the effect of increasing the synaptic receptor antagonist concentrations to ensure that inhibitory synaptic blockade was sufficient. In the case of the $GABA_A$ antagonists, neither a 500% increase in picrotoxin concentration (Figure 5.11A), nor a switch to bicuculline (10 μM) was capable of abolishing THs (Figure 5.11B). Likewise for the glycine receptor, a 200% increase in strychnine concentration was incapable of abolishing THs (Figure 5.11A). Therefore we found no evidence suggesting that inhibitory synaptic blockade was insufficient. The above facts, taken together with the reversal potential, and voltage dependence of THs, suggest a non-synaptic mechanism.

5.2.3.2 Voltage Gated Ion Channels: A Mechanism for Transient Hyperpolarizations?

Since the mechanism underlying THs did not appear to be synaptic in nature, we examined the possibility of voltage gated ion channel involvement.

To investigate the requirement of voltage gated sodium channels, and hence action potential generation, we investigated the presence of THs upon blockade of voltage gated sodium channels with 200 nM tetrodotoxin (TTX). THs were observed following TTX application despite blockade sufficient to abolish action potentials (Figure 5.12B). Two conclusions can be drawn from this result. First, sodium current is not necessary to elicit the outward current responsible for the TH. Second, action potential generation in presynaptic neurons or projecting axons is not involved in generation of

Figure 5.11 THs remained despite either increasing the concentration of synaptic blockers, or switching picrotoxin for bicuculline.

A) THs were observed despite increases in synaptic receptor agonist concentrations, with picrotoxin and strychnine increased to 500% (50µM) and 200% (10uM) respectively (see arrow for single TH). B) THs were observed ten minutes after a switch from picrotoxin (10 µM) to bicuculline (10 µM) (see arrow for single TH). The current command in (A) was changed from -36 pA to -23 pA, and the current pulse amplitudes started at -75 pA and increased in 10 pA steps in (B).

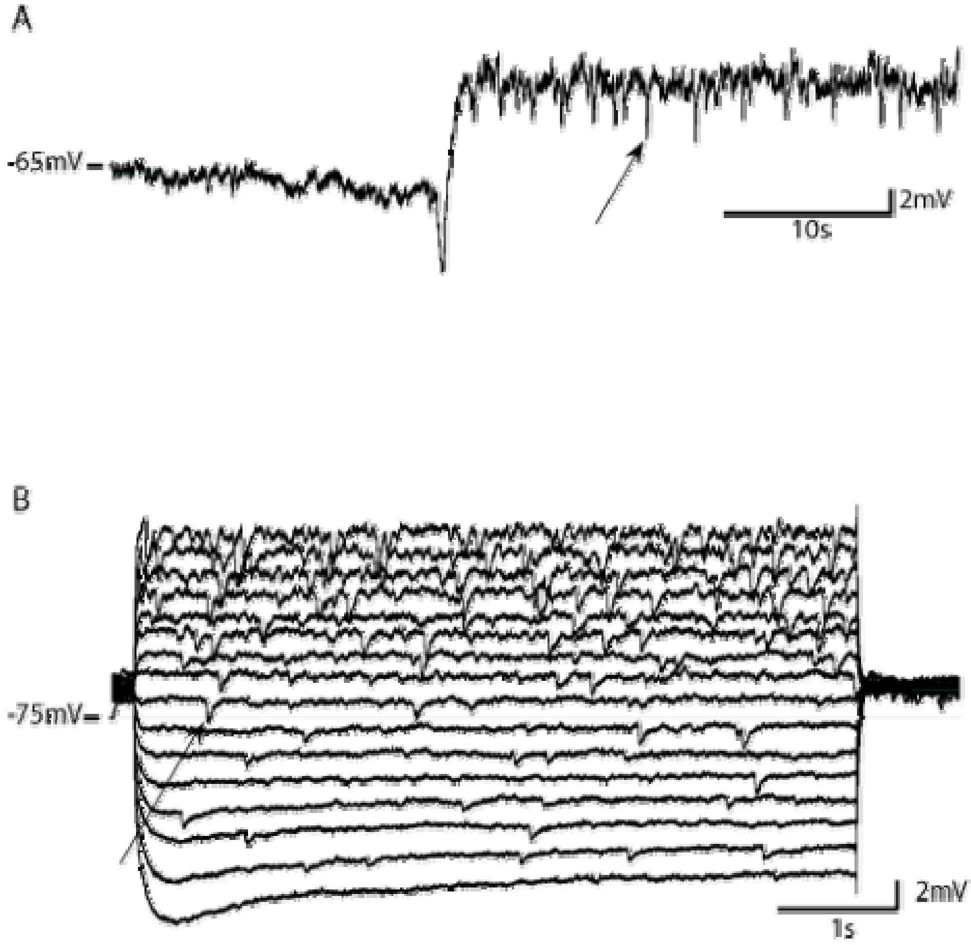
A
-65mV
2mV
10s
B
-75mV
2mV
1s

Figure 5.12 The transient hyperpolarizations are insensitive to voltage gated sodium channel blockade by TTX.

A) Sodium mediated spikes and THs are observed under control conditions (arrow indicates one example TH). B) Spikes are blocked by TTX application, while the hyperpolarizations remain (arrow indicates one example TH). Again, hyperpolarizing events are observed below the chloride equilibrium potential (-74.2 mV), at -81 mV (bottom trace in B). Current command amplitudes for (A) were from 20 pA to 80 pA in 20 pA steps, and from -100 pA to 350 pA in 50 pA steps in (B).

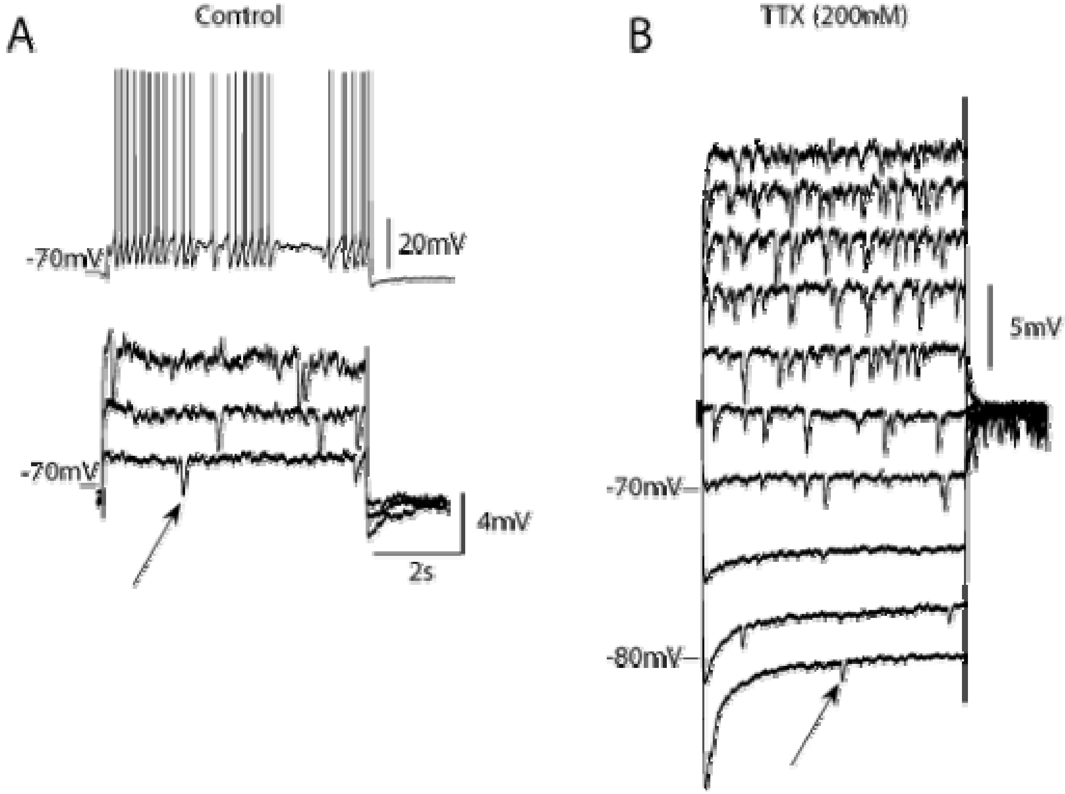
A
Control
20mV
-70mV
-70mV
4mV
2s
B
TTX (200nM)
5mV
-70mV
-80mV

THHs. This last conclusion corroborates with previous evidence suggesting that synaptic activity is not responsible for THs.

Since the reversal potential of the hyperpolarizations is inconsistent with that of the chloride ion and an outward current is likely, we investigated the role of potassium conductances as a mechanism of THs. We investigated the contribution of potassium inward rectifier current (KIR) given that KIR/Ih mediated hyperpolarizations have been observed in acetylcholinergic neurons of the striatum, and have a similar time scale as the THs observed here (Wilson 2005). However application of the KIR blocker, barium (Ba^{2+}), did not abolish THs (Figure 5.13A), nor did the application of the Ih blocker, caesium (Cs^{+}) (not shown).

Other potassium conductances that operate on a sufficiently fast time scale include the SK (calcium activated potassium channel), and its involvement is suggested from the similarity in time course between the AHP and the TH (Figure 5.3B). We propose that blockade of all voltage gated calcium channels with a broad spectrum blocker, cadmium (Cd^{2+}), should hinder the activation of SK, as observed elsewhere (Abel et al. 2004; Maher and Westbrook 2005), and hence affect THs. However the application of Cd^{2+} did not abolish THs (Figure 5.13B), suggesting that if SK activation is responsible for THs, they are not activated by influx of calcium from the extracellular space. This is consistent with the observation of THs despite the absence of a voltage deflection large enough to open these voltage gated calcium channels. One further possibility, SK activation via calcium release from intracellular stores (i.e. the endoplasmic reticulum) was not investigated, however possible, as observed elsewhere in

Figure 5.13 Transient Hyperpolarizations are insensitive to both KIR blockade with barium, and calcium channel blockade with cadmium.

THs were observed in excess of five minutes following application of either the inward rectifier blocker Ba^{2+} (200 μM) (A), or the broad spectrum calcium channel blocker Cd^{2+} (50 μM) (B). The relationship between event frequency and mean membrane voltage also remains in the presence of Cd^{2+}. The current-clamp command in (A) was -35 pA, and pulses with amplitudes -75 pA to +65 pA in 10 pA steps were used in (B). Single examples of THs are indicated with arrows.

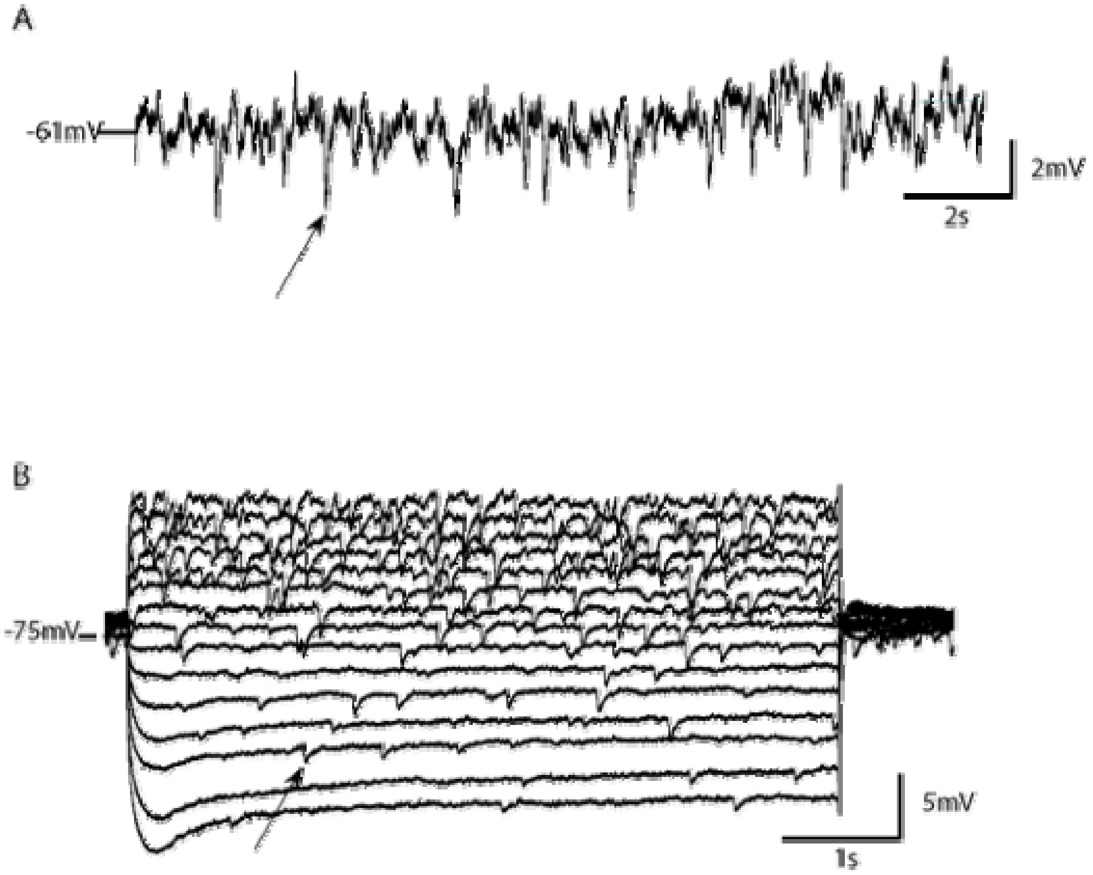
A
-61mV
2mV
2s
B
-75mV
5mV
1s

the mammalian brain (Fiorillo and Williams 2000; Morikawa et al. 2003; Gulledge and Stuart 2005; Hagenston et al. 2007).

We restricted our investigation of the involvement of voltage or calcium gated ion channels as to whether or not it was possible to abolish THs. We did not attempt to quantify the effect of drug application on TH amplitude or frequency because TH amplitude was observed to decrease in control conditions over the 10 or so minutes necessary to test the affect of ion channel blocking agents. We attribute this run down to a decline in cell health during this time, as ICC neurons proved less resilient to whole cell recording than neurons of the cortex, hippocampus, and cerebellum. In a project unrelated to the one described in this manuscript, the time span over which healthy recordings could be obtained was considerably longer (>30 minutes) for cortical neurons in old mice (three month old); suggesting that the short life time of whole cell recordings in ICC neurons is not due to unfavourable condition by way of reagents, equipment, or experimenter.

5.2.4 Mechanism of Spikelets

5.2.4.1 Voltage Gated Ion Channels: A Mechanism for Spikelets?

The initial fast depolarization present in the spikelet suggests the activation of voltage gated sodium channels. The subsequent hyperpolarization present in the spikelet suggests the activation of the same unknown outward current as that responsible for the TH (Figure 5.10B). Blockade of voltage gated sodium current by TTX (200 mM) abolished both action potential generation and spikelets (Figure 5.14). Unfortunately, the presence of spikelets upon washout could not be ascertained, as is necessary to rule out rundown of a different conductance mediating the spikelets.

Figure 5.14 Spikelets are abolished following blockade of voltage gated sodium channels by TTX.

A) Spikelets were observed in control conditions (one example indicated by arrow). B.) Spikelets were not observed following application of TTX (200 μM). In (A) current pulse amplitudes started at 0 pA with 10 pA intervals in, and started at 20 pA with 20 pA intervals in (B). Sufficient blockade is indicated by the absence of action potential generation in (B), which were otherwise observed when the membrane potential exceeded that of the most depolarized trace in (A).

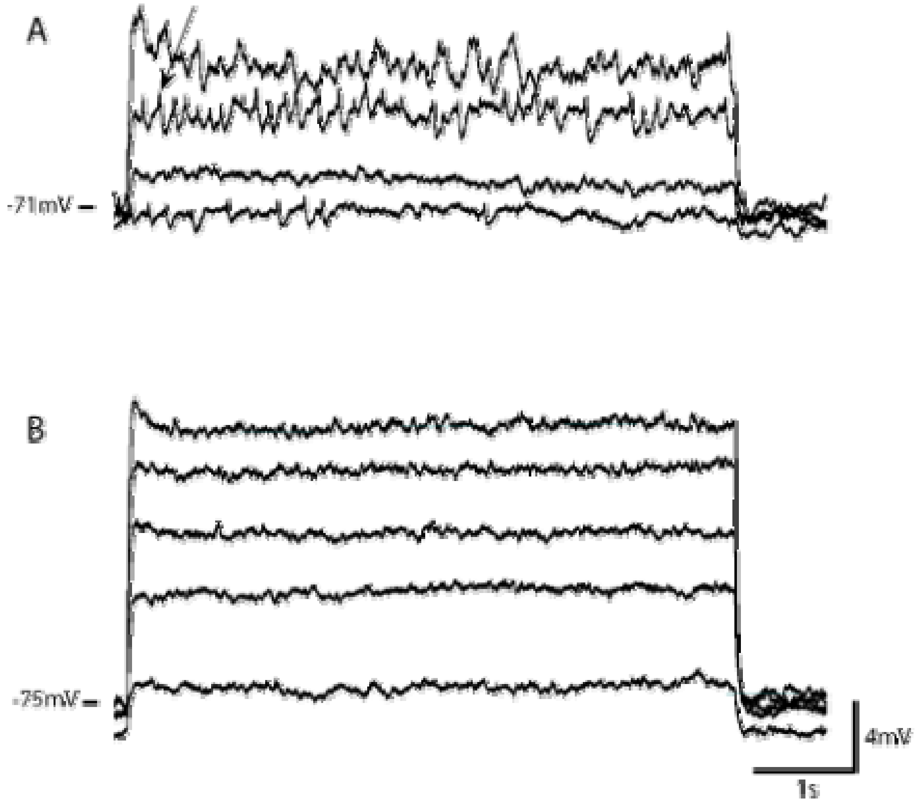
A
-71mV
B
-75mV
4mV
1s

Given that the spikelets did not assume the TH waveform upon blockade of voltage gated sodium current, indicates a difference between neurons that exhibit THs versus those that exhibit spikelets. Where THs were observed in the presence of TTX in neurons that exhibited THs (Figure 5.12B), spikelets do not simply become THs upon TTX application. Instead, it appears that the initial depolarization is required for the hyperpolarization to appear. If calcium induced activation of SK channels is responsible for THs, and the hyperpolarizing phase of the spikelet, this dependence on voltage gated sodium channels suggests a very different source of calcium than the one creating THs, possibly through voltage-gated calcium channels. Alternatively, spikelets may result from action potential generation in neighbouring neurons and communicated to the cell in question via gap junctions (Sohl et al. 2005); however the correlation of event frequency with membrane potential suggests that the mechanism of the spikelets is intrinsic to the neuronal membrane that they are recorded from.

5.3 Summary of Results

The uniform shape of THs distinguishes them from subthreshold oscillations. Both the TH amplitude and the event frequency are dependent on mean membrane potential, where the amplitude relationship indicates a reversal potential similar to that of the potassium equilibrium potential, and event frequency correlates positively with mean membrane potential. THs are observed amongst all firing response type neurons, but are most common in the accelerating response type neuron.

The mechanism underlying THs most likely does not involve an ionotropic postsynaptic receptor, given a lack of quanta in the amplitude and initial slope, an insensitivity to action potential propagation blockade by TTX, a dependence on a small range of post-synaptic membrane potentials, and a reversal potential more hyperpolarized than the chloride equilibrium potential. Instead, the involvement of SK channels is suggested by the similarity of the TH wave form with the AHP following an action potential. However, interference of the calcium influx from the extracellular space by Cd^{2+} application was unable to abolish THs, suggesting that SK activation, if involved, occurs via calcium release from intracellular stores. Unfortunately, the direct involvement of SK channels was not tested at this time. An alternative mechanism generating similar voltage dependent spontaneous hyperpolarizations due to hyperpolarization activated KIR channels (Wilson 2005) was rejected by TH insensitivity to Ba^{2+}.

Few neurons exhibited spikelets. However spikelets share properties with THs, including the positive correlation between event frequency and the membrane potential, and a similar time course. However TTX sensitivity is limited to spikelets, suggesting that voltage gated sodium channels are involved in spikelet generation. This suggestion is also supported by the spikelet’s rapid initial depolarization.

5.4 Discussion

The occurrence of individual THs was largely stochastic. However, a positive correlation between TH event frequency and the mean membrane potential was observed, and suggests an influence of the membrane potential on TH generation. Moreover there are clear distinctions between THs and membrane potential oscillations (chapter three), namely the nearly identical shape of the TH. THs are present in previous reports of current-clamp recordings (see Figure 9A of (Peruzzi et al. 2000)), however these studies paid no attention to the event, mostly likely dismissing them as un-antagonized postsynaptic inhibitory potentials.

5.4.1 Mechanism of Transient Hyperpolarization Generation

From the evidence presented, it is unlikely that a postsynaptic ionotropic receptor is involved in TH generation. Specific evidence includes: a reversal potential lower than the chloride equilibrium potential, a lack of quanta in the distribution of amplitude or slope, insensitivity to action potential blockade by TTX, and insensitivity to blockade of voltage gated calcium channels with Cd^{2+}. Additionally, the mechanism underlying hyperpolarizations in striatal cholinergic interneurons (Wilson 2005) was ruled out by TH insensitivity to Ba^{2+} and Cs^{+}, the respective KIR and I_h blockers. Instead, the involvement of SK in TH generation is indicated by evidence of a potassium conductance responsible for the hyperpolarization, and the similarity in time course between the TH and the AHP. Additionally, BK involvement is possible, either alone or in concert with SK activation.

The TH wave form is similar to that of the spontaneous miniature outward currents (SMOCs) observed in other neurons (Cui et al. 2004), or the homologous spontaneous transient outward currents (STOCs) in muscle cells (Bolton and Imaizumi 1996). Activation of calcium-activated potassium channels by calcium induced calcium release (CICR) via the ryanodine receptor is a common mechanism underlying SMOCs. Specifically, activation of SK is responsible for SMOCs in midbrain dopamine neurons (Cui et al. 2004), and Meynert neurons (Arima et al. 2001); whereas, activation of the big conductance calcium-activated potassium channel (BK) is responsible for SMOCs in retinal amacrine cells (Mitra and Slaughter 2002; Mitra and Slaughter 2002), presynaptic nerve terminals in the chick ciliary ganglion (Fletcher and Chiappinelli 1992), dorsal root ganglion neurons (Mathers and Barker 1981; Mathers and Barker 1984), and mudpuppy parasympathetic cardiac neurons (Merriam et al. 1999; Scornik et al. 2001; Parsons et al.

2002). The correlation between SMOC event frequency and the mean membrane potential is an additional similarity between SMOCs and THs, and this correlation is observed regardless of the type of calcium-activated potassium channel responsible for SMOC generation (Satin and Adams 1987; Merriam et al. 1999; Arima et al. 2001; Mitra and Slaughter 2002).

As an alternative to CICR via the ryanodine receptor, internal calcium release might involve activation of the inositol triphosphate (IP3) receptor; however, this possibility has not been observed in SMOC generation. Nevertheless, SK mediated fast hyperpolarizations are known to occur, via the IP3 receptor mediated internal calcium release, upon focal activation of either the metabotropic glutamate receptor (Morikawa et al. 2003; Hagenston et al. 2007), or the metabotropic M1-type muscarinic acetylcholine receptor (mACh) (Fiorillo and Williams 2000; Gulledge and Stuart 2005). Specifically, activation of the muscarinic acetylcholine receptor is known to activate SK by release of internal calcium via the IP3 receptor. The cascade following activation of mACh occurs as follows: activation of the G-protein G_q, activation of phospholipase C, production of inositol triphosphate (IP3), and release of calcium from internal stores via the IP3 receptor (Fiorillo and Williams 2000; Gulledge and Stuart 2005). Since muscarinic acetylcholine receptors were not antagonized during our study, we explore the possibility that TH generation arises from muscarinic acetylcholine receptor activation.

Synaptic release is blocked, for the most part, following blockade of action potential generation by TTX; nevertheless, spontaneous release is still possible, and these events are referred to as action potential independent miniature postsynaptic events (minis). However, the application of the broad spectrum voltage gated calcium channel

(VGCC) blocker Cd^{2+} is known to inhibits mini events, by reducing their event frequency (Schoppa and Westbrook 1997; Bao et al. 1998; De Lorenzo et al. 2006). The role of muscarinic acetylcholine receptor activation in TH generation is therefore tenuous, as only low frequency synaptic release events were available for muscarinic acetylcholine receptor activation. Nevertheless, muscarinic synaptic communication is possible in the IC, as indicated by the presence of acetylcholine containing axonal fibers (Tatehata et al. 1987; Henderson and Sherriff 1991; Raza et al. 1994), and mACh receptor expression (Schwartz et al. 1982; Cortes et al. 1984; Regenold et al. 1989; Morley and Happe 2000). Additionally, the mACh receptor might confer the voltage sensitivity necessary to explain the correlation between event frequency and mean membrane potential, as depolarization is known to increase acetylcholine (ACh) affinity of the M1 mACh receptor (Ben-Chaim et al. 2006; Parnas and Parnas 2007). Regardless, we attempt to explain TH generation with another simpler mechanism involving CICR.

The similarity of wave form shape between THs and SMOCs suggests that the mechanism behind TH generation is similar to that responsible for SMOC generation. Spontaneous activation of the ryanodine receptor and subsequent activation of SK or BK via CICR is the mechanism behind SMOC generation. This mechanism offers a simpler alternative to explain TH generation in comparison to a mechanism requiring mACh activation. The frequency of SMOC events is modulated by cytoplasmic calcium level, which is influenced by calcium influx via voltage gated calcium channels, as observed in SMOCs (Mathers and Barker 1981; Mathers and Barker 1984; Fletcher and Chiappinelli 1992; Merriam et al. 1999; Scornik et al. 2001; Mitra and Slaughter 2002; Mitra and Slaughter 2002; Parsons et al. 2002). Modulation of spontaneous CICR is likely the mechanism behind the observed positive correlation between TH event frequency and membrane potential, where depolarization increases the activation of VGCCs thereby increasing the cytoplasmic calcium level. This is a realistic proposal given the assortment of high voltage activated calcium channels (L,N,P,Q, and R-type) expressed in ICC neurons (N'Gouemo and Morad 2003). Broad spectrum VGCC blockade by Cd^{2+} application does not abolish SMOC generation (Arima et al. 2001), instead a reduction in event frequency is observed following Cd^{2+} application, further indicative of VGCC's modulatory role in SMOC generation. Likewise, VGCC blockade by Cd^{2+} does not abolish TH generation. Unfortunately, the affect of Cd^{2+} on TH event frequency was not investigated. Nevertheless, the similarities between SMOCs and THs suggest that they are one in the same, and we propose further experimentation to confirm this conclusion.

5.4.1.1 Proposed Experiments to Determine the Mechanism of TH Generation

The hypothesis of SK or BK involvement in TH generation is testable. The expression of SK channels in the ICC is known from an apamin competitive binding assay (McCown and Breese 1990), and the effect of apamin on AHP amplitude and shape during intracellular recording (Ono et al. 2005). The involvement of SK in TH generation should be tested by application of apamin (1-10 μM), where involvement would be indicated by an abolishment of TH generation. Additionally, it might be possible to augment the TH amplitude by application of 1-ethyl-2-benzimidazolinone (EBIO) (1 mM), which prolongs SK open time and increases calcium sensitivity (Olesen et al. 1994; Pedarzani et al. 2005). Conclusions drawn from the apamin experiments should be made with caution, given that apamin-resistant SK subtype (SK1) might be expressed in rat ICC, as is known in the case of the mouse IC (Sailer et al. 2004). Therefore to fully explore the contribution of SK channels to TH generation, blockade of SK1 should also be attempted with high concentration bicuculline methiodide (>100 μM) (Strobaek et al. 2000).

Like SK, BK expression is indicated by pharmacological blockade. Change in AHP shape following iberiotoxin application suggests BK expression in ICC neurons (Ono et al. 2005). The involvement BK activation in TH generation would be indicated by abolishment of TH generation following application of either BK specific blockers iberiotoxin (100 nM) (Mitra and Slaughter 2002), or charybdotoxin (100 nM) (Sah 1996). Similarly, high concentrations of broad spectrum potassium channel blockers tetraethylammonium (TEA, 1 mM), or Ba^{2+} (1 mM) could also be used (Mathers and Barker 1984).

Assuming either BK or SK activation is responsible for TH generation, a question remains as to how SK channels are activated, or more specifically, what is the identity of the calcium source responsible for activation. Blockade of voltage gated calcium channels with Cd^{2+} is known to affect the size and amplitude of the SK mediated AHP following an action potential in the IC (Ono et al. 2005). However, blockade of the external calcium source with Cd^{2+} does not abolish THs, even after 15 minutes of bath application. Therefore we suggest that Ca^{2+} involved in BK or SK activation must arise from internal Ca^{2+} release instead. To test this possibility, the effect of internal calcium store depletion on TH generation should be investigated. This depletion might be brought about by inhibition of endoplasmic reticulum calcium ATPases including thapsigargin (1 μM), or cyclopiazonic acid (CPA) (30 μM) (Gordon et al. 2005; Gulledge and Stuart 2005). Additionally, it might be possible to identify the receptor responsible for internal calcium release, of which there are two options, the IP3 receptor or the ryanodine receptor (Emptage et al. 1999; Ross et al. 2005). To test the involvement of these receptors, 2-aminoethoxydiphenyl borate (2-APB) (100 μM), or ryanodine (10 μM) could be applied, which block IP3 and ryanodine sensitive stores, respectively (Lohmann et al. 2002). Also, the involvement of the ryanodine receptor might be indicated by an increase in TH event frequency following application of caffeine, which is an agonist of the ryanodine receptor (Mitra and Slaughter 2002).

The identity of the internal calcium release receptor indicates the initial stage involved in TH generation. If the ryanodine receptor is implicated in internal calcium release, then CICR is implicated, with calcium influx from the extracellular space as the initial stage of TH generation. This calcium influx might occur via VGCCs, or ligand gated channels such as the NMDA receptor, or the calcium conducting variant of the AMPA receptor (Tempia et al. 1996). Calcium influx via ionotropic glutamate receptors was ruled out, because both receptor types were antagonized during our study. However, the role of VGCCs in providing calcium influx should be investigated in regard to TH generation. Application of the broad spectrum calcium channel blocker Cd^{2+} should decrease event frequency as observed in the case of SMOCs; and more specifically, the individual role of each of the many high voltage activated calcium channels could be determined with further pharmacological blockade (N'Gouemo and Morad 2003).

In contrast, implication of the IP3 receptor in internal calcium release indicates IP3 production via activation of the catalyst phospholipase-C. However, since there is no specific phospholipase C inhibitor (Mogami et al. 1997), we can only test the involvement of its upstream activators in TH generation. As mentioned previously, the mACh receptor was not antagonized during our experiments, and the M1-type mACh receptor represents a possible mechanism of phospholipase C activation by activation of the G-protein G_Q. The role of G-protein activation in TH generation can be tested by dialysis of the internal pipette with the inactive guanosine diphosphate (GDP) analog guanosine-5’-*O*-(2-thiodiphosphate) (GDP-β-S) (Xie et al. 1999). Likewise the role of the M1-type mACh receptor can also be investigated by application of the antagonist atropine (10 μM) or pirenzepine (500 nM) (Gulledge and Stuart 2005).

The mechanism that ensures discrete TH events is unknown. The calcium source responsible for BK or SK activation must be transient in order to produce discrete TH events. However, we cannot at this time propose any specific mechanism as to how this occurs.

5.4.2 The Functional Role of Transient Hyperpolarizations

The positive correlation of TH event frequency with mean membrane potential suggests a form of feedback, which may contribute to the computational ability of ICC neurons. This correlation may provide a form of inhibitory feedback, where an increase in hyperpolarizing events following a prolonged transient depolarization might reduce the occurrence of spiking. This is suggested by the similarity of the TH to the hyperpolarization observed at the onset of the pulse response in the accelerating response type neuron (Figure 3.38B), where the hyperpolarization appears to inhibit or delay subsequent spiking. Recall in case of the accelerating response type, this hyperpolarization at spike onset causes a jump in latency and creates a longer first interspike interval (ISI) than those that follow.

TH induced interruption of spiking was never observed, suggesting that THs do not necessarily modulate spiking, but might have an effect on spiking by interaction with synaptic input. Specifically, THs may facilitate spiking by transiently hyperpolarizing the membrane, thereby facilitating anode break excitation, a response provided by the Andronov Hopf (AH) bifurcation, and the slow accommodating currents I_h and I_{CaLVA}, as discussed in chapter three. Likewise, a smaller hyperpolarization can facilitate spiking in response to a subsequent depolarization, a phenomenon referred to as post-inhibitory facilitation (Dodla et al. 2006). Consistent with this, we occasionally see THs preceding spiking, with the spike coming off of the decay phase of the TH.

5.4.3 Spikelets: Mechanism

The difference between spikelets and THs is evident following TTX application. THs are resistant to sodium channel blockade by TTX, whereas spikelets are not. The major difference between the spikelet and the TH is a fast upward depolarization at the beginning of the spikelet waveform that is not present in the TH. The speed of this depolarization suggests involvement of voltage gated sodium current. Therefore, upon TTX application, this fast depolarization is most likely blocked, along with the entire spikelet waveform. The hyperpolarized portion of the waveform is present, and highly similar, in both spikelets and THs. Nevertheless, TTX application does not simply convert spikelets into THs, suggesting that this fast depolarization is required for recruitment of the hyperpolarized portion of the spikelet waveform, and that the mechanism underlying THs and spikelets are not equivalent. Whether or not the hyperpolarized portions of the spikelet and TH waveforms have a conserved mechanism is unknown, and the possibility of SK involvement in the hyperpolarized portions of the spikelet should be investigated with apamin and bicuculline methiodide.

Spikelets are observed elsewhere, and are thought to be due to action potential generation in a neighbouring neuron, where the membrane potential of this neighbour is communicated to the recorded cell in question via gap junctions (Hughes et al. 2002; Heister et al. 2007). Other spikelets appear to arise from a spike initiation zone at a distance from the soma in the dendrite (Pinato and Midtgaard 2005). It may be impossible to sort out the specific source of spikelets in the brain slice preparation due to the rarity of these events in this preparation. The greater occurrence in vivo and the greater number of inter-neuronal connections available in vivo suggests that large quantities of inter-neuronal connections are required for spikelets to occur. Alternatively, the absence of spikelets in the brain slice preparation might reflect a disruption of extracellular signalling that is present in the intact brain in vivo. Therefore it might be possible to induce spikelets with the application of carbachol, as observed in the subcoeruleus nucleus (Heister et al. 2007).

5.4.4 Spikelets: Functional Role

The role of spikelets in the mammalian brain is still uncertain, however when spikelets are the result of inter-neuronal communication via gap junction connections, spikelets might be involved in synchronization of spiking between neurons (Fuentealba et al. 2004). The positive correlation between spikelet frequency and mean membrane voltage is also observed in the lateral geniculate nucleus (Hughes et al. 2002), where gap junctions are thought to be responsible.

Chapter Six: General Discussion

6.1 Overview

In this study, we obtained whole cell *in vitro* recordings in order to investigate subthreshold and spiking responses in ICC neurons. We began by classifying neurons based on their spiking response types, and subsequently investigated spiking and subthreshold membrane responses in order to determine the type of fixed point bifurcation. This description offers insight into the interactions of the fast non-linear elements (e.g. fast voltage gated conductances: I_{Na} and I_K) that govern subthreshold and spiking responses and provides a basis for constructing conductance models of these neurons. The type of fixed point bifurcation predicts certain response properties of the neuron. If the cell loses stability and begins to spike through an Andronov-Hopf bifurcation, the membrane filters synaptic currents, and exhibits a bi-directional phase response to spiking.

In addition to spiking and oscillations, transient hyperpolarizations (THs) were also observed. THs are observed as discrete small amplitude hyperpolarizing events, which are apparently intrinsic to the membrane and may perform a yet unknown computation by interaction with synaptic inputs. The ionic mechanism underlying these events remains to be determined; however, they may be mediated by a calcium activated potassium conductance.

Additionally, a second type of discrete subthreshold event was observed, the spikelet. Similar to the TH in many ways, the initial depolarization in its waveform and its sensitivity to voltage gated ion channel blockade by TTX distinguishes the spikelet from the TH. Spikelets are more prevalent in *in vivo* recordings, and might involve inter-neuronal synchronization in the ICC.

Unfortunately, we were unable to correlate neuronal morphology with spiking response types. Out of twenty-three biotin filled neurons, we were unable to detect any distinguishing morphological features amongst neurons grouped according to their firing response type, or other response features such as resonance or transient hyperpolarizations. Due to biotin labelling of adjacent vasculature (Appendix A) we were unable to obtain the 90º rotations necessary to classify dendrite morphology into the generally accepted flat versus less-flat categories.

6.2 Firing Responses and the Governing Ion Channel Dynamics

ICC neurons were separated into four firing response types—onset, adapting, accelerating, and constant—according to spiking responses to depolarizing current clamp pulses. Regardless of the spiking response, the membrane voltage responses were those of a system that exhibits an Andronov-Hopf (AH) fixed point bifurcation (Strogatz 2000; Izhikevich 2007), where the type of fixed point bifurcation is determined by dynamic interactions between fast voltage gated currents (i.e. I_{Na} and I_K). The indicative membrane voltage responses include a minimum tonic spiking frequency, a monotonic steady state current-voltage relationship, bistability between the rest and spiking states, the presence of subthreshold oscillations, and the absence of long first spike latency following a smooth monotonic voltage trajectory. This finding contradicts our hypothesis that different firing response types observed in the ICC are the result of different fixed point bifurcation types. Alternatively, we suggest that the different firing response types result from differences in expression of slow accommodating currents, such as I_h, and currents arising from voltage gated calcium channels.

The type of fixed point bifurcation provides predictions of the neuronal response to different types of stimuli. Specifically, the presence of an AH bifurcation predicts the ability of small perturbations to advance or delay spikes in a tonic spiking train of action potentials depending on when the perturbation is delivered in relation to the spiking cycle (Hansel et al. 1995; Ermentrout 1996; Izhikevich 2007). In other words, we expect ICC neurons should exhibit the potential for both a positive and negative phase reset depending on when the perturbation of the membrane potential is delivered in relation to the tonic spiking period. This prediction remains to be tested, and is difficult to test in a high noise situation (Reyes and Fetz 1993; Ermentrout 1996); however certain techniques employing weak broadband stimuli could be used to quickly and effectively measure the phase-resetting curve (Kuramoto 1984; Galan et al. 2005).

The fast transient spiking observed in the ICC neurons *in vivo* following afferent auditory stimulation indicates the importance of the burst spiking response. Tonic spiking in response to current clamp pulses does not exceed 50-60 Hz regardless of *in vivo* or *in vitro* conditions (Sivaramakrishnan and Oliver 2001; Tan et al. 2007), whereas *in vivo* afferent stimulation with monaural tones, or binaural tones (with or with out interaural time difference) exhibit much larger instantaneous spiking frequencies in the range of 100-350 Hz (Kuwada et al. 1997; Sterbing et al. 2003; Sivaramakrishnan et al. 2004). Fast burst spiking *in vitro* in the range from 100-350 Hz, is observed only in response to fast large amplitude deflections of the membrane potential, and is distinct from the tonic firing spike frequency, which does not exceed ≈50 Hz. A formal investigation of the burst response was not conducted in this study; however we note that it was typically observed in onset and strong adapting response type ICC neurons. The ability to respond with either a burst or tonic response is important, as it is known elsewhere to provide a means of segregating two parallel and complementary streams of information transfer in a single spike train (Oswald et al. 2004). This proposed segregation could be investigated in the ICC by investigating superthreshold responses to broadband stimuli, namely the low pass filtered Gaussian white noise, which we employed to investigate resonance. Additionally, the underlying ionic mechanism of the burst response should also be investigated, so that we might gain some insight as to whether or not it might be regulated, and to any possible functions it may contribute to coding in the ICC.

Essentially, the method used here to identify the neuronal response of the ICC neurons goes beyond simply counting spikes in response to a current-clamp pulse. Instead we attempt to describe the neuronal responses in such a way that we can predict responses to all forms of stimuli. With the final goal being an understanding of how processing of auditory information is achieved at the level of the IC, these neuronal models might be useful in explaining the function of the system as a whole. The information collected here to determine the fixed point bifurcation provides a large number of constraints which will improve the accuracy of modelling, most specifically, the interaction between the steady-state activation profiles of the voltage gated sodium and potassium currents.

6.3 Temporal Filtering and Resonance

We examined frequency selectivity by way of subthreshold resonance, and we attribute ICC neuronal frequency selectivity to two distinct mechanisms; namely, a slow accommodating current (I_h), and the non-linear dynamics provided by faster sodium and potassium currents under the condition of an AH bifurcation. These two mechanisms work synergistically, as they provide similar frequency selectivity, yet they are separable by the voltage range over which they are active, where the former mechanism involving I_h operates at more hyperpolarized potentials than the mechanism provided by the AH bifurcation.

The AH bifurcation confers frequency selectivity by providing a spiral voltage trajectory due to the imaginary component of the eigenvalues of the fixed point. Since this voltage trajectory is reliant on both sodium and potassium dynamics, the resonant response at depolarized potentials is sensitive to blockade of voltage gated sodium current by TTX. Additionally, this mechanism can also be responsible for subthreshold oscillations of the membrane potential, where the intrinsic noise, provided by channel flicker (White et al. 2000; Dorval and White 2005), is filtered by the spiral trajectories to produce oscillations of the membrane potential at a frequency similar to the resonant frequency. The involvement of noise was not tested directly in this study, however its involvement in oscillations has been demonstrated in the entorhinal layer 2 stellate neuron, which exhibits a great deal of similarity to ICC neurons, especially an AH bifurcation (Dorval and White 2005). Additionally, it should be possible to disrupt this frequency selectivity (both resonance and oscillation) by blocking voltage gated potassium channels with the broad spectrum potassium channel blocker TEA. Further pharmacological interventions might indicate the identity of the potassium channel involved, where application of alpha-dendrotoxin might indicate the involvement of a low threshold potassium current, like that provided by the delayed rectifier (Kv1.x) channel.

In contrast, the mechanism of resonance at hyperpolarized potentials is dependent only on a single resonant current, I_h, as indicated by its sensitivity to Cs^+. Being an outward current activated by hyperpolarization, where the voltage of half maximal activation is lower than the reversal potential, I_h provides resonance by attenuation of low frequency inputs that are slow enough that I_h can adjust its gating and track the deflections of the membrane potential in a compensatory manner.

Membrane potential oscillations and resonance has been described in other regions of the brain (Crawford and Fettiplace 1981; Puil et al. 1986; Strohmann et al. 1994; Hutcheon et al. 1996; Kim and Chung 1999; Ulrich 2002; Antal et al. 2006), however their functional role in these brain regions is for the most part speculative. In the case of the ICC however, we are certain that most responses arise in response to auditory stimulation. This offers an opportunity to determine how oscillations, resonance, and the type of fixed point bifurcation contribute to sensory processing. Mitral cells of the olfactory system might also provide a substrate to investigate the role of oscillations and resonance in processing sensory information (Galan et al. 2005; Antal et al. 2006; Galan et al. 2006; Galan et al. 2006; Izhikevich 2007), however a great deal more is known of temporal response patterns to afferent stimulation in the case of the auditory system. In contrast, the role of layer 2 entorhinal stellate neurons in brain function is somewhat more elusive, although, the resonance frequency exhibits a spatial gradient, to which an attempt has been made to associate functional implications of grid cell responses (O'Keefe and Burgess 2005; Giocomo et al. 2007).

6.4 Spontaneous Stochastic Events in ICC Neurons (Transient Hyperpolarizations, and Spikelets)

Both THs and spikelets are largely stochastic events that exhibit a positive correlation between event frequency and the membrane potential. Both event types are distinct from subthreshold oscillations, by their discrete and relatively invariant waveform.

In the case of THs, potassium is likely the ion directly responsible for the hyperpolarization. The spontaneous nature of TH events and the large voltage range over which they are observed suggest the involvement of calcium activated potassium conductances via SK or BK following Ca^{2+} release from internal stores. These possible mechanisms need to be explored. We can test whether SK or BK are specifically involved with toxins specific to BK and SK (e.g. charybdotoxin, and apamin respectively).

Additionally, the source of calcium necessary to activate BK or SK remains to be determined, and is thought to be the result of calcium induced calcium release from the endoplasmic reticulum. These proposed components of TH generation are those of spontaneous miniature outward currents, observed in a handful of other neurons (Mathers and Barker 1981; Mathers and Barker 1984; Fletcher and Chiappinelli 1992; Merriam et al. 1999; Arima et al. 2001; Scornik et al. 2001; Mitra and Slaughter 2002; Parsons et al. 2002; Cui et al. 2004), where calcium is spontaneously released from internal calcium stores via the ryanodine receptor, and activates either SK or BK. The frequency of the internal calcium release is augmented by calcium influx from the extracellular space via voltage gated calcium channels.

The exact role of THs in the auditory response remains to be determined, with our suggestion that they may provide hyperpolarization of the membrane sufficient to encourage burst firing in response to excitatory synaptic potentials. Most importantly, the demonstration of THs *in vivo* is also important, to ensure that they are not simply an artefact resulting from poor cell health. We feel this is unlikely however, as THs tend to dissipate towards the end of long recordings, when cell health is deteriorating.

Spikelets differ from THs, by a small initial upward (depolarizing) deflection in the waveform, which is thought to be mediated by voltage gated sodium channels. Blockade of these channels by TTX affects not only this initial deflection, but the entire event altogether, suggesting that the initial deflection is mediated by sodium current, and that this deflection elicits the subsequent hyperpolarizing phase of the spikelet. The exact role of spikelets in auditory processing remain to be determined, however they indicate communication between neurons, possibly via gap junctions. The involvement of gap junctions might be difficult to ascertain given the lack of specific pharmacological blockers. Nevertheless, it might be possible to increase the prevalence of spikelets following application of neuromodulators like carbachol (Heister et al. 2007).

6.5 Association of Neurochemistry to Firing Response Types

In order to gain a full appreciation of the role of the ICC as an integrative center of auditory information, a correlation between the neurochemistry and firing response type is needed. The neurochemistry of the ICC is relatively simple, where the majority of neurons are either GABAergic or glutamatergic (Winer and Schreiner 2005). Nevertheless, neither our study, nor other reported studies have been able to correlate firing response with neuronal morphology (Oliver et al. 1991; Peruzzi et al. 2000). As such, it has not been possible to identify the neurochemistry of ICC neurons in relation to their firing phenotypes via the intermediate of morphological identity. The lack of distinguishing morphological features in these intracellular studies might be due in part to the young age of the animals, where mature cellular morphology is not attained elsewhere in the brain until well after post natal day 17, as in the case of the cerebellar purkinje cell (McKay and Turner 2005), which corroborates with the onset of hearing at post natal day 14 (Winer and Schreiner 2005). Additionally, a correlation of firing response with expression of the enzyme necessary for GABA production has been unsuccessful (Ono et al. 2005), which may not be surprising given the diversity of neuronal morphologies that are immunoreactive for GABA in the adult (Oliver et al. 1994). Instead, such correlations will likely occur via identification of specific ion channel expression in relation to a spiking response type, which will serve as an extracellular label that can be co-localized with both a membrane potential response and the neurochemistry of the neuron, as has been achieved in the case of GABAergic neurons of the deep cerebellar nucleus (Molineux et al. 2006). It is therefore essential to have a detailed knowledge of ion channel expression in these neurons in relation to membrane potential responses of ICC neurons.

The biotin labelling of vasculature in the ICC we observed is unusual, because the histological techniques employed here did not label vasculature in other brain regions such as the cerebellum or deep cerebellar nuclei (McKay and Turner 2005; Molineux et al. 2006). Further, there is an absence of endogenous biotin in the IC, as observed in fixed tissue (McKay et al. 2004). Instead, we propose that high affinity biotin receptors exist on either the vasculature or the astrocytic end feet that cover the vasculature, and binds biotin released from the patch electrode. The release of biotin from the patch electrode is inadvertent, and occurs before the whole cell configuration is achieved. This release is effectively a focal application of biotin, and vascular labelling was typically limited in area to within 1 mm proximity to the recorded neuron. However, this binding process only occurs while the tissue is alive, but not fixed (McKay et al. 2004), possibly because the biotin is sequestered by an active mechanism. We do not believe that this observation is an artefact of the histological method, because the labelling reaction is simple with an avidin-conjugated fluorophore, which obviates cross reactivity that might be inherent in antibody mediated labelling. Additionally, the vascular labelling was observed for most neurons and was reproducible across many different batches of histological processing. As to the functional role of this apparent uptake of biotin, we cannot offer any speculation, and only point at the unique demands on the vascular system placed on it by the high metabolic demands of the auditory midbrain (Ball et al. 2007).

6.6 Conclusion

Current-clamp stimuli used in this study permitted the identification of various previously unreported responses in ICC neurons. The identification of the fixed point bifucation as an Andronov-Hopf type suggests certain response properties, such as resonance, and bi-directional phase resetting response. Additionally, this identification indicates the relationship between activation of fast voltage gated sodium and potassium currents, as is necessary for the development of accurate conductance based models. Frequency selectivity, observed as resonance, was also a product of the fixed point bifucation type, in addition to contributions made by the slow accommodating current I_h. Aside from responses related to spike generation, discrete subthreshold events were also observed, and included transient hyperpolarizations and spikelets. The sensitivity of spikelets to TTX indicates a distinct mechanism in comparison to transient hyperpolarizations, where the involvement of calcium activated potassium channels is indicated in the generation of transient hyperpolarizations. Unfortunately, no morphological correlation was observed between spiking response types, or other response features.

APPENDIX A: INTRACELLULAR BIOTIN LABELLING

Two examples of intracellular biotin labelled neurons are shown, with thin dendritic processes emanating from the soma (*). Biotin labelling was also observed in vasculature (arrow), and can be distinguished from the dendrites by its larger size. Scale bar is 10 µM.

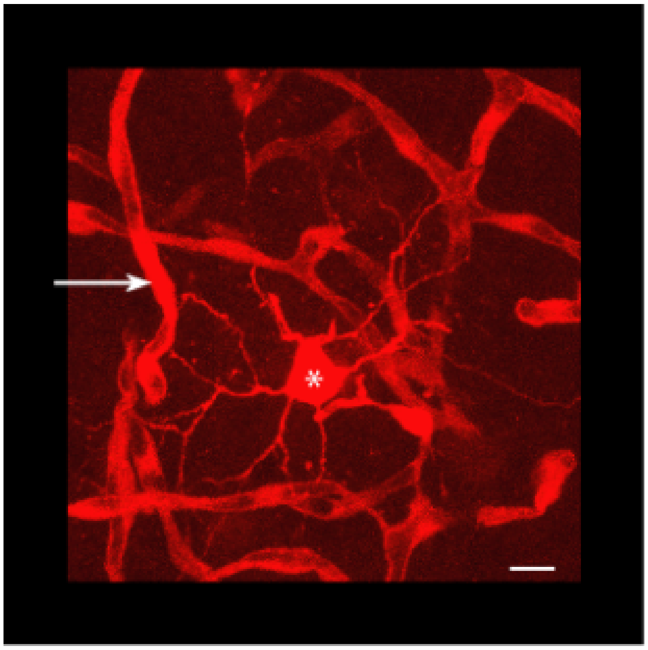

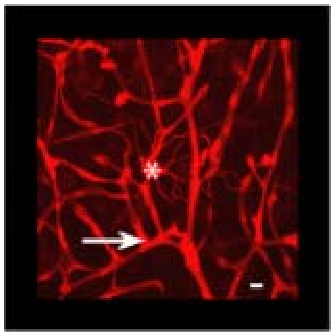

References

Abel, H. J., J. C. Lee, et al. (2004). "Relationships between intracellular calcium and afterhyperpolarizations in neocortical pyramidal neurons." J Neurophysiol **91**(1): 324-35.

Adams, J. C. and E. Mugnaini (1987). "Patterns of glutamate decarboxylase immunostaining in the feline cochlear nuclear complex studied with silver enhancement and electron microscopy." J Comp Neurol **262**(3): 375-401.

Aitkin, L. M., H. Dickhaus, et al. (1978). "External nucleus of inferior colliculus: auditory and spinal somatosensory afferents and their interactions." J Neurophysiol **41**(4): 837-47.

Aitkin, L. M. and S. C. Phillips (1984). "The interconnections of the inferior colliculi through their commissure." J Comp Neurol **228**(2): 210-6.

Aitkin, L. M. and S. C. Phillips (1984). "Is the inferior colliculus an obligatory relay in the cat auditory system?" Neurosci Lett **44**(3): 259-64.

Aizenman, C. D. and D. J. Linden (1999). "Regulation of the rebound depolarization and spontaneous firing patterns of deep nuclear neurons in slices of rat cerebellum." J Neurophysiol **82**(4): 1697-709.

Alitto, H. J. and W. M. Usrey (2003). "Corticothalamic feedback and sensory processing." Curr Opin Neurobiol **13**(4): 440-5.

Andersen, R. A., G. L. Roth, et al. (1980). "The efferent projections of the central nucleus and the pericentral nucleus of the inferior colliculus in the cat." J Comp Neurol **194**(3): 649-62.

Antal, M., M. Eyre, et al. (2006). "External tufted cells in the main olfactory bulb form two distinct subpopulations." Eur J Neurosci **24**(4): 1124-36.

Arima, J., N. Matsumoto, et al. (2001). "Spontaneous miniature outward currents in mechanically dissociated rat Meynert neurons." J Physiol **534**(Pt 1): 99-107.

Bal, R., G. G. Green, et al. (2002). "Firing patterns of inferior colliculus neurons-histology and mechanism to change firing patterns in rat brain slices." Neurosci Lett **317**(1): 42-6.

Ball, K. K., G. K. Gandhi, et al. (2007). "Astrocytic connexin distributions and rapid, extensive dye transfer via gap junctions in the inferior colliculus: Implications for [(14)C]glucose metabolite trafficking." J Neurosci Res.

Bao, J., J. J. Li, et al. (1998). "Differences in Ca2+ channels governing generation of miniature and evoked excitatory synaptic currents in spinal laminae I and II." J Neurosci **18**(21): 8740-50.

Barry, P. H. (1994). "JPCalc, a software package for calculating liquid junction potential corrections in patch-clamp, intracellular, epithelial and bilayer measurements and for correcting junction potential measurements." J Neurosci Methods **51**(1): 107-16.

Ben-Chaim, Y., B. Chanda, et al. (2006). "Movement of 'gating charge' is coupled to ligand binding in a G-protein-coupled receptor." Nature **444**(7115): 106-9.

Berrebi, A. S. and E. Mugnaini (1991). "Distribution and targets of the cartwheel cell axon in the dorsal cochlear nucleus of the guinea pig." Anat Embryol (Berl) **183**(5): 427-54.

Bleakman, D., J. D. Roback, et al. (1993). "Calcium homeostasis in rat septal neurons in tissue culture." Brain Res **600**(2): 257-67.

Bolton, T. B. and Y. Imaizumi (1996). "Spontaneous transient outward currents in smooth muscle cells." Cell Calcium **20**(2): 141-52.

Brown, P. D., S. L. Davies, et al. (2004). "Molecular mechanisms of cerebrospinal fluid production." Neuroscience **129**(4): 957-70.

Casseday, J. H., E. Covey, et al. (1997). "Neural selectivity and tuning for sinusoidal frequency modulations in the inferior colliculus of the big brown bat, Eptesicus fuscus." J Neurophysiol **77**(3): 1595-605.

Casseday, J. H., D. Ehrlich, et al. (2000). "Neural measurement of sound duration: control by excitatory-inhibitory interactions in the inferior colliculus." J Neurophysiol **84**(3): 1475-87.

Chatfield, C. (2004). The analysis of time series : an introduction. Boca Raton, FL, Chapman & Hall/CRC.

Connors, B. W. and M. J. Gutnick (1990). "Intrinsic firing patterns of diverse neocortical neurons." Trends Neurosci **13**(3): 99-104.

Cortes, R., A. Probst, et al. (1984). "Quantitative light microscopic autoradiographic localization of cholinergic muscarinic receptors in the human brain: brainstem." Neuroscience **12**(4): 1003-26.

Crawford, A. C. and R. Fettiplace (1981). "An electrical tuning mechanism in turtle cochlear hair cells." J Physiol **312**: 377-412.

Cui, G., T. Okamoto, et al. (2004). "Spontaneous opening of T-type Ca2+ channels contributes to the irregular firing of dopamine neurons in neonatal rats." J Neurosci **24**(49): 11079-87.

D'Angelo, W. R., S. J. Sterbing, et al. (2003). "Effects of amplitude modulation on the coding of interaural time differences of low-frequency sounds in the inferior colliculus. II. Neural mechanisms." J Neurophysiol **90**(5): 2827-36.

De Lorenzo, S., M. Veggetti, et al. (2006). "Presynaptic inhibition of spontaneous acetylcholine release mediated by P2Y receptors at the mouse neuromuscular junction." Neuroscience **142**(1): 71-85.

Dickson, C. T., J. Magistretti, et al. (2000). "Properties and role of I(h) in the pacing of subthreshold oscillations in entorhinal cortex layer II neurons." J Neurophysiol **83**(5): 2562-79.

Dickson, C. T., A. R. Mena, et al. (1997). "Electroresponsiveness of medial entorhinal cortex layer III neurons in vitro." Neuroscience **81**(4): 937-50.

Dodla, R., G. Svirskis, et al. (2006). "Well-timed, brief inhibition can promote spiking: postinhibitory facilitation." J Neurophysiol **95**(4): 2664-77.

Donishi, T., A. Kimura, et al. (2006). ""Ventral" area in the rat auditory cortex: a major auditory field connected with the dorsal division of the medial geniculate body." Neuroscience **141**(3): 1553-67.

Dorval, A. D., Jr. and J. A. White (2005). "Channel noise is essential for perithreshold oscillations in entorhinal stellate neurons." J Neurosci **25**(43): 10025-8.

Emptage, N., T. V. Bliss, et al. (1999). "Single synaptic events evoke NMDA receptor-mediated release of calcium from internal stores in hippocampal dendritic spines." Neuron **22**(1): 115-24.

Erchova, I., G. Kreck, et al. (2004). "Dynamics of rat entorhinal cortex layer II and III cells: characteristics of membrane potential resonance at rest predict oscillation properties near threshold." J Physiol **560**(Pt 1): 89-110.

Ermentrout, B. (1996). "Type I membranes, phase resetting curves, and synchrony." Neural Comput **8**(5): 979-1001.

Escabi, M. A., L. M. Miller, et al. (2003). "Naturalistic auditory contrast improves spectrotemporal coding in the cat inferior colliculus." J Neurosci **23**(37): 11489-504.

Fernandez, F. R., J. D. Engbers, et al. (2007). "Firing dynamics of cerebellar purkinje cells." J Neurophysiol **98**(1): 278-94.

Fernandez, F. R., W. H. Mehaffey, et al. (2005). "High-threshold K+ current increases gain by offsetting a frequency-dependent increase in low-threshold K+ current." J Neurosci **25**(2): 363-71.

Fernandez, F. R., W. H. Mehaffey, et al. (2005). "Dendritic Na+ current inactivation can increase cell excitability by delaying a somatic depolarizing afterpotential." J Neurophysiol **94**(6): 3836-48.

Fiorillo, C. D. and J. T. Williams (2000). "Cholinergic inhibition of ventral midbrain dopamine neurons." J Neurosci **20**(20): 7855-60.

Fitzhugh, R. (1960). "Thresholds and plateaus in the Hodgkin-Huxley nerve equations." J Gen Physiol **43**: 867-96.

Fletcher, G. H. and V. A. Chiappinelli (1992). "Spontaneous miniature hyperpolarizations of presynaptic nerve terminals in the chick ciliary ganglion." Brain Res **579**(1): 165-8.

Fransen, E., A. A. Alonso, et al. (2004). "Ionic mechanisms in the generation of subthreshold oscillations and action potential clustering in entorhinal layer II stellate neurons." Hippocampus **14**(3): 368-84.

Fuentealba, P., S. Crochet, et al. (2004). "Experimental evidence and modeling studies support a synchronizing role for electrical coupling in the cat thalamic reticular neurons in vivo." Eur J Neurosci **20**(1): 111-9.

Galan, R. F., G. B. Ermentrout, et al. (2005). "Efficient estimation of phase-resetting curves in real neurons and its significance for neural-network modeling." Phys Rev Lett **94**(15): 158101.

Galan, R. F., N. Fourcaud-Trocme, et al. (2006). "Correlation-induced synchronization of oscillations in olfactory bulb neurons." J Neurosci **26**(14): 3646-55.

Galan, R. F., M. Weidert, et al. (2006). "Sensory memory for odors is encoded in spontaneous correlated activity between olfactory glomeruli." Neural Comput **18**(1): 10-25.

Gibson, J. R., M. Beierlein, et al. (1999). "Two networks of electrically coupled inhibitory neurons in neocortex." Nature **402**(6757): 75-9.

Giocomo, L. M., E. A. Zilli, et al. (2007). "Temporal frequency of subthreshold oscillations scales with entorhinal grid cell field spacing." Science **315**(5819): 1719-22.

Gordon, G. R., D. V. Baimoukhametova, et al. (2005). "Norepinephrine triggers release of glial ATP to increase postsynaptic efficacy." Nat Neurosci **8**(8): 1078-86.

Grabe, M., H. C. Lai, et al. (2007). "Structure prediction for the down state of a potassium channel voltage sensor." Nature **445**(7127): 550-3.

Guckenheimer, J. and J. S. Labouriau (1992). "Bifurcation of the Hodgkin and Huxley equations: A new twist." Bulletin of Mathematical Biology **55**(5): 937-952.

Gulledge, A. T. and G. J. Stuart (2005). "Cholinergic inhibition of neocortical pyramidal neurons." J Neurosci **25**(44): 10308-20.

Haas, J. S., A. D. Dorval, 2nd, et al. (2007). "Contributions of Ih to feature selectivity in layer II stellate cells of the entorhinal cortex." J Comput Neurosci **22**(2): 161-71.

Hagenston, A. M., J. S. Fitzpatrick, et al. (2007). "MGluR-Mediated Calcium Waves that Invade the Soma Regulate Firing in Layer V Medial Prefrontal Cortical Pyramidal Neurons." Cereb Cortex.

Hansel, D., G. Mato, et al. (1995). "Synchrony in excitatory neural networks." Neural Comput **7**(2): 307-37.

Harty, T. P. and P. B. Manis (1998). "Kinetic analysis of glycine receptor currents in ventral cochlear nucleus." J Neurophysiol **79**(4): 1891-901.

Heister, D. S., A. Hayar, et al. (2007). "Evidence for Electrical Coupling in the SubCoeruleus (SubC) Nucleus." J Neurophysiol **97**(4): 3142-7.

Henderson, Z. and F. E. Sherriff (1991). "Distribution of choline acetyltransferase immunoreactive axons and terminals in the rat and ferret brainstem." J Comp Neurol **314**(1): 147-63.

Heyward, P., M. Ennis, et al. (2001). "Membrane bistability in olfactory bulb mitral cells." J Neurosci **21**(14): 5311-20.

Hille, B. (2001). Ion channels of excitable membranes. Sunderland, Mass., Sinauer.

Hodgkin, A. L. (1948). "The local electric changes associated with repetitive action in a non-medullated axon." J Physiol **107**(2): 165-81.

Hodgkin, A. L. and A. F. Huxley (1952). "A quantitative description of membrane current and its application to conduction and excitation in nerve." J Physiol **117**(4): 500-44.

Hodgkin, A. L. and B. Katz (1949). "The effect of sodium ions on the electrical activity of the giant axon of the squid." J Physiol **108**(1): 37-77.

Hu, B. (2003). "Functional organization of lemniscal and nonlemniscal auditory thalamus." Exp Brain Res **153**(4): 543-9.

Hu, H., K. Vervaeke, et al. (2002). "Two forms of electrical resonance at theta frequencies, generated by M-current, h-current and persistent Na+ current in rat hippocampal pyramidal cells." J Physiol **545**(Pt 3): 783-805.

Huang, C. L. and J. A. Winer (2000). "Auditory thalamocortical projections in the cat: laminar and areal patterns of input." J Comp Neurol **427**(2): 302-31.

Huffman, R. F. and O. W. Henson, Jr. (1990). "The descending auditory pathway and acousticomotor systems: connections with the inferior colliculus." Brain Res Brain Res Rev **15**(3): 295-323.

Hughes, S. W., K. L. Blethyn, et al. (2002). "Properties and origin of spikelets in thalamocortical neurones in vitro." Neuroscience **110**(3): 395-401.

Hughes, S. W., D. W. Cope, et al. (1999). "All thalamocortical neurones possess a T-type Ca2+ 'window' current that enables the expression of bistability-mediated activities." J Physiol **517 (Pt 3)**: 805-15.

Hutcheon, B., R. M. Miura, et al. (1996). "Subthreshold membrane resonance in neocortical neurons." J Neurophysiol **76**(2): 683-97.

Hutcheon, B. and Y. Yarom (2000). "Resonance, oscillation and the intrinsic frequency preferences of neurons." Trends Neurosci **23**(5): 216-22.

Imig, T. J. and A. Morel (1985). "Tonotopic organization in ventral nucleus of medial geniculate body in the cat." J Neurophysiol **53**(1): 309-40.

Izhikevich, E. M. (2007). Dynamical systems in neuroscience : the geometry of excitability and bursting. Cambridge, Mass., MIT Press.

Izhikevich, E. M., J. A. Gally, et al. (2004). "Spike-timing dynamics of neuronal groups." Cereb Cortex **14**(8): 933-44.

Jen, P. H. and X. Zhou (2003). "Corticofugal modulation of amplitude domain processing in the midbrain of the big brown bat, Eptesicus fuscus." Hear Res **184**(1-2): 91-106.

Jen, P. H., X. Zhou, et al. (2002). "Brief and short-term corticofugal modulation of acoustic signal processing in the bat midbrain." Hear Res **168**(1-2): 196-207.

Johnston, D. and S. M.-s. Wu (1995). Foundations of cellular neurophysiology. Cambridge, Mass., MIT Press.

Joris, P. X., C. E. Schreiner, et al. (2004). "Neural processing of amplitude-modulated sounds." Physiol Rev **84**(2): 541-77.

Kim, H. C. and M. K. Chung (1999). "Voltage-dependent sodium and calcium currents in acutely isolated adult rat trigeminal root ganglion neurons." J Neurophysiol **81**(3): 1123-34.

Kimura, A., T. Donishi, et al. (2003). "Auditory thalamic nuclei projections to the temporal cortex in the rat." Neuroscience **117**(4): 1003-16.

Koch, C. and I. Segev (1998). Methods in neuronal modeling : from ions to networks. Cambridge, Mass., MIT Press.

Koch, U., M. Braun, et al. (2004). "Distribution of HCN1 and HCN2 in rat auditory brainstem nuclei." Eur J Neurosci **20**(1): 79-91.

Koch, U. and B. Grothe (2003). "Hyperpolarization-activated current (Ih) in the inferior colliculus: distribution and contribution to temporal processing." J Neurophysiol **90**(6): 3679-87.

Komura, Y., R. Tamura, et al. (2005). "Auditory thalamus integrates visual inputs into behavioral gains." Nat Neurosci **8**(9): 1203-9.

Kulesza, R. J., A. Vinuela, et al. (2002). "Unbiased stereological estimates of neuron number in subcortical auditory nuclei of the rat." Hear Res **168**(1-2): 12-24.

Kuno, M. and J. N. Weakly (1972). "Quantal components of the inhibitory synaptic potential in spinal mononeurones of the cat." J Physiol **224**(2): 287-303.

Kuramoto, Y. (1984). Chemical oscillations, waves, and turbulence. Berlin ; New York, Springer-Verlag.

Kuwabara, N. and J. M. Zook (2000). "Geniculo-collicular descending projections in the gerbil." Brain Res **878**(1-2): 79-87.

Kuwada, S., R. Batra, et al. (1997). "Intracellular recordings in response to monaural and binaural stimulation of neurons in the inferior colliculus of the cat." J Neurosci **17**(19): 7565-81.

Lacinova, L. (2005). "Voltage-dependent calcium channels." Gen Physiol Biophys **24 Suppl 1**: 1-78.

Las, L., E. A. Stern, et al. (2005). "Representation of tone in fluctuating maskers in the ascending auditory system." J Neurosci **25**(6): 1503-13.

Leung, L. S. and H. W. Yu (1998). "Theta-frequency resonance in hippocampal CA1 neurons in vitro demonstrated by sinusoidal current injection." J Neurophysiol **79**(3): 1592-6.

Li, Y., M. S. Evans, et al. (1998). "In vitro electrophysiology of neurons in subnuclei of rat inferior colliculus." Hear Res **121**(1-2): 1-10.

Linke, R., A. D. De Lima, et al. (1999). "Direct synaptic connections of axons from superior colliculus with identified thalamo-amygdaloid projection neurons in the rat: possible substrates of a subcortical visual pathway to the amygdala." J Comp Neurol **403**(2): 158-70.

Lohmann, C., K. L. Myhr, et al. (2002). "Transmitter-evoked local calcium release stabilizes developing dendrites." Nature **418**(6894): 177-81.

Longtin, A. and J. G. Milton (1989). "Modelling autonomous oscillations in the human pupil light reflex using non-linear delay-differential equations." Bull Math Biol **51**(5): 605-24.

Luthi, A. and D. A. McCormick (1999). "Modulation of a pacemaker current through Ca(2+)-induced stimulation of cAMP production." Nat Neurosci **2**(7): 634-41.

Ma, X. and N. Suga (2001). "Corticofugal modulation of duration-tuned neurons in the midbrain auditory nucleus in bats." Proc Natl Acad Sci U S A **98**(24): 14060-5.

Ma, X. and N. Suga (2007). "Multiparametric corticofugal modulation of collicular duration-tuned neurons: modulation in the amplitude domain." J Neurophysiol **97**(5): 3722-30.

Magistretti, J., L. Castelli, et al. (2006). "Kinetic and functional analysis of transient, persistent and resurgent sodium currents in rat cerebellar granule cells in situ: an electrophysiological and modelling study." J Physiol **573**(Pt 1): 83-106.

Maher, B. J. and G. L. Westbrook (2005). "SK channel regulation of dendritic excitability and dendrodendritic inhibition in the olfactory bulb." J Neurophysiol **94**(6): 3743-50.

Malmierca, M. S., M. A. Merchan, et al. (2002). "Direct projections from cochlear nuclear complex to auditory thalamus in the rat." J Neurosci **22**(24): 10891-7.

Malmierca, M. S., R. L. Saint Marie, et al. (2005). "Laminar inputs from dorsal cochlear nucleus and ventral cochlear nucleus to the central nucleus of the inferior colliculus: two patterns of convergence." Neuroscience **136**(3): 883-94.

Manis, P. B., S. C. Molitor, et al. (2003). "Subthreshold oscillations generated by TTX-sensitive sodium currents in dorsal cochlear nucleus pyramidal cells." Exp Brain Res **153**(4): 443-51.

Marmarelis, P. Z. and V. Z. Marmarelis (1978). Analysis of physiological systems : the white-noise approach. New York, Plenum Press.

Mathers, D. A. and J. L. Barker (1981). "Spontaneous hyperpolarizations at the membrane of cultured mouse dorsal root ganglion cells." Brain Res **211**(2): 451-5.

Mathers, D. A. and J. L. Barker (1984). "Spontaneous voltage and current fluctuations in tissue cultured mouse dorsal root ganglion cells." Brain Res **293**(1): 35-47.

Mattson, M. P., C. Culmsee, et al. (2000). "Apoptotic and antiapoptotic mechanisms in stroke." Cell Tissue Res **301**(1): 173-87.

McCormick, D. A. and H. C. Pape (1990). "Properties of a hyperpolarization-activated cation current and its role in rhythmic oscillation in thalamic relay neurones." J Physiol **431**: 291-318.

McCown, T. J. and G. R. Breese (1990). "Effects of apamin and nicotinic acetylcholine receptor antagonists on inferior collicular seizures." Eur J Pharmacol **187**(1): 49-58.

McKay, B. E., M. L. Molineux, et al. (2004). "Biotin is endogenously expressed in select regions of the rat central nervous system." J Comp Neurol **473**(1): 86-96.

McKay, B. E. and R. W. Turner (2005). "Physiological and morphological development of the rat cerebellar Purkinje cell." J Physiol **567**(Pt 3): 829-50.

Merriam, L. A., F. S. Scornik, et al. (1999). "Ca(2+)-induced Ca(2+) release activates spontaneous miniature outward currents (SMOCs) in parasympathetic cardiac neurons." J Neurophysiol **82**(2): 540-50.

Mitra, P. and M. M. Slaughter (2002). "Calcium-induced transitions between the spontaneous miniature outward and the transient outward currents in retinal amacrine cells." J Gen Physiol **119**(4): 373-88.

Mitra, P. and M. M. Slaughter (2002). "Mechanism of generation of spontaneous miniature outward currents (SMOCs) in retinal amacrine cells." J Gen Physiol **119**(4): 355-72.

Mogami, H., C. Lloyd Mills, et al. (1997). "Phospholipase C inhibitor, U73122, releases intracellular Ca2+, potentiates Ins(1,4,5)P3-mediated Ca2+ release and directly activates ion channels in mouse pancreatic acinar cells." Biochem J **324 (Pt 2)**: 645-51.

Molineux, M. L., F. R. Fernandez, et al. (2005). "A-type and T-type currents interact to produce a novel spike latency-voltage relationship in cerebellar stellate cells." J Neurosci **25**(47): 10863-73.

Molineux, M. L., J. E. McRory, et al. (2006). "Specific T-type calcium channel isoforms are associated with distinct burst phenotypes in deep cerebellar nuclear neurons." Proc Natl Acad Sci U S A **103**(14): 5555-60.

Møller, A. R., P. Boston, et al. (1973). Basic mechanisms in hearing. New York,, Academic Press.

Morikawa, H., K. Khodakhah, et al. (2003). "Two intracellular pathways mediate metabotropic glutamate receptor-induced Ca2+ mobilization in dopamine neurons." J Neurosci **23**(1): 149-57.

Morley, B. J. and H. K. Happe (2000). "Cholinergic receptors: dual roles in transduction and plasticity." Hear Res **147**(1-2): 104-12.

Morris, M. E., J. J. Friedlich, et al. (1987). "Intracellular calcium in mammalian brain cells: fluorescence measurements with quin2." Exp Brain Res **65**(3): 520-6.

Morris, M. E., J. F. MacDonald, et al. (1987). "Intracellular calcium recordings from isolated cells of the mammalian central nervous system." Can J Physiol Pharmacol **65**(5): 926-33.

Namura, S., M. Takada, et al. (1997). "Collateral projections of single neurons in the posterior thalamic region to both the temporal cortex and the amygdala: a fluorescent retrograde double-labeling study in the rat." J Comp Neurol **384**(1): 59-70.

Nayagam, D. A., J. C. Clarey, et al. (2005). "Powerful, onset inhibition in the ventral nucleus of the lateral lemniscus." J Neurophysiol **94**(2): 1651-4.

Nelson, P. C. and L. H. Carney (2007). "Neural rate and timing cues for detection and discrimination of amplitude-modulated tones in the awake rabbit inferior colliculus." J Neurophysiol **97**(1): 522-39.

N'Gouemo, P. and M. Morad (2003). "Voltage-gated calcium channels in adult rat inferior colliculus neurons." Neuroscience **120**(3): 815-26.

Nowak, L. G., R. Azouz, et al. (2003). "Electrophysiological classes of cat primary visual cortical neurons in vivo as revealed by quantitative analyses." J Neurophysiol **89**(3): 1541-66.

O'Keefe, J. and N. Burgess (2005). "Dual phase and rate coding in hippocampal place cells: theoretical significance and relationship to entorhinal grid cells." Hippocampus **15**(7): 853-66.

Olesen, S. P., E. Munch, et al. (1994). "Selective activation of Ca(2+)-dependent K+ channels by novel benzimidazolone." Eur J Pharmacol **251**(1): 53-9.

Oliver, D. L., S. Kuwada, et al. (1991). "Dendritic and axonal morphology of HRP-injected neurons in the inferior colliculus of the cat." J Comp Neurol **303**(1): 75-100.

Oliver, D. L., J. A. Winer, et al. (1994). "Morphology of GABAergic neurons in the inferior colliculus of the cat." J Comp Neurol **340**(1): 27-42.

Olsen, J. F. and N. Suga (1991). "Combination-sensitive neurons in the medial geniculate body of the mustached bat: encoding of relative velocity information." J Neurophysiol **65**(6): 1254-74.

Olsen, J. F. and N. Suga (1991). "Combination-sensitive neurons in the medial geniculate body of the mustached bat: encoding of target range information." J Neurophysiol **65**(6): 1275-96.

Ono, M., Y. Yanagawa, et al. (2005). "GABAergic neurons in inferior colliculus of the GAD67-GFP knock-in mouse: electrophysiological and morphological properties." Neurosci Res **51**(4): 475-92.

Osen, K. K. (1972). "Projection of the cochlear nuclei on the inferior colliculus in the cat." J Comp Neurol **144**(3): 355-72.

Ospeck, M., V. M. Eguiluz, et al. (2001). "Evidence of a Hopf bifurcation in frog hair cells." Biophys J **80**(6): 2597-607.

Oswald, A. M., M. J. Chacron, et al. (2004). "Parallel processing of sensory input by bursts and isolated spikes." J Neurosci **24**(18): 4351-62.

Parnas, H. and I. Parnas (2007). "The chemical synapse goes electric: Ca2+- and voltage-sensitive GPCRs control neurotransmitter release." Trends Neurosci **30**(2): 54-61.

Parsons, R. L., K. L. Barstow, et al. (2002). "Spontaneous miniature hyperpolarizations affect threshold for action potential generation in mudpuppy cardiac neurons." J Neurophysiol **88**(3): 1119-27.

Pedarzani, P., J. E. McCutcheon, et al. (2005). "Specific enhancement of SK channel activity selectively potentiates the afterhyperpolarizing current I(AHP) and modulates the firing properties of hippocampal pyramidal neurons." J Biol Chem **280**(50): 41404-11.

Peruzzi, D., S. Sivaramakrishnan, et al. (2000). "Identification of cell types in brain slices of the inferior colliculus." Neuroscience **101**(2): 403-16.

Pinato, G. and J. Midtgaard (2005). "Dendritic sodium spikelets and low-threshold calcium spikes in turtle olfactory bulb granule cells." J Neurophysiol **93**(3): 1285-94.

Popper, A. N. and R. R. Fay (1992). The Mammalian auditory pathway : neurophysiology. New York, Springer-Verlag.

Puil, E., B. Gimbarzevsky, et al. (1986). "Quantification of membrane properties of trigeminal root ganglion neurons in guinea pigs." J Neurophysiol **55**(5): 995-1016.

Puil, E., B. Gimbarzevsky, et al. (1987). "Voltage dependence of membrane properties of trigeminal root ganglion neurons." J Neurophysiol **58**(1): 66-86.

Puil, E., B. Gimbarzevsky, et al. (1988). "Primary involvement of K+ conductance in membrane resonance of trigeminal root ganglion neurons." J Neurophysiol **59**(1): 77-89.

Puil, E., H. Meiri, et al. (1994). "Resonant behavior and frequency preferences of thalamic neurons." J Neurophysiol **71**(2): 575-82.

Puil, E., R. M. Miura, et al. (1989). "Consequences of 4-aminopyridine applications to trigeminal root ganglion neurons." J Neurophysiol **62**(3): 810-20.

Raza, A., J. C. Milbrandt, et al. (1994). "Age-related changes in brainstem auditory neurotransmitters: measures of GABA and acetylcholine function." Hear Res **77**(1-2): 221-30.

Reetz, G. and G. Ehret (1999). "Inputs from three brainstem sources to identified neurons of the mouse inferior colliculus slice." Brain Res **816**(2): 527-43.

Regenold, W., D. M. Araujo, et al. (1989). "Quantitative autoradiographic distribution of [3H]AF-DX 116 muscarinic-M2 receptor binding sites in rat brain." Synapse **4**(2): 115-25.

Reyes, A. D. and E. E. Fetz (1993). "Two modes of interspike interval shortening by brief transient depolarizations in cat neocortical neurons." J Neurophysiol **69**(5): 1661-72.

Richardson, M. J., N. Brunel, et al. (2003). "From subthreshold to firing-rate resonance." J Neurophysiol **89**(5): 2538-54.

Ross, W. N., T. Nakamura, et al. (2005). "Synaptically activated ca2+ release from internal stores in CNS neurons." Cell Mol Neurobiol **25**(2): 283-95.

Rothman, J. S. and P. B. Manis (2003). "Differential expression of three distinct potassium currents in the ventral cochlear nucleus." J Neurophysiol **89**(6): 3070-82.

Rothman, J. S. and P. B. Manis (2003). "Kinetic analyses of three distinct potassium conductances in ventral cochlear nucleus neurons." J Neurophysiol **89**(6): 3083-96.

Rotstein, H. G., T. Oppermann, et al. (2006). "The dynamic structure underlying subthreshold oscillatory activity and the onset of spikes in a model of medial entorhinal cortex stellate cells." J Comput Neurosci **21**(3): 271-92.

Sah, P. (1996). "Ca(2+)-activated K+ currents in neurones: types, physiological roles and modulation." Trends Neurosci **19**(4): 150-4.

Sah, P. and E. S. Faber (2002). "Channels underlying neuronal calcium-activated potassium currents." Prog Neurobiol **66**(5): 345-53.

Sailer, C. A., W. A. Kaufmann, et al. (2004). "Comparative immunohistochemical distribution of three small-conductance Ca2+-activated potassium channel subunits, SK1, SK2, and SK3 in mouse brain." Mol Cell Neurosci **26**(3): 458-69.

Saint Marie, R. L., A. Shneiderman, et al. (1997). "Patterns of gamma-aminobutyric acid and glycine immunoreactivities reflect structural and functional differences of the cat lateral lemniscal nuclei." J Comp Neurol **389**(2): 264-76.

Saldana, E., M. Feliciano, et al. (1996). "Distribution of descending projections from primary auditory neocortex to inferior colliculus mimics the topography of intracollicular projections." J Comp Neurol **371**(1): 15-40.

Satin, L. S. and P. R. Adams (1987). "Spontaneous miniature outward currents in cultured bullfrog neurons." Brain Res **401**(2): 331-9.

Schoppa, N. E. and G. L. Westbrook (1997). "Modulation of mEPSCs in olfactory bulb mitral cells by metabotropic glutamate receptors." J Neurophysiol **78**(3): 1468-75.

Schreiber, S., I. Erchova, et al. (2004). "Subthreshold resonance explains the frequency-dependent integration of periodic as well as random stimuli in the entorhinal cortex." J Neurophysiol **92**(1): 408-15.

Schwartz, R. D., R. McGee, Jr., et al. (1982). "Nicotinic cholinergic receptors labeled by [3H]acetylcholine in rat brain." Mol Pharmacol **22**(1): 56-62.

Scornik, F. S., L. A. Merriam, et al. (2001). "Number of K(Ca) channels underlying spontaneous miniature outward currents (SMOCs) in mudpuppy cardiac neurons." J Neurophysiol **85**(1): 54-60.

Shapiro, N. P. and R. H. Lee (2007). "Synaptic amplification versus bistability in motoneuron dendritic processing: a top-down modeling approach." J Neurophysiol **97**(6): 3948-60.

Sherman, S. M. and R. W. Guillery (2006). Exploring the thalamus and its role in cortical function. Cambridge, Mass., MIT Press.

Shore, S. E. and J. Zhou (2006). "Somatosensory influence on the cochlear nucleus and beyond." Hear Res **216-217**: 90-9.

Sivaramakrishnan, S. and D. L. Oliver (2001). "Distinct K currents result in physiologically distinct cell types in the inferior colliculus of the rat." J Neurosci **21**(8): 2861-77.

Sivaramakrishnan, S. and D. L. Oliver (2006). "Neuronal responses to lemniscal stimulation in laminar brain slices of the inferior colliculus." J Assoc Res Otolaryngol **7**(1): 1-14.

Sivaramakrishnan, S., S. J. Sterbing-D'Angelo, et al. (2004). "GABA(A) synapses shape neuronal responses to sound intensity in the inferior colliculus." J Neurosci **24**(21): 5031-43.

Smith, E. and M. S. Lewicki (2005). "Efficient coding of time-relative structure using spikes." Neural Comput **17**(1): 19-45.

Smith, E. C. and M. S. Lewicki (2006). "Efficient auditory coding." Nature **439**(7079): 978-82.

Sodickson, D. L. and B. P. Bean (1996). "GABAB receptor-activated inwardly rectifying potassium current in dissociated hippocampal CA3 neurons." J Neurosci **16**(20): 6374-85.

Sohl, G., S. Maxeiner, et al. (2005). "Expression and functions of neuronal gap junctions." Nat Rev Neurosci **6**(3): 191-200.

Sterbing, S. J., W. R. D'Angelo, et al. (2003). "Effects of amplitude modulation on the coding of interaural time differences of low-frequency sounds in the inferior colliculus. I. Response properties." J Neurophysiol **90**(5): 2818-26.

Stocker, M. (2004). "Ca(2+)-activated K+ channels: molecular determinants and function of the SK family." Nat Rev Neurosci **5**(10): 758-70.

Strobaek, D., T. D. Jorgensen, et al. (2000). "Pharmacological characterization of small-conductance Ca(2+)-activated K(+) channels stably expressed in HEK 293 cells." Br J Pharmacol **129**(5): 991-9.

Strogatz, S. H. (2000). Nonlinear dynamics and chaos : with applications to physics, biology, chemistry, and engineering. Cambridge, MA, Westview Press.

Strohmann, B., D. W. Schwarz, et al. (1994). "Subthreshold frequency selectivity in avian auditory thalamus." J Neurophysiol **71**(4): 1361-72.

Strohmann, B., D. W. Schwarz, et al. (1995). "Electrical resonances in central auditory neurons." Acta Otolaryngol **115**(2): 168-72.

Suga, N. and X. Ma (2003). "Multiparametric corticofugal modulation and plasticity in the auditory system." Nat Rev Neurosci **4**(10): 783-94.

Takahashi, T. T., A. D. Bala, et al. (2003). "The synthesis and use of the owl's auditory space map." Biol Cybern **89**(5): 378-87.

Talley, E. M., L. L. Cribbs, et al. (1999). "Differential distribution of three members of a gene family encoding low voltage-activated (T-type) calcium channels." J Neurosci **19**(6): 1895-911.

Tan, M. L. and J. G. Borst (2007). "Comparison of responses of neurons in the mouse inferior colliculus to current injections, tones of different durations, and sinusoidal amplitude-modulated tones." J Neurophysiol **98**(1): 454-66.

Tan, M. L., H. P. Theeuwes, et al. (2007). "Membrane properties and firing patterns of inferior colliculus neurons: an in vivo patch-clamp study in rodents." J Neurophysiol **98**(1): 443-53.

Tatehata, T., S. Shiosaka, et al. (1987). "Immunocytochemical localization of the choline acetyltransferase containing neuron system in the rat lower brain stem." J Hirnforsch **28**(6): 707-16.

Tateno, T., A. Harsch, et al. (2004). "Threshold firing frequency-current relationships of neurons in rat somatosensory cortex: type 1 and type 2 dynamics." J Neurophysiol **92**(4): 2283-94.

Tempia, F., M. Kano, et al. (1996). "Fractional calcium current through neuronal AMPA-receptor channels with a low calcium permeability." J Neurosci **16**(2): 456-66.

Ulrich, D. (2002). "Dendritic resonance in rat neocortical pyramidal cells." J Neurophysiol **87**(6): 2753-9.

Vale, C., J. Schoorlemmer, et al. (2003). "Deafness disrupts chloride transporter function and inhibitory synaptic transmission." J Neurosci **23**(20): 7516-24.

Vogalis, F., J. F. Storm, et al. (2003). "SK channels and the varieties of slow after-hyperpolarizations in neurons." Eur J Neurosci **18**(12): 3155-66.

Vogels, T. P. and L. F. Abbott (2005). "Signal propagation and logic gating in networks of integrate-and-fire neurons." J Neurosci **25**(46): 10786-95.

Wagner, H., T. Takahashi, et al. (1987). "Representation of interaural time difference in the central nucleus of the barn owl's inferior colliculus." J Neurosci **7**(10): 3105-16.

Wang, W. T., Y. H. Wan, et al. (2006). "Theta-frequency membrane resonance and its ionic mechanisms in rat subicular pyramidal neurons." Neuroscience **140**(1): 45-55.

Webster, D. B., A. N. Popper, et al. (1992). The Mammalian auditory pathway : neuroanatomy. New York, Springer-Verlag.

White, J. A., R. Klink, et al. (1998). "Noise from voltage-gated ion channels may influence neuronal dynamics in the entorhinal cortex." J Neurophysiol **80**(1): 262-9.

White, J. A., J. T. Rubinstein, et al. (2000). "Channel noise in neurons." Trends Neurosci **23**(3): 131-7.

Williams, S. R., S. R. Christensen, et al. (2002). "Membrane potential bistability is controlled by the hyperpolarization-activated current I(H) in rat cerebellar Purkinje neurons in vitro." J Physiol **539**(Pt 2): 469-83.

Wilson, C. J. (2005). "The mechanism of intrinsic amplification of hyperpolarizations and spontaneous bursting in striatal cholinergic interneurons." Neuron **45**(4): 575-85.

Winer, J. A., D. T. Larue, et al. (1998). "Auditory cortical projections to the cat inferior colliculus." J Comp Neurol **400**(2): 147-74.

Winer, J. A. and C. C. Lee (2007). "The distributed auditory cortex." Hear Res **229**(1-2): 3-13.

Winer, J. A. and C. Schreiner (2005). The inferior colliculus : with 168 illustrations. New York, NY, Springer.

Wu, N., A. Enomoto, et al. (2005). "Persistent sodium currents in mesencephalic v neurons participate in burst generation and control of membrane excitability." J Neurophysiol **93**(5): 2710-22.

Wu, S. H., C. L. Ma, et al. (2002). "Synaptic modification in neurons of the central nucleus of the inferior colliculus." Hear Res **168**(1-2): 43-54.

Xie, L. H., M. Horie, et al. (1999). "Phospholipase C-linked receptors regulate the ATP-sensitive potassium channel by means of phosphatidylinositol 4,5-bisphosphate metabolism." Proc Natl Acad Sci U S A **96**(26): 15292-7.

Yan, J. (2003). "Canadian Association of Neuroscience Review: development and plasticity of the auditory cortex." Can J Neurol Sci **30**(3): 189-200.

Yan, J. and G. Ehret (2002). "Corticofugal modulation of midbrain sound processing in the house mouse." Eur J Neurosci **16**(1): 119-28.

Yan, J., Y. Zhang, et al. (2005). "Corticofugal shaping of frequency tuning curves in the central nucleus of the inferior colliculus of mice." J Neurophysiol **93**(1): 71-83.

Yan, W. and N. Suga (1998). "Corticofugal modulation of the midbrain frequency map in the bat auditory system." Nat Neurosci **1**(1): 54-8.

Yin, T. C. and J. C. Chan (1990). "Interaural time sensitivity in medial superior olive of cat." J Neurophysiol **64**(2): 465-88.

Zar, J. H. (1974). Biostatistical analysis. Englewood Cliffs, N.J.,, Prentice-Hall.

Zhang, J. P., P. H. Jen, et al. (2000). "Direction-dependent corticofugal modulation of frequency-tuning curves of inferior collicular neurons in the big brown bat, Eptesicus fuscus." J Comp Physiol [A] **186**(10): 913-22.

Zhou, J. and S. Shore (2006). "Convergence of spinal trigeminal and cochlear nucleus projections in the inferior colliculus of the guinea pig." J Comp Neurol **495**(1): 100-12.

Zhou, X. and P. H. Jen (2000). "Corticofugal inhibition compresses all types of rate-intensity functions of inferior collicular neurons in the big brown bat." Brain Res **881**(1): 62-8.

Zhou, X. and P. H. Jen (2005). "Corticofugal modulation of directional sensitivity in the midbrain of the big brown bat, Eptesicus fuscus." Hear Res **203**(1-2): 201-15.